



National Library  
of Canada

Acquisitions and  
Bibliographic Services Branch

395 Wellington Street  
Ottawa, Ontario  
K1A 0N4

Bibliothèque nationale  
du Canada

Direction des acquisitions et  
des services bibliographiques

395, rue Wellington  
Ottawa (Ontario)  
K1A 0N4

Notice - Acquisitions

Notice - Acquisitions

## NOTICE

The quality of this microform is heavily dependent upon the quality of the original thesis submitted for microfilming. Every effort has been made to ensure the highest quality of reproduction possible.

If pages are missing, contact the university which granted the degree.

Some pages may have indistinct print especially if the original pages were typed with a poor typewriter ribbon or if the university sent us an inferior photocopy.

Reproduction in full or in part of this microform is governed by the Canadian Copyright Act, R.S.C. 1970, c. C-30, and subsequent amendments.

## AVIS

La qualité de cette microforme dépend grandement de la qualité de la thèse soumise au microfilmage. Nous avons tout fait pour assurer une qualité supérieure de reproduction.

S'il manque des pages, veuillez communiquer avec l'université qui a conféré le grade.

La qualité d'impression de certaines pages peut laisser à désirer, surtout si les pages originales ont été dactylographiées à l'aide d'un ruban usé ou si l'université nous a fait parvenir une photocopie de qualité inférieure.

La reproduction, même partielle, de cette microforme est soumise à la Loi canadienne sur le droit d'auteur, SRC 1970, c. C-30, et ses amendements subséquents.

**Canada**

**KINETICS OF REMOVAL OF CALCIUM AND SODIUM  
BY CHLORINATION FROM  
ALUMINUM AND ALUMINUM-1WT% MAGNESIUM ALLOYS**

by

**Bahadır Külünk**

A thesis submitted to the Faculty of Graduate Studies  
and Research in partial fulfillment of the  
requirements for the Degree of  
Doctor of Philosophy

**Department of Mining and Metallurgical Engineering  
McGill University  
Montreal, Canada  
© October 1992**



National Library  
of Canada

Acquisitions and  
Bibliographic Services Branch

395 Wellington Street  
Ottawa, Ontario  
K1A 0N4

Bibliothèque nationale  
du Canada

Direction des acquisitions et  
des services bibliographiques

395, rue Wellington  
Ottawa (Ontario)  
K1A 0N4

Author: Author/Thèse

Co-Editor: Acquisitions

**The author has granted an irrevocable non-exclusive licence allowing the National Library of Canada to reproduce, loan, distribute or sell copies of his/her thesis by any means and in any form or format, making this thesis available to interested persons.**

**The author retains ownership of the copyright in his/her thesis. Neither the thesis nor substantial extracts from it may be printed or otherwise reproduced without his/her permission.**

**L'auteur a accordé une licence irrévocable et non exclusive permettant à la Bibliothèque nationale du Canada de reproduire, prêter, distribuer ou vendre des copies de sa thèse de quelque manière et sous quelque forme que ce soit pour mettre des exemplaires de cette thèse à la disposition des personnes intéressées.**

**L'auteur conserve la propriété du droit d'auteur qui protège sa thèse. Ni la thèse ni des extraits substantiels de celle-ci ne doivent être imprimés ou autrement reproduits sans son autorisation.**

ISBN 0-315-87542-9

**Canada**

**Student's name: Bahadir Kulunk**

**Department: Mining and Metallurgical Engineering**

**Degree sought: Ph.D**

**Thesis title:**

**Kinetics of removal of Ca and Na by chlorination from Al and Al-1wt% Mg alloys**

## ABSTRACT

The kinetics of calcium and sodium removal at 730 °C by chlorination from commercial purity(99.7% Al) and aluminum-1wt% magnesium alloys has been investigated. The contribution of chlorine containing gas bubbles, of intermediate reaction products generated by the chlorination process, as well as evaporation through the melt surface, to the removal of calcium and/or sodium has been documented quantitatively. Experimental parameters investigated were chlorine concentration in the gas bubbles and gas flow rate. The measurement of frequency of bubble formation at the tip of the gas bubbling nozzle enabled the surface areas of the bubbles to be estimated which in turn enabled melt phase mass transfer coefficients for the bubbles to be calculated.

It was demonstrated that the removal of calcium and sodium followed first order reaction kinetics with respect to calcium and sodium concentrations. The removal of the above mentioned elements was represented well by a kinetic model in which mass transfer of sodium and calcium in melt phase was rate limiting.

In the case of the magnesium containing alloys, the  $MgCl_2$  salt phase that was generated during chlorination was found to have a profound effect on the removal of calcium and sodium. The contribution of the salt phase to the removal of these elements was calculated to reach as high as 60%. In commercial purity aluminum, however, while the major contribution to the removal of calcium was from the chlorine containing gas bubbles, the major contribution to the removal of sodium was calculated to be evaporation of sodium through the melt surface.

## RÉSUMÉ

Les cinétiques d'élimination du calcium et du sodium à 730°C par chloruration, des alliages d'aluminium de pureté commerciale (99.7% Al) et des alliages d'aluminium contenant 1% en poids de magnésium ont été étudiées. La contribution du chlore contenant des bulles de gaz, des produits de réactions intermédiaires générés par le processus de chloruration, ainsi que de l'évaporation à travers la surface du métal fondu, à l'élimination du calcium et/ou du sodium a été quantitativement analysée. Les paramètres expérimentaux examinés ont été la concentration de chlore dans les bulles de gaz et le débit de gaz. La mesure de la fréquence de formation des bulles à l'extrémité de la tuyère qui produit les bulles de gaz, a permis d'estimer la surface des bulles, paramètre qui, à son tour a permis le calcul des coefficients de transfert de masse.

Il a été démontré que l'élimination du calcium et du sodium suit des cinétiques de réaction du premier ordre relativement aux concentrations de calcium et de sodium. L'élimination des éléments mentionnés ci-dessus a été bien représentée par un modèle cinétique dans lequel le transfert de masse du sodium et du calcium dans la phase fondue limitait le processus.

Dans le cas des alliages contenant du magnésium, la phase saline  $MgCl_2$  générée pendant la chloruration, s'est révélée avoir un effet important sur l'élimination du calcium et du sodium. La contribution de la phase saline à l'élimination de ces éléments a été calculée et est de l'ordre de 60%. Cependant, dans l'aluminium de pureté commerciale, le chlore contenant des bulles de gaz a le plus contribué à l'élimination du calcium tandis que le sodium est éliminé davantage par évaporation à travers la surface du métal fondu.

## ACKNOWLEDGMENTS

The present work has been carried out under the supervision of Prof. R. Guthrie. The author is indebted to him for his encouragement and financial support during the course of this study.

Special thanks to Dr. Deutre of Alcan Ltd. who made the emission spectrometer at the Research Centre in Kingston available to the author. The author would also like to convey his gratitude to him for valuable discussions on the subject matter and for his willingness to provide the author with technical and logistic support whenever needed.

The author would like to thank to Mr. Peter Whales of Alcan Ltd. for his assistance and excellent hospitality during the author's visits to Kingston.

Mr. J.P Martin of Alcan Ltd. made the Analytical group available for the independent checks on the melt samples. It is also him who provided the author with commercial purity aluminum ingots and LiMCA sampling tubes. The author is indebted to him for his relentless assistance.

Thanks to Mr. Denis Choquette, the chief of the Analytical Group at Alcan Int., Arvida, for his supervision on the chemical analysis of the melt samples.

The author would like to convey his appreciation of valuable discussions on the subject matter with Dr. Cesur Celik, formerly with Alcan Int. now with Noranda Technology Centre, on the subject matter.

The author would like to thank Dr. Bernard Closset and Dr. Francisco Dimayuga for providing the author with magnesium metal and aluminum-calcium alloy ingots.

The author would like to express his gratitude to Mr. Francois Dallaire of McGill University for his technical assistance during LiMCA tests.

The author is indebted to Mr. Frank Sebo, the chief technician, for providing the author with technical assistance in construction and the maintenance of the experimental apparatus.

I would like to convey my gratitude to Dr. Dipak Mazumdar, a very good friend of mine and a valuable colleague, for reading the entire manuscript and making valuable suggestions.

During my stay in Montreal, I had the privilege to meet Dr. Hasim Mulazimoglu, Mr. Dominic Verhelst, Mr. Ramani Sankaranarayanan, Dr. Sanghoon Joo, Mr. Hyoung Chul Lee, Ms. Florace Paray, Mr. Chenquo Tian, Mr. Hussein Abuluwefa, Mr. Reza Abutalebi and Mr. Allain Charbonier whose presence at McGill created an enjoyable working environment for the author.

Finally, I would like to express my gratitude to my parents and my sister whose constant moral support was a great source of inspiration which helped the author immensely to complete his thesis.

TABLE OF CONTENTS

	<u>Page</u>
ABSTRACT	i
RESUME	ii
ACKNOWLEDGEMENTS	iii
TABLE OF CONTENTS	v
LIST OF TABLES	ix
LIST OF FIGURES	xi
LIST OF SYMBOLS	xviii
CHAPTER 1: Introduction	1
I.1. Detrimental effects of Sodium and Calcium on aluminum alloys	1
I.2. The origin of Sodium and Calcium in Aluminum	4
I.3. Removal of Sodium and Calcium from Aluminum	8
I.4. The purpose of the present study	13
CHAPTER 2: Theory	14
II.A. Thermodynamics of chlorination	14
II.A.1. Aluminum-Chlorine System	17
II.A.1.a. Aluminum-Calcium-Chlorine System	19
II.A.1.b. Aluminum-Sodium-Chlorine System	21
II.A.2. Aluminum-Magnesium-Chlorine System	23
II.A.2.a. Aluminum-Magnesium-Calcium-Chlorine System	25
II.A.2.b. Aluminum-Magnesium-Sodium-Chlorine System	25
II.B. Kinetics of chlorination	30
II.B.1. Kinetic Models for Impurity Removal	33
II.B.1.a. Stoichiometrically Controlled Impurity Removal	33
II.B.1.b. Mass Transfer Controlled Impurity Removal	36
II.C. Shape Regimes for Fluid Particles in Liquid Aluminum	37

CHAPTER 3:Experimental Set-up and Procedure	40
III.A. Melt Gas Fluxing Unit	40
III.A.1. Preparation for the Gas Fluxing Experiments	42
III.A.1.a. Preparation of the Charge and the Melt	42
III.A.1.b. Preparation of Impurity Additions	43
III.A.1.c. Preparation of Gas Fluxing Lances	43
III.A.1.d. Preparation of the Impeller	43
III.A.2. Materials	43
III.A.3. Calibration of Flowmeters	46
III.A.4. Experimental Procedure	46
III.A.5. Preparation of Samples and Dross for Chemical Analyses	49
III.A.6. Experimental Schedule	49
III.A.7. Measurement of Frequency of Bubble Formation	51
III.A.7.a. Principle of Operation	51
III.A.7.b. Gas Supply Line	55
III.B. LiMCA(Liquid Metal Cleanliness Analyzer) Unit	57
III.B.1. Principle of Operation	57
III.B.2. Components of the LiMCA Unit	59
III.B.2.a. Melt Sampling Unit	59
III.B.2.b. Power Supply Unit	61
III.B.3. Voltage Pulse Measurement System	61
III.B.3.a. Recording Session	61
III.B.3.b. Playback Session	63
III.B.3.c. Calibration of Voltage Pulses	64
III.B.4. Preparation for the LiMCA Tests	67
III.B.5. Experimental Procedure	68
III.B.6. Experimental Schedule	70

<b>CHAPTER 4: Results and Discussion: Kinetics of Calcium Removal</b>	<b>71</b>
IV.A. Presentation of the experimental results in graphical and tabular form	71
IV.B. Stoichiometrically Controlled Removal of Calcium	83
IV.C. Mass Transfer Controlled Removal of Calcium	89
IV.D. Calculation of Rate Constants for Bubbles and Intermediate Reaction Products that are Separated from the Bubbles	94
IV.D.1. Effect of Chlorine Concentration	97
IV.D.2. Effect of Gas Flow Rate	98
IV.E. Calculation of the Melt Phase Mass Transfer Coefficients for Bubbles	99
IV.F. Summary	106
<b>CHAPTER 5: Results and Discussion: Kinetics of Sodium Removal</b>	<b>108</b>
V.A. Presentation of the experimental results in graphical and tabular form	108
V.B. Stoichiometrically Controlled Removal of Sodium	119
V.C. Mass Transfer Controlled Removal of Sodium	125
V.D. Calculation of Rate Constants for Bubbles, for Evaporation through the melt surface and for the Intermediate Reaction Products that are Separated from the bubbles	130
V.D.1. Effect of Chlorine Concentration	134
V.D.2. Effect of Gas Flow Rate	134
V.E. Calculation of the Melt Phase Mass Transfer Coefficients for Bubbles	135
V.F. Calculation of the Melt Phase Mass Transfer Coefficients for Evaporation through the melt surface	142
V.G. Summary	149
<b>CHAPTER 6: Results and Discussion: Analysis of Contribution of the Intermediate         Reaction Products that are Separated From the Bubbles</b>	<b>151</b>
VI.1. Introduction	151

VI.2. Calculation of Rate Constants for Droplets	157
VI.3. Summary	164
CONCLUSIONS TO THE THESIS	165
CLAIMS TO THE ORIGINAL CONTRIBUTIONS TO THE KNOWLEDGE	167
SUGGESTIONS FOR FUTURE WORK	168
REFERENCES	169
APPENDIX	177

LIST OF TABLES:

<u>Table</u>	<u>Page</u>
1.1 Analytical results of impurities in some typical samples of alumina, coke and primary aluminum(amounts in wt-ppm)[17]	6
2.1 The mole fraction of $\text{CaCl}_2$ with respect to $\text{Cl}_2$ concentration in the bubbles	19
2.2 The mole fraction of $\text{NaCl}$ with respect to $\text{Cl}_2$ concentration in the bubbles	21
2.3 The mole fraction of $\text{MgCl}_2$ with respect to $\text{Cl}_2$ concentration in the bubbles bubbles	23
2.4 Standard Free Energy of Formation of some chlorides[43] at 1000 K (Joules/g-mole of chlorine)	32
3.1 Major impurities in commercial purity aluminum	45
3.2 Major impurities in magnesium metal	45
3.3 Experimental schedule followed for the gas fluxing experiments	50
3.4 Magnitude of calibration pulses and their theoretical location in the MCA	65
3.5 Experimental schedule followed for the LiMCA experiments	70
4.1 Rate constants for various chlorine concentrations in the gas bubbles; $Q=26.22 \text{ cc/sec}(730 \text{ }^\circ\text{C}, 1 \text{ Atm.})$	80
4.2 Rate constants for various gas flow rates( $730 \text{ }^\circ\text{C}, 1 \text{ Atm.}$ ); Vol% $\text{Cl}_2=10$	81
4.3 Rate constants for various argon gas flow rates( $730 \text{ }^\circ\text{C}, 1 \text{ Atm.}$ )	82
4.4 Summary of the rate constants for various chlorine concentrations in the gas bubbles; $Q=26.22 \text{ cc/sec}(730 \text{ }^\circ\text{C}, 1 \text{ Atm.})$	95
4.5 Summary of the rate constants for various gas flow rates( $730 \text{ }^\circ\text{C}, 1 \text{ Atm.}$ ); Vol% $\text{Cl}_2=10$	96
4.6 Experimental melt phase mass transfer coefficients for bubbles for various chlorine concentrations; $Q=26.22 \text{ cc/sec}(730 \text{ }^\circ\text{C}, 1 \text{ Atm.})$	100
4.7 Experimental melt phase mass transfer coefficients for bubbles for various gas flow rates( $730 \text{ }^\circ\text{C}, 1 \text{ Atm.}$ ); Vol% $\text{Cl}_2=10$	101

5.1	Rate constants for various chlorine concentrations in the gas bubbles; Q=26.22 cc/sec(730 °C, 1 Atm.)	117
5.2	Rate constants for various gas flow rates(730 °C, 1 Atm.); Vol% Cl <sub>2</sub> =10	118
5.3	Summary of the rate constants for various chlorine concentrations in the gas bubbles; Q=26.22 cc/sec(730 °C, 1 Atm.)	132
5.4	Summary of the rate constants for various gas flow rates(730 °C, 1 Atm.); Vol% Cl <sub>2</sub> =10	133
5.5	Experimental melt phase mass transfer coefficients for bubbles for various chlorine concentrations; Q=26.22 cc/sec(730 °C, 1 Atm.)	137
5.6	Experimental melt phase mass transfer coefficients for bubbles for various gas flow rates(730 °C, 1 Atm.); Vol% Cl <sub>2</sub> =10	138
5.7	Rate constants, R <sub>Ar</sub> and R <sub>sat</sub> , for various argon gas flow rates(730 °C, 1 Atm.)	145
6.1	Overall rate constants and rate constants for the droplets as a function of chlorine concentration(Vol%) and gas flow rate(730 °C, 1 Atm.)	161
6.2	Rate constants for various gas flow rates(730 °C, 1 Atm.)	163

LIST OF FIGURES:

<u>Figure</u>		<u>Page</u>
1.1	Al-5wt% Mg alloy after hot rolling, showing the effect of increasing Na contents(between 3 and 81 wt-ppm Na) on surface cracking, which starts at about 10 wt-ppm Na[2]	2
1.2	Appearance of hot rolled sheet edges in 5182(4.1 wt% Mg) alloy[3] a)Edge cracked, b)Free from edge cracking	2
1.3	Relationship between bath ratio and sodium and calcium contents[17]	7
1.4	Influence of magnesium on the interface resistance[30]	11
1.5	First order rate constant for Calcium removal vs chlorine concentration[31]	12
1.6	Demonstration of persistence of Ca removal from an alloy containing 1 wt% Mg after the cessation of chlorine addition[31]	13
2.1	The output of the Equilibrium programme	15
2.2	The mole fraction of major gaseous reaction products for Al-Cl <sub>2</sub> system as a function of Cl <sub>2</sub> concentration at 1000 K and 1 Atm.	18
2.3	The mole fraction of major gaseous product species for Al-Ca-Cl <sub>2</sub> system as a function of Cl <sub>2</sub> concentration at 1000 K and 1 Atm.	20
2.4	The mole fraction of major gaseous product species for Al-Na-Cl <sub>2</sub> system as a function of Cl <sub>2</sub> concentration at 1000 K and 1 Atm.	22
2.5	The mole fraction of major gaseous product species for Al-Mg-Cl <sub>2</sub> system as a function of Cl <sub>2</sub> concentration at 1000 K and 1 Atm.	24
2.6	The mole fraction of major gaseous product species for Al-Mg-Ca-Cl <sub>2</sub> system as a function of Cl <sub>2</sub> concentration at 1000 K and 1 Atm.	26
2.7	The mole fraction of CaCl <sub>2</sub> and MgCl <sub>2</sub> in the ideal salt solution at 1000 K and 1 Atm.	27
2.8	The mole fraction of major gaseous product species for Al-Mg-Na-Cl <sub>2</sub> system as a function of Cl <sub>2</sub> concentration at 1000 K and 1 Atm.	28
2.9	The mole fraction of NaCl and MgCl <sub>2</sub> in the ideal salt solution at 1000 K and 1 Atm.	29

2.10	A general schematic description of chlorination process	31
2.11	Shape regimes of the fluid particles as a function of $Re$ , $Eo$ , And $M$ [44]	39
3.1	Schematic of the melt gas fluxing unit	41
3.2	The crucible and its graphite cover used in the experiments	42
3.3	The quartz gas bubbling lance used in the experiments	44
3.4	Impeller head used in the experiments	44
3.5	Calibration chart for chlorine gas	47
3.6	Calibration chart for argon gas	48
3.7	The standard Alcan mould and a disk sample	49
3.8	Variation of pressure in a gas bubble forming at an orifice[56]	51
3.9	A train of pressure pulses generated in the gas chamber by the release of bubbles from the orifice. Frequency is 13 bubbles/sec(horizontal scale is 0.1 sec/division)	53
3.10	Comparison of bubble formation frequencies by simultaneous measurement by using a light stroboscope and microphone	54
3.11	The frequency of bubble formation as a function of gas flow rate( $730^{\circ}C$ , 1 Atm.) for several nozzle diameters in molten aluminum	56
3.12	The schematic of LiMCA melt sampling unit	60
3.13	The flow chart of the recording and playback sessions	62
3.14	The theoretical and actual locations of the calibration pulses in the MCA	66
3.15	Assignment of the theoretical values of the calibration voltage pulses to new MCA channels according to the correction done through Eqns.(3.22) and (3.23)	67
3.16	The flow chart of the experimental procedure followed for the LiMCA experiments	69
4.1	Change in calcium concentration in commercial purity aluminum melts versus bubbling time for various chlorine concentrations in $Ar-Cl_2$ gas mixture injected at a gas flow rate of 26.22 cc/sec( $730^{\circ}C$ , 1 Atm.)	72

- 4.2 Change in calcium concentration in Al-1wt% Mg alloys versus bubbling time for various chlorine concentrations in Ar-Cl<sub>2</sub> gas mixture injected at a gas flow rate of 26.22 cc/sec(730 °C, 1 Atm.) 73
- 4.3 Change in calcium concentration in commercial purity aluminum melts versus bubbling time for various gas flow rates(730 °C, 1 Atm.); Vol% Cl<sub>2</sub>=10 74
- 4.4 Change in calcium concentration in Al-1wt% Mg alloys versus bubbling time for various gas flow rates(730 °C, 1 Atm.); Vol% Cl<sub>2</sub>=10 75
- 4.5 Change in calcium concentration in commercial purity aluminum melts versus time for various chlorine concentrations and gas flow rates(730 °C, 1 Atm.) during intermittent tests 76
- 4.6 Change in calcium concentration in Al-1wt% Mg alloys versus time for various chlorine concentrations and gas flow rates(730 °C, 1 Atm.) during intermittent tests 77
- 4.7 Change in calcium concentration in commercial purity aluminum melts versus time for various chlorine concentrations and gas flow rates(730 °C, 1 Atm.) during argon injection tests 78
- 4.8 Change in calcium concentration in Al-1wt% Mg alloys versus time for various chlorine concentrations and gas flow rates(730 °C, 1 Atm.) during argon injection tests 79
- 4.9 Comparison of stoichiometrically controlled removal of calcium versus experimental results for commercial purity aluminum melts; Q=26.22 cc/sec(730 °C, 1 Atm.) 85
- 4.10 Comparison of stoichiometrically controlled removal of calcium versus experimental results for commercial purity aluminum melts at higher gas flow rates(730 °C, 1 Atm.); Vol% Cl<sub>2</sub>=10 86
- 4.11 Comparison of stoichiometrically controlled removal of calcium versus experimental results for Al-1wt% Mg alloys; Q=26.22 cc/sec(730 °C, 1 Atm.) 87

- 4.12 Comparison of stoichiometrically controlled removal of calcium versus experimental results for Al-1wt% Mg alloys at higher gas flow rates(730 °C, 1 Atm.); Vol% Cl<sub>2</sub>=10 88
- 4.13 Comparison of mass transfer controlled removal of calcium versus experimental results for commercial purity aluminum melts; Q=26.22 cc/sec(730 °C, 1 Atm.) 90
- 4.14 Comparison of mass transfer controlled removal of calcium versus experimental results for commercial purity aluminum melts at higher gas flow rates(730 °C, 1 Atm.); Vol% Cl<sub>2</sub>=10 91
- 4.15 Comparison of mass transfer controlled removal of calcium versus experimental results for Al-1wt% Mg alloys; Q=26.22 cc/sec(730 °C, 1 Atm.) 92
- 4.16 Comparison of mass transfer controlled removal of calcium versus experimental results for Al-1wt% Mg alloys at higher gas flow rates(730 °C, 1 Atm.); Vol% Cl<sub>2</sub>=10 93
- 4.17 Determination of melt phase mass transfer coefficients for bubbles graphically through Eqn.(4.22) 105
- 5.1 Change in sodium concentration in commercial purity aluminum melts versus bubbling time for various chlorine concentrations in Ar-Cl<sub>2</sub> gas mixture injected at a gas flow rate of 26.22 cc/sec(730 °C, 1 Atm.) 109
- 5.2 Change in sodium concentration in Al-1wt% Mg alloys versus bubbling time for various chlorine concentrations in Ar-Cl<sub>2</sub> gas mixture injected at a gas flow rate of 26.22 cc/sec(730 °C, 1 Atm.) 110
- 5.3 Change in sodium concentration in commercial purity aluminum melts versus bubbling time for various gas flow rates(730 °C, 1 Atm.); Vol% Cl<sub>2</sub>=10 111
- 5.4 Change in sodium concentration in Al-1wt% Mg alloys versus bubbling time for various gas flow rates(730 °C, 1 Atm.); Vol% Cl<sub>2</sub>=10 112

- 5.5 Change in sodium concentration in commercial purity aluminum melts versus time for various chlorine concentrations and gas flow rates(730 °C, 1 Atm.) during intermittent tests 113
- 5.6 Change in sodium concentration in Al-1wt% Mg alloys versus time for various chlorine concentrations and gas flow rates(730 °C, 1 Atm.) during intermittent tests 114
- 5.7 Change in sodium concentration in commercial purity aluminum melts versus time for various chlorine concentrations and gas flow rates(730 °C, 1 Atm.) during argon injection tests 115
- 5.8 Change in sodium concentration in Al-1wt% Mg alloys versus time for various chlorine concentrations and gas flow rates(730 °C, 1 Atm.) during argon injection tests 116
- 5.9 Comparison of stoichiometrically controlled removal of sodium versus experimental results for commercial purity aluminum melts; Q=26.22 cc/sec(730 °C, 1 Atm.) 121
- 5.10 Comparison of stoichiometrically controlled removal of sodium versus experimental results for commercial purity aluminum melts at higher gas flow rates(730 °C, 1 Atm.); Vol% Cl<sub>2</sub>=10 122
- 5.11 Comparison of stoichiometrically controlled removal of sodium versus experimental results for Al-1wt% Mg alloys; Q=26.22 cc/sec(730 °C, 1 Atm.) 123
- 5.12 Comparison of stoichiometrically controlled removal of sodium versus experimental results for Al-1wt% Mg alloys at higher gas flow rates(730 °C, 1 Atm.); Vol% Cl<sub>2</sub>=10 124
- 5.13 Comparison of mass transfer controlled removal of sodium versus experimental results for commercial purity aluminum melts; Q=26.22 cc/sec(730 °C, 1 Atm.) 126

5.14	Comparison of mass transfer controlled removal of sodium versus experimental results for commercial purity aluminum melts at higher gas flow rates(730 °C, 1 Atm.); Vol% Cl <sub>2</sub> =10	127
5.15	Comparison of mass transfer controlled removal of sodium versus experimental results for Al-1wt% Mg alloys; Q=26.22 cc/sec(730 °C, 1 Atm.)	128
5.16	Comparison of mass transfer controlled removal of sodium versus experimental results for Al-1wt% Mg alloys at higher gas flow rates(730 °C, 1 Atm.); Vol% Cl <sub>2</sub> =10	129
5.17	Melt phase mass transfer coefficients for bubbles as a function of equivalent bubble diameter	139
5.18	Graphical determination of melt phase mass transfer coefficients for bubbles	141
5.19	Comparison of the experimental melt phase mass transfer coefficients for the evaporation through the melt surface with the theoretical values calculated according to Eqn.(5.25) for commercial purity aluminum	147
5.20	Comparison of the experimental melt phase mass transfer coefficients for the evaporation through the melt surface with the theoretical values calculated according to Eqn.(5.25) for Al-1wt% Mg alloys	148
6.1	Number of particles that are greater than 21 microns in a 7.5 kg melt before and after chlorination as a function of chlorine concentration(Vol%) and gas flow rate(730 °C, 1 Atm.)	152
6.2	A typical LiMCA signal observed before chlorination; Horizontal scale=0.1 ms per division, Vertical scale=0.1 mV per division	153
6.3	A typical LiMCA signal observed after chlorination; Horizontal scale=0.1 ms per division, Vertical scale=0.1 mV per division	154
6.4	An X-Ray diffraction pattern of a typical dross sample(at the top) together with that of MgCl <sub>2</sub> (at the bottom)	156
6.5	Reynolds number as a function of droplet diameter	160

6.6 An SEM picture of  $\text{MgCl}_2$  particles

LIST OF SYMBOLS

A	Surface area ( $m^2$ )
C	Concentration (wt-ppm)
CH	Channel number (-)
d,D	Diameter (m)
D	Diffusion coefficient ( $m^2/sec$ )
Eo	Eotvos number (-)
f	Activity coefficient (-)
f	Bubble frequency (1/sec)
G	Amplifier gain (-)
G	Molar gas flow rate (kg-mole/sec)
g	Gravitational acceleration ( $m/sec^2$ )
I	Impurity concentration (wt-ppm)
I	Electric current (Amp)
k	Mass transfer coefficient (m/sec)
m	Molecular weight (kg/kg-mole)
M	Mass of the melt (kg)
M	Morton number (-)
N	Number of particles and/or droplets in a particular size range (-)
$\dot{N}$	Mass flux ( $kg/m^2\text{-sec}$ )
P	Pressure ( $N/m^2$ )
Pe	Peclet number (-)
Q	Gas flow rate ( $m^3/sec$ );( $cm^3/sec$ )
r	Radius of the vessel (m)
R	Rate constant (1/sec)
$\Delta R$	Magnitude of electrical resistance change (ohm)
Re	Reynolds number (-)
Sc	Schmidt number (-)
Sh	Sherwood number (-)
t	Time (sec);(min)

U	Velocity (m/sec);(cm/sec)
V	Volume (m <sup>3</sup> )
V	Sampling rate (cc/min)
$\Delta V$	Magnitude of the voltage change (volt)
X	Mole fraction (-)
$\Delta G^{xs}$	Excess molar free energy of solution (Joules/mole)
$\alpha$	Volume fraction (-)
$\mu$	Dynamic viscosity of the continuous phase (kg/m-sec)
$\nu$	Turbulent kinematic viscosity (m <sup>2</sup> /sec)
$\rho$	Density (kg/m <sup>3</sup> )
$\Delta\rho$	Density difference between continuous and dispersed phase (kg/m <sup>3</sup> )
$\sigma$	Surface tension (kg/sec <sup>2</sup> )
$\Omega$	Electrical resistivity (ohm-m)

Subscripts:

Al	Aluminum
Ar	Argon; related to argon injection tests
atm	Atmospheric
b	Bubble
c	Capacitance; chamber
Ca	Calcium
Cl <sub>2</sub>	Chlorine
drp	Droplet
e	Related to volume equivalent sphere; equilibrium value
eff	Effective
f	Final
i	Initial
irp	Intermediate reaction products that are separated from the bubbles
g	Gas
h.s	Hydrostatic

intermittent Related to intermittent tests

I Impurity

l Liquid

l.s Light stroboscope

m Microphone

max Maximum

Mg Magnesium

min Minimum

Na Sodium

o Atmospheric

o Overall

p Plume

r Radial direction

s Melt surface

sat Saturation

t Transient

w Material of the crucible wall

- Surface area averaged

' Related to intermediate reaction products that cover the crucible wall

Superscripts:

B Bulk

Ca Calcium

Na Sodium

\* Interface

# Chapter 1

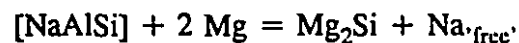
## Introduction

---

### I.1. Detrimental effects of Sodium and Calcium on aluminum alloys:

Despite being good modifying agents for aluminum-silicon alloys[1], sodium and calcium are undesirable elements in several aluminum alloys as these elements adversely affect the mechanical properties and cause problems during forming of these alloys.

Ransley and Talbot[2] showed that aluminum alloys in which magnesium is the major alloying element are susceptible to brittle behaviour in hot working when contaminated with sodium. These authors showed that the effect of sodium, even when present at a concentration level of 10 wt-ppm, is remarkable especially for alloys containing more than 2 wt% magnesium. These authors demonstrated that above 2 wt% Mg concentration there will be a phase change involving a ternary Al-Si-Na compound and dissolved magnesium to result in the following equilibrium at around 400 °C



These authors proposed that the free sodium will be absorbed on the pore surfaces that are created by the plastic deformation, leading to an appreciable decrease in the pore-grain boundary surface energy which would reduce the stress required to initiate fracture. Figure 1.1 shows the effect of increasing sodium content on an Al-5 wt% Mg alloy after hot deformation.

Calcium even when present at a concentration level of 15 wt-ppm is known to cause edge cracking during hot deformation of aluminum-4 wt% magnesium alloys[3]. Figure 1.2 shows such a rolled sheet with and without edge cracks. The mechanism behind this phenomenon, however, is not known.

Fager et al.[4] were the first to report on the effects of sodium concentration on the

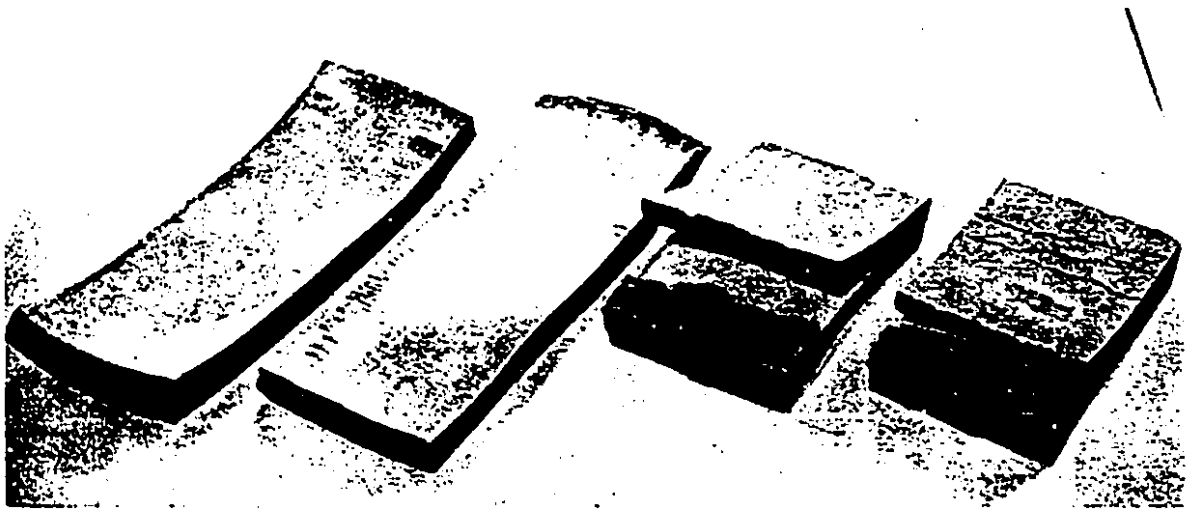


Figure 1.1 Al-5wt% Mg alloy after hot rolling, showing the effect of increasing Na contents (between 3 and 81 wt-ppm Na) on surface cracking, which starts at about 10 wt-ppm Na[2]

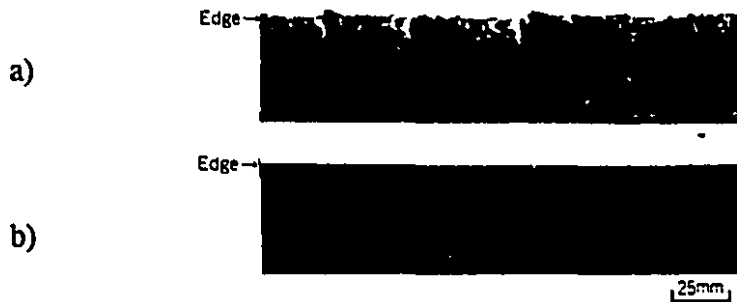


Figure 1.2 Appearance of hot rolled sheet edges in 5182 (4.1 wt% Mg) alloy[3] a) Edge cracked, b) Free from edge cracking

cleavage fracture in aluminum-lithium alloys (Al-2.2wt% Li-2.7 wt% Cu-0.13 wt% Zr). They showed that there is a correlation between the number of cleavage facets observed and the sodium content of the alloy. All the aluminum-lithium alloys with 20 wt-ppm or higher Na contained numerous cleavage cracks after tensile and bend tests at room temperature. These authors suggested that liquid metal embrittlement (LME) by the formation of low melting point Na-K compounds would be responsible for this phenomenon.

Later, Miller et al. [5], after examining a number of aluminum-lithium alloys, showed that cleavage fracture was present only when the sodium content was in excess of 10 wt-ppm. These authors also examined an alloy which did not contain lithium (Al-5.85 wt% Zn-2.11 wt% Mg-1.61 wt% Cu) for cleavage fracture by deliberate addition of sodium. They observed that the fracture surfaces were covered by numerous cleavage facets identical in appearance to those observed in the lithium containing alloys. These authors came to the conclusion that the cleavage phenomenon was common to all aluminum alloys, provided that they are strained under appropriate strain rates and temperatures and they contain an impurity concentration of sodium. They speculated that the defects are initiated at intermetallic particles situated on grain boundaries which act as stress concentrators. Sodium which might be expected to segregate to grain boundaries and precipitate-matrix interfaces, could then diffuse under the influence of the applied stress ahead of the crack tip thereby reducing the interfacial energy along specific crystallographic planes and causing failure.

Webster [6] investigated the effect of sodium and potassium on the properties of aluminum-lithium alloys. He showed that sodium and potassium are concentrated in grain boundary particles and reduce the toughness of Al-Li alloys at temperatures above approximately 200 K. He demonstrated that these elements occur as isolated grain boundary particles rather than grain boundary films which would act as grain boundary cracks which cause extensive local deformation in the grain boundary region. He also suggested that a liquid phase could also contribute embrittlement by decreasing the surface energy of the crack surface leading to reduction in the stress required to propagate the crack. Webster proposed that two conditions are necessary to produce room temperature liquid phases in aluminum alloys. These are (a) the presence of Na together with K, Cs or Rb and (b) the presence of a substantial quantity of an element that forms a stable silicide so that the ternary

[NaAlSi] compounds do not form.

Kobayashi et al.[7] investigated the temperature dependence of the impact toughness in Al-Li-Cu-Mg-Zr alloys. They observed that the impact toughness of the alloy below 423 K increased with decreasing temperature. The spectra of sodium and potassium were detected on the fracture of the specimens tested at the room temperature. They suggested that a low melting point metal phase in the alloy with 60 wt-ppm sodium effects the impact toughness near room temperature by LME locally at grain boundaries.

Lynch[8] studied the effects of temperature, stress intensity factor, sodium impurity content and aging conditions on the short transverse sustained load(creep) cracking of Al-Li-Cu-Mg-Zr alloy plates. He observed that for a given stress intensity factor, cracking rates were three to five times higher for alloys with about 40 wt-ppm Na than for alloys with about 10 wt-ppm Na. Based on metallographic and fractographic observations they suggested that the presence of liquid sodium rich impurity phases promote creep cracking by the migration of impurity atoms to crack tips thereby weakening interatomic bonds hence facilitating dislocation injection from crack tips.

### 1.2. The origin of Sodium and Calcium in Aluminum:

Since the success of Hall in the U.S.A and Heroult in France, the production of aluminum has been almost universally realized by the electrolytic reduction of alumina in so called Hall-Heroult reduction cells.

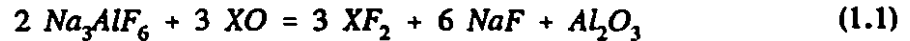
The electrolyte used in the electrolysis is cryolite( $\text{Na}_3\text{AlF}_6$ ) which has melting point of  $1012 \pm 2$  °C[9]. Molten cryolite is a good solvent for alumina and forms a simple eutectic system with alumina with a eutectic composition of 10 wt%  $\text{Al}_2\text{O}_3$  occurring around 961-962 °C[10-11].

In order to decrease its melting point and adjust its physical properties several additions are made to cryolite[12]. These additions are usually lithium, magnesium, calcium fluorides as well as aluminum and sodium fluorides which are in excess quantity to form the cryolite( $\text{NaF}/\text{AlF}_3 = 3$  on molar basis).

Apart from the fluorides that are purposely introduced into the electrolyte, there are also foreign substances(impurities) that are inevitably present in the electrolyte. These

impurities are introduced into the electrolyte by the alumina feed, anode materials and to a minor extent, by fluorides used for optimization of the electrolyte composition [13]. Table 1.1 shows such impurities in the row materials.

According to Grjotheim et al.[12], the oxides will react with cryolite in the following fashion



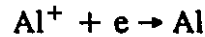
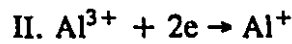
and create additional fluorides which will ionize in the electrolyte. Ions with less negative reduction potentials than that of aluminum will deposit on the cathode(aluminum) and contaminate the aluminum produced. Those ions with more negative reduction potentials than that of aluminum e.g Na and Ca will not in principle be deposited on the cathode. However, they will contaminate aluminum by an overall equilibrium of type[14]



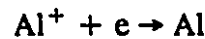
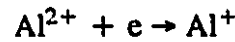
Sodium is also known to co-deposit with aluminum under certain conditions. According to Grjotheim et al.[12], deposition of aluminum may either occur in one step



or via mechanisms involving subvalent species such as



or



Any of the above discharge reactions may be preceded by a dissociation of aluminum complexes such as



Grjotheim et al.[12], suggested that primary sodium discharge is conceivable only if the dissociation or the aluminum discharge steps are retarded therefore leading to charge

**Table 1.1** Analytical results of impurities in some typical samples of alumina, coke and primary aluminum (amounts in wt-ppm) [17]

Elements	Alumina		Coke		Cell Metal		Holding-Furnace Metal		
	A	B	C	D	E	F-1	F-2	F-3	
Popular Impurities	B	<1	1	3	2	2	2	2	2
	Na	3500	200	240	60	62	12	5	5
	Mg	5	110	12	24	25	17	11	11
	Si	61	210	230	630	610	610	620	620
	Ca	72	120	9	11	11	10	7	7
	Ti	32	10	13	66	64	66	62	66
	V	2	220	10	104	13	13	13	13
	Cr	3	1	0.6	4	4	4	4	5
	Mn	<1	4	2	11	10	12	12	12
	Fe	56	290	310	1330	810	810	810	810
	Ni	<1	230	5	10	7	7	7	8
	Cu	1	1	3	16	16	18	17	17
	Zn	9	9	12	34	36	36	33	38
	Ga	51	14	1	99	88	85	85	85
	Sn	10	0.2	0.6	24	21	20	19	24
	Pb	6	3	16	6	6	6	5	8
	Non-metallic Inclusions	Al <sub>2</sub> O <sub>3</sub>	--	--	--	42	42	41	21
AlN		--	--	--	3	3	4	2	10
Al <sub>2</sub> C <sub>3</sub>		--	--	--	5	5	2	0.4	12
Other Impurities	P	4	--	--	1	1	1	1	1
	S	20	12000	3000	0.2	0.2	0.2	0.2	0.2
	Cl*	--	--	--	<0.1	<0.1	<0.1	0.1	0.1
	Sc*	--	--	--	0.04	0.04	0.04	0.04	0.04
	Co*	--	--	--	0.2	0.2	0.2	0.2	0.2
	Sb*	--	--	--	0.01	0.01	0.01	0.01	0.01
	Ln*	--	--	--	0.4	0.6	0.6	0.6	1.2
	Sm*	--	--	--	0.5	0.4	0.4	0.4	0.4
	Tb*	--	--	--	0.1	0.1	0.1	0.1	0.1
	Dy*	--	--	--	0.1	0.1	0.1	0.1	0.1
	Hf*	--	--	--	1.5	2.0	2.0	2.0	2.0

\*Activation analysis.

**Note:**

A is alumina.

B is petroleum coke.

C is pitch coke.

D is the sample taken from the reduction cell:

anode: petroleum coke,

sampling: between crust breaking operations,

cell age: 1 year old,

bath ratio: 1.35.

E is the sample taken from the reduction cell:

anode: pitch coke.

The other conditions are the same as in D.

F-1 is the sample taken from the holding furnace after 30 min of holding.

The metal was from the cell in which a pitch coke anode was used.

F-2 is the sample taken from the tap hole at the time of 80 pct casting.

F-3 is the sample taken from the tap hole at the time of 96 pct casting (usually not cast into pigs).

overpotential or if the electrolyte near the cathode(liquid aluminum) becomes strongly enriched with NaF. This would cause a cathodic overvoltage to reach the deposition potential of sodium which, being only about 250 mV more negative at 1000°C than that of aluminum, would lead to the deposition of sodium.

Calcium fluoride is known to increase the current efficiency of the aluminum reduction process[15] but this is accompanied by a decrease in the solubility of alumina in the electrolyte[11]. Even though calcium fluoride is not added intentionally, CaO in the raw feed materials will add up to 3 to 7 wt% CaF<sub>2</sub> in the electrolyte[16] and calcium will enter aluminum via an equilibrium of Eqn.(1.2).

Figure 1.3 shows typical sodium and calcium concentrations in the liquid aluminum produced in the Hall-Heroult reduction cell as a function of NaF/AlF<sub>3</sub> ratio(by weight)[17]

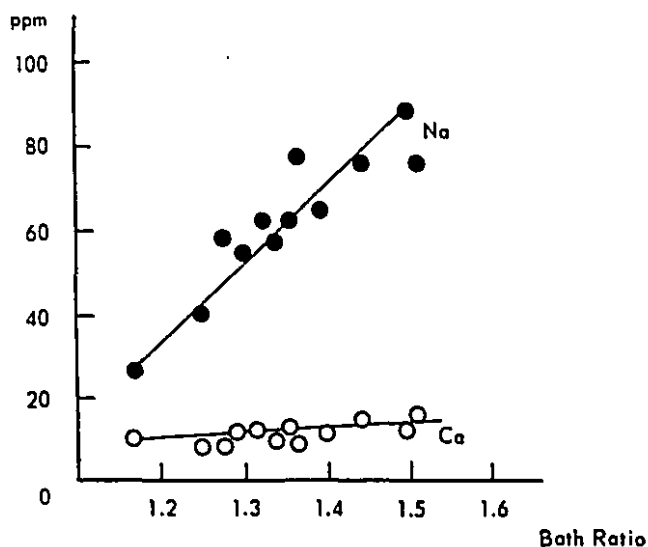


**Figure 1.3** Relationship between bath ratio and sodium and calcium contents[17]

Since sodium and calcium will always be present in the aluminum produced in the electrolysis cells, their removal from the liquid aluminum at an early stage is essential as these elements will adversely affect the mechanical properties of several aluminum alloys as already explained.

### 1.3. Removal of Sodium and Calcium from Aluminum:

As explained in the previous section, the liquid aluminum produced in the Hall-Heroult cells will contain several impurities depending on the composition of the raw materials used in the process.

Depending on the particular producer and the final product, refining of aluminum can be carried out in the pots or transfer crucibles carrying the liquid metal from the electrolysis cells, in the holding furnaces where alloying additions are done and/or between the holding furnace and the caster in so called in-line units just ahead of the casting operation.

In the last twenty years, several methods have been developed to remove alkali and alkaline earth metals as well as hydrogen and non-metallic inclusions from liquid aluminum[18-36]. Except for the vacuum treatment of liquid aluminum[19] all these methods aim to bring impurity containing liquid aluminum in contact with reactive gas and/or salt mixtures containing chlorine and/or fluorine.

The first laboratory tests to assess the effect of holding, stirring with an impeller with or without inert and reactive gas injections on the removal of sodium from liquid aluminum was carried out by Kastner et al[24].

Their experiments covered a melt temperature range between 735-850 °C. In the case of gas injection, a porous frit or a high velocity nozzle with a 0.5 mm diameter was used to introduce the gas into the melt. Reactive gases of Cl<sub>2</sub>, CF<sub>2</sub>Cl<sub>2</sub> and SF<sub>6</sub> with 5 vol% concentration were injected into the melt with N<sub>2</sub> as a carrier gas.

Their results showed that an increase in the temperature from 735 to 830 °C had almost no effect on the rate of removal of sodium from the melt during holding and stirring the melt with an impeller. The removal rate of sodium, when the melt was stirred with the impeller was decidedly faster(an almost 5-fold increase).

It was observed that when the inert N<sub>2</sub> gas was injected into the impeller stirred melts, the rate of removal of sodium became less compared to only impeller stirred melts. However, the authors neither explained nor elaborated on these results.

From the way their results are presented for the reactive gas injection tests, it is not possible to determine which of the reactive gases was more efficient(although Cl<sub>2</sub> seems to be the one) since the experimental conditions such as the impeller speed and temperature

varied widely for injection systems studied.

Nevertheless, these authors came to the overall conclusion that the rate of removal of sodium was the highest with impeller stirring only. They added, however, that almost equal rates of removal could be achieved by the use of reactive gases.

These authors could only calculate melt phase mass transfer coefficients for the removal of sodium through the melt surface. No attempt was made to calculate mass transfer coefficients for the bubbles as a further check to verify their results as they could not measure the bubble volumes. Based on water model experiments they claimed that minimum bubble size achieved in their system was about 1 cm in diameter.

Hjelle et al[25]. examined the effect of impeller stirring, impeller stirring with argon gas injection, impeller stirring with top salt( $\text{MgCl}_2 \cdot 6\text{H}_2\text{O}$ ) addition, impeller stirring + top salt addition with argon injection on the removal of sodium from 50 kg batch of aluminum-5 wt% magnesium alloys. Experimental melt temperature was kept at 720 °C in all the experiments. The gas was injected into the melt through a hole at the bottom of the impeller. This was done to achieve small bubble sizes by shearing the gas bubbles by the impeller blades.

Their results showed that injection of argon during impeller stirring(without top salt addition) increased the rate of removal of sodium with increase in impeller rotation speed as well as gas flow rate. This is contradictory to the results of Kastner et al.

These authors calculated melt phase mass transfer coefficients for the removal of sodium at the melt surface. The highest mass transfer coefficients( $\sim 2.5 \cdot 10^{-4}$  m/sec) were calculated for cases where the melt was stirred with a top salt addition. However, with the injection of gas through the impeller, the mass transfer coefficient dropped below  $2 \cdot 10^{-4}$  m/sec. These authors attributed this to the suppression of the vortex around the axis of the impeller by the rising gas bubbles. These authors speculated that this would prevent  $\text{MgCl}_2$  droplets that formed by the vortexing action to be dispersed into the melt and to react readily with sodium. These authors, however, could not verify the existence of these droplets inside the melt, nor could they show quantitatively the effect of these second phase liquid particles on the removal rate of sodium.

These authors also carried out experiments in which a gas mixture containing argon

and-2 vol%  $\text{Cl}_2$  was injected into the melt through the impeller. They argued that on contact with the melt first  $\text{AlCl}_3(\text{g})$  would form which will then react with Mg in the melt to form a layer of  $\text{MgCl}_2$  on the surface of the bubbles. They proposed that if there is sufficient contact area between the melt and the bubbles such that this  $\text{MgCl}_2$  layer will be consumed completely by reaction with sodium before the bubbles leave the melt. Their results showed that they achieved this. They could not measure the volume of the individual bubbles. The bubble surface areas were predicted from water model experiments.

Stevens and Yu[27] were the first to report on calcium removal from liquid aluminum. They carried out experiments in an ALCOA 622 unit. The dimensions of this unit were 1.08 m long x 0.851 m wide x 0.94 m high. The capacity of the unit was reported to be 998 kg liquid aluminum. Melt temperature was kept at 732 °C. Chlorine and argon gas mixtures (with an initial 20 vol%  $\text{Cl}_2$ ) were introduced into the melt through a 0.305 m diameter impeller.

These authors demonstrated that below 60 wt-ppm calcium concentration, removal of calcium followed first order reaction kinetics, whereas above 60 wt-ppm Ca concentration, removal rates became independent of calcium concentration.

Two years later the same authors[30] reported on the removal of calcium, sodium and hydrogen by chlorination in the same ALCOA 622 unit. Experimental conditions were the same as before with the difference that the maximum  $\text{Cl}_2$  concentration used was reported to be 5 vol%.

The authors claimed that with the use of excess chlorine, (they did not specify the amount), the rate of removal of sodium, calcium and hydrogen was slowed down especially when treating magnesium containing aluminum alloys. Their results for calcium removal are shown in Figure 1.4. On the Y-axis, their normalized rate constant is defined by the fraction of the impurity that was removed/unit time when magnesium was present in the melt divided by the fraction of calcium that was removed/unit time when there was no magnesium in the melt. As seen, the rate of removal of calcium from aluminum-magnesium alloys decreased with increase in magnesium concentration. The authors argued that this was owing to a  $\text{MgCl}_2$  product layer formation on the surface of the bubbles which increased the resistance to the mass transport of calcium. These authors also hypothesised that  $\text{MgCl}_2$

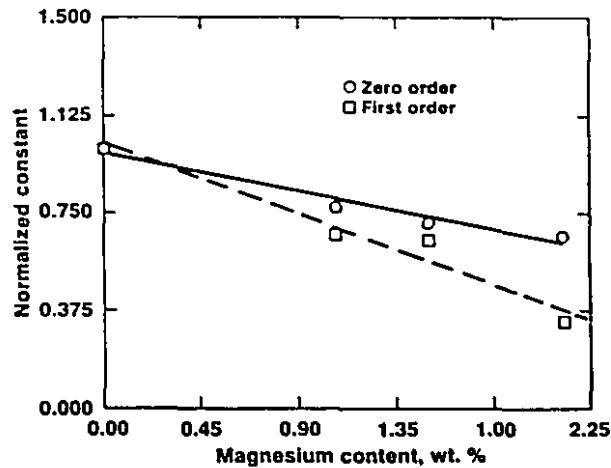


Figure 1.4 Influence of magnesium on the interface resistance[30]

salts generated by the chlorination action were absorbed onto the refractories of the ALCOA 622 unit and contributed to the removal of calcium and sodium.

There appears to be a contradiction in their interpretation of their results as  $MgCl_2$  was being claimed to be contributing on one hand, while on the other hand posing a resistance to the removal of calcium and sodium. These authors also hypothesised that the rate of removal of sodium was always higher than that of removal of calcium due to high volatility of sodium. No information regarding the composition of the melt nor experimental conditions were mentioned.

Exactly one year later, Celik and Doutre[31] reported on the removal of calcium from aluminum and aluminum magnesium alloys. They carried out tests in 0.75 ton and 6 ton melts. Melt temperature was kept around  $750^{\circ}C$ [37]. Mixtures of nitrogen and chlorine gases were injected into the melt through an impeller, through a static lance away from the impeller, with or without impeller stirring. The concentration of chlorine in the gas bubbles was changed between 6.25 and 25 vol%. They reported that under all conditions examined, the removal rates were found to follow first order reaction kinetics.

These authors demonstrated that the rate of removal of calcium was always higher from aluminum-magnesium alloys than from magnesium-free metal. Their results are shown in Figure 1.5.

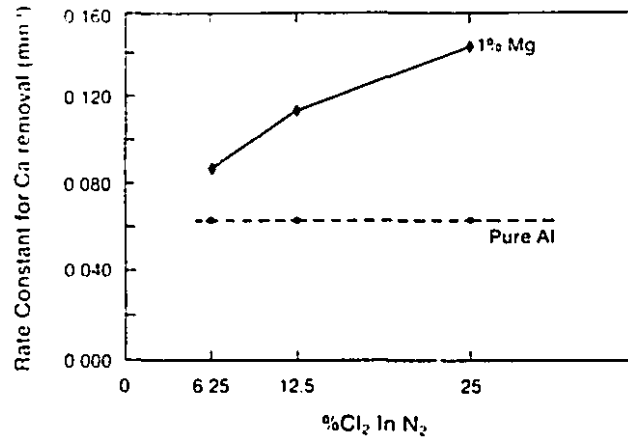


**Figure 1.5** First order rate constant for Calcium removal vs chlorine concentration[31]

It is seen that as the chlorine concentration increased the rate of removal of calcium from aluminum-magnesium alloy increased, whereas, the removal rate from magnesium-free aluminum did not change.

In order to explain this observation, the authors carried out intermittent tests in which the melt was chlorinated for a certain period which was followed by only nitrogen gas injection. Their results are shown in Figure 1.6. As seen after the termination of chlorine gas injection the rate of removal of calcium from the aluminum-magnesium alloy continued at a much faster rate than from magnesium-free aluminum. The authors attributed this to  $\text{MgCl}_2$  droplets that were generated by the chlorination action. These were stated to be as big as  $100 \mu\text{m}$  in diameter and provided additional reaction sites for calcium removal.

These authors did not provide any data as to the size and number distribution of these droplets generated under varying experimental conditions. They also did not undertake a systematic study to quantify the effect of these droplets on the removal of calcium from aluminum-magnesium alloys.

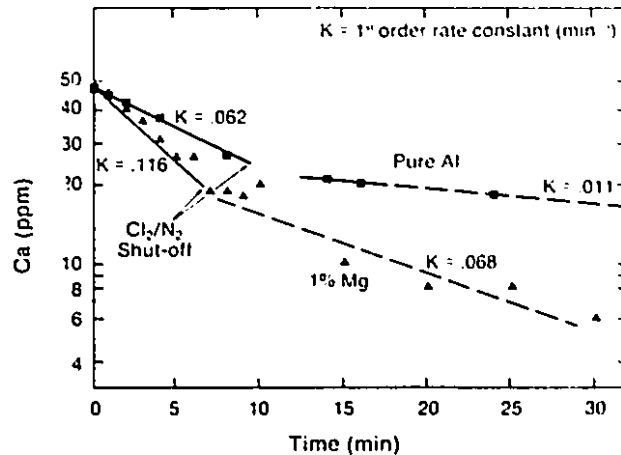


**Figure 1.6** Demonstration of the persistence of Ca removal from an alloy containing 1 wt% Mg after the cessation of chlorine addition[31]

#### I.4. The Purpose of the Present Study:

It was apparent from the forgoing discussion on the refining of aluminum for calcium and sodium by chlorination, that the number of systematic and careful investigations on the subject matter is scarce and that the outcome of some of these investigations are in complete contradiction with each other. Given the results of these investigations, it is difficult to arrive at any conclusion regarding the kinetics of calcium and sodium removal from aluminum and aluminum-magnesium alloys as the experimental conditions and methods differed from one investigator to another.

The present study was therefore, undertaken to investigate the removal of calcium and sodium by chlorination from aluminum and aluminum-1wt% magnesium alloys under the same experimental conditions so as to help clarify and understand the mass transfer mechanisms behind the chlorination process.

## Chapter 2

### Theory

---

#### II.A. Thermodynamics of chlorination:

In order to predict thermodynamically possible reaction products and corresponding magnitudes in the process of chlorination of aluminum and aluminum-1wt% magnesium alloys containing minute amounts of calcium or sodium, use was made of the Equilibrium programme of the F\*A\*C\*T(Facility for the Analysis of Chemical Thermodynamics)library of programs[38] available on McGill University's main frame computer.

By using this programme, one can determine the identity and quantity of the possible reaction products that would be in equilibrium for a given number of reactants under specified conditions such as temperature, pressure and concentration of each reactant species. Under the specified conditions, the desired solution, i.e the most stable products, is the one that has the lowest Gibbs energy.

The user enters a number of chemical species and/or compounds that will form the reactants side of equilibrium reaction. Such an entry is shown for an argon, chlorine and aluminum system in Figure 2.1. The user is asked to specify the values of a number of intensive and/or extensive property of the system. The number of properties that one can specify is limited by the phase rule. For this particular case the temperature and pressure are specified.

The program then searches through a data base to give a list of possible product species which is solely based on the elements that make up the reactants. One could choose all the species to be included in the calculations. However, in order to decrease the time of the calculations, the user has to chose the product species that are likely to form under the specified conditions.

After making the selection of product species, the program is executed to give the results of the calculations in the form of the total number of moles of each phase in equilibrium with each other containing the mole fractions of each chemical species and/or

EQUILIBRIUM PRODUCT CALCULATION  
\*\*\*\*\*

- incorporating SAGE, the latest version of SOLGASMIX

```
(16NOV90)
***** ENTER REACTANTS *****
(OR PRESS "RETURN" FOR LAST ENTRY)
?
278 AL + 0.000155 AR + 0.00001723 CL2 =
ENTER SUPSCRIPTS, ENTER "HELP", OR PRESS "RETURN"
?
(1000,1,L) (1000,1,G) (1000,1,G)
*****
  T PROD  P PROD  DELTA H  DELTA G  DELTA V  DELTA S  DELTA U  DELTA A
  (K)    (ATM)   (J)      (J)      (L)      (J/K)   (J)      (J)
*****
?
1000 1
- DATABASES BEING SEARCHED
GASEOUS SPECIES 1 - 15
LIQUID  SPECIES 16 - 16
SOLID   SPECIES 17 - 18

ENTER CODE NUMBERS, ENTER "LIST" TO DISPLAY, OR ENTER "HELP"
****(CHANGES TO EQUILIB REQUIRE THE USE OF SLASHES ABOUT GASEOUS SPECIES)***
?
LIST
POSSIBLE PRODUCT COMPOUNDS FOUND:
"<---" IDENTIFIES YOUR PRIVATE COMPOUNDS DATA CREATED WITH "DATAENTRY"
"<--S" IDENTIFIES YOUR PRIVATE SOLUTION DATA CREATED WITH "SOLUTION"
      UNNUMBERED SPECIES MEANS INCOMPLETE DATA SET

  1  AR[+]          G1  GAS          298.0 K - 6000.0 K 2
  2  AR            G1  GAS          298.0 K - 6000.0 K 1
  3  AL2CL6        G1  GAS          298.0 K - 2000.0 K 1
  4  AL*CL3        G1  GAS          298.0 K - 2000.0 K 1
  5  AL*CL2[+]    G1  GAS          298.0 K - 6000.0 K 2
  6  AL*CL2[-]    G1  GAS          298.0 K - 6000.0 K 2
  7  AL*CL2        G1  GAS          298.0 K - 2000.0 K 1
  8  AL*CL[+]     G1  GAS          298.0 K - 6000.0 K 2
  9  AL*CL         G1  GAS          298.0 K - 2000.0 K 2
 10  CL2           G1  GAS          298.0 K - 3000.0 K 1
 11  CL[+]        G1  GAS          298.0 K - 6000.0 K 2
 12  CL           G1  GAS          298.0 K - 3000.0 K 1
 13  AL2          G1  GAS          295.0 K - 300.0 K 1
 14  AL[+]        G1  GAS          298.0 K - 6000.0 K 2
 15  AL           G1  GAS          2767.0 K - 3200.0 K 1

 16  AL           L1  LIQUID        933.0 K - 2767.0 K 1

 17  AL*CL3       S1  SOLID          298.0 K - 454.0 K 1
 18  AL           S1  SOLID          298.0 K - 933.0 K 1

ENTER CODE NUMBERS, ENTER "LIST" TO DISPLAY, OR ENTER "HELP"
****(CHANGES TO EQUILIB REQUIRE THE USE OF SLASHES ABOUT GASEOUS SPECIES)***
?
```

Figure 2.1 The output of the Equilibrium programme

/2-4,7,9,10,12/16  
PRESS "RETURN" WHEN READY FOR OUTPUT  
ENTER AN OPTION NUMBER, OR ENTER "0" FOR OPTIONS MENU  
?

\*\*EXCESSIVE TIME ESTIMATED..ASSUMING 180 SERVICE UNITS  
278 AL + 0.000155 AR + 0.00001723 CL2 =  
(1000,1,L) (1000,1,G) (1000,1,G)

0.16874E-03	(	0.91856	AR	
	+	0.42408E-01	ALCL3	
	+	0.36955E-01	ALCL2	
	+	0.18732E-02	ALCL	
	+	0.20177E-03	AL2CL6	
	+	0.68532E-13	CL	
	+	0.31930E-19	CL2)	
		( 1000.0, 1.00	,G)	
	+	278.00	AL	
		( 1000.0, 1.00	,L1, 1.0000	)

compounds present in that particular phase.

In order to take into account the departure from ideal solution behaviour of alloy systems in the calculations, one can either create and use a separate solution data file which contains expressions to calculate Excess Gibbs Free Energy of solution,  $\Delta G^{xs}$ , for a given composition and temperature or input activity coefficient expressions of the solution components during input to the Equilibrium programme.

In the following calculations, a 7.5 kg charge of pure aluminum or an aluminum-1wt% magnesium alloy was taken to represent the liquid phase. This phase was assumed to come to equilibrium with a gas phase in the form of gas bubbles of argon and chlorine mixtures of various composition. The total number of moles of the reactant gas species was taken to be  $172.3 \times 10^{-6}$  g-moles which is the amount of gas contained in approximately 8 bubbles in a liquid metal column of 0.18 m and 0.14 m diameter. The concentration of calcium and sodium was taken to be 50, and 25 wt-ppm, respectively.

#### II.A.1. Aluminum-Chlorine System:

Figure 2.2 shows the mole fraction of major gaseous reaction products as a function of chlorine concentration in the gas bubbles at 1000 K.

When gas bubbles containing 100%  $\text{Cl}_2$  were utilised,  $\text{AlCl}_3$  was the most favoured gas species to form. This was followed by  $\text{AlCl}_2$ ,  $\text{Al}_2\text{Cl}_6$  and  $\text{AlCl}$  in decreasing order of magnitude. There were also some  $\text{Cl}$  and  $\text{Cl}_2$  present in the products. However, these were at least 10 to 16 orders of magnitude smaller in value and therefore were not included in the graph.

As the chlorine concentration in the gas bubbles decreased, equilibrium conditions shifted such that below 10%  $\text{Cl}_2$  the most favoured gas species to form was  $\text{AlCl}_2$ , followed by  $\text{AlCl}_3$ ,  $\text{AlCl}$  and  $\text{Al}_2\text{Cl}_6$ . Calculations showed that below 30%  $\text{Cl}_2$ , formation of  $\text{AlCl}$  was thermodynamically more favourable than  $\text{Al}_2\text{Cl}_6$ .

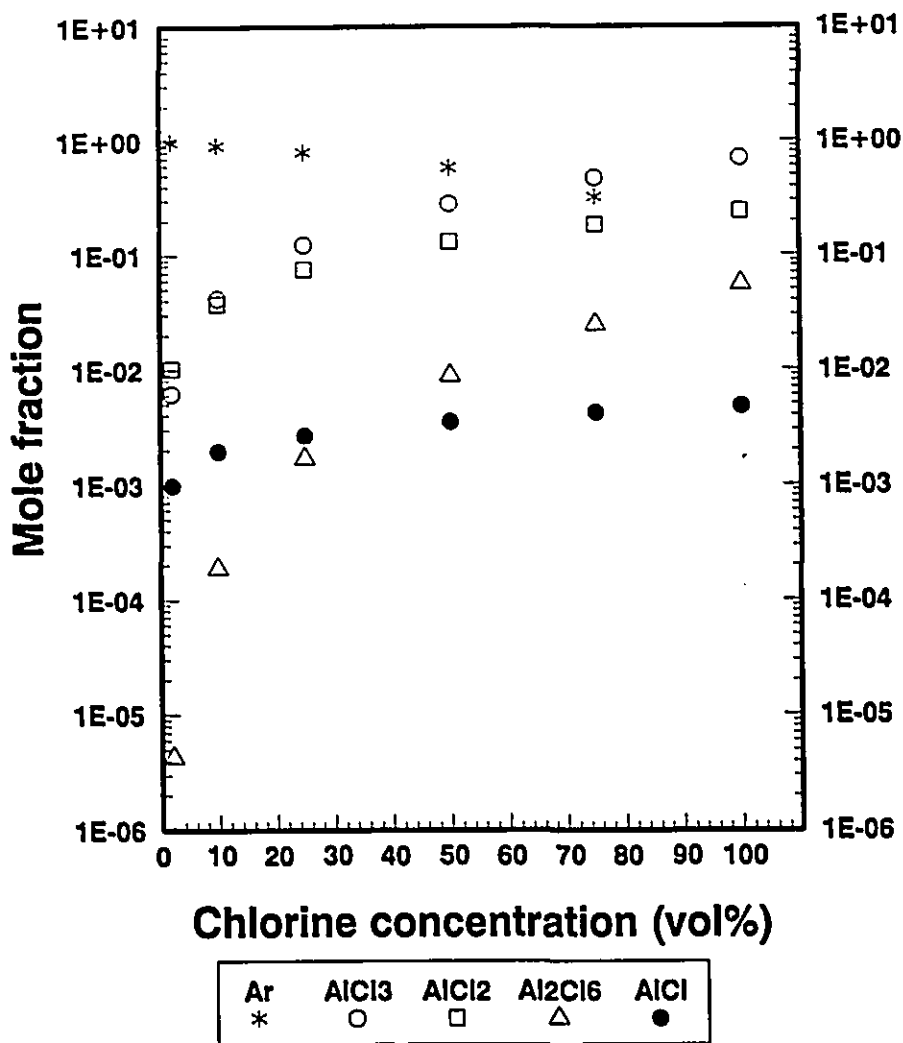


Figure 2.2 The mole fraction of major gaseous reaction products for Al-Cl<sub>2</sub> system as a function of Cl<sub>2</sub> concentration at 1000 K and 1 Atm.

II.A.1.a. Aluminum-Calcium-Chlorine System:

In the calculations for this system, the activity coefficient of calcium in solution at 1000 K was calculated assuming aluminum-calcium is a regular solution. The activity coefficient of calcium at 1100 K was calculated[39] to be 0.0086, assuming the aluminum-calcium system constitutes a regular solution. Therefore, the activity coefficient at 1000 K can be calculated through[40]:

$$\ln f_{1000} = \frac{1100 \ln f_{1100}}{1000} \quad (2.1)$$

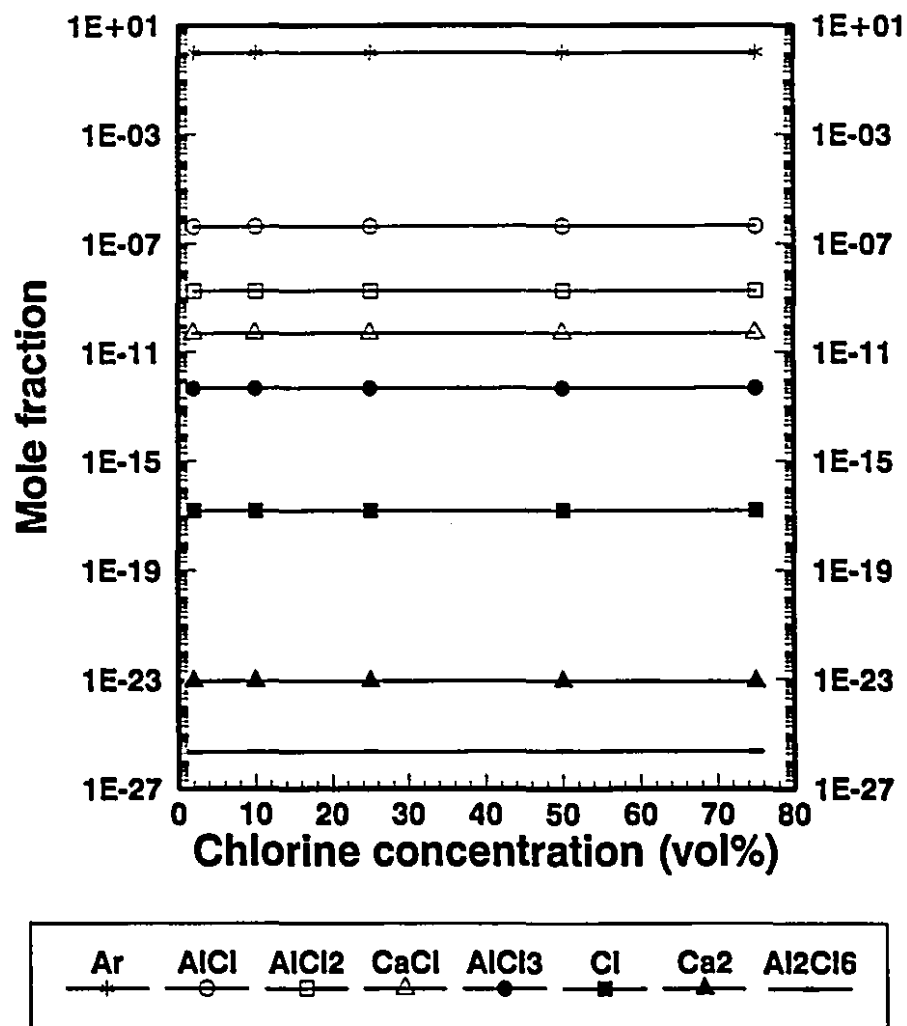
to be  $5.35 \cdot 10^{-3}$ .

Figure 2.3 shows the mole fraction of gaseous product species as a function of chlorine concentration at 1000 K. Under equilibrium conditions the most favourable gas species to form was AlCl. The mole fraction of gaseous species stayed practically constant over the entire range of chlorine concentration.

Calculations showed that the condensed reaction product was solid CaCl<sub>2</sub>. The amount of CaCl<sub>2</sub> increased practically in proportion to an increase in chlorine concentration(as shown in Table 2.1).

**Table 2.1** The mole fraction of CaCl<sub>2</sub> with respect to Cl<sub>2</sub> concentration in the bubbles

Cl <sub>2</sub> (Vol%)	2	10	25	50	75	100
X <sub>CaCl<sub>2</sub></sub>	$345 \cdot 10^{-8}$	$172 \cdot 10^{-7}$	$431 \cdot 10^{-7}$	$862 \cdot 10^{-7}$	$129 \cdot 10^{-6}$	$172 \cdot 10^{-6}$



**Figure 2.3** The mole fraction of major gaseous product species for Al-Ca-Cl<sub>2</sub> system as a function of Cl<sub>2</sub> concentration at 1000 K and 1 Atm.

II.A.1.b. Aluminum-Sodium-Chlorine System:

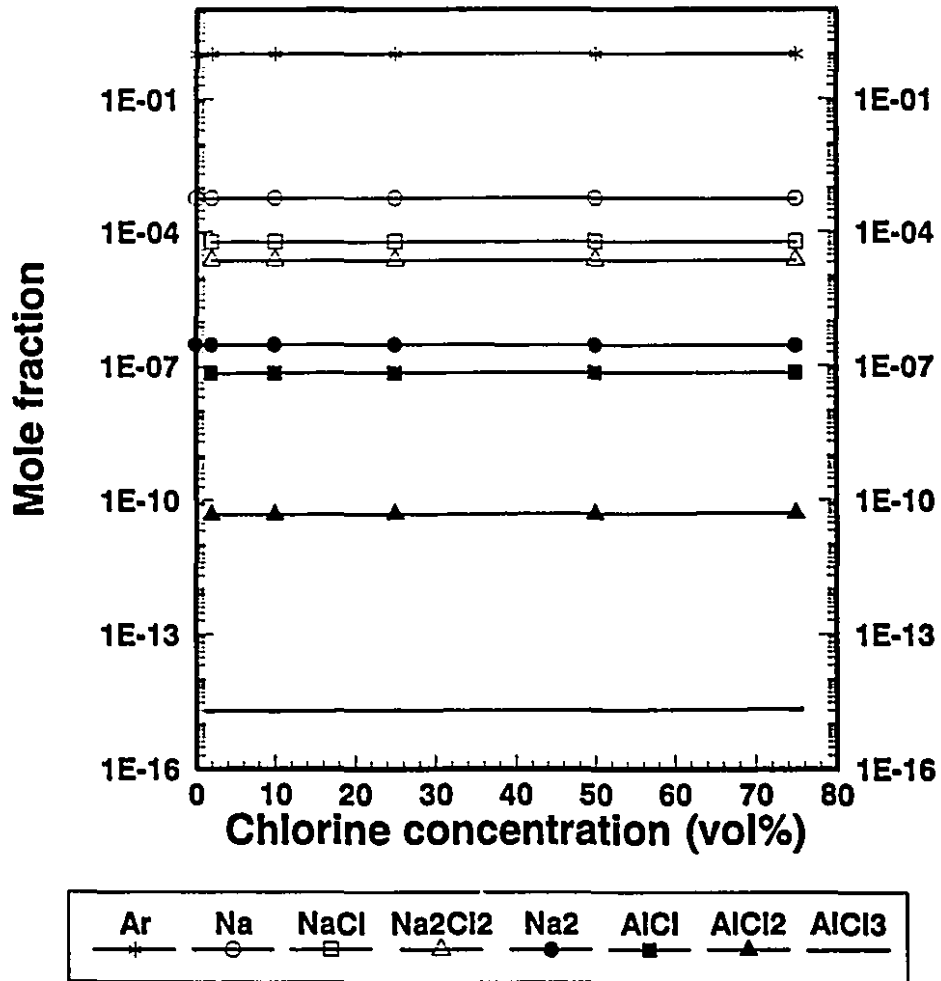
In the calculations for this system, the activity coefficient of sodium,  $f_{\text{Na}}$ , at 1000 K was taken from the data of Mitchell and Samis[41] to be 88.72.

Figure 2.4 gives the mole fraction of major gaseous product species as a function of chlorine concentration at 1000 K. Under equilibrium conditions the most favourable gas species to form was Na. This was followed by NaCl,  $\text{Na}_2\text{Cl}_2$ ,  $\text{Na}_2$ , AlCl,  $\text{AlCl}_3$  and Cl in decreasing order. There were also some  $\text{Cl}_2$  and  $\text{Al}_2\text{Cl}_6$  present in the system. However, they were about 10 orders of magnitude smaller in value than that of Cl. Calculations showed that mole fraction of gaseous species did not change appreciably with increase in chlorine concentration in the gas. The maximum change was in  $\text{AlCl}_3$ , an increase of 13%, with increase in chlorine concentration from 2 to 100%.

Calculations showed that the condensed reaction product was solid NaCl, the amount of which increased practically in proportion to increase in chlorine concentration as shown in Table 2.2.

**Table 2.2** The mole fraction of NaCl with respect to  $\text{Cl}_2$  concentration in the bubbles

$\text{Cl}_2$ (Vol%)	2	10	25	50	75	100
$X_{\text{NaCl}}$	$687 \cdot 10^{-8}$	$344 \cdot 10^{-7}$	$861 \cdot 10^{-7}$	$172 \cdot 10^{-6}$	$258 \cdot 10^{-6}$	$344 \cdot 10^{-6}$



**Figure 2.4** The mole fraction of major gaseous product species for Al-Na-Cl<sub>2</sub> system as a function of Cl<sub>2</sub> concentration at 1000 K and 1 Atm.

II.A.2. Aluminum-Magnesium-Chlorine System:

In order to take into account the deviation from ideality for aluminum-magnesium liquid solution, a private data file was created which included Excess Molar Free Energy of solution according to[42]:

$$\Delta G^{ex} = -15062X_{Al}X_{Mg} + 8.37X_{Al}X_{Mg} T \quad (\text{Joules}) \quad (2.2)$$

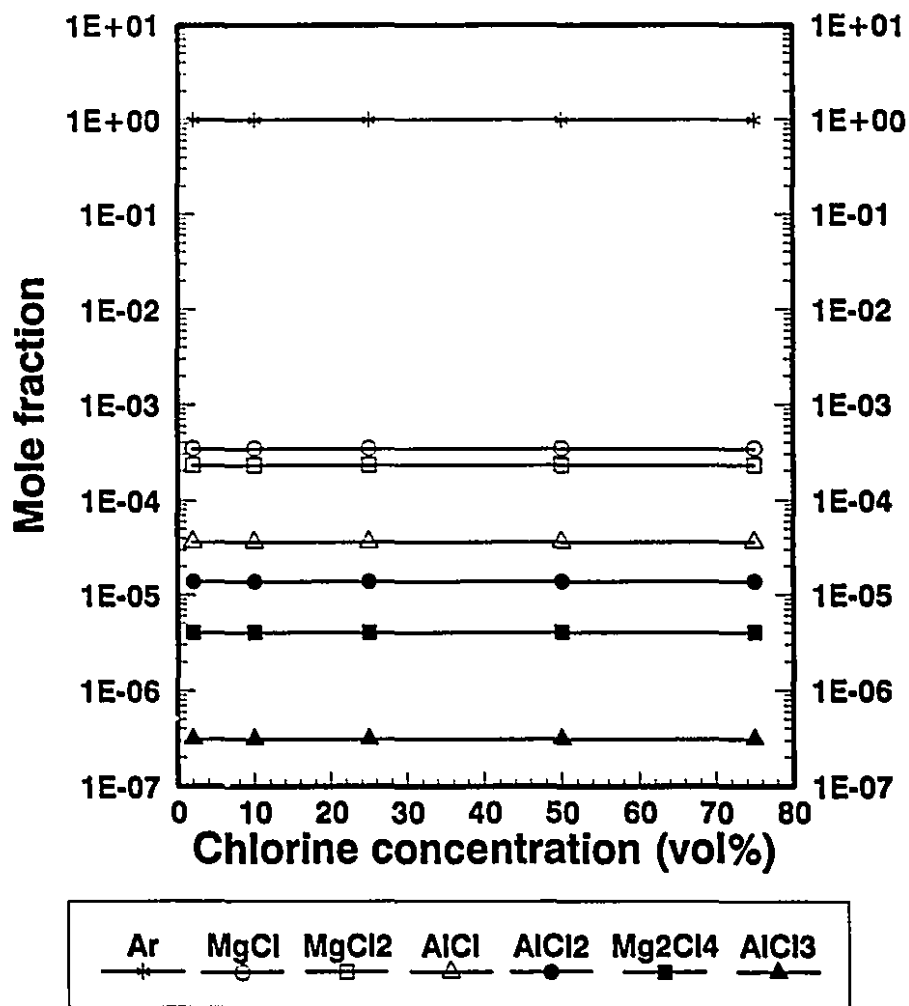
where  $X_{Al}$  and  $X_{Mg}$  are the mole fractions of aluminum and magnesium respectively.

Figure 2.5 shows the mole fraction of gaseous product species as a function of chlorine concentration at 1000 K. As seen, the most favourable gaseous species to form was MgCl. The mole fraction of gaseous species did not change over the entire range of chlorine concentration.

Calculations showed that the condensed reaction product was liquid  $MgCl_2$ , the amount of which increased proportionally to chlorine concentration(see Table 2.3).

**Table 2.3** The mole fraction of  $MgCl_2$  with respect to  $Cl_2$  concentration in the gas bubbles

$Cl_2$ (Vol%)	2	10	25	50	75
$X_{MgCl_2}$	$337 \cdot 10^{-8}$	$172 \cdot 10^{-7}$	$430 \cdot 10^{-7}$	$861 \cdot 10^{-6}$	$129 \cdot 10^{-6}$



**Figure 2.5** The mole fraction of major gaseous product species for Al-Mg-Cl<sub>2</sub> system as a function of Cl<sub>2</sub> concentration at 1000 K and 1 Atm.

#### II.A.2.a. Aluminum-Magnesium-Calcium-Chlorine System:

In the absence of any thermodynamic data for the Al-Mg-Ca system, the solution file originally created for Al-Mg system together with the activity coefficient of calcium in Al-Ca system were used in the calculations. The reaction products,  $\text{MgCl}_2$  and  $\text{CaCl}_2$  were treated as forming an ideal solution.

Figure 2.6 shows the mole-fraction of gaseous product species as a function of chlorine concentration at 1000 K. As seen the most favourable gaseous species to form was  $\text{MgCl}$ . The mole fraction of gaseous species did not change more than 3% over the entire range of chlorine concentration.

Figure 2.7 shows the mole fraction of  $\text{CaCl}_2$  and  $\text{MgCl}_2$  in the ideal salt solution. Calculations showed that the mole fraction of  $\text{MgCl}_2$  and  $\text{CaCl}_2$  stayed practically constant over the entire range of chlorine concentration.

#### II.A.2.b. Aluminum-Magnesium-Sodium-Chlorine System:

In the absence of any thermodynamic data for the Al-Mg-Na ternary system, the solution file originally created for Al-Mg system were used together with the activity coefficient of sodium for the Al-Na system in the calculations. Reaction products  $\text{MgCl}_2$  and  $\text{NaCl}$  were treated as forming an ideal solution.

Figure 2.8 shows mole fraction of gaseous product species as a function of chlorine concentration at 1000 K. As seen sodium was the primary gaseous product.

Calculations showed that mole fraction of  $\text{NaCl}$  and  $\text{Na}_2\text{Cl}_2$  did not change with change in chlorine concentration, whereas the mole fraction of the  $\text{Na}$  and  $\text{Na}_2$  decreased only 3 and 6% respectively in increase in chlorine concentration from 0 to 75%. The mole fraction of other gas species increased between 3 and 15% with increase in chlorine concentration.

Figure 2.9 shows the mole fraction of  $\text{NaCl}$  and  $\text{MgCl}_2$  in the ideal salt solution. Although the mole fraction of  $\text{MgCl}_2$  increased by 6% with increase in chlorine concentration from 2 to 75%, the mole fraction of  $\text{NaCl}$  did not change at all.

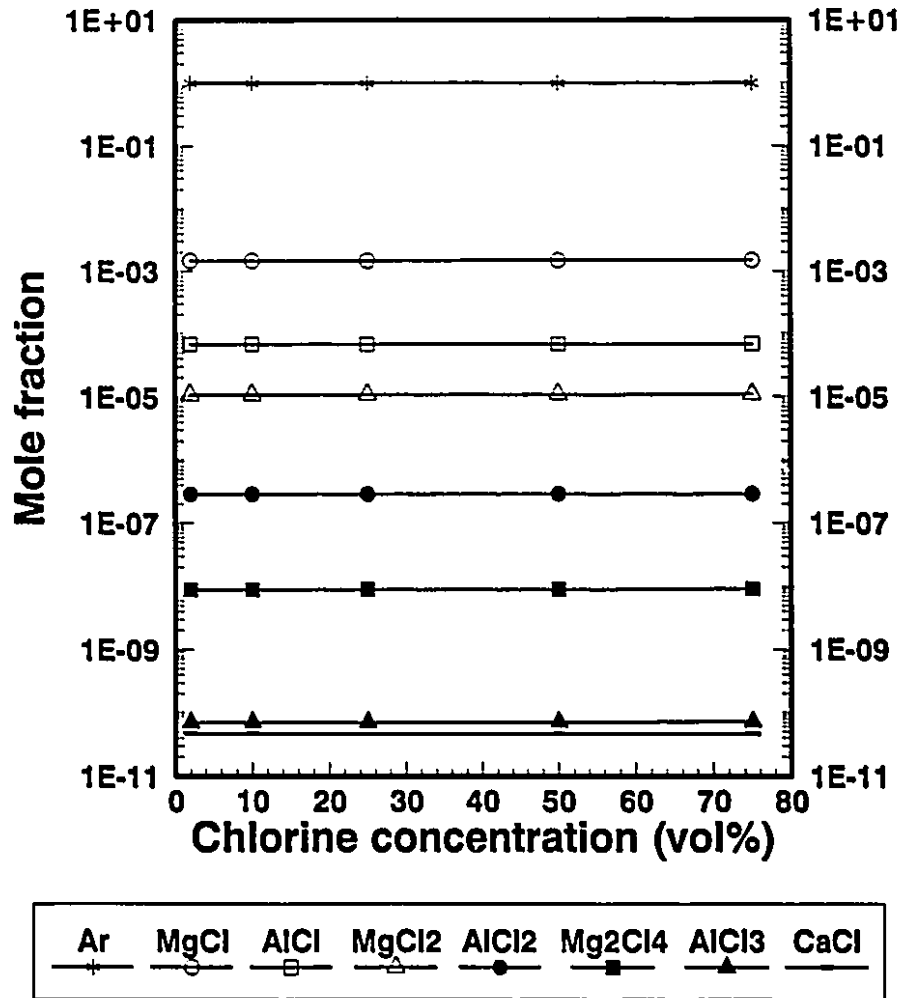


**Figure 2.6** The mole fraction of major gaseous product species for Al-Mg-Ca-Cl<sub>2</sub> system as a function of Cl<sub>2</sub> concentration at 1000 K and 1 Atm.

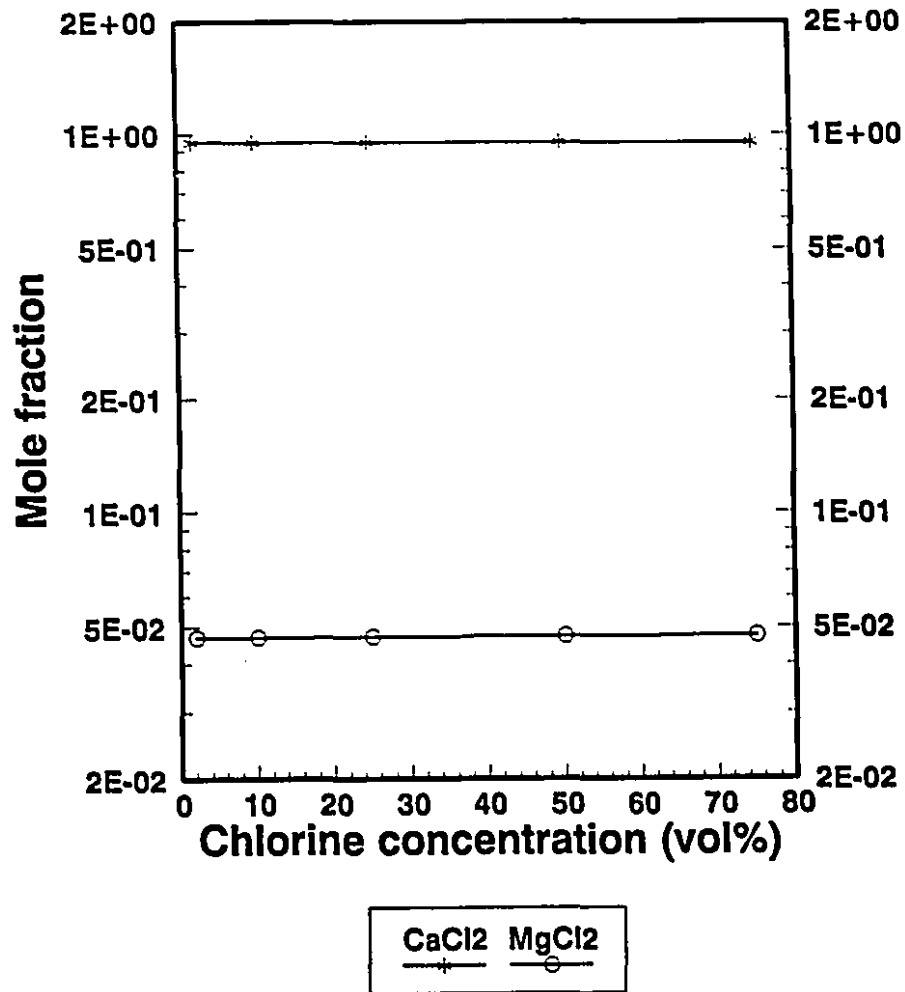


**Figure 2.7** The mole fraction of CaCl<sub>2</sub> and MgCl<sub>2</sub> in the ideal salt solution at 1000 K and 1 Atm.

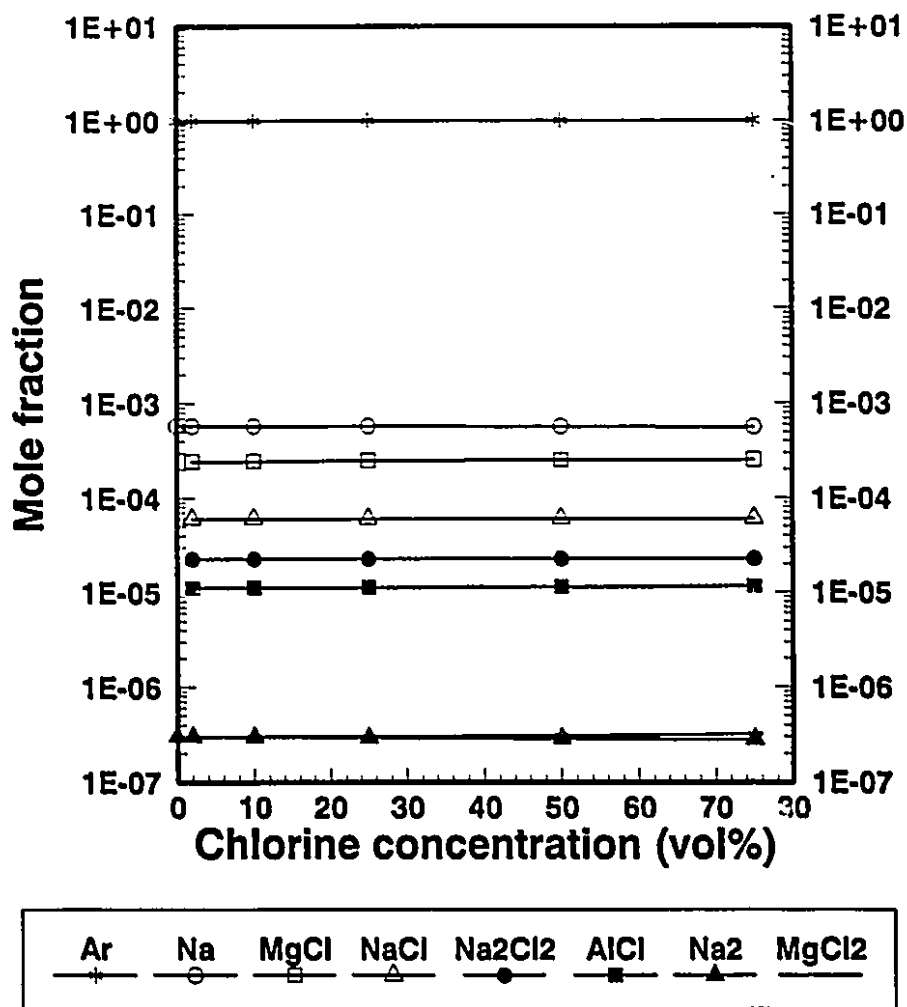


**Figure 2.8** The mole fraction of major gaseous product species for Al-Mg-Na-Cl<sub>2</sub> system as a function of Cl<sub>2</sub> concentration at 1000 K 1 Atm.

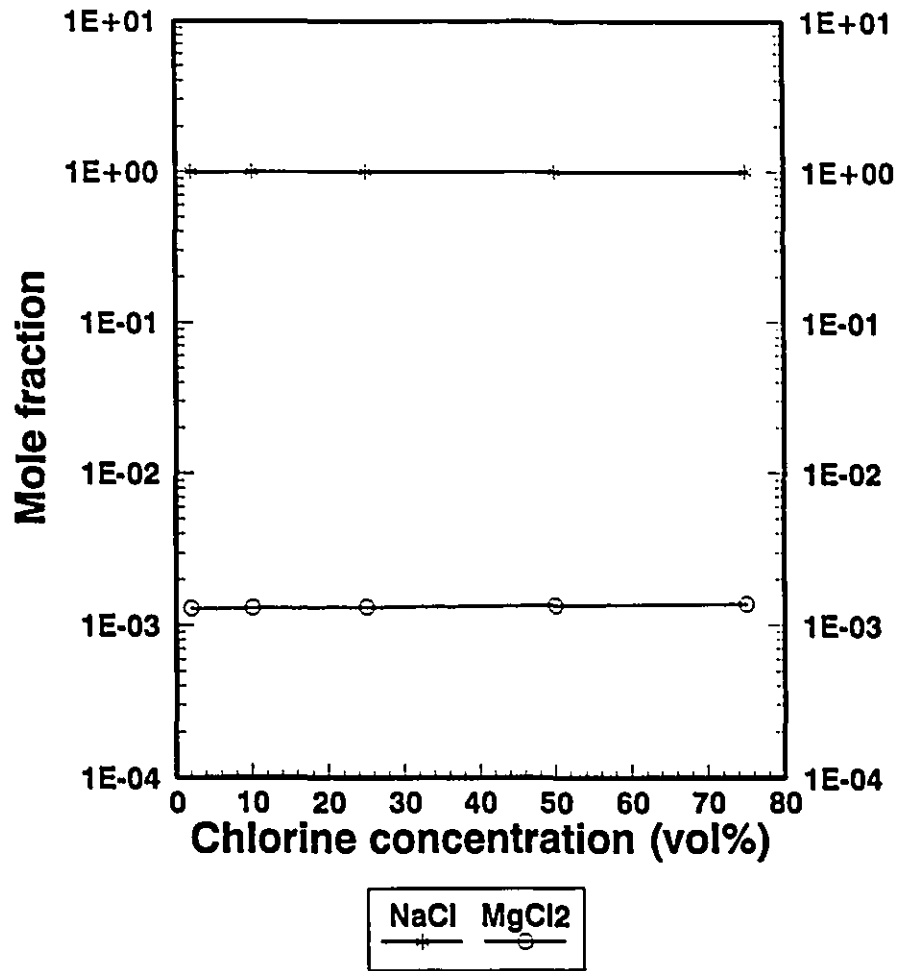


Figure 2.9 The mole fraction of NaCl and MgCl<sub>2</sub> in the ideal salt solution at 1000 K and 1 Atm.

### II.B. Kinetics of chlorination:

While the preceding thermodynamic calculations were useful in identifying the nature and the quantity of the reaction products that would be in equilibrium with a given set of reactants under specified conditions of temperature pressure and concentration, associated kinetics may preclude their formation.

Before constructing a kinetic model of the process of the removal of calcium and sodium, which will be referred to freely as impurities, from aluminum and aluminum-magnesium alloys by chlorination, it is instructive to visualize the chlorination process.

A general schematic description of the chlorination process is shown in Figure 2.10. There, a bath of liquid aluminum is held in a refractory crucible. At the bottom of the crucible, bubbles, comprising a mixture of argon and chlorine gas are introduced into the melt through a gas injection device. The chlorine inside the gas bubbles, will react with chloride forming elements to form gaseous, liquid and solid reaction products depending on the composition and temperature of the melt.

In the case of aluminum base, aluminum-impurity or aluminum-magnesium-impurity systems, possible reaction products that would be in equilibrium with the reactants were determined as noted in the thermodynamics section.

As pointed out in Chapter 1, aluminum that leaves the reduction cells would contain several other elements. Generally, the major elements are iron and silicon. In the commercial purity aluminum that was used in the present study, some manganese and copper were also present. The Standard Free Energy of Formation of magnesium, iron, silicon, manganese, copper, calcium and sodium is presented in Table 2.4. As seen, the most stable chloride is calcium chloride which is followed by sodium, magnesium, manganese, silicon, iron and copper chlorides.

If one considers the relative proportions of aluminum, magnesium and small amounts of silicon, iron, manganese, and copper that would be inevitably present in commercial purity aluminum compared to the minute amounts of calcium and sodium within the melt, one would anticipate that kinetics factors will play an important role in determining how reactions will proceed in practice.

In the case of the aluminum-chlorine system, it was seen that on contact with pure

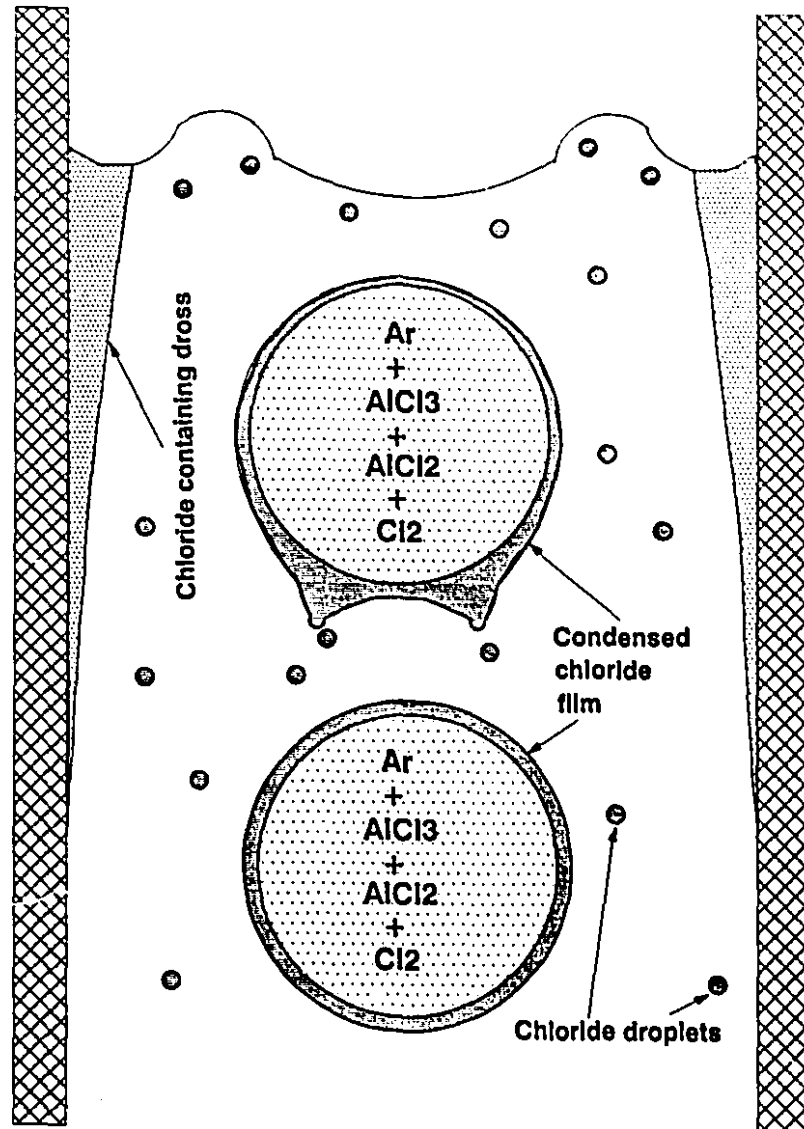


Figure 2.10 A general schematic description of the chlorination process

Table 2.4 Standard Free Energy of Formation of some chlorides[43] at 1000 K  
(Joules/g-mole of chlorine)

$\text{Ca(s)} + \text{Cl}_2(\text{g}) = \text{CaCl}_2(\text{s})$	$\Delta G^0 = -653000$
$2\text{Na(l)} + \text{Cl}_2(\text{g}) = 2\text{NaCl(s)}$	$\Delta G^0 = -639000$
$\text{Mg(l)} + \text{Cl}_2(\text{g}) = \text{MgCl}_2(\text{l})$	$\Delta G^0 = -482000$
$\text{Mn(s)} + \text{Cl}_2(\text{g}) = \text{MnCl}_2(\text{l})$	$\Delta G^0 = -355000$
$1/2\text{Si(s)} + \text{Cl}_2(\text{g}) = 1/2\text{SiCl}_4(\text{g})$	$\Delta G^0 = -238000$
$\text{Fe(s)} + \text{Cl}_2(\text{g}) = \text{FeCl}_2(\text{l})$	$\Delta G^0 = -220000$
$2\text{Cu(s)} + \text{Cl}_2(\text{g}) = \text{Cu}_2\text{Cl}_2(\text{l})$	$\Delta G^0 = -161000$

aluminum,  $\text{AlCl}_3$  or  $\text{AlCl}_2$  would form as a primary gaseous reaction product depending on the chlorine concentration in the gas bubbles. It can therefore be anticipated that  $\text{AlCl}_3$  or  $\text{AlCl}_2$  gas will be the first dominant species to form on initial contact with a base aluminum melt, containing magnesium, iron, silicon, copper, manganese, calcium or sodium as solutes owing to aluminum's much larger mole fraction inside the melt.

Aluminum chlorides will subsequently react with Mg, Fe, Si, Mn, Cu, Ca or Na to form the chlorides of these elements. Again, due to their much larger mole fractions, the dominant reaction products in the case of aluminum-magnesium alloy will be  $\text{MgCl}_2$ , whereas in commercial purity aluminum they will be the chlorides of Fe, Si, Cu, or Mn.

Depending on the composition and temperature, these *intermediate reaction products* can form a solid or liquid film on the bubble surfaces. It is possible that such films cover the bubbles during their passage through the melt while reacting with minute amount of calcium or sodium. It is also possible that such films can be continuously stripped off from

the bubbles by hydrodynamic shear, depending on the physical properties of the film and adhesion characteristics at the melt-salt interface. Such intermediate reaction products, stripped from the bubbles, will form liquid droplets or solid particles which, in turn, can be effective reaction sites for impurity removal.

Any remaining unreacted portion of such films will be carried to the melt surface where, again depending on hydrodynamic conditions, then carried towards the crucible wall where they can adhere or be re-entrained into the melt.

Impurities can also be eliminated from the melt as a result of evaporation from the melt surface and by evaporation into the bubbles.

Finally, crucible walls, depending on the composition of the crucible material, may also provide a reaction site for the removal of the impurities.

After having considered kinetic factors in the removal of calcium and sodium by chlorination from aluminum and aluminum-magnesium alloys, two kinetic models will be presented. Later these models will be used in the interpretation of the experimental results.

### II.B.1. Kinetic Models for Impurity Removal:

#### II.B.1.a. Stoichiometrically Controlled Impurity Removal:

In the formulation of this case, the following assumptions will be made:

- i) There is sufficient contact surface area between the bubbles and the melt so that the impurity will react quantitatively with chlorine on bubble surfaces.
- ii) Any chlorides that form as *intermediate reaction products* on the bubble surfaces will be consumed completely through reactions with the impurity before the bubbles leave the melt.
- iii) Gas phase resistance to mass transfer is negligible
- iv) The impurity will attain its equilibrium partial pressure inside the gas bubbles by evaporation
- v) The rate of evaporation of the impurity at the melt surface and the rate of consumption of the impurity by reaction with the crucible wall will be controlled by the transport of the impurity through a melt phase mass transfer boundary layer.

With these assumptions, making a molar mass balance for the impurity gives:

$$-\frac{M d\%I^B}{100 m_I dt} = \frac{1}{n} G_{Cl_2} + \frac{G_{Ar} P_I}{P_{atm} - P_I} + \frac{k_s A_s \rho [\%I^B - \%I_s^*]}{100 m_I} + \frac{k_w A_w \rho [\%I^B - \%I_w^*]}{100 m_I} \quad (2.3)$$

In the above equation,  $M$  is the mass of the melt,  $m_I$  is the molecular weight of the impurity,  $t$  is the time,  $I^B$  and  $I^*$  are the bulk and interface concentrations of the impurity,  $G_{Cl_2}$  and  $G_{Ar}$  are the molar flow rates of chlorine and argon gases,  $P_I$  and  $P_{atm}$  are the partial pressure of the impurity in the gas bubbles and atmospheric pressure respectively,  $\rho$  is the density of the melt,  $k_s$  and  $k_w$  are the melt phase mass transfer coefficients for the impurity removal through the melt surface and on the crucible wall respectively,  $A_s$  and  $A_w$  are the surface area of the melt surface and the crucible wall respectively.

In Eqn.(2.3), the term on the left hand side represents the change of bulk concentration of the impurity by time. The first term on the right hand side gives the rate of impurity removal by reaction of the impurity with chlorine stoichiometrically on the bubble surfaces according to:



The second term in Eqn.(2.3) represents the rate of removal of the impurity by attaining its equilibrium partial pressure within the bubbles. In the derivation of this term, hydrostatic pressure of the melt was ignored owing to its relatively low value compared to the atmospheric pressure ( $\sim 0.5\%$  of  $P_{atm}$  under the present experimental conditions). Therefore in this term

$$\frac{P_I}{P_{atm} - P_I} \quad (2.5)$$

represents the mole fraction of the impurity inside the gas bubbles. The partial pressure of the impurity in the denominator of the second term in Eqn.(2.3) can be dropped because of its much smaller value compared to that of the atmosphere. For the partial pressure of the impurity,  $P_I$ , in the denominator, its value that is in equilibrium with the impurity

concentration in the melt will be taken according to:

$$P_I = K f_I \%I^B \quad (2.6)$$

In the above equation,  $f_I$  is the activity coefficient of the impurity and  $K$  is the equilibrium constant for the equilibrium:

$$I = I(g) \quad (2.7)$$

The third term in Eqn.(2.3) represents the rate of removal of the impurity due to evaporation through the melt surface. In this term, the interfacial concentration of the impurity,  $I_s^*$ , will be taken to be zero on the grounds that the surface of the melt was flushed with the argon gas during the experiments and assuming that the mass transfer is controlled in the melt phase mass transfer boundary layer. The last term in Eqn.(2.3) represents the rate of removal of the impurity by reaction with crucible wall. In this term, the interfacial concentration of the impurity,  $I_w^*$ , will be taken to be zero assuming that chemical reaction on the crucible melt interface is fast and assuming that the mass transfer is controlled in the melt phase mass transfer boundary layer. With these assumptions Eqn.(2.3) becomes:

$$\begin{aligned} -\frac{M d\%I^B}{100 m_I dt} = & \frac{1}{n} G_{Cl_2} + \frac{G_{Ar} K f_I \%I^B}{P_{atm}} + \frac{k_s A_s \rho \%I^B}{100 m_I} \\ & + \frac{k_w A_w \rho \%I^B}{100 m_I} \end{aligned} \quad (2.8)$$

Upon integration of this equation, one obtains:

$$\frac{E/F + \%I_t^B}{E/F + \%I_i^B} = e^{-Ft} \quad (2.9)$$

where  $E$  and  $F$  are defined by the following equations:

$$E = \frac{\frac{1}{n} G_{Cl_2} 100 m_I}{M} \quad (2.10)$$

$$F = \frac{G_{Ar} K f_I 100 m_I}{M P_{atm}} + \frac{k_s A_s \rho}{M} + \frac{k_w A_w \rho}{M} \quad (2.11)$$

### II.B.1.b. Mass Transfer Controlled Impurity Removal:

For this case it will be assumed that *the flux of the impurity to the gas bubbles is not sufficient to consume all the chlorine and/or intermediate reaction products that form on the bubble surfaces before the bubbles leave the melt.* Consequently, in the formulation for this case, the following assumptions will be made:

- i) The contact surface area between the bubbles and the melt is limited, such that the rate of removal of the impurity by reaction on the bubble surface will be controlled by the speed of transport of the impurity through a melt phase boundary layer,
- ii) the rate of evaporation of the impurity at the melt surface, the rate of consumption of the impurity by reaction with the crucible wall and by reaction with the *intermediate reaction products that are separated from the bubbles* will be controlled by the transport of the impurity through a melt phase mass transfer boundary layer.
- iii) Gas phase resistance to mass transfer is negligible
- iv) The impurity will not attain its equilibrium partial pressure inside the gas bubbles.

With these assumptions, making a molar mass balance for the impurity, one obtains:

$$\begin{aligned} -\frac{M d\%I^B}{100 m_I dt} = & \frac{k_b \rho A_b [\%I^B - \%I_b^*]}{100 m_I} + \frac{k_s \rho A_s [\%I^B - \%I_s^*]}{100 m_I} \\ & + \frac{k_{tp} \rho A_{tp} [\%I^B - \%I_{tp}^*]}{100 m_I} + \frac{k_w \rho A_w [\%I^B - \%I_w^*]}{100 m_I} \end{aligned} \quad (2.12)$$

The term on the left side of Eqn.(2.12) gives the change in the bulk concentration of the impurity,  $\%I^B$ , with time. The terms on the right hand side represent in order from left to right, the rate of removal of the impurity 1) by reaction on bubble surfaces 2) by

evaporation through the melt surface 3) by reaction with the *intermediate reaction products that are separated from the bubble surfaces* and finally 4) by reaction with the crucible wall.

Interfacial impurity concentrations,  $\%I_b^*$ ,  $\%I_{irp}^*$ ,  $\%I_w^*$  will be taken to be zero assuming that chemical reactions at these interfaces are fast and mass transfer in the associated melt phase boundary layer is rate limiting. For the evaporation term,  $\%I_s^*$  will be taken to be zero since the surface of the melt was flushed with argon gas during the experiments.

Upon integration of Eqn.(2.12), with these assumptions, one obtains:

$$\frac{\%I_i^B}{\%I_i^B} = -\exp \left( \frac{k_b \rho A_b}{M} + \frac{k_s \rho A_s}{M} + \frac{k_{irp} \rho A_{irp}}{M} + \frac{k_w \rho A_w}{M} \right) t \quad (2.13)$$

In this equation, the terms in the brackets represent, in order from left to right, the rate constants for impurity removal 1) by bubbles,  $R_b$ , 2) by evaporation through the melt surface,  $R_s$ , 3) by *intermediate reaction products that are separated from the bubbles*,  $R_{irp}$ , and 4) by the crucible wall,  $R_w$ .

Each rate constant contains a melt phase mass transfer coefficient,  $k$ , the total surface area involved at any instant,  $A$ , and terms representing the density,  $\rho$ , and mass of the melt,  $M$ . The combination of the rate constants gives the overall rate constant,  $R_o$ .

### II.C. Shape Regimes for Fluid Particles in Liquid Aluminum:

Before carrying on further to the following chapter, it is instructive to consider the shape regimes that fluid particles will assume, in liquid aluminum. Clift et al[44]. have presented a generalized graphical solution for droplets and bubbles rising or falling freely in Newtonian media of infinite extent, in terms of an Eotvos number,  $Eo$ ; a Morton number,  $M$ ; and a Reynolds number,  $Re$ ;

$$Eo = \frac{g \Delta \rho d_e^2}{\sigma} \quad (2.14)$$

$$M = \frac{g \mu^4 \Delta \rho}{\rho^2 \sigma^3} \quad (2.15)$$

$$Re = \frac{\rho U d_c}{\mu} \quad (2.16)$$

In the above equations,  $\rho$  is the density of the medium,  $\Delta\rho$  is the density difference between the bubbles or droplets and the medium,  $\mu$  is the viscosity of the medium,  $\sigma$  is surface tension,  $U$  is the terminal velocities of the droplets, and bubbles,  $g$  is the gravitational acceleration, and  $d_c$  represents the diameter of a volume equivalent sphere. Their resulting plot is shown in Figure 2.11. Taking surface tension,  $\sigma=0.84$  N/m[45]; viscosity,  $\mu=1.083 \cdot 10^{-3}$  kg/m-s[46]; and density,  $\rho=2350$  kg/m<sup>3</sup>[46]; for liquid aluminum at 730 °C, one would obtain a Morton number of  $9.67 \cdot 10^{-15}$ , the logarithm of which is -14. According to Figure 2.11, bubbles with equivalent diameter,  $d_c$ , between 3 and 38mm can be assumed to fall in the ellipsoidal shape regime. Bubbles with  $d_c$  less than 3mm would be spherical whereas with  $d_c > 38$ mm will be in spherical cap regime.

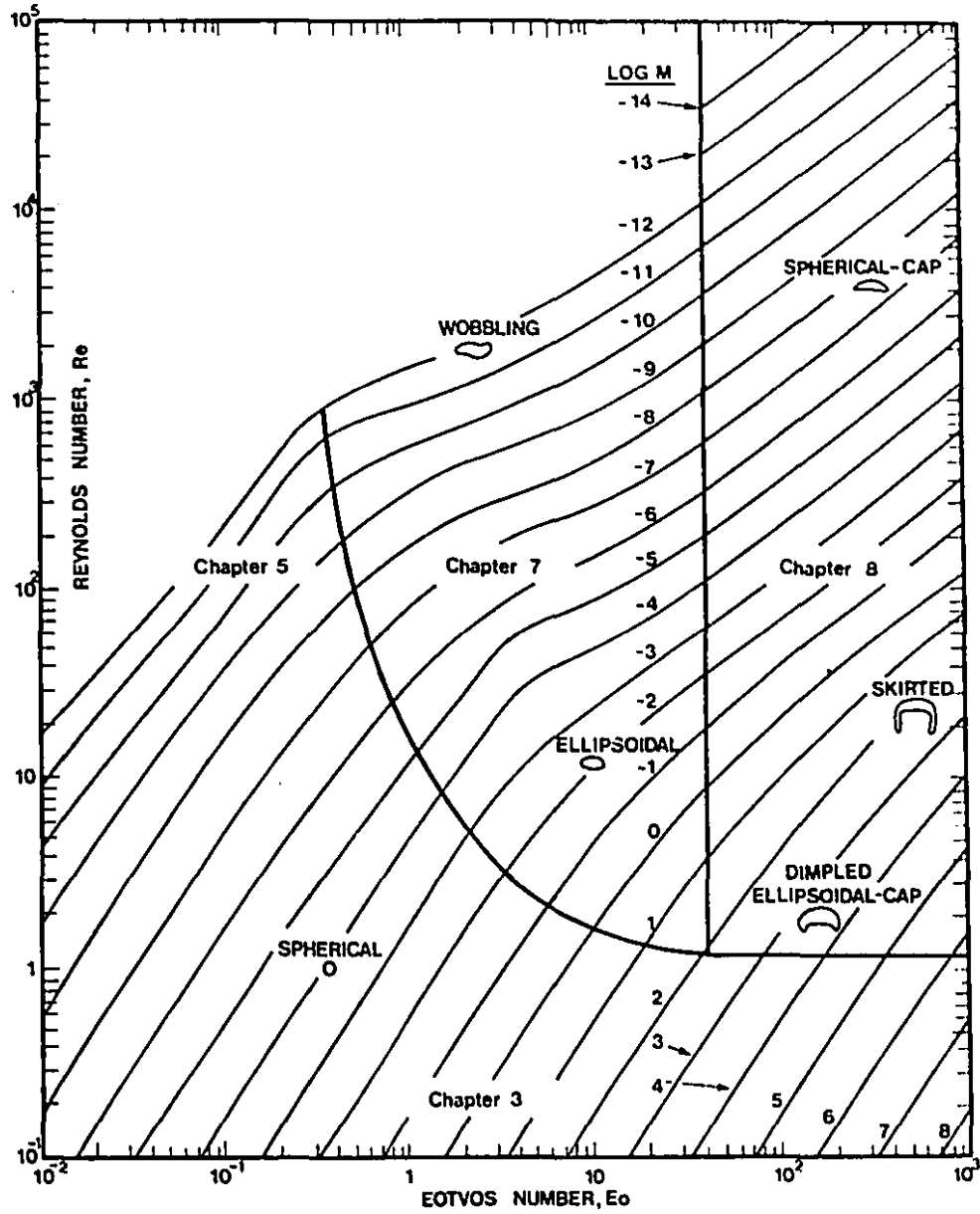


Figure 2.11 Shape regimes of the fluid particles as a function of  $Re$ ,  $Eo$  and  $M$ [44]

## Chapter 3

### Experimental Set-up and Procedure

---

#### III.A. Melt Gas Fluxing Unit:

A schematic of the melt gas fluxing unit is shown in Figure 3.1. A 6.4 kW electric resistance furnace was used to melt a 7.5 kg charge contained in an alumina crucible. The crucible was 0.34 m in height and had an inside diameter of 0.142 m. The top of the crucible was covered with a graphite lid which provided inlets for a gas bubbling lance, impeller, protective argon atmosphere and a sampling ladle. The inlets had screw-in graphite caps. Figure 3.2 shows the crucible and its graphite cover.

High purity chlorine and argon gases were first passed through separate columns of  $\text{CaSO}_4$  to remove moisture. The flow rates of the gases were regulated through calibrated flowmeters.

In order to provide homogeneity in the gas mixture before it was injected into the melt, argon and chlorine gases were passed through a flask containing 3 mm diameter glass balls. The gas mixture was then injected into the melt through an upward facing quartz nozzle.

To measure the frequency of bubble formation, a microphone was inserted into the gas line. The output of the microphone was transmitted to an oscilloscope (Gould 1421) to monitor the bubble frequencies.

The temperature of the melt was measured periodically with a K-Type dip-tip thermocouple through an Omega HH 81 thermometer. The melt temperature was maintained within  $\pm 3$  °C by controlling the power input to the furnace by an Omega 4001 temperature controller.

The top of the melt was flushed with high purity argon gas beneath the graphite lid continuously during experiments at 2 litres/min to avoid oxidation of the melt as much as possible.

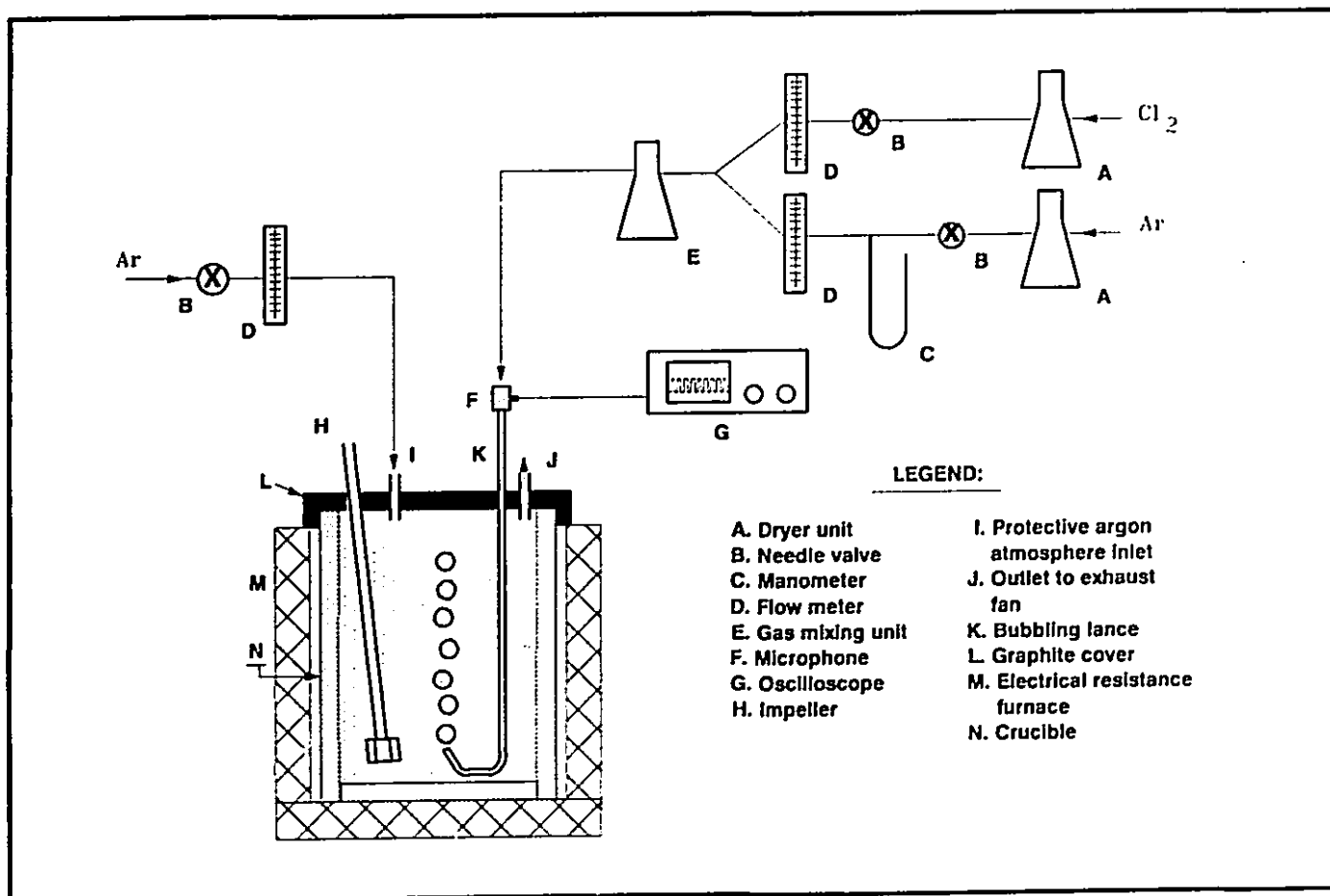
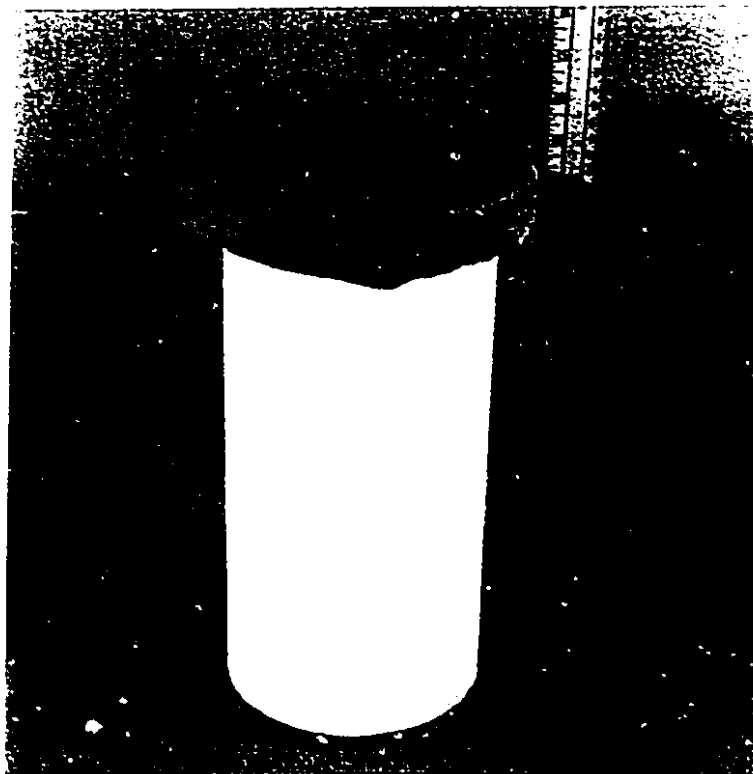


Figure 3.1 Schematic of melt gas fluxing unit



**Figure 3.2** The crucible and its graphite cover used in the experiments

### III.A.1. Preparation for the Gas Fluxing Experiments:

#### III.A.1.a. Preparation of the Charge and the Melt:

First, aluminum and magnesium ingots were cut into small manageable pieces by using a saw. These small pieces were then cleaned thoroughly by using methyl alcohol to remove any lubricant that was induced during the cutting operation. The aluminum pieces were then charged into the crucible and the graphite cover was placed on top of the crucible. The furnace was then turned on to heat the charge. Approximately two hours later, the argon supply was turned on to flush the inside of the crucible before the charge started to melt. It took about 3.5 to 4 hours to melt the charge completely. If needed, magnesium was added only after all the charge was melted and the temperature became steady around the experimental temperature. Before adding magnesium through one of the ports in the graphite

cover, the gas flow rate into the crucible was increased, the surface of the melt was skimmed and magnesium was plunged into the melt with a bell-shape plunger. The impeller was then turned on for 5 minutes to homogenize the melt.

III.A.1.b. Preparation of Impurity Additions:

In the case of calcium, an aluminum-5wt% calcium master alloy was prepared in small quantities(500 gm) by diluting an aluminum-40% calcium alloy in a small crucible by using an induction furnace. The melt was then cast into 30 cm long 1 cm diameter bars in graphite mould. These bars were then cut into small pieces and cleaned thoroughly by using methyl alcohol. In the case of sodium, technical grade sodium was used as is.

III.A.1.c. Preparation of Gas Fluxing Lances:

0.4 cm ID x 0.6 cm OD quartz tubes were first cut into lengths of 45 cm. One end of the tubes were bent by using a torch to make an upward facing nozzle.

During experiments, particularly with magnesium containing alloys, frequent subsurface lance breakages occurred. In order to remedy this, the surface of the lance was covered with a thin layer of iron oxide paste leaving about a 3 mm wide strip of uncovered area at the tip of the lance. The lances were first dried in air and in a drying oven to remove the moisture before they were introduced into the melt. Figure 3.3 shows the quartz lance used in the experiments.

III.A.1.d. Preparation of the Impeller:

The impeller head used in the experiments is shown in Figure 3.4. The impeller blades and the stem was machined from graphite. The impeller was connected to a motor by a steel rod. The surface of the steel rod that was in contact with the melt was covered with a thin layer of iron oxide paste to prevent it from dissolving into the melt.

III.A.2. Materials:

Aluminum metal that was used in the experiments was provided by Alcan Int. Ltd. and was of commercial purity grade(99.7 wt% Al). Table 3.1 shows the concentration of

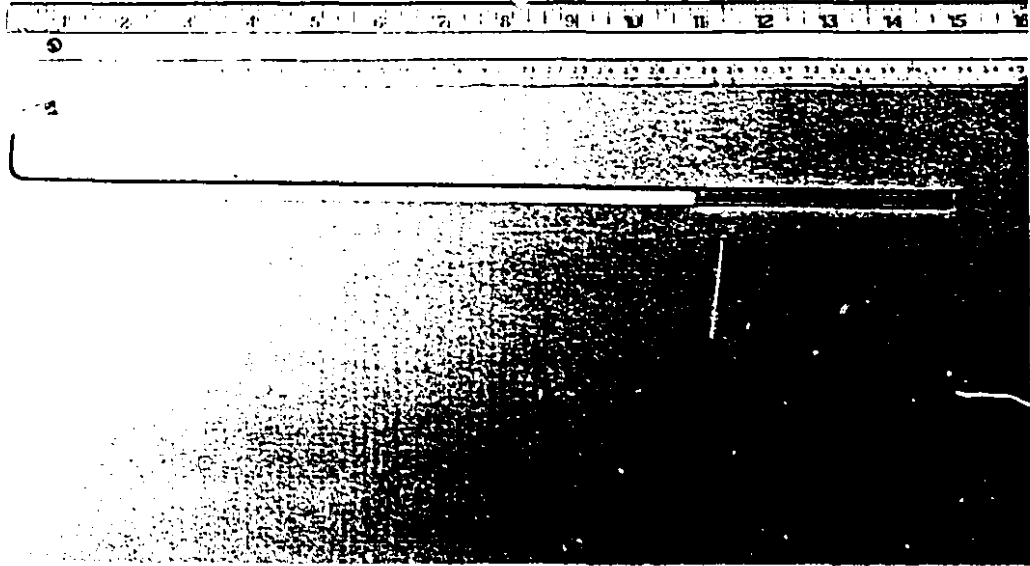


Figure 3.3 The quartz gas bubbling lance used in the experiments

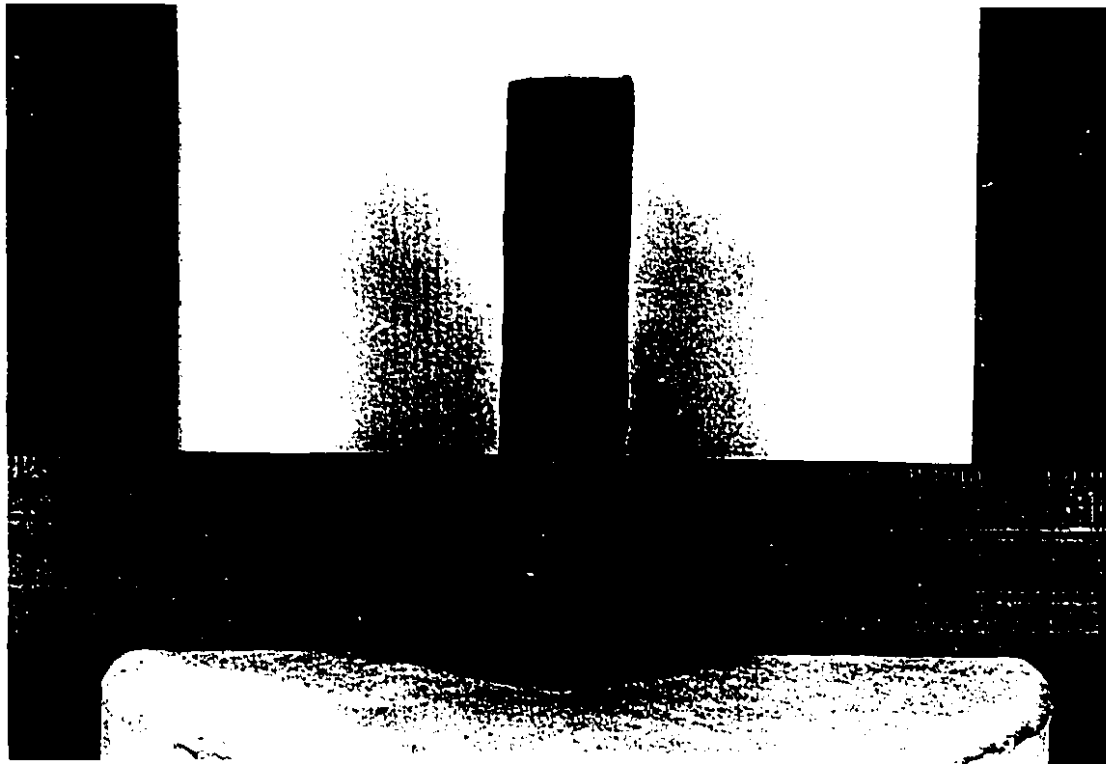


Figure 3.4 The impeller head used in the experiments

major impurities in commercial purity aluminum.

**Table 3.1** Major impurities in commercial purity aluminum

Element	wt%
Si	$0.036 \pm 0.005$
Fe	$0.081 \pm 0.02$
Cu	$0.004 \pm 0.002$
Mn	$0.09 \pm 0.01$

Magnesium metal that was used to alloy commercial purity aluminum was provided by Timminco Metals and was of 99.8% pure. The major impurities in this metal are given in Table 3.2.

**Table 3.2** Major impurities in magnesium metal

Element	wt%
Mn	0.1 max
Ni	0.001 max
Cu	0.02 max
Pb	0.01 max
Sn	0.01 max
Ca	0.01 max

Sodium was purchased from Anachemia Ltd. and was of technical grade.

High purity argon(99.998%) and chlorine(99.5%) were purchased from Linde and Air-Liquid respectively.

### III.A.3. Calibration of Flowmeters:

The flowmeter that was used to measure chlorine flow rate was calibrated by a soap-meter. Figure 3.5 shows the result of the calibration. Correction for the pressure under experimental conditions was done by using the correction charts supplied for this particular flowmeter. The flowmeter that was used to measure argon flow rate was calibrated by a wet test meter. Figure 3.6 shows the result of the calibration. Correction for pressure under the experimental conditions was done by using correction charts supplied for this particular flow meter.

### III.A.4. Experimental Procedure:

In order to generate an initial impurity concentration, sodium or aluminum-calcium master alloy was wrapped in a commercially available aluminum foil and dipped into the melt using a bell shape plunger. The weight of the impurities was adjusted to give a 20 wt-ppm sodium or 50 wt-ppm calcium concentration in the melt. After the addition of the impurity, the melt was stirred by the impeller at 175 rpm for 5 minutes to achieve chemical homogeneity. After this, the first sample(approximately 90 gm) was taken by using a small ladle and poured into a standard Alcan mould to produce a disk-shape sample. The standard Alcan mould and a disk sample are shown in Figure 3.7. Immediately after taking the first sample, gas injection was started and samples were taken periodically.

In the course of the experiments, the frequency of bubble formation was monitored on the screen of the oscilloscope. The temperature of the melt was measured periodically and adjusted through the temperature controller of the furnace.

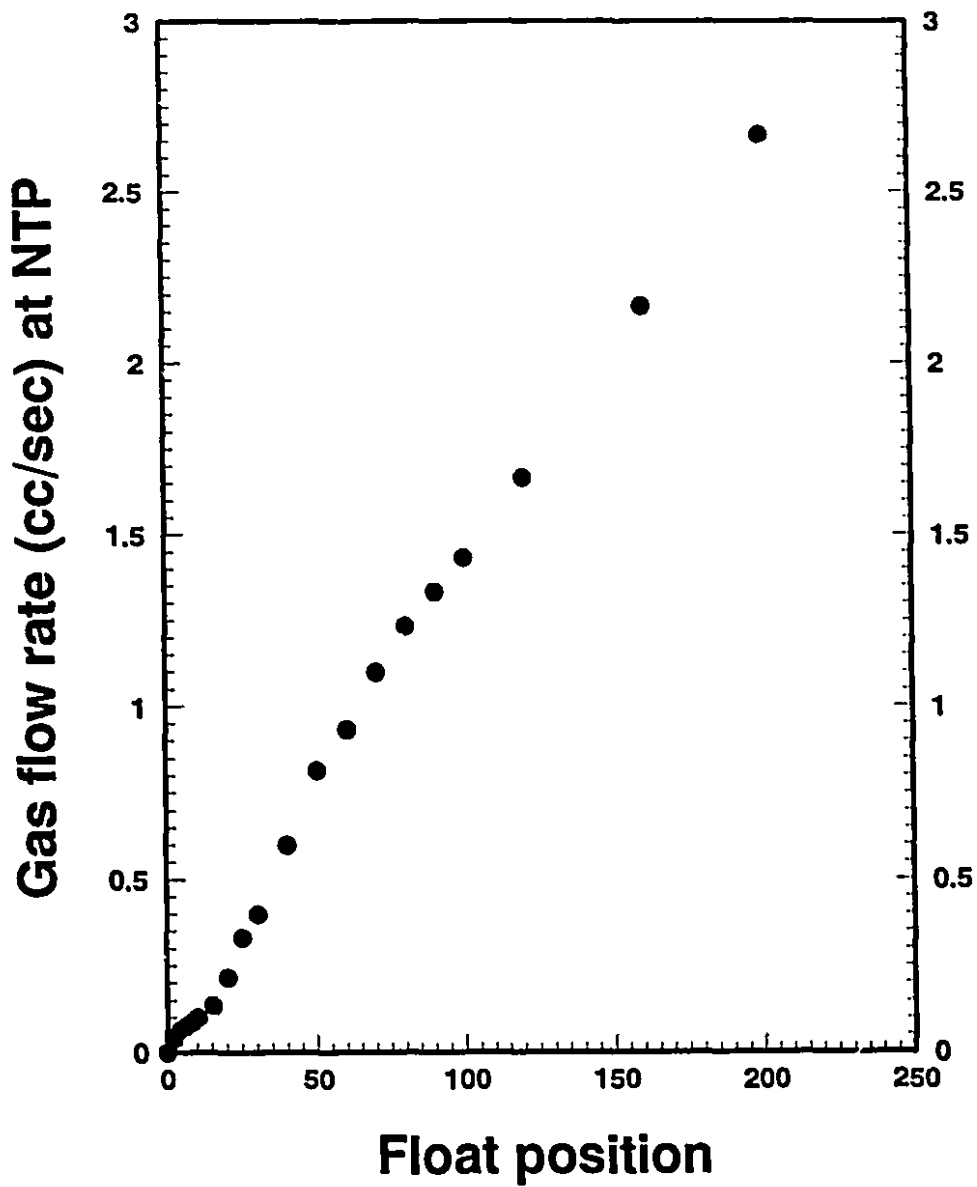


Figure 3.5 Calibration chart for chlorine gas

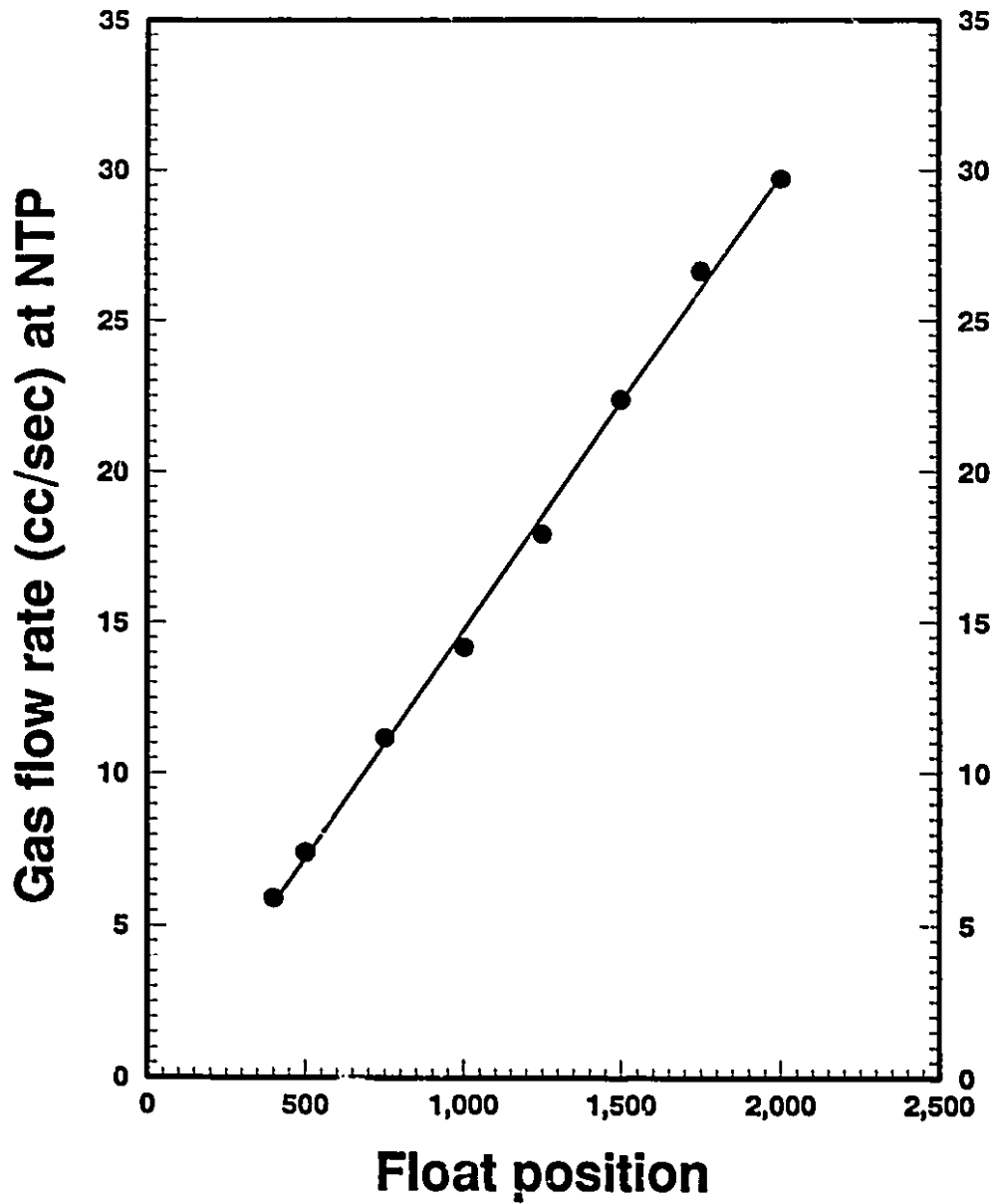


Figure 3.6 Calibration chart for argon gas

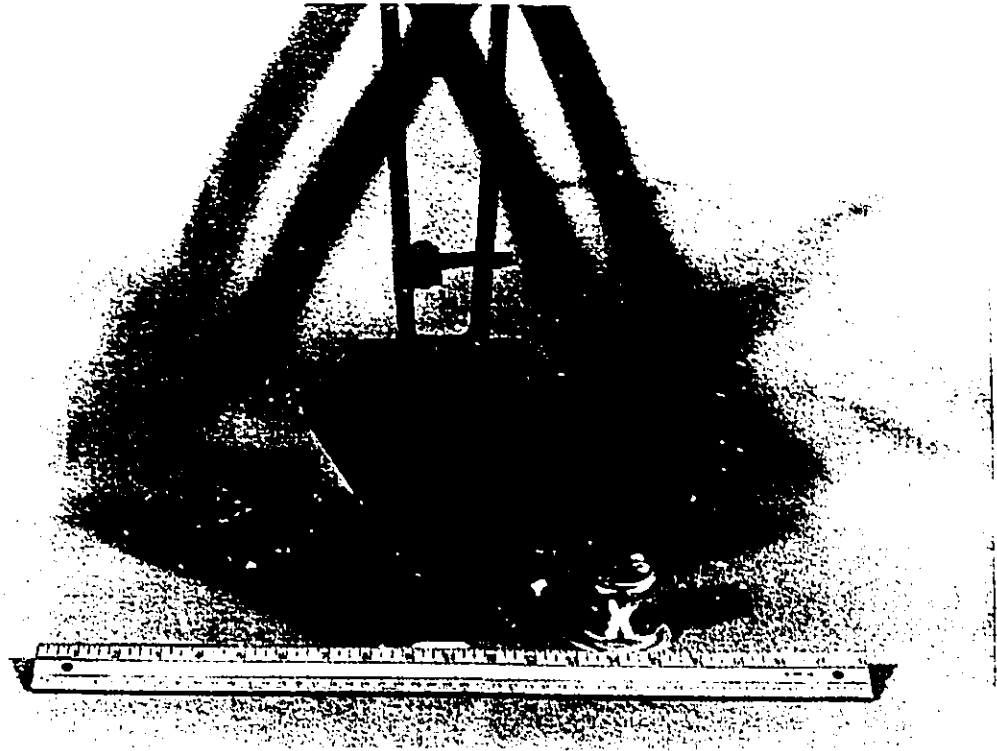


Figure 3.7 The standard Alcan mould and a disk sample

#### III.A.5. Preparation of Samples and Dross for Chemical Analysis:

The riser of the samples were cut and the bottom surface of the samples was machined to remove 1.5 mm metal layer. The samples were then analyzed by using an optical emission spectrometer at Alcan R&D Centre in Kingston. Independent checks on these samples were carried out at Alcan R&D Centre in Arvida.

Dross samples were collected only after the experiments were completed. These were cooled down to room temperature in a small silica crucible. The dross was then ground below 200 mesh and analyzed by using an X-Ray diffractometer. Some dross samples were also analyzed by the same method at Alcan R&D centre in Kingston.

#### III.A.6. Experimental Schedule:

Table 3.3 shows the schedule followed for the gas fluxing experiments during the course of this study. This set was carried out for calcium and sodium separately.

Experiments were carried out for three different gas flow rates(26.22, 56.45, 91.12

cc/sec at 730 °C and 1 Atm) using three different chlorine concentrations(2, 10, 25% by volume).

Table 3.3 Experimental schedule followed for the gas fluxing experiments

Q (cc/sec) 730 °C & 1 Atm	Chlorine concentration(Vol%)			
	Al		Al-1wt% Mg	
	Continuous	Intermittent	Continuous	Intermittent
26.22	0	-	0	-
	2	2	2	2
	10	10	10	10
	25	25	25	25
56.45	0	-	0	-
	10	10	10	10
91.12	0	-	0	-
	10	10	10	10

In the case of the intermittent tests, regardless of the chlorine concentration and gas flow rate, a fixed quantity of chlorine,  $4 \times 10^{-2}$  gm-moles, was injected into the melt together with argon gas. At the end of this period, injection of chlorine was terminated and only argon gas was injected into the melt by using a completely separate gas line(except for the gas bubbling lance) so as to avoid any contamination by chlorine. In these tests, impurity addition to the melt was done 1 minute prior to the cessation of the chlorine gas injection. Samples were taken starting from argon only injection period. The purpose of the intermittent tests was to determine the contribution of the intermediate reaction products that are separated from the bubbles on the removal of calcium and sodium from the melts.

III.A.7. Measurement of Frequency of Bubble Formation:

In order to estimate the surface area and rising velocities of bubbles for mass transfer calculation purposes, the frequency of bubbles that formed at the tip of the lance was measured by a pressure pulse technique[47-49].

III.A.7.a. Principle of Operation:

The principle of operation of the pressure pulse technique is based on the fact that formation and the detachment of bubbles from an orifice are accompanied by pressure fluctuations in the gas chamber.

Siemes[50] has shown that the pressure inside a bubble and gas chamber behind an orifice varies according to the bubble volume as shown in Figure 3.8.

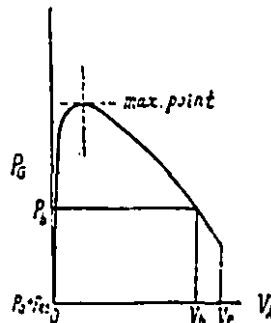


**Figure 3.8** Variation of pressure in a gas bubble forming at an orifice[56]

Immediately after detachment of the bubble from the orifice the pressure in the gas chamber becomes

$$P_{\min} = P_o + P_{hs} \quad (3.1)$$

where  $P_o$  and  $P_{hs}$  are atmospheric and hydrostatic pressure respectively. As the gas flows into the gas chamber, the pressure attains a maximum value,  $P_{\max}$ , which is given by

$$P_{\max} = P_{\min} + \frac{4 \sigma}{d} \quad (3.2)$$

where  $\sigma$  is the surface tension and  $d$  is the diameter of the orifice. At this point the gas expands rapidly and the pressure in the gas chamber drops to  $P_b$ . The bubble, however, does not detach from the orifice until its volume reaches an equilibrium value,  $V_e$ , which is determined by a balance between the buoyancy and the surface tension forces acting on the bubble according to

$$V_e = \frac{\pi d \sigma}{(\rho_l - \rho_g) g} \quad (3.3)$$

Upon detachment of the bubble from the orifice, the pressure drops back again to  $P_{\min}$  and the same cycle repeats for the next bubble.

Although the theoretical treatment of Siemes is valid for bubbles forming at orifices at very low gas flow rates, it nevertheless shows that each bubble forming under identical conditions should have similar pattern of pressure variations in the gas chamber.

Since the formation of the bubbles from an orifice is accompanied by a unique pattern of pressure variation, the frequency of bubble formation can be measured by counting the number of repetitions of these identical individual patterns over a certain time period.

In the present study, the pressure pulses generated by the detachment of the bubbles from the tip of the nozzle were detected by inserting a microphone into the gas line. The output of the microphone was transmitted to an oscilloscope where the bubble frequencies were counted by freezing the image of the pressure pulses on the graduated screen of the oscilloscope. Figure 3.9 shows a train of such pressure pulses. In order to make sure that the frequency of pulses read from the oscilloscope screen indeed corresponded to frequency of bubble formation, argon gas was injected into water that was contained in a plexiglass container through a downward facing 2 mm ID x 6 mm OD and 3 mm ID x 4.2 mm OD glass nozzles and bubble frequencies were measured simultaneously by using a light stroboscope and the microphone. Figure 3.10 shows the comparison of the frequencies obtained by the two separate methods. As seen the frequencies agreed well.

The volume of each individual gas bubbles were calculated from:

$$V_b = \frac{Q}{f} \quad (3.4)$$

The surface areas of the bubbles were calculated from the bubble volumes, assuming that bubbles were spherical in shape.

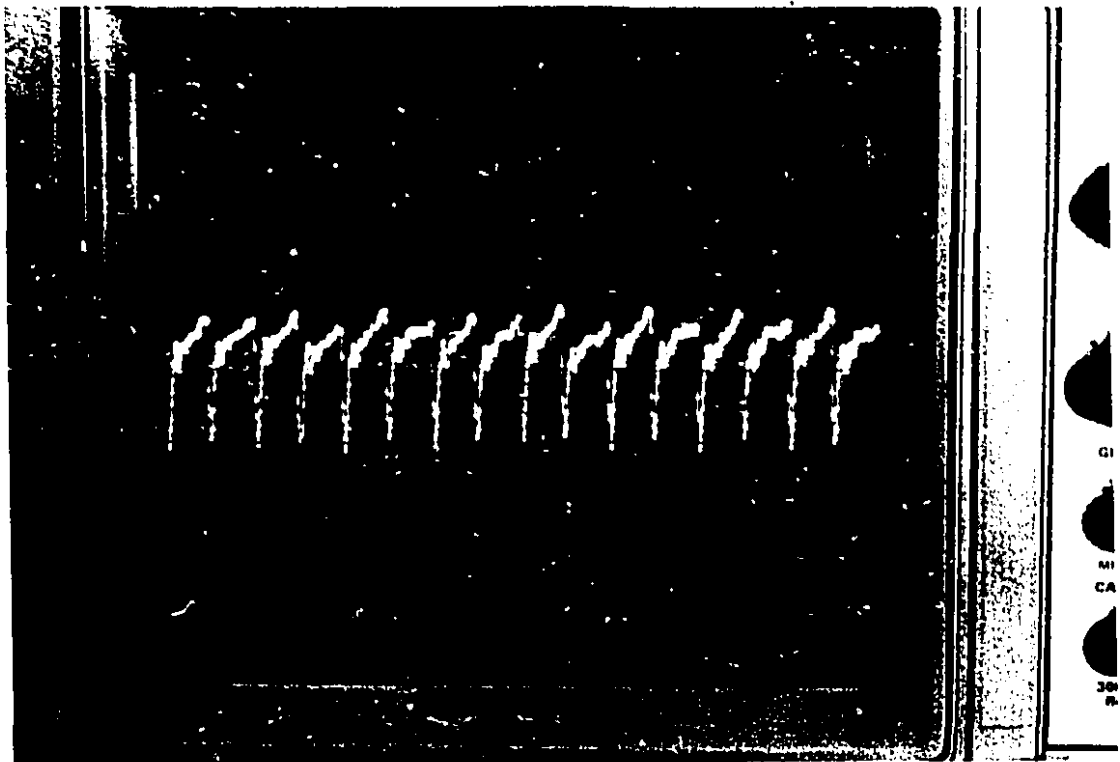


**Figure 3.9** A train of pressure pulses generated in the gas chamber by the release of bubbles from the orifice. Frequency is 16 bubbles/sec(horizontal scale is 0.1sec/division)

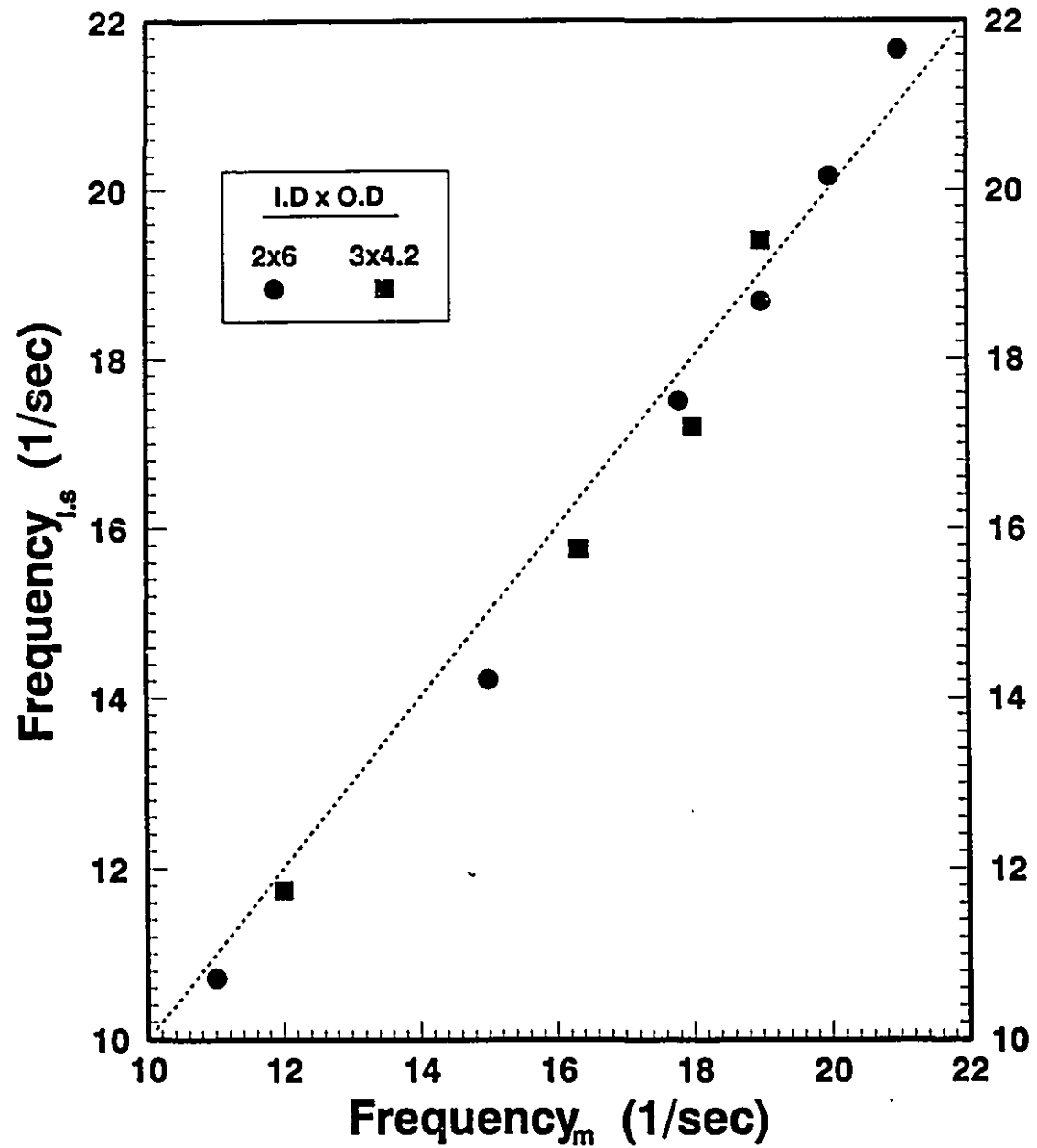


Figure 3.10 Comparison of bubble formation frequencies by simultaneous measurement by using a light stroboscope and microphone

III.A.7.b. Gas Supply Line:

Several investigators[49,51-57] showed that the volume of the gas chamber,  $V_c$ , which is the entire volume of the gas supply train extending back to the nearest effective restriction governing the flow, may have a pronounced effect on the volume of the bubbles forming at orifices. Because of the compressibility of the gases, more and more surplus gas will accumulate in the gas chamber to increase bubble sizes and delays the time between bubble releases. Tadaki and Maeda[56] showed experimentally that the bubble volumes at very low gas flow rates were given by

$$V_b = V_c N_c \quad 1 < N_c < 9 \quad (3.5)$$

$$V_b = V_c \quad N_c < 1 \quad (3.6)$$

where  $N_c$  is the dimensionless capacitance number which they defined as

$$N_c = \frac{4 V_c \rho_l g}{P_{\min} d^2 \pi} \quad (3.7)$$

With increasing gas flow rates, the inertial forces become dominant and bubble volume cannot be predicted any more by a simple balance of buoyancy and interfacial tension forces. Davidson and Amick[52] showed that at high gas flow rates, the critical capacitance number below which gas chamber volume has negligible effect on the forming bubbles to be 0.2. For  $N_c < 0.2$  they showed that with increasing gas flow rate, bubble volumes will be a function of gas flow rate and diameter of the orifice. They demonstrated that as the gas flow rate increased, a stage will arrive at which the frequency of bubble formation becomes constant.

Sano and Mori[47] and Irons and Guthrie[49] showed that in liquid metals the conditions are such that liquid metals do not wet the orifice, so that the diameter of the orifice in Eqns. (3.2), (3.3) and (3.7) should be taken as the outer diameter.

In the chlorination experiments the chamber volume  $V_c$ , was kept as small as possible ( $5.8 \times 10^{-4} \text{ m}^3$ ) by constructing the gas supply line from very small diameter

tubing(0.5-1mm ID). The portion of the gas supply line between the gas mixing unit and the quartz lance was constructed from latex and polyethylene capillary tubing.

Figure 3.11 shows frequency of bubble formation in liquid aluminum at 730 °C as a function of gas flow rate(730 °C, 1Atm) for several nozzle diameters.

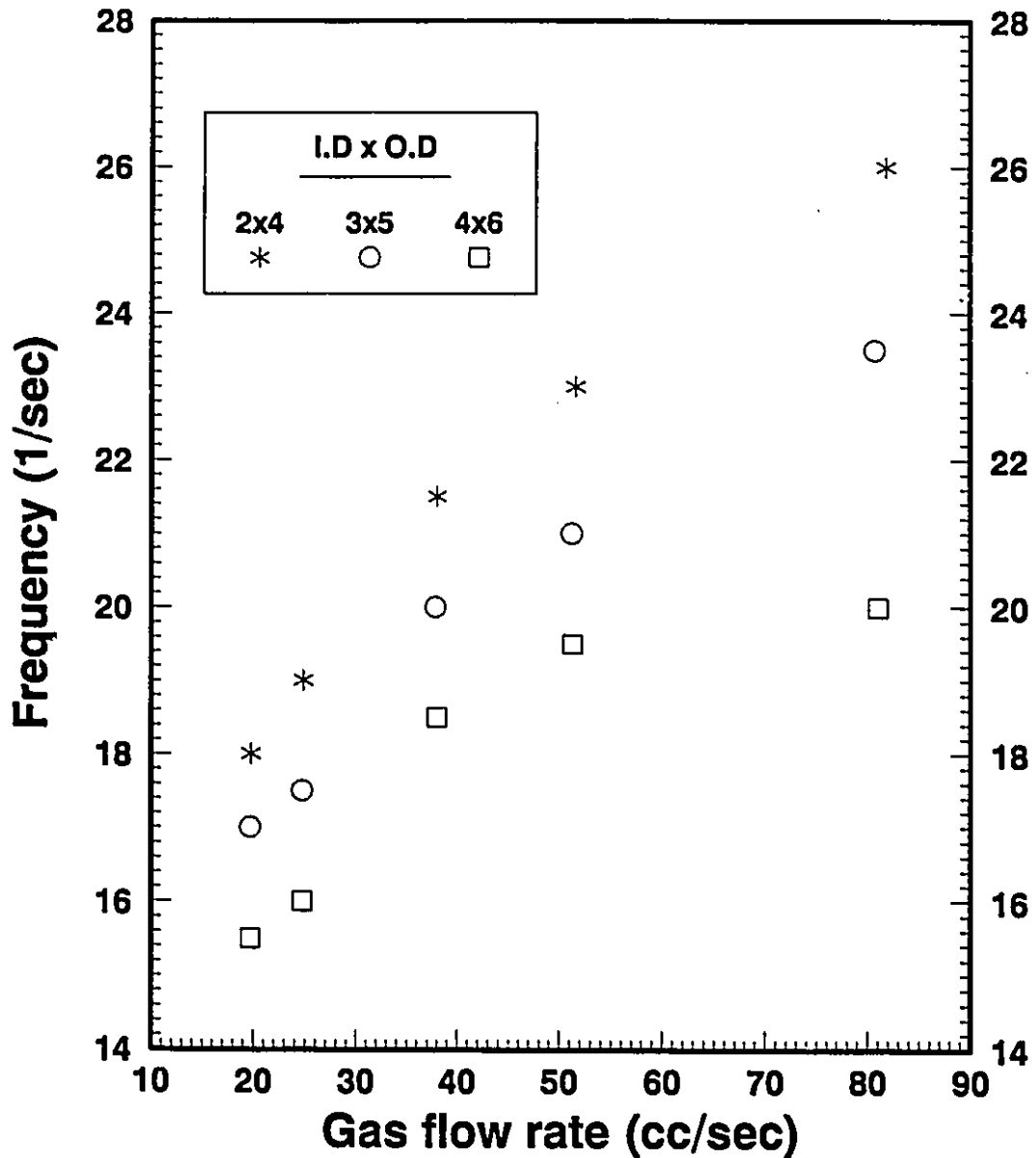


Figure 3.11 The frequency of bubble formation as a function of gas flow rate(730 °C, 1 Atm.) for several nozzle diameters in molten aluminum

III.B. LiMCA (Liquid Metal Cleanliness Analyzer) Unit:

In order to determine size and number distributions of intermediate reaction products that are present in the melt (other than those on the bubble surfaces, on the melt surface and on the crucible wall) LiMCA apparatus readily available in the Department of Mining and Metallurgical Engineering of McGill University was used.

III.B.1. Principle of Operation:

The principle of operation of LiMCA is based on the resistive pulse technique first used by Coulter[58] for counting blood cells in aqueous suspensions. The underlining principle of resistive pulse technique is that when a less-conducting particle passes through an insulating channel, submerged in a conductive fluid, it will cause a temporary rise in the electrical resistance of the conductive fluid in the channel and this increase in resistance will be proportional to the volume of the particle[59].

According to Maxwell[60], the effective resistivity,  $\Omega_{eff}$ , of a dilute solution containing insulating spheres could be expressed by

$$\Omega_{eff} = \Omega (1 + 3\alpha / 2 + \dots + \dots) \quad (3.8)$$

where  $\alpha$  is the volume fraction of the insulating spheres. According to Ohm's law, the electrical resistance of the fluid contained in a cylindrical channel of diameter  $D$  and length  $L$  is given by:

$$R_1 = \Omega \frac{4L}{\pi D^2} \quad (3.9)$$

When an insulating sphere of diameter  $d$  is introduced into the channel, the volume fraction,  $\alpha$ , of the sphere in the channel will be

$$\alpha = \frac{2d^3}{3D^2L} \quad (3.10)$$

Inserting for the volume fraction,  $\alpha$ , into Eqn.(3.8), the effective resistivity of the fluid then becomes

$$\Omega_{eff} = \Omega \left( 1 + \frac{d^3}{D^2 L} \right) \quad (3.11)$$

The electrical resistance of the fluid in the channel in the presence of the insulating particle therefore becomes

$$R_2 = \Omega \left( 1 + \frac{d^3}{D^2 L} \right) \frac{\rho L}{\pi D^2} \quad (3.12)$$

The difference,  $\Delta R = R_2 - R_1$  is the increase in the electrical resistance of the fluid in the channel due to the presence of the insulating sphere and is given by

$$\Delta R = \frac{4 \Omega d^3}{\pi D^4} \quad (3.13)$$

$\Delta R$  is also called the resistive pulse. Eqn.(3.13) is valid for a system in which  $d/D \ll 1$ . For bigger particle diameters approaching the diameter of the channel DeBloise and Bean[59] modified Egn.(3.13) to obtain:

$$\Delta R = \frac{4 \rho d^3}{\pi D^4} f(d/D) \quad (3.14)$$

where  $f(d/D)$  is given by

$$f(d/D) = [1 - 0.8(d/D)^3]^{-1} \quad (3.15)$$

If a constant current is applied across the channel(orifice) the resistive pulse will then become a voltage pulse according to:

$$\Delta V = \frac{4 I \rho d^3}{\pi D^4} f(d/D) \quad (3.16)$$

Therefore, by measuring the magnitude of the voltage pulses generated by the passage of the non-conductive particles through an electrically insulating orifice, the size of the particles can be predicted from the knowledge of physical properties of the melt and experimental parameters.

III.B.2. Components of the LiMCA Unit:

The LiMCA unit consisted of a melt sampling unit, power supply unit and voltage pulse measurement unit.

III.B.2.a. Melt Sampling Unit:

A schematic of the melt sampling unit is shown in Figure 3.12. The melt sampling unit consisted of a sampling tube, its head assembly, an outlet which was connected to a 3-way valve and two electrodes of low carbon steel.

The sampling tube was a Kimax brand borosilicate culture tube which had a 300  $\mu\text{m}$  diameter orifice located about 1 cm above the closed end of the tube. The tube had a diameter of 2.54 cm and were 25 cm in length. These sampling tubes with ready made orifices were provided by Alcan Int. Ltd. The sampling tube was fixed to an aluminum head assembly by a brass fixture and a teflon O-ring.

The liquid metal was aspirated into the sampling tube by connecting the outlet on the head assembly to a 20 litre vacuum reservoir. The vacuum pressure in the reservoir was created by a laboratory vacuum pump. Volumetric flow rate of the metal into the sampling tube was calculated from the following relationship[61]:

$$\dot{V} = \frac{\pi d^2}{4} C_D \left[ \frac{2(\Delta P + \rho g \Delta h)}{\rho} \right]^{1/2} 60 \cdot 10^6 \quad \text{cc/min} \quad (3.17)$$

where  $d$  is the diameter of the orifice,  $C_D$  is the orifice discharge coefficient,  $\Delta P$  is the vacuum gauge pressure,  $\Delta h$  is the half of the depth of submergence of the orifice below the melt surface during sampling,  $\rho$  is the density of the melt and  $g$  is the gravitational acceleration. Under the experimental conditions, in calculating the sample volume of the melt the following parameters were used:

$$d = 300 \mu\text{m}$$

$$\Delta P = 16932 \text{ N/m}^2$$

$$\rho = 2345 \text{ kg/m}^3$$

$$\Delta h = 0.015 \text{ m}$$

$$C_D = 0.97$$

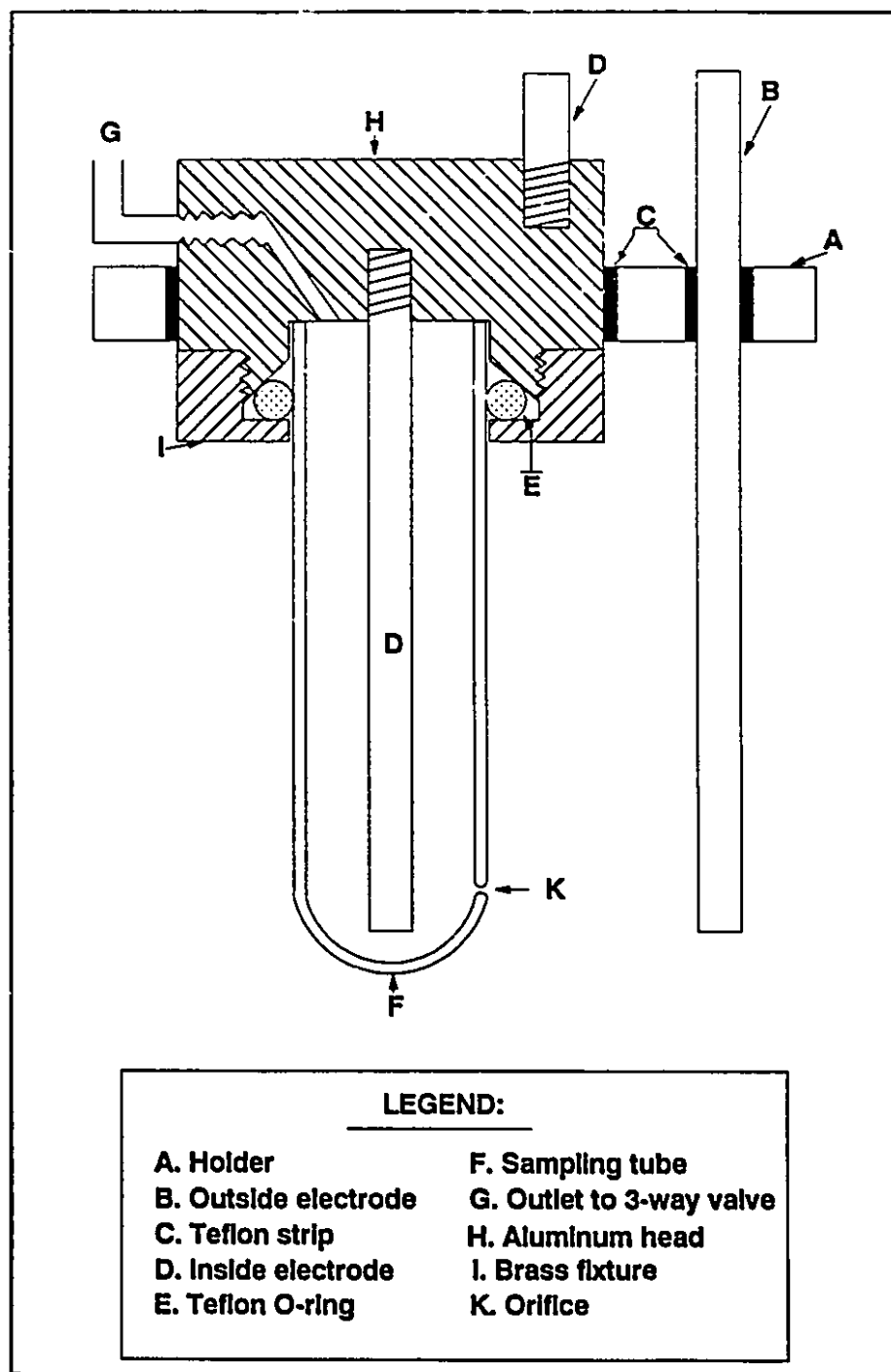


Figure 3.12 The schematic of the LiMCA melt sampling unit

In order to empty the sampling tube, pressure was applied through the outlet by turning the valve to a pressurized argon cylinder. When taking the tube out of the melt, the 3-way valve was turned to atmospheric pressure for safety.

The electrode that was kept in the sampling tube i.e the inside electrode was screwed into the head assembly. The connection of this electrode to the power supply was made by connecting the head assembly to the power cord through another piece of a mild steel rod that was screwed on to the head assembly. The head assembly and the outside electrode were then fixed onto an aluminum platform which was connected to a manual crane to move the electrode-head assembly vertically up and down. The head assembly and the outside electrode was electrically insulated from the metal platform by separating them by 1mm thick teflon strips sandwiched between the head assembly, electrode and the platform.

#### III.B.2.b. Power Supply Unit:

A 6V automotive battery was used together with resistance elements to keep a constant current of 55 Amperes across the orifice.

#### III.B.3. Voltage Pulse Measurement System:

The voltage pulses generated by the passage of the particles through the orifice were converted into particle sizes in two separate stages, namely recording and playback sessions.

##### III.B.3.a. Recording Session:

Referring to Figure 3.13, voltage pulses generated by the passage of the particles through the orifice were fed in the oscilloscope input. The oscilloscope used was a Tektronix 5223 Digitizing scope that had a 5A22N differential amplifier. This oscilloscope was used for both monitoring and amplifying the incoming voltage pulses.

By using the differential amplifier, the DC component of the voltage signal i.e  $I \cdot R_1$  + voltage drop due to the resistance in the power line between the power supply unit and the melt was eliminated and only the changes in voltage occurring by the passage of particles

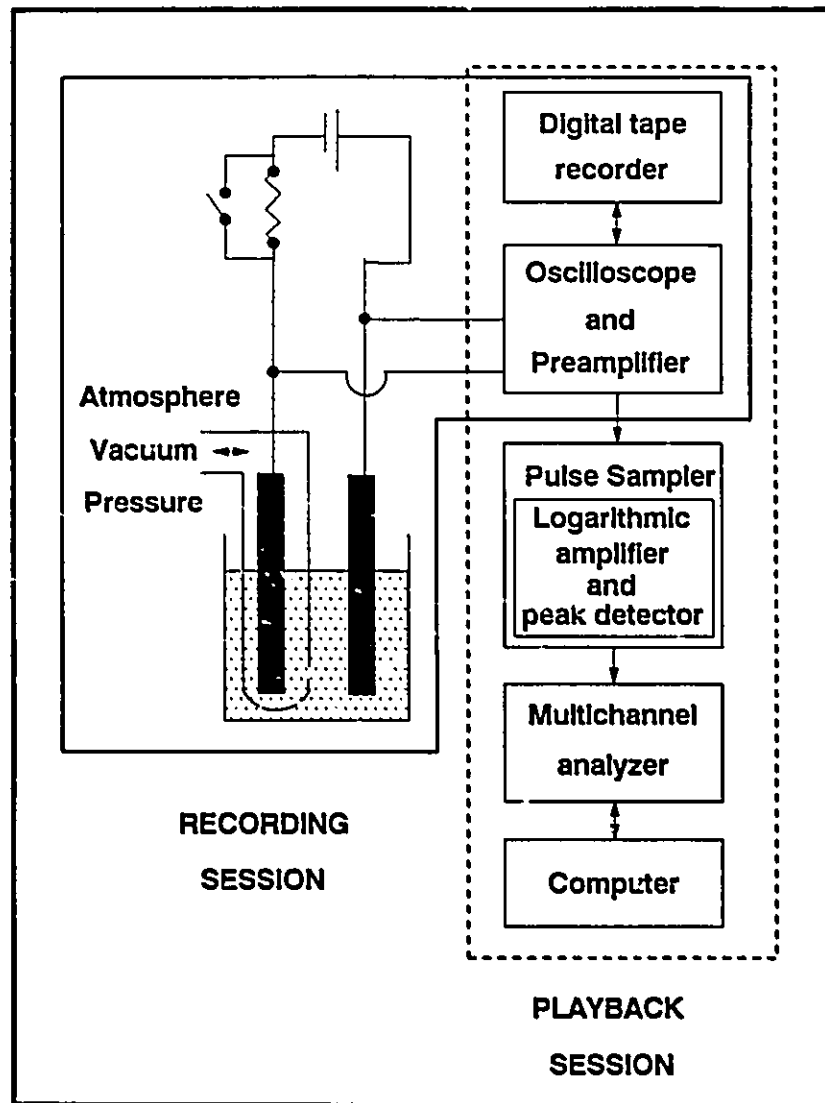


Figure 3.13 The flow chart of the recording and playback sessions

through the orifice were amplified according to

$$\Delta V_1 = I * \Delta R * G \quad (3.18)$$

where G is the gain of the amplifier.

The output of the oscilloscope was fed to a TEAC RD101 T data recorder. This recorder was used to record the voltage signals on digital audio tapes(DAT) for later examination of the data. In addition to 4 data channels, the recorder had channels for voice, time and data ID# recording and reproduction.

#### III.B.3.b. Playback Session:

After each experiment, the voltage pulses recorded on DAT were played back and conversion to particle sizes was carried out through a voltage pulse measuring system and data acquisition unit.

First, voltage pulses recorded on DAT were fed to the oscilloscope input from the output of the recorder. From the oscilloscope, the voltage pulses were sent to a Pulse Sampler(TN 1246). The purpose of the Pulse Sampler was to detect a maximum in the incoming signal. As soon as a peak was detected, the Pulse Sampler sent a strobe signal to a multichannel analyzer(MCA) to control the passage of the input pulse to the MCA. In its logarithmic mode, the Pulse Sampler amplified the input signal to give an output signal of the following magnitude

$$\Delta V_2 = \frac{10}{3} [\log \Delta V_1 + 2] \quad (3.19)$$

The output of the Pulse Sampler(a strobe signal and a voltage signal) was sent to the MCA(TN 7200) where analog to digital conversion of the incoming pulses was performed and their magnitudes were measured. According to their magnitudes, the input pulses were then mapped linearly on 512 channels of the MCA which had a 0-8 volt input range according to

$$\text{Channel No} = 512 \frac{\Delta V_2}{8} \quad (3.20)$$

The operation of the MCA and the transfer of the data to a personal computer were controlled by LiMCA software developed by Lee and Dallaire[62].

### III.B.3.c. Calibration of Voltage Pulses:

Although the relationship between the Channel Number and the magnitude of the voltage pulse is given by Eqn.(3.20), certain deviations from this equation are expected to occur[63]. The main source of the deviation was reported to stem from the calibration of the Pulse Sampler. It was reported[63] that the proper functioning of the Pulse Sampler is sensitive to its warm-up period and that the instrument should be calibrated frequently. Even when calibrated strictly following the calibration procedure, the Pulse Sampler was reported not to perform exactly as it should. Another source of deviation was reported to be the offset of amplification gain introduced during recording/playback session of the signals. It was reported that the magnitude of these errors was not easy to quantify.

However, if voltage pulses of known magnitude are transmitted to the oscilloscope and are processed the same way as the real electric sensing zone(ESZ) signals, a calibration can be made to obtain an empirical relationship between the Channel Number and the magnitude of the voltage pulse. In this study this was achieved by generating a train of pulses of known magnitude with a Bomem Calibrator. This instrument generated 96 trains of 8 pulses of decreasing magnitude each time it was activated. Table 3.4 gives the magnitude of these pulses with their theoretical locations in the MCA for an amplifier gain of 500. In reality, however, some deviations are expected to occur as already explained. Figure 3.14 shows the MCA channels that the calibration pulses should be theoretically in(dotted lines) and the actual distribution of the calibration pulses(solid line) in the MCA. Since the magnitude of the calibration pulses are known, a new relationship between the channel number as a function of voltage pulse value can be determined. The way to achieve this was presented by Dallaire[63].

In its final form, theoretically, the magnitude of the voltage pulses will be stored in

one of the 512 channels of MCA according to Eqn.(3.20) which can be written in the following form

$$\text{Channel No} = 64 (mx + b) \quad (3.21)$$

Eqn.(3.21) is an equation for a straight line in which the theoretical values of m and b are 3.33 and 6.67 respectively. For the actual distribution of the voltage pulses in the MCA, however, m and b were modified as follows:

$$\hat{m} = \frac{CH^I - CH^{II}}{64 \log \frac{V^I}{V^{II}}} \quad (3.22)$$

$$\hat{b} = \frac{CH^I \log V^{II} - CH^{II} \log V^I}{64 \log \frac{V^{II}}{V^I}} \quad (3.23)$$

**Table 3.4** Magnitude of the calibration pulses and their theoretical location in the MCA

Pulse #	Pulse amplitude ( $\mu\text{V}$ )	$\Delta V_2$ (V)	MCA Channel #
1	1280	6.021	384
2	640	5.107	320
3	320	4.014	256
4	160	3.101	192
5	80	2.007	128
6	40	1.003	64
7	20	0	0
8	10	-1.003	-

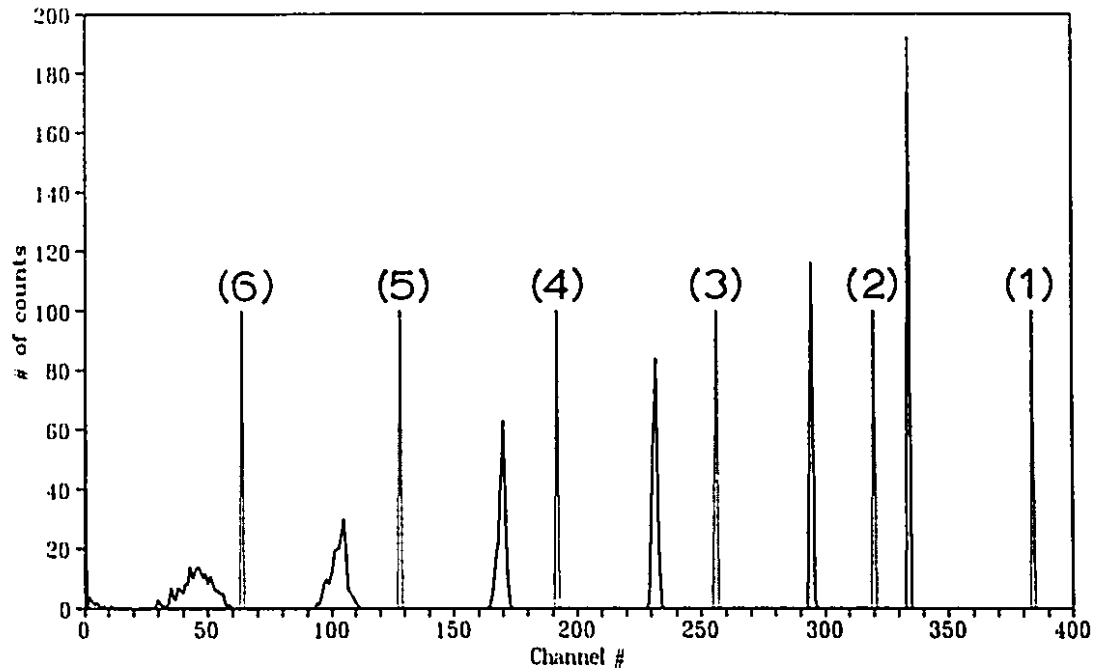


**Figure 3.14** The theoretical and actual locations of the calibration pulses in the MCA

In Eqns.(3.22) and (3.23), Channel Numbers,  $CH^I$  and  $CH^{II}$ , are the two actual location of any two separate calibration pulses in the MCA whereas  $V^I$  and  $V^{II}$  are their theoretical voltage values taken from column III of Table 3.4

With the modifications introduced by Eqns.(3.22) and (3.23) the relationship between the channel number and magnitude of the voltage pulse takes the following form

$$\text{Channel No} = 64 (\dot{m}x + \dot{b}) \quad (3.24)$$

Figure 3.15 shows the result of the modification for the case presented in Figure 3.14. As can be seen from Figure 3.15, Eqn(3.24) holds well in assigning the magnitude of the theoretical voltage pulses to actual MCA locations except for Pulse# 1. This particular pulse was originally truncated because its magnitude had exceeded the dynamic

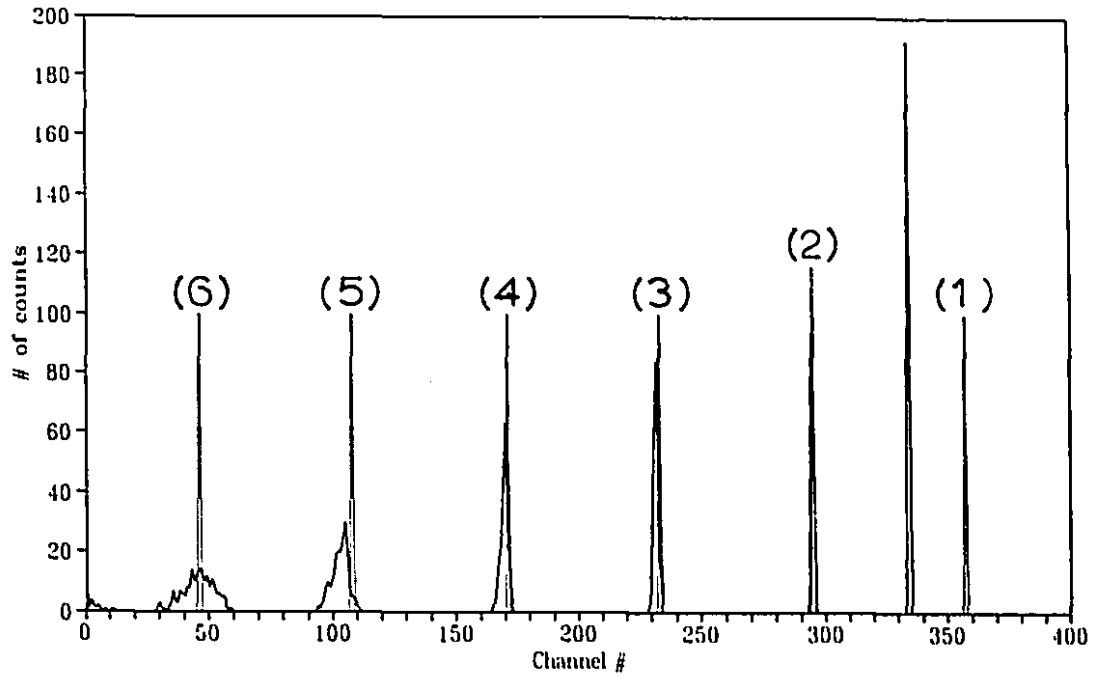


**Figure 3.15** Assignment of the theoretical values of the calibration voltage pulses to new MCA channels according to the correction done through Eqns.(3.22) and (3.23)

range of the amplifier. As a result, this pulse was already excluded when choosing the channel numbers and corresponding theoretical voltage values for Eqns.(3.22) and (3.23).

#### III.B.4. Preparation for the LiMCA tests:

For the LiMCA tests the same procedure for the chlorination tests was followed for the preparation of the melt, impeller and the lance. The electrodes were prepared from 5mm diameter bars of low carbon steel. One end of the inside electrode was machined to make threads to fit in the head assembly.

All the electronic instruments were turned on approximately 2 hours before the start of the LiMCA test to warm-up.

### III.B.5. Experimental Procedure:

Figure 3.16 shows the experimental procedure followed for the LiMCA tests. After the melt down and addition of the magnesium as described in section III.A.1.a the melt was injected with a 2% Cl<sub>2</sub>-Ar mixture for 10 minutes while stirred with the impeller at 175 rpm. After the termination of injection, the melt continued to be stirred by the impeller for five more minutes. This was followed by 15 minutes of holding period without stirring the melt by the impeller. After the surface of the melt was skimmed and the melt was stirred for two minutes by the impeller, a LiMCA test was carried out to assess the initial condition of the melt. Immediately after this, a mixture of chlorine and argon gas was injected into the melt to give  $42.3 \times 10^{-3}$  gm-moles of chlorine. During chlorination, the melt was stirred with the impeller. Immediately following the gas injection, a LiMCA test was carried out to assess the final condition of the melt.

In the LiMCA tests, the same melt gas fluxing unit was used. Before the sampling tube and the outside electrode were introduced into the melt through the ports in the graphite cover, the output of the Bomem calibrator was connected to the electrodes and the train of voltage pulses of known magnitudes was recorded on the DAT for the setting of the voltage pulse measuring system. The magnitudes of these pulses were checked by freezing the image on the screen of the oscilloscope. The sampling unit was then positioned to have the orifice of the sampling tube 3 cm below the melt surface, half way between the center and the circumference of the crucible.

During the tests, the surface of the melt was flushed with the argon gas under a graphite cover.

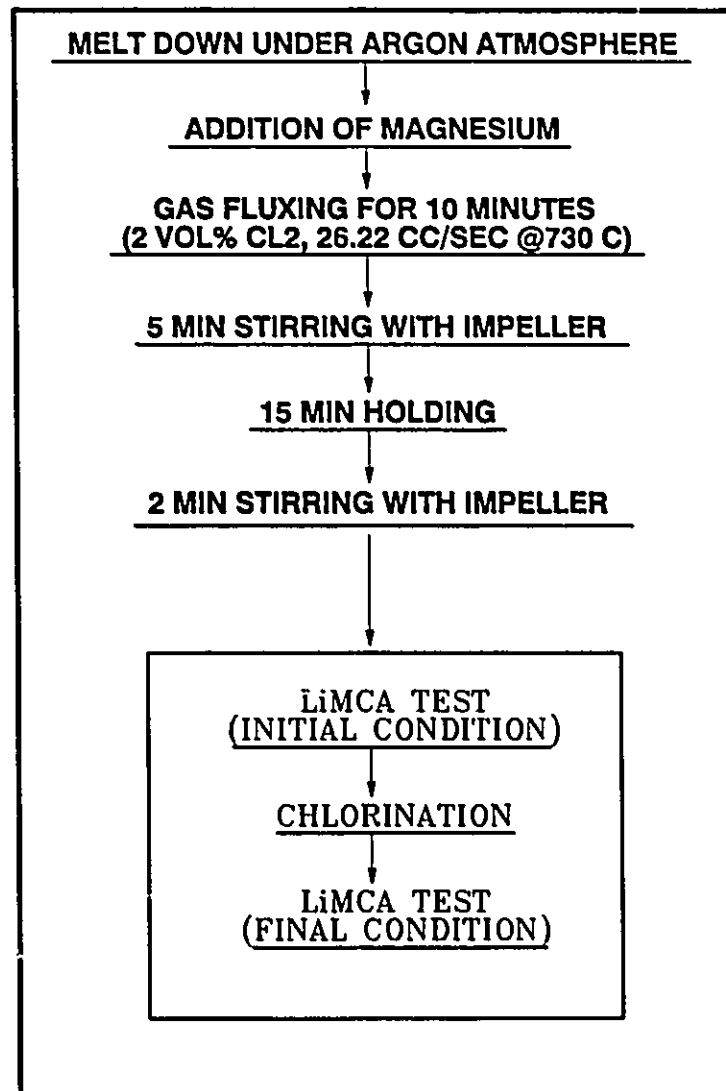


Figure 3.16 The flow chart of the experimental procedure followed for the LiMCA experiments

III.B.6. Experimental Schedule:

The experimental schedule followed for the LiMCA tests are given in Table 3.5. LiMCA experiments were carried out only for aluminum-1wt% magnesium alloys for 3 different gas flow rates(730 °C, 1 Atm) and chlorine concentrations(Vol%).

**Table 3.5** Experimental schedule followed for the LiMCA experiments

Q (cc/sec) 730 °C & 1 Atm	Chlorine concentration (vol%)
26.22	2
	10
	25
56.45	10
91.12	10

## Chapter 4

### Results and Discussion: Kinetics of Calcium Removal

---

#### IV.A. Presentation of the experimental results in graphical and tabular form:

Figures 4.1 through 4.8 show the change in the bulk calcium concentration for commercial purity aluminum and aluminum-1wt% magnesium alloys for various experimental conditions.

The change in the bulk concentration of calcium with time could be represented by an exponentially decaying curve which suggests that transient bulk concentration of calcium can be represented by an equation of the following form:

$$\%Ca_t^B = \%Ca_i^B e^{-Rt} \quad (4.1)$$

In the above equation,  $\%Ca_t^B$  and  $\%Ca_i^B$  are the transient and initial calcium concentrations respectively,  $t$  is time and  $R$  is the rate constant.

Rearranging Eqn.(4.1), one obtains:

$$-\ln \frac{\%Ca_t^B}{\%Ca_i^B} = Rt \quad (4.2)$$

A plot of  $-\ln(\%Ca_t^B / \%Ca_i^B)$  vs  $t$  will give a straight line, the slope of which is equal to the rate constant  $R$ . The rate constant  $R$  represents the fraction of the impurity that is consumed by reaction per unit time and is therefore a useful measure of the rate of chemical reaction at a specified temperature.

Tables 4.1 through 4.3 present the rate constants obtained graphically through Eqn.(4.2). In these tables,  $R_o$ ,  $R_{intermittent}$  and  $R_{Ar}$  represent the individual experimental rate constants obtained from continuous chlorination, intermittent and argon injection tests respectively. The numbers in parenthesis represent the correlation coefficients for linear regression analysis, which is a measure of determination of how closely the data fits a straight line. When the correlation coefficient is  $|1|$  the data falls exactly on a straight line,

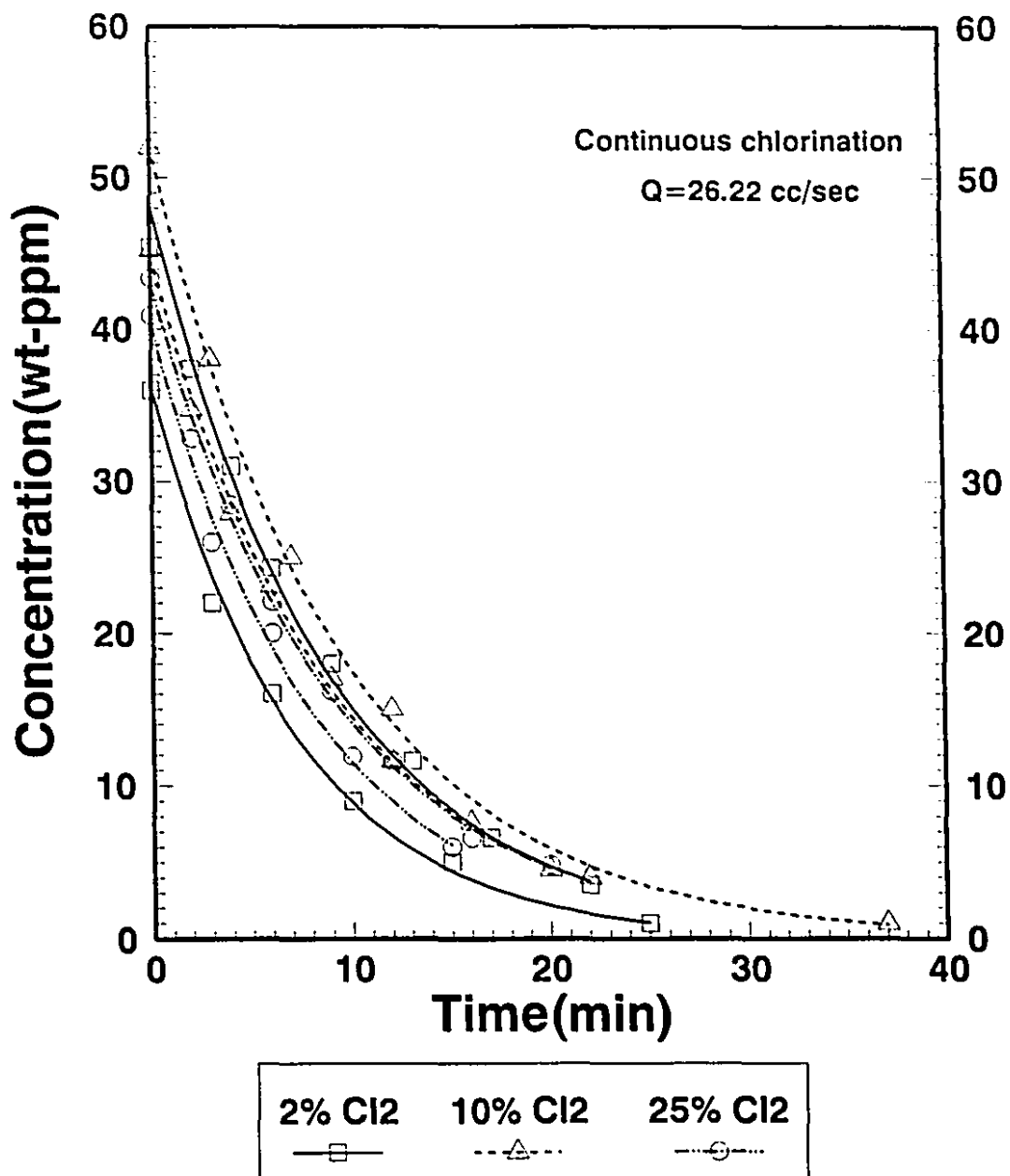
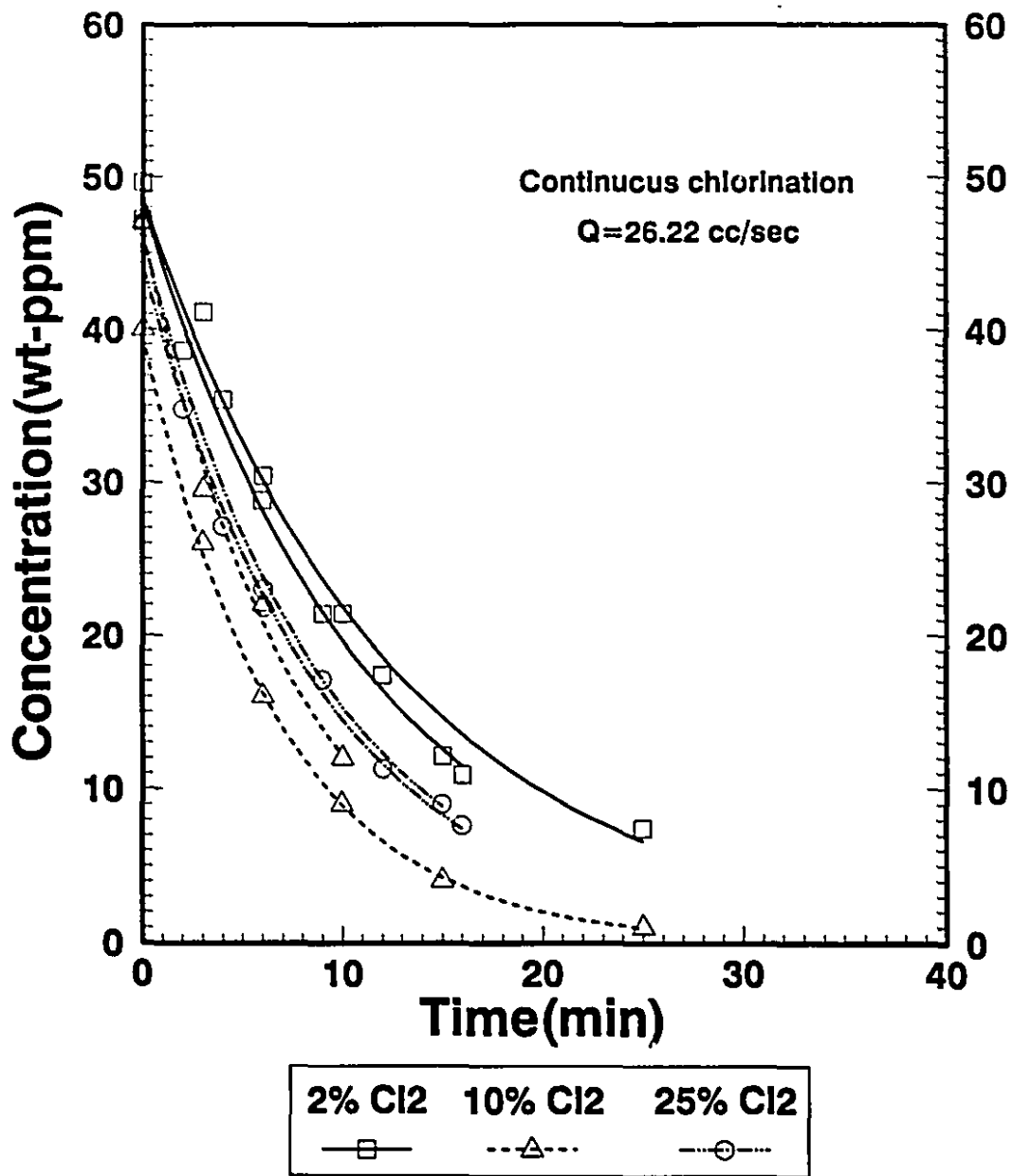
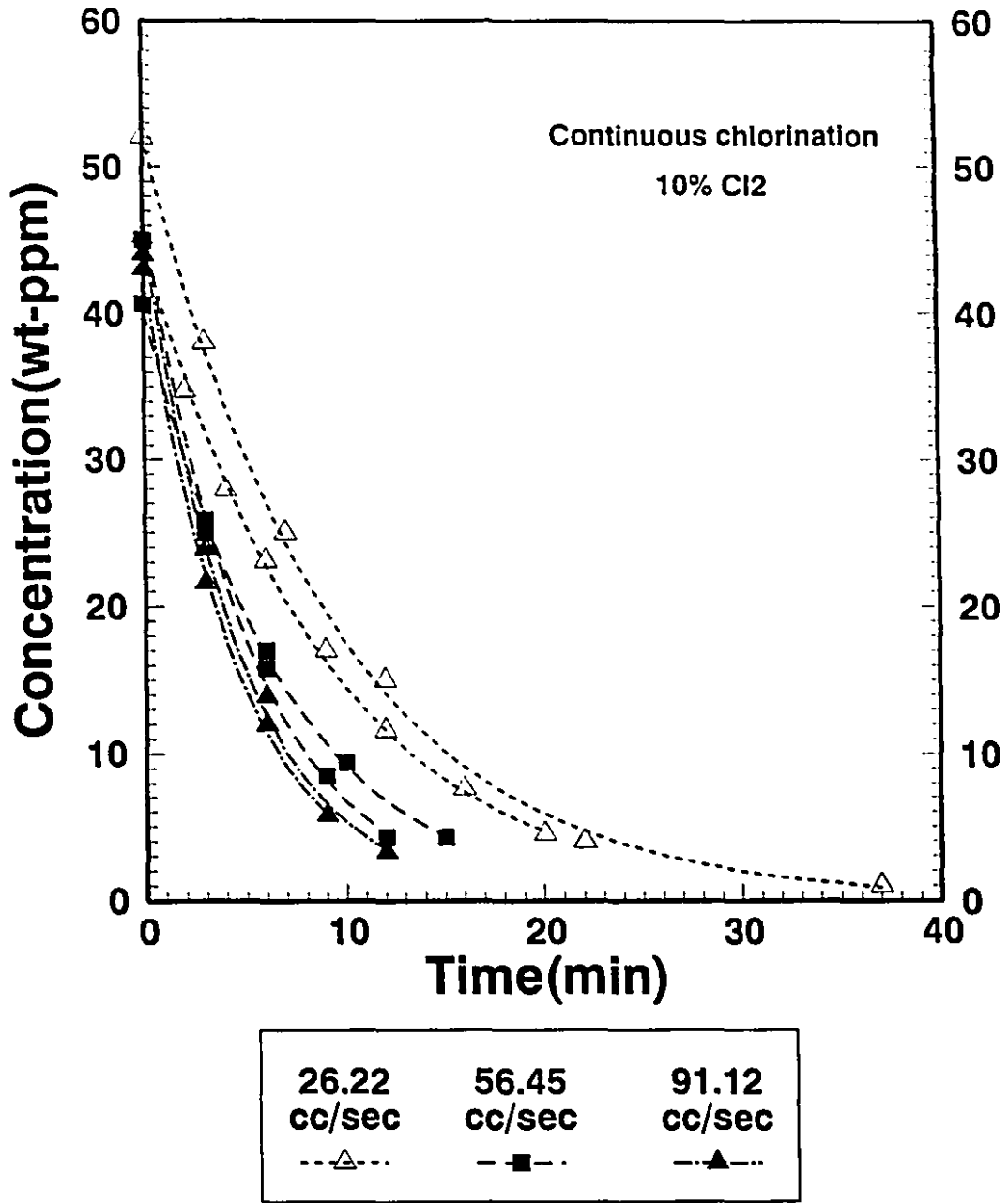


Figure 4.1 Change in calcium concentration in commercial purity aluminum melts versus bubbling time for various chlorine concentrations in Ar-Cl<sub>2</sub> gas mixture injected at a gas flow rate of 26.22 cc/sec (730 °C, 1 Atm.)



**Figure 4.2** Change in calcium concentration in Al-1wt% Mg alloys versus bubbling time for various chlorine concentrations in Ar-Cl<sub>2</sub> gas mixture injected at a gas flow rate of 26.22 cc/sec (730 °C, 1 Atm.)



**Figure 4.3** Change in calcium concentration in commercial purity aluminum melts versus bubbling time for various gas flow rates(730 °C, 1 Atm.); Vol% Cl<sub>2</sub>=10

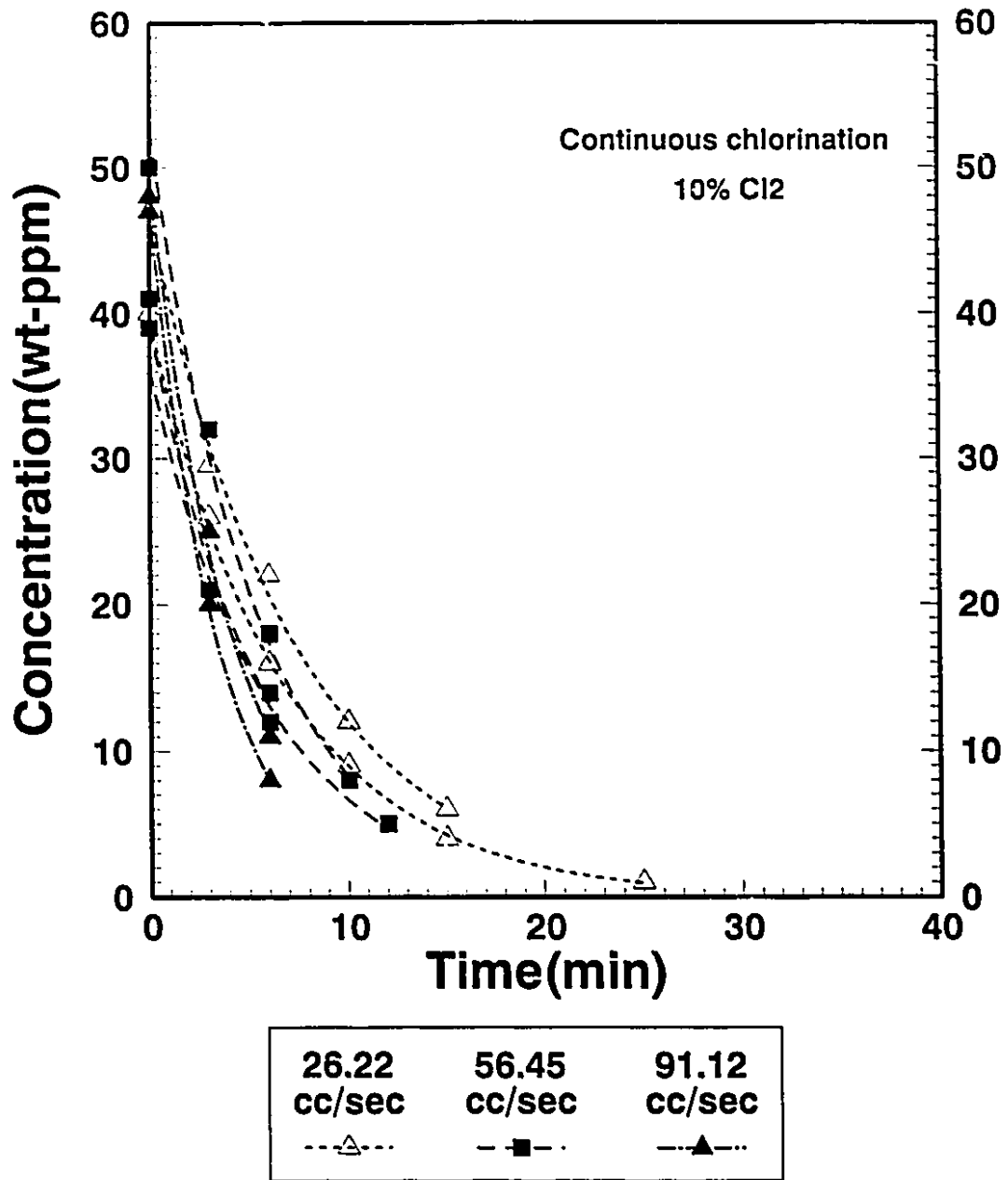


**Figure 4.4** Change in calcium concentration in Al-1wt% Mg alloys versus bubbling time for various gas flow rates(730 °C, 1 Atm.); Vol% Cl<sub>2</sub>=10

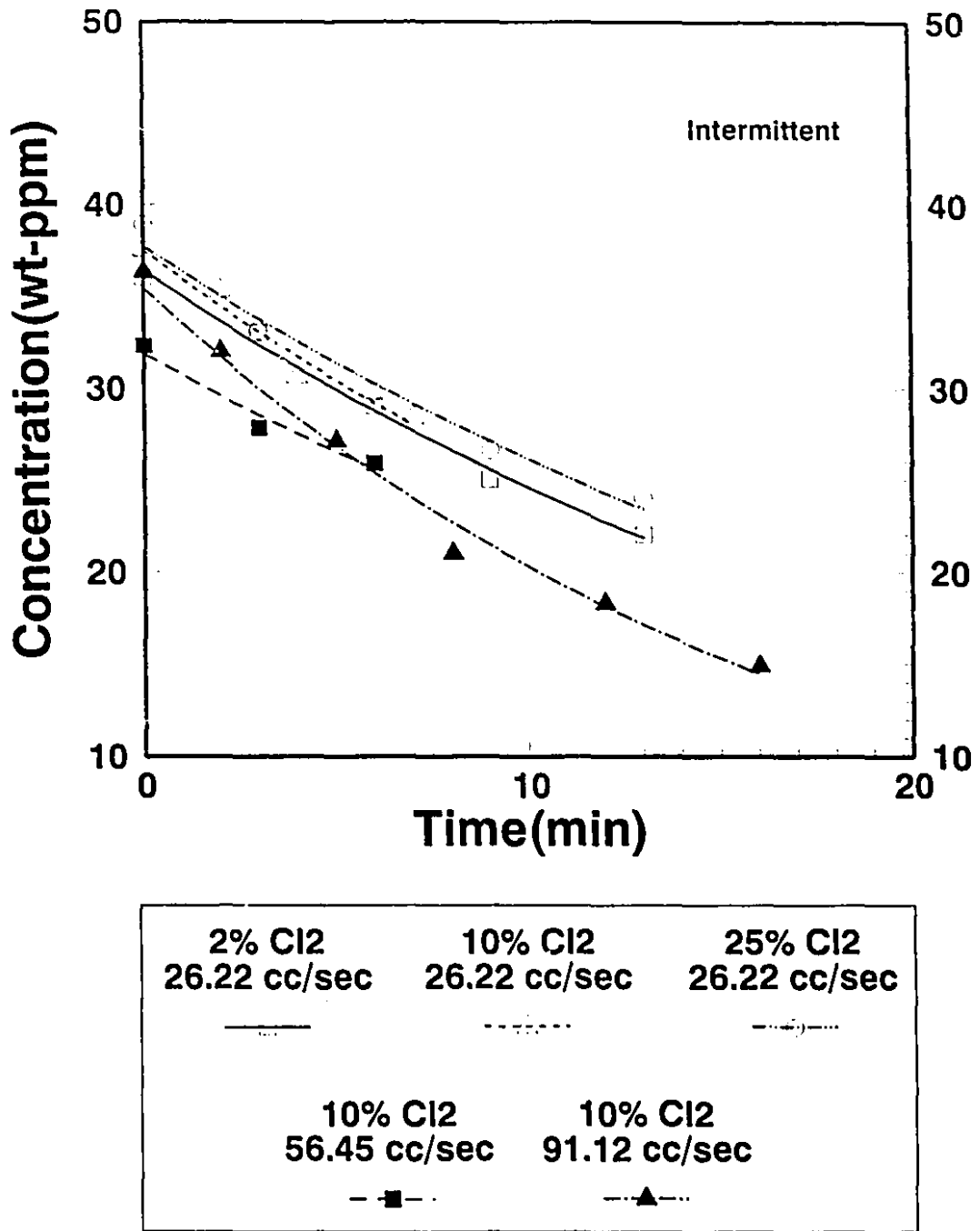
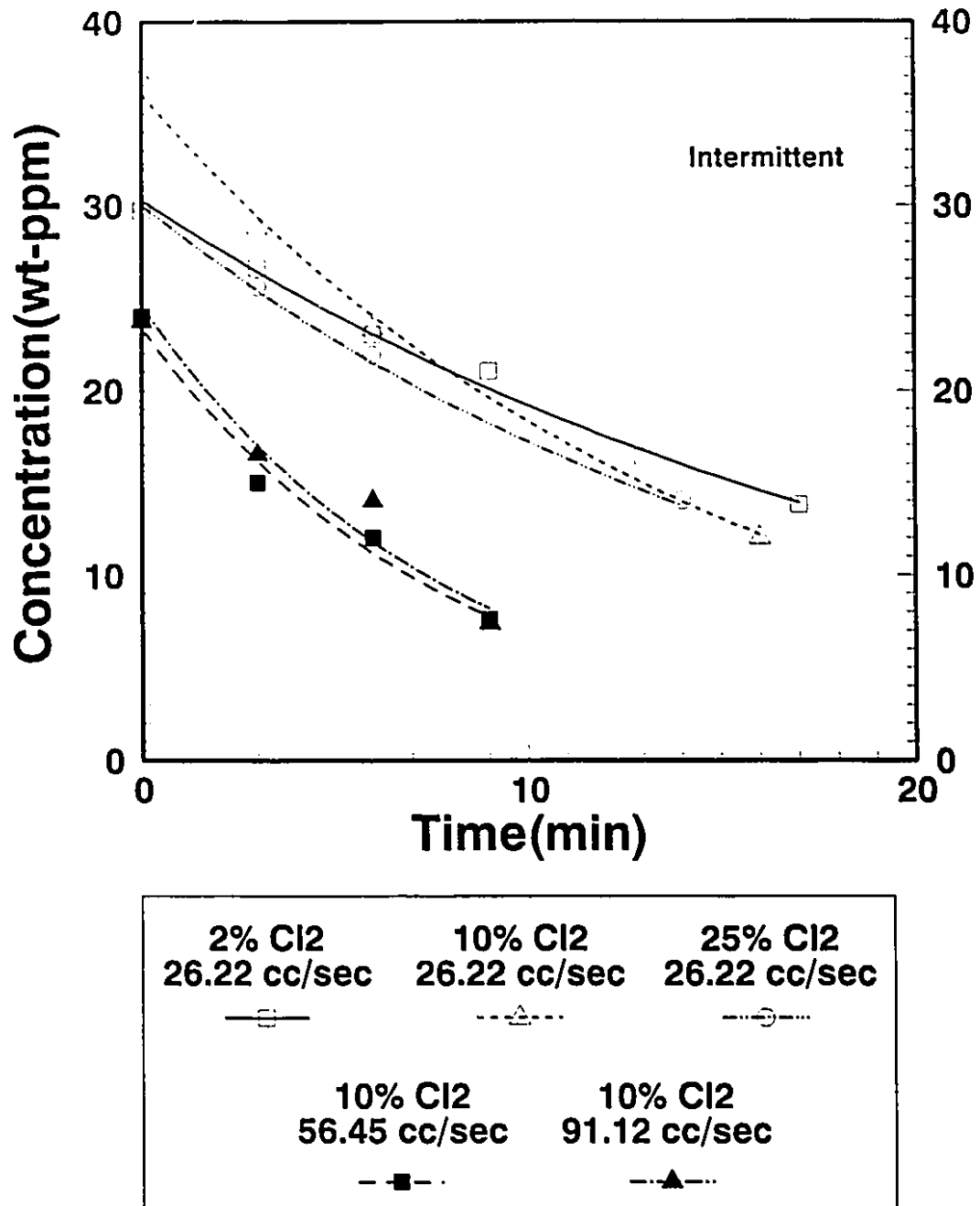


Figure 4.5 Change in calcium concentration in commercial purity aluminum melts versus time for various chlorine concentrations and gas flow rates(730 °C, 1 Atm.) during intermittent tests



**Figure 4.6** Change in calcium concentration in Al-1wt% Mg alloys versus time for various chlorine concentrations and gas flow rates(730 °C, 1 Atm.) during intermittent tests

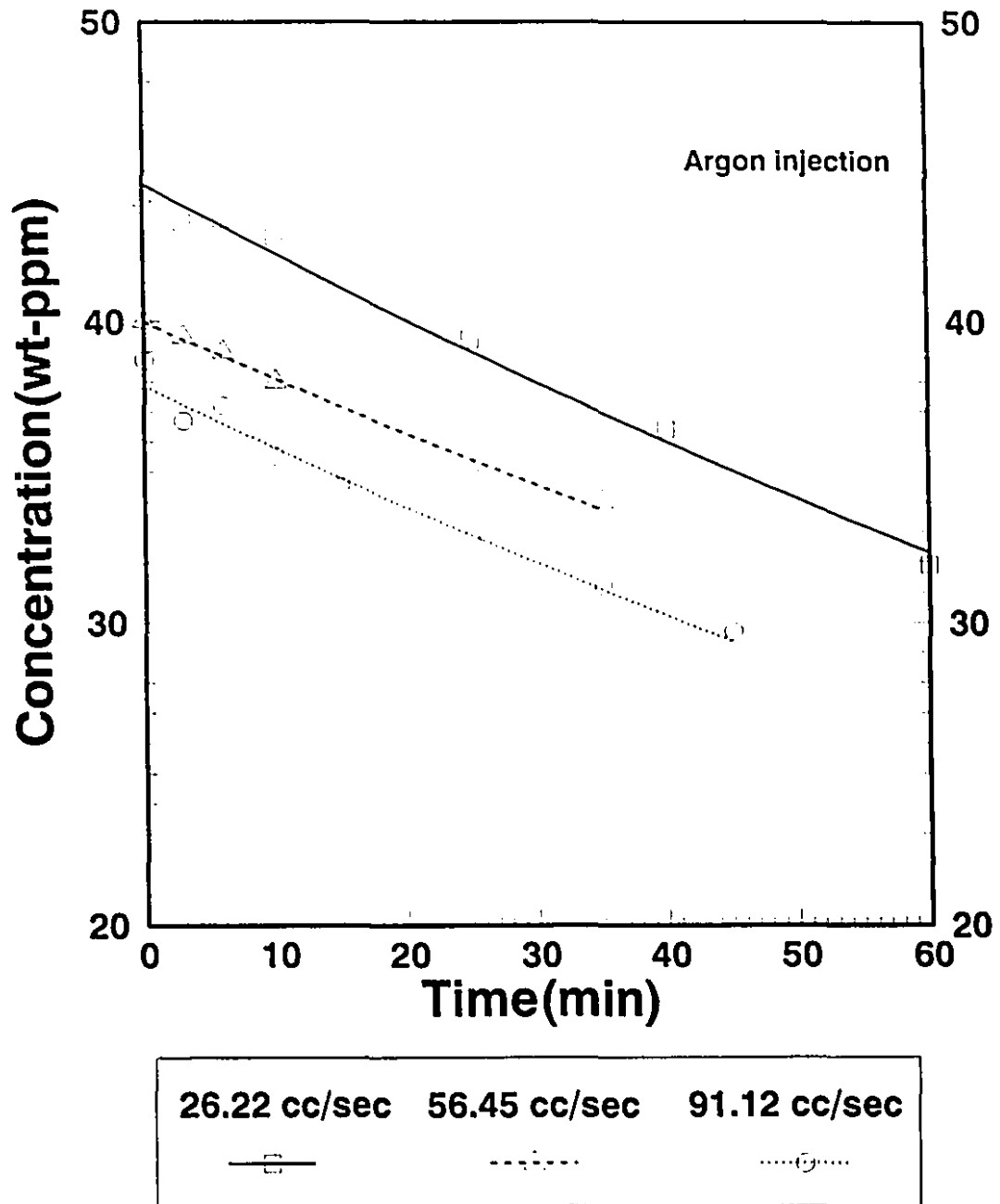
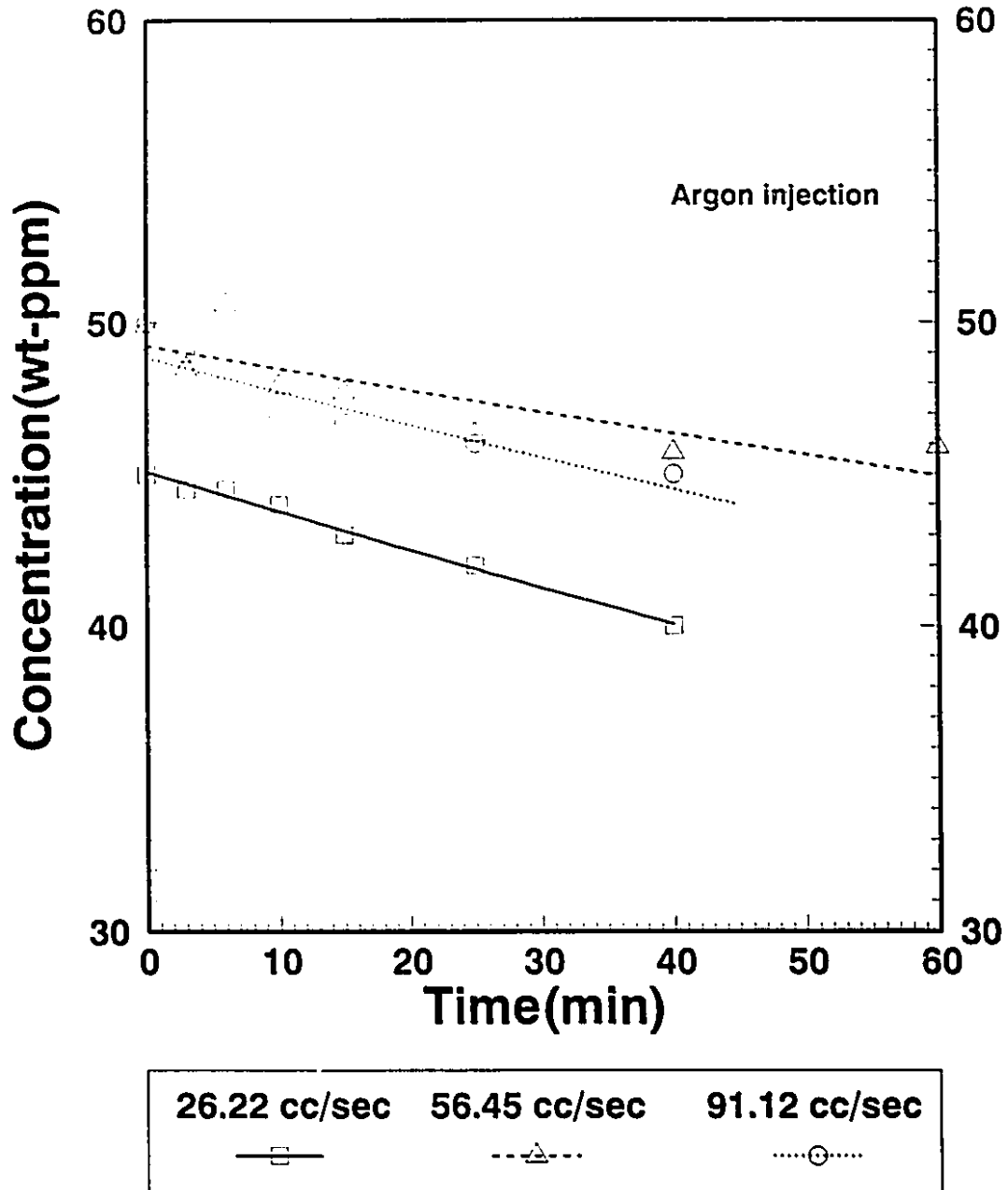


Figure 4.7 Change in calcium concentration in commercial purity aluminum melts versus time for various gas flow rates (730 °C, 1 Atm.) during argon injection tests



**Figure 4.8** Change in calcium concentration in Al-1wt% Mg alloys versus time for various gas flow rates(730 °C, 1 Atm.) during argon injection tests

**Table 4.1** Rate constants for various chlorine concentrations in the gas bubbles;  $Q=26.22$  cc/sec(730 °C, 1 Atm.)

	Rate constant (1/sec)*10 <sup>6</sup>			
	Al		Al-1wt% Mg	
Cl <sub>2</sub> Concentration (Vol %)	R <sub>o</sub>	R <sub>intermittent</sub>	R <sub>o</sub>	R <sub>intermittent</sub>
2	2343 (0.998) 1933 (0.998) Av: 2138	655 (0.996)	1331 (0.989) 1490 (0.996) Av:1411	765 (0.996)
10	1815 (0.998) 1833 (0.999) Av:1824	696 (0.978)	2217 (0.996) 2550 (0.999) Av:2384	1133 (0.997)
25	1833 (0.998) 2088 (0.998) Av:1961	613 (0.99)	1828 (0.999) 1883 (0.997) Av:1856	917 (0.996)

Table 4.2 Rate constants for various gas flow rates(730 °C, 1 Atm.); Vol% Cl<sub>2</sub>=10

Q (cc/sec) @ 730 °C	Rate constant (1/sec)*10 <sup>6</sup>			
	Al		Al-1wt% Mg	
	R <sub>o</sub>	R <sub>intermittent</sub>	R <sub>o</sub>	R <sub>intermittent</sub>
26.22	1815 (0.998) 1833 (0.999) Av: 1824	697 (0.978)	2217 (0.999) 2550 (0.996) Av:2384	1133 (0.997)
56.45	3225 (0.998) 2467 (0.999) Av:2846	613 (0.979)	3067 (0.997) 2983 (0.99) 2817 (0.996) Av:2956	2040 (0.99)
91.12	3665 (0.999) 3592 (0.998) Av:3629	933 (0.994)	4090 (0.997) 4917 (0.999) Av:4504	2030 (0.97)

Table 4.3 Rate constants for various argon gas flow rates(730 °C, 1 Atm.)

Q (cc/sec) @ 730 °C	$R_{Ar}$ (1/sec)* $10^6$	
	Al	Al-1wt% Mg
26.22	88 (0.995)	47 (0.995)
56.45	83 (0.999)	20 (0.75)
91.12	93 (0.987)	39 (0.83)

whereas when it is 0 the data can not be represented by a straight line at all. As seen from the tables, the data are well represented by straight lines except for a couple of data points for argon injection tests.

Having presented the raw data in graphical and tabular forms, the results can now be tested against the kinetic models described in Chapter 2.

IV.B. Stoichiometrically Controlled Removal of Calcium:

Experimental results were first tested for stoichiometrically controlled removal of calcium from aluminum and aluminum-1wt% magnesium alloys.

Through appropriate substitution for calcium, Eqn.(2.9) becomes:

$$\frac{E/F + \%Ca_i^B}{E/F + \%Ca_i^B} = e^{-Ft} \quad (4.3)$$

where E and F are:

$$E = \frac{G_{Cl_2} 100 m_{Ca}}{M} \quad (4.4)$$

$$F = \frac{k_w A_w \rho}{M} \quad (4.5)$$

In Eqn.(4.3) the evaporation of calcium from the melt surface and into the bubbles was ignored on the assumption that calcium has very low vapour pressure,  $9.184 \cdot 10^{-9}$  atm @ 1000 K for 1wt% standard state[39].

The amount of inert rinsing gas @STP required per kg of metal in order to reduce an initial calcium concentration of 5 ppm to 1 ppm can be calculated from the equation given by Geller[64]:

$$(S) = \frac{224}{m_{Ca}} ([\%Ca]_i - [\%Ca]_f) \left( \frac{P}{K[\%Ca]_f} - 1 \right) \quad (4.6)$$

In the above equation, P is the total pressure( $\sim P_{atm}$ ),  $m_{Ca}$  is the molecular weight of

calcium,  $\%Ca_i$  and  $\%Ca_f$  are initial and final calcium concentrations respectively, and  $K$  is the equilibrium constant for the following equilibrium:



where underline indicates the component in solution.  $K$  is equal to vapour pressure of the impurity at 1wt% standard state which is  $9.18 \times 10^{-9}$  atm at 1000 K. Substituting the initial and final values of calcium concentration and that for  $K$ , one would obtain a value of  $2.44 \times 10^9$  litres of inert gas @STP for each kg of liquid aluminum.

In Eqn.(4.3) the term  $F$ , the rate constant for the consumption of calcium through reaction with the crucible wall,  $R_w$ , was therefore taken to be the value of  $R_{Ar}$  which was obtained from the results of the argon injection tests owing to calcium's low vapour pressure.

Experimental results can now be tested with this model by plotting the left hand side against the right hand side of Eqn.(4.3). Such plots for commercial purity aluminum and aluminum-1wt% magnesium alloys are shown in Figures 4.9. through 4.12. In each graph, the diagonal line represents the theoretical line that the experimental points should follow if the removal of calcium can be presented by this model.

As seen from the figures, except for the lowest chlorine concentration, experimental points lie well below the theoretical line for both commercial purity aluminum and aluminum-1wt% magnesium alloy. As the chlorine concentration and gas flow rate increased, the downward departure from the theoretical line increased.

At the lowest chlorine concentration, experimental points lie mostly over the theoretical line. This should not be possible unless  $Ca$  was consumed at sites other than those already mentioned. Further, the experimental points should have followed a straight line rather than a curve. It is therefore suspected that error in the measurement of chlorine flow rate at such low level of flow could account for this observation. For instance a 75% increase in the molar gas flow rate of chlorine would bring the experimental points below the theoretical line.

These results show that the flux of calcium to the gas bubbles was insufficient to consume all the chlorine in the gas bubbles due to insufficient contact surface area between the bubbles and the melt and/or insufficient residence time of the bubbles in the melt.

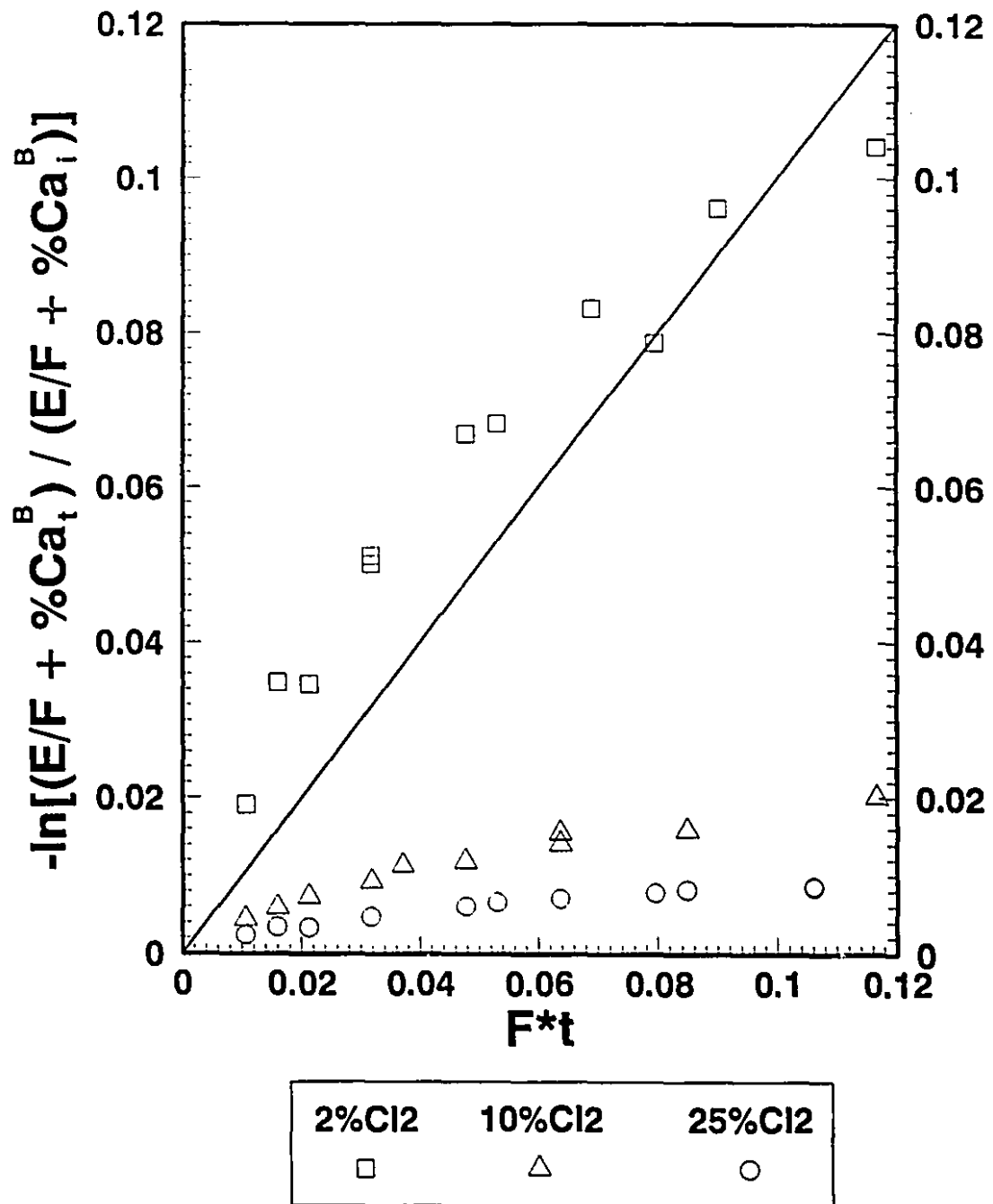


Figure 4.9 Comparison of stoichiometrically controlled removal of calcium versus experimental results for commercial purity aluminum melts;  $Q=26.22$  cc/sec(730 °C, 1 Atm.)

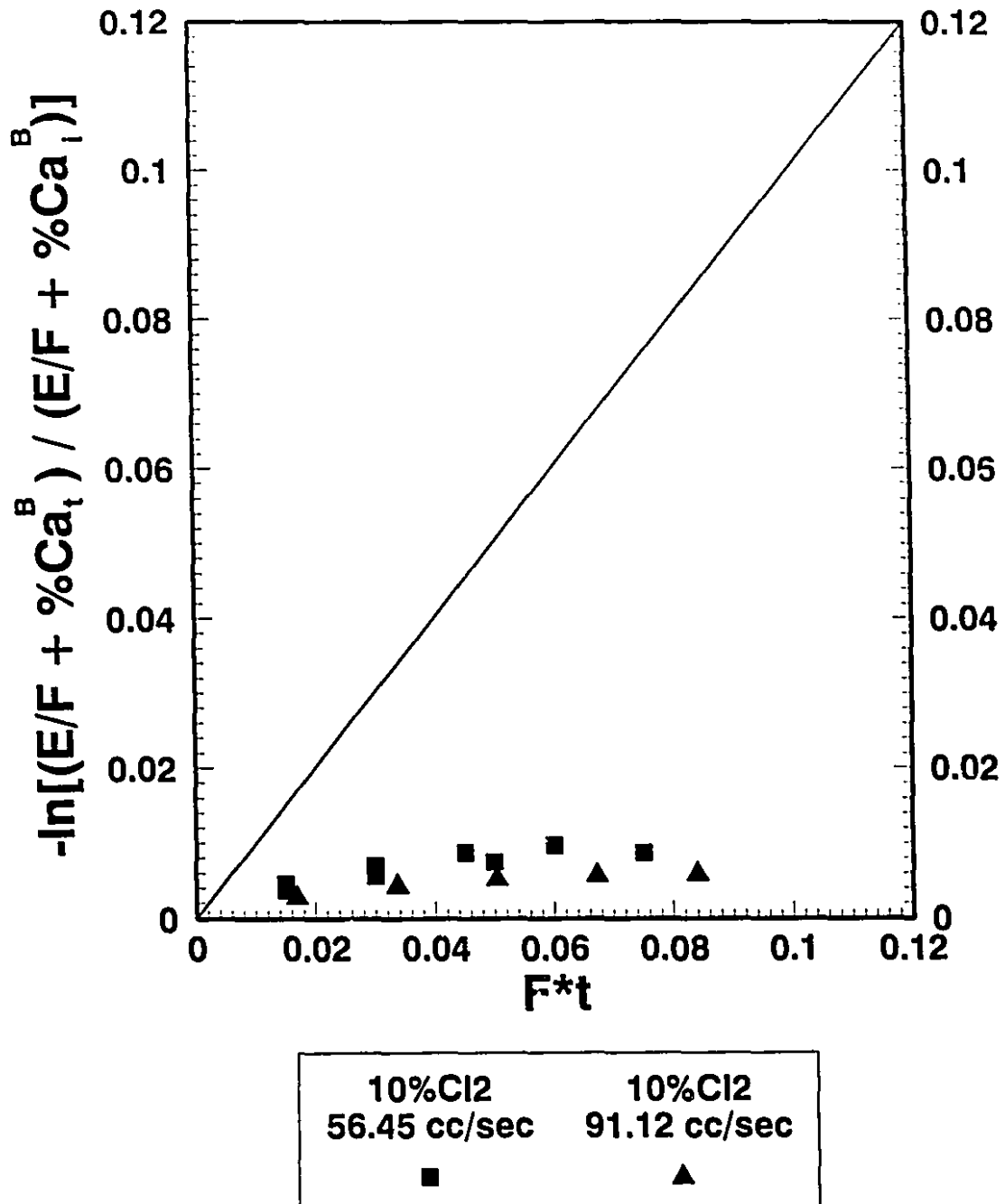


Figure 4.10 Comparison of stoichiometrically controlled removal of calcium versus experimental results for commercial purity aluminum melts at higher gas flow rates (730 °C, 1 Atm.); Vol% Cl<sub>2</sub> = 10

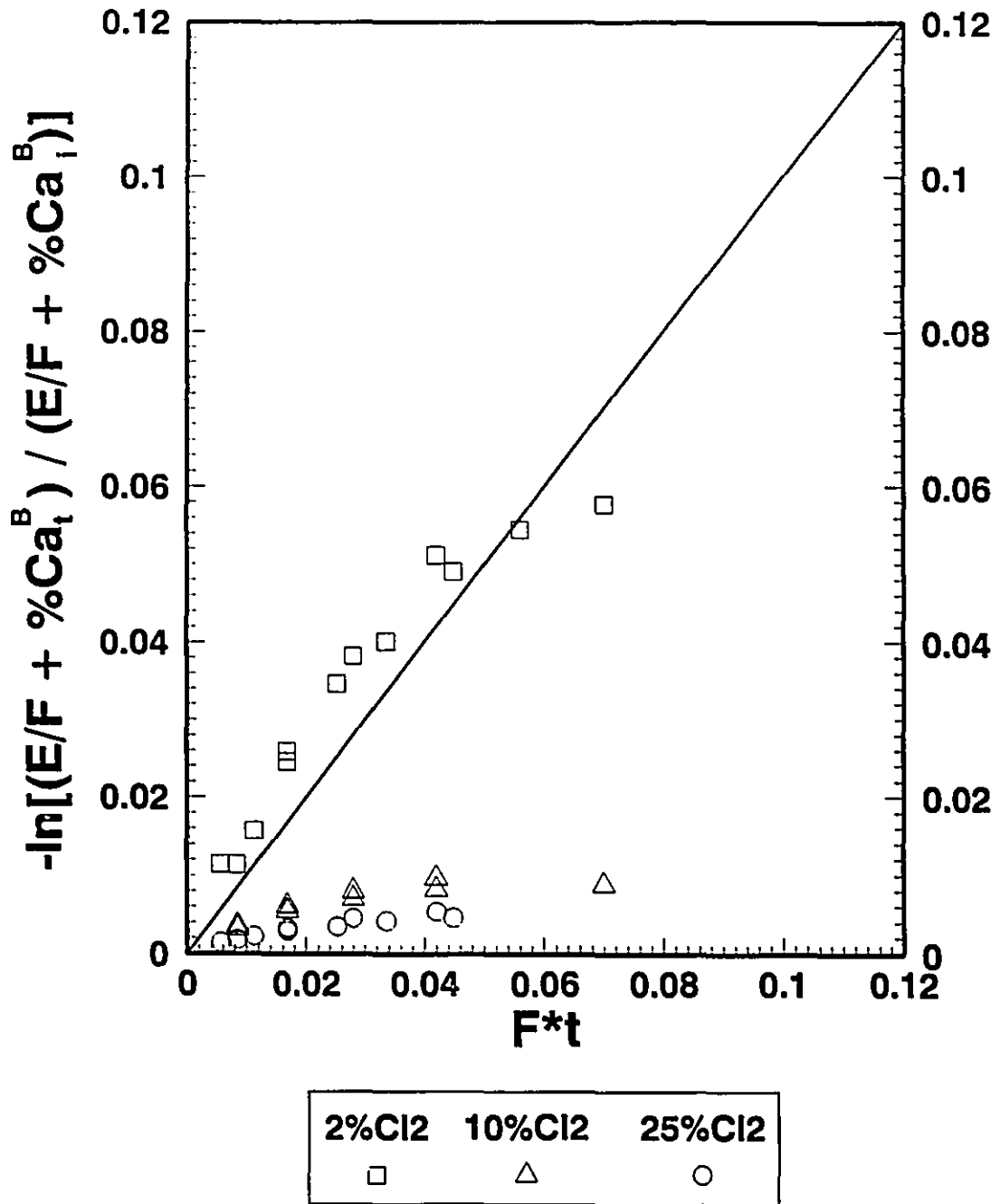


Figure 4.11 Comparison of stoichiometrically controlled removal of calcium versus experimental results for Al-1wt% Mg alloys; Q=26.22 cc/sec(730 °C, 1 Atm.)

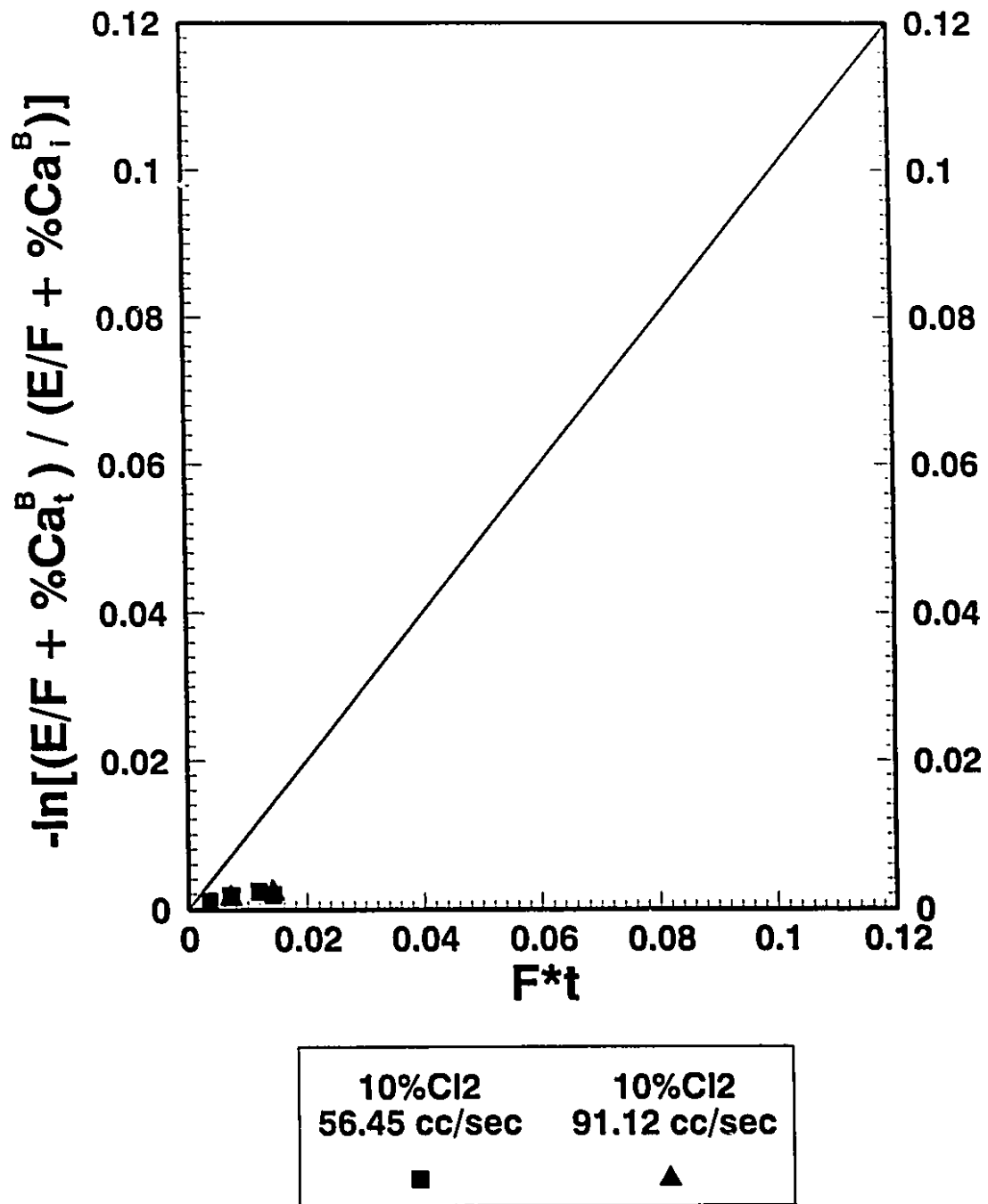


Figure 4.12 Comparison of stoichiometrically controlled removal of calcium versus experimental results for Al-1wt% Mg alloys at higher gas flow rates (730 °C, 1 Atm.); Vol% Cl<sub>2</sub>=10

IV.C. Mass Transfer Controlled Removal of Calcium:

For this case, Eqn.(2.13) applies. With proper substitution for calcium and assuming that the evaporation of calcium is negligibly small, Eqn.(2.13) becomes:

$$\frac{M d\%Ca^B}{100 m_{Ca} dt} = \frac{k_b \rho A_b \%Ca^B}{100 m_{Ca}} + \frac{k_{irp} \rho A_{irp} \%Ca^B}{100 m_{Ca}} + \frac{k_w \rho A_w \%Ca^B}{100 m_{Ca}} \quad (4.8)$$

Upon integration of the above equation, one obtains:

$$-\ln \frac{\%Ca_t^B}{\%Ca_i^B} = \left( \frac{k_b \rho A_b}{M} + \frac{k_{irp} \rho A_{irp}}{M} + \frac{k_w \rho A_w}{M} \right) t \quad (4.9)$$

which can be represented in the following form:

$$-\ln \frac{\%Ca_t^B}{\%Ca_i^B} = R_o t \quad (4.10)$$

In Figures 4.13 through 4.16 experimental results for commercial purity aluminum and aluminum-1wt% magnesium alloys are presented by plotting the left hand side of Eqn.(4.10) against the right hand side. The line in each figure represents the theoretical line that has a slope of 1. In the figures, the slope of the straight line that would represent the experimental data and the correlation coefficient, C.C, are presented in numerical form on the top left hand side of each figure.

As seen for both melts, the agreement between the experimental data and the model presented in Chapter 2 is very good.

Since the equation that was used to describe a mass transfer controlled removal of calcium was a first order differential equation and there was a good agreement between the experimental data and the model, calcium removal, under the present experimental conditions, was therefore shown to follow first order reaction kinetics.

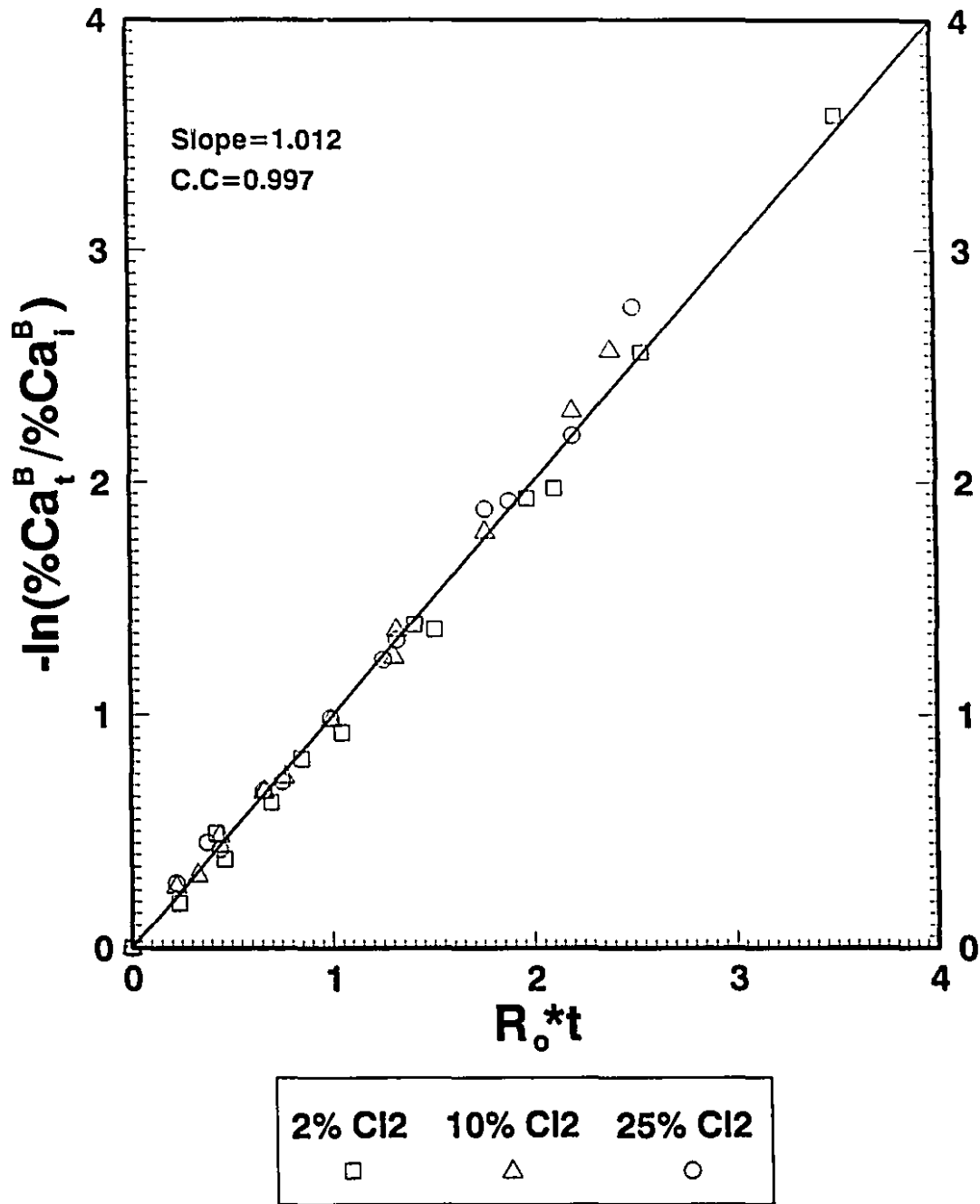


Figure 4.13 Comparison of mass transfer controlled removal of calcium versus experimental results for commercial purity aluminum melts;  $Q=26.22$  cc/sec(730 °C, 1 Atm.)

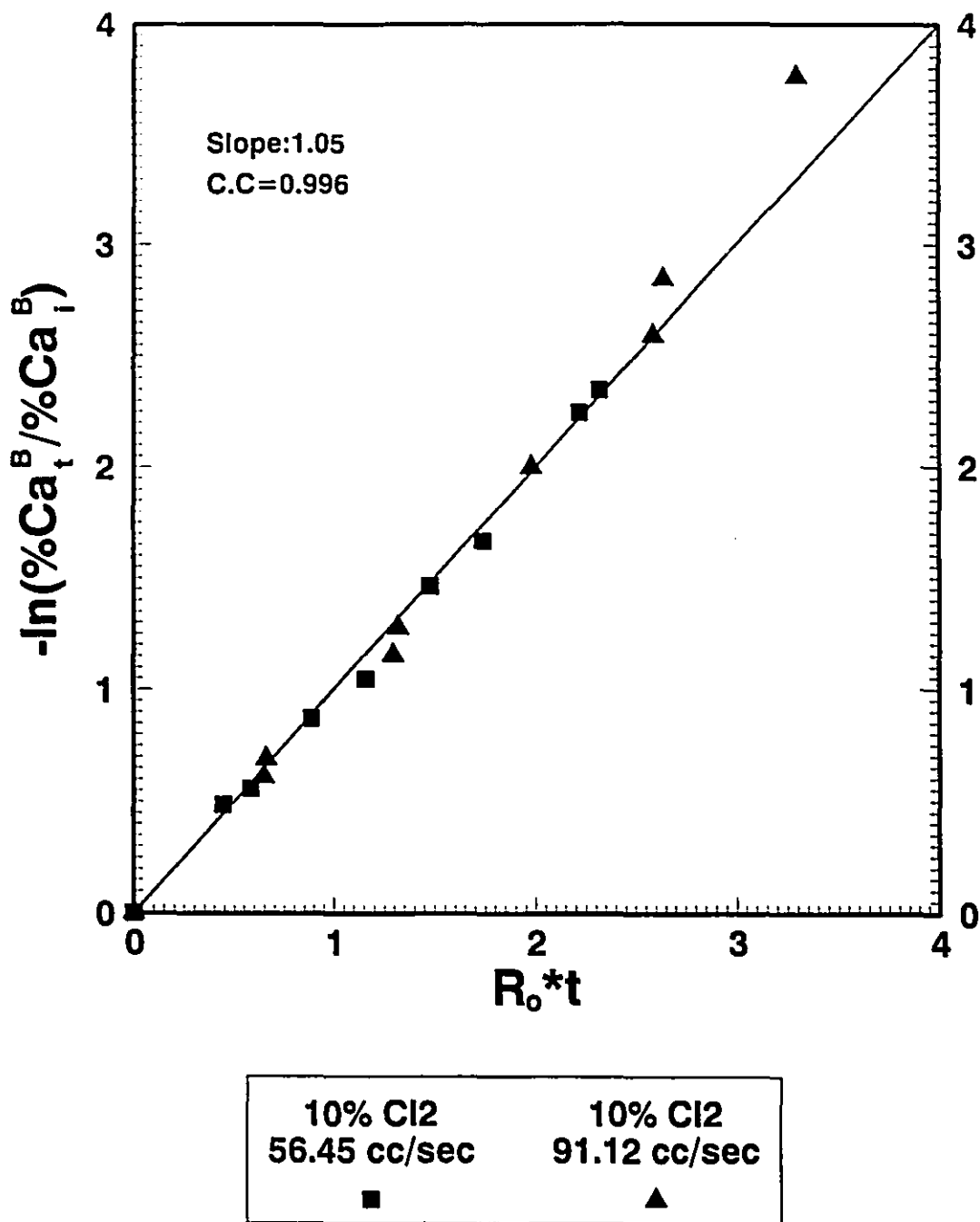


Figure 4.14 Comparison of mass transfer controlled removal of calcium versus experimental results for commercial purity aluminum melts at higher gas flow rates (730 °C, 1 Atm.); Vol% Cl<sub>2</sub> = 10

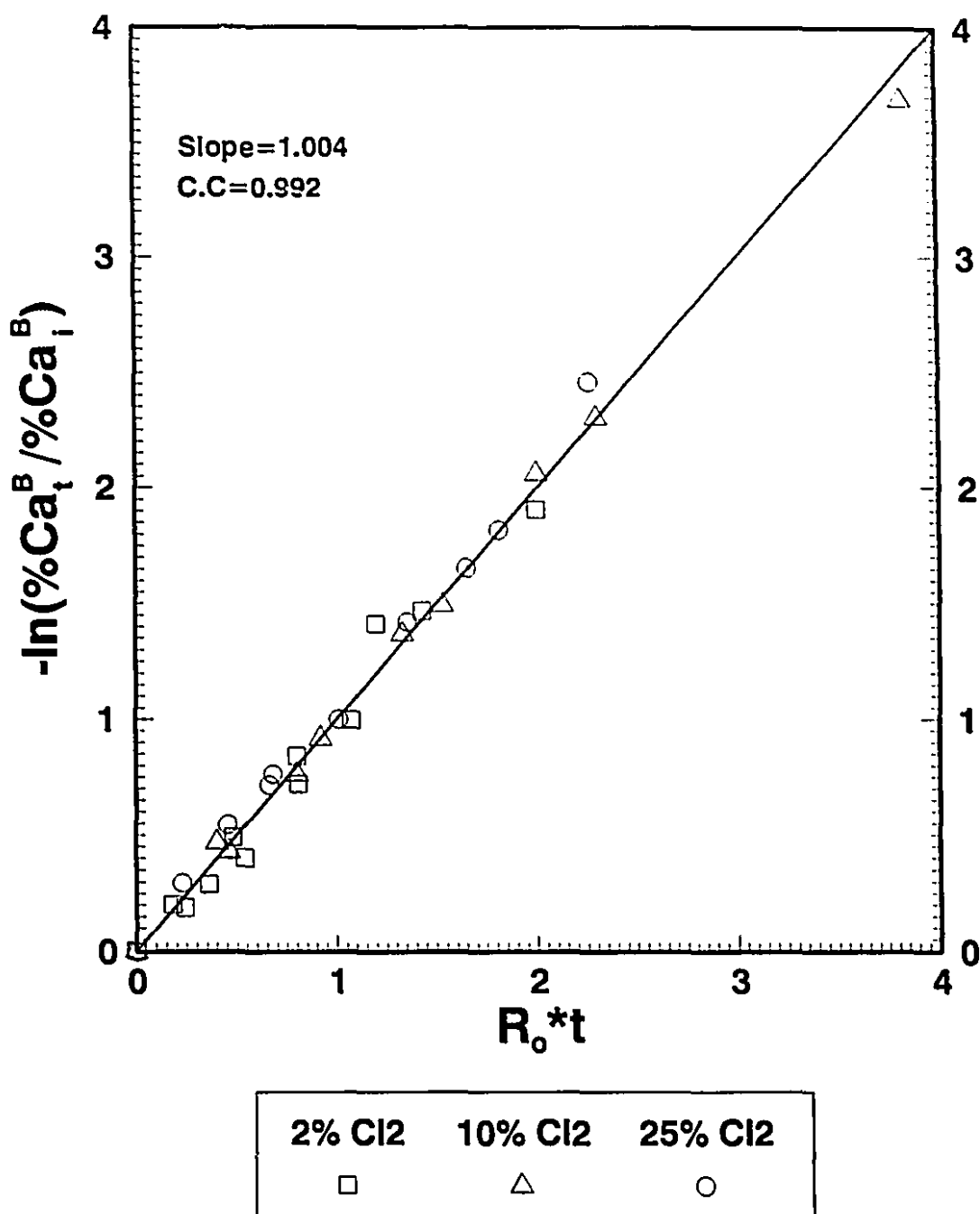


Figure 4.15 Comparison of mass transfer controlled removal of calcium versus experimental results for Al-1wt% Mg alloys; Q=26.22 cc/sec(730 °C, 1 Atm.)

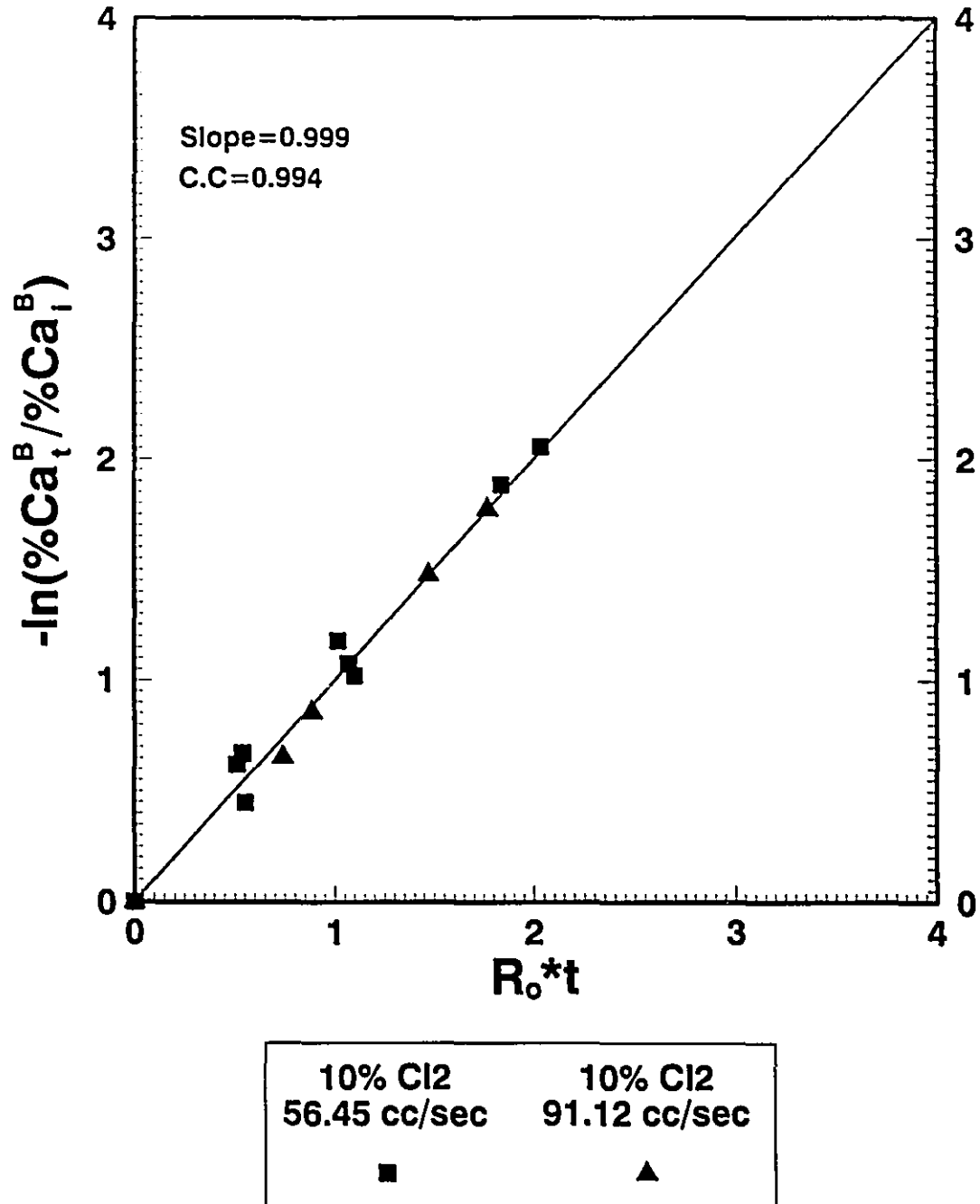


Figure 4.16 Comparison of mass transfer controlled removal of calcium versus experimental results for Al-1wt% Mg alloys at higher gas flow rates(730 °C, 1 Atm.); Vol% Cl<sub>2</sub>=10

IV.D. Calculation of Rate Constants for Bubbles and Intermediate Reaction Products that are Separated from the Bubbles:

Having determined that under the present experimental conditions the removal of calcium by chlorination from commercial purity aluminum and aluminum-1wt% magnesium alloys followed first order reaction kinetics, the rate constants that made up the overall rate constant in Eqn.(4.9) can now be presented.

In Eqn.(4.9), the overall rate constant,  $R_o$ , contained rate constants for the removal of calcium by reaction on bubble surfaces,  $R_b$ , on *intermediate reaction products that are separated from the bubbles*,  $R_{irp}$ , and on the crucible wall,  $R_w$ .

The overall rate constant can therefore be represented in the following form:

$$R_o = R_b + R_{irp} + R_w \quad (4.11)$$

The overall rate constants were obtained from the results of the continuous chlorination tests.  $R_w$  was obtained from the results of argon injection tests with the assumption that the evaporation of calcium was negligible. Argon injection tests can be viewed as blank tests to determine the fraction of consumption of calcium due to reaction of calcium with the material of the crucible wall ( $Al_2O_3$ ). Argon injection tests to determine  $R_w$  is not to be confused with the argon injection period during the intermittent tests in which the purpose was the determination of contribution of the intermediate reaction products that are separated from the bubbles. The rate constant  $R_{irp}$  was determined from the results of the intermittent tests by making use of  $R_w$  as follows:

$$R_{irp} = R_{intermittent} - R_w \quad (4.12)$$

In the above equation,  $R_{intermittent}$  is the rate constant that was obtained from the results of intermittent chlorination tests.

Finally,  $R_b$  was calculated from:

$$R_b = R_o - R_{intermittent} \quad (4.13)$$

Rate constants calculated through Eqns.(4.12) and (4.13) together with  $R_o$  and  $R_w$  are presented in Tables 4.4 and 4.5.

Table 4.4 Summary of the rate constants for various chlorine concentrations in the gas bubbles;  
 $Q=26.22$  cc/sec(730 °C, 1 Atm.)

Cl <sub>2</sub> Concentration (Vol%)	Rate constant (1/sec)*10 <sup>6</sup>							
	Al				Al-1wt% Mg			
	R <sub>o</sub>	R <sub>b</sub>	R <sub>irp</sub>	R <sub>w</sub>	R <sub>o</sub>	R <sub>b</sub>	R <sub>irp</sub>	R <sub>w</sub>
2	2343	1688			1331	566		
	1933	1278	567	88	1490	725	718	47
	Av:2138	Av:1483			Av:1411	Av:646		
10	1815	1118			2217	1084		
	1833	1136	608	88	2550	1417	1086	47
	Av:1824	Av:1127			Av:2384	Av:1251		
25	1833	1220			1828	911		
	2088	1475	525	88	1883	966	870	47
	Av:1961	Av:1348			Av:1856	Av:939		

Table 4.5 Summary of the rate constants for various gas flow rates(730 °C, 1 Atm.); Vol% Cl<sub>2</sub>=10

Q (cc/sec) @ 730 °C	Rate constant (1/sec)*10 <sup>6</sup>							
	Al				Al-1wt% Mg			
	R <sub>o</sub>	R <sub>b</sub>	R <sub>irp</sub>	R <sub>w</sub>	R <sub>o</sub>	R <sub>b</sub>	R <sub>irp</sub>	R <sub>w</sub>
26.22	1815	1118			2217	1084		
	1833	1136	609	88	2550	1417	1086	47
	Av:1824	Av:1127			Av:2384	Av:1251		
56.45	3225	2612			3067	1027		
	2467	1854	530	83	2983	943	2020	20
	Av:2846	Av:2233			2817	777		
				Av:2956	Av:916			
91.12	3665	2732			4090	2060		
	3592	2659	840	93	4917	2887	1991	39
	Av:3629	Av:2696			Av:4504	Av:2474		

IV.D.1. Effect of Chlorine Concentration:

Table 4.4 gives the rate constants for various chlorine concentrations for commercial purity aluminum and aluminum-1wt% magnesium alloys.

Except for the Ar-2% Cl<sub>2</sub> concentration, the removal rate of removal of calcium was practically the same for both commercial purity aluminum and aluminum-1wt% magnesium alloy.

In the case of commercial purity aluminum, over the range of chlorine concentrations considered, the overall rate constant, R<sub>o</sub>, did not change by more than 10% of its mean. The maximum contribution to the removal of calcium was from bubbles. This was calculated to be about 67%, whereas the contribution of intermediate reaction products that are separated from the bubbles was calculated to be about 28%. The contribution of the crucible wall (i.e the contribution of the material that the crucible was made of) to the removal of calcium was negligibly small (about 5%).

In the case of aluminum-1wt% magnesium alloy, following an increase in chlorine concentration from 2 to 10%, the overall rate constant increased by about 70%. With further increase in chlorine concentration, the overall rate constant dropped back to about 1.9\*10<sup>-3</sup>/sec. While an increase of the rate constant from 2 to 10% chlorine in the gas mixture would imply that the gas phase resistance may not be negligible, the decrease in the rate constant beyond 10% Cl<sub>2</sub> concentration would not confirm this hypothesis. Further, this trend was not observed in the magnesium free metal in which the mass transfer was confirmed to be governed in the melt phase. One could also argue that the reason for the lower overall rate constant at the lowest chlorine concentration would be due to formation of an MgCl<sub>2</sub> film over the bubble surfaces which would decrease the convective circulation inside the gas bubbles leading to slower transport of chlorine gas to the bubble melt interface. The data for the lowest chlorine concentration, however, showed that the removal of calcium followed first order reaction kinetics with respect to calcium concentration. Further, the magnitude of the rate constant for the intermediate reaction products that are separated from the bubbles was comparable to the ones obtained at higher chlorine concentrations indicating that the formation of the intermediate reaction products was still possible.

It is instructive to note that in the case of the magnesium containing alloy, the contribution of the intermediate reaction products that are separated from the bubbles to the removal of calcium was appreciable. Over the range of chlorine concentrations investigated, this contribution was calculated to be about 50%. The contribution of the bubbles was calculated to be around 48%. The contribution of the crucible wall was negligibly small (~2%).

The implication of these results is that the achievement of large bubble-metal contact surface area is more critical in commercial purity aluminum than it is in the magnesium containing alloy as the removal of the impurity largely depends on the bubbles as the primary reaction site. In the case of the magnesium containing alloys, however, more reaction sites will be provided by the intermediate reaction products that are separated from the bubbles.

#### IV.D.2. Effect of Gas Flow Rate:

Table 4.5 gives the rate constants for various gas flow rates for commercial purity aluminum and aluminum-1wt% magnesium alloys. At each gas flow rate, the percent concentration of the chlorine in the gas bubbles was 10%.

For the case of commercial purity aluminum, the maximum contribution to the removal of calcium was from the gas bubbles which was calculated to be around 73%. The contribution of intermediate reaction products that were separated from the bubbles was calculated to be 24%. The contribution of the crucible wall was again negligibly small (~3%).

In the case of aluminum-1wt% magnesium alloy, the maximum contribution to the removal of calcium came from the intermediate reaction products that are separated from the bubbles. This contribution was calculated to be 52%. The contribution of the bubbles was calculated to be 45%. The contribution of the crucible wall was negligibly small (~3%).

In both commercial purity aluminum and the magnesium containing alloys, the rate of removal of calcium increased with increases in gas flow rate. This points to the importance of increased melt circulation to bring the impurity containing melt to the reaction

zones(i.e to bubbles, and intermediate reaction products that are separated from the bubbles)

#### IV.E. Calculation of the Melt Phase Mass Transfer Coefficients for Bubbles:

Experimental melt phase mass transfer coefficients for the bubbles were first calculated from the rate constant expression for bubbles,  $R_b$ , according to:

$$k_b = \frac{M R_b}{A_b \rho} \quad (4.14)$$

In the above equation, the total surface area of the bubbles,  $A_b$ , at any instant in the bath was calculated from:

$$A_b = \frac{6 Q h}{U d_c} \quad (4.15)$$

where  $Q$  is the gas flow rate,  $h$  is the height of the melt,  $U$  is the terminal rising velocity of the bubbles and  $d_c$  is the diameter of the equivalent sphere.

The terminal rising velocity of the bubbles was calculated from the following equation obtained by Andreini et al[65]:

$$U = 29.69 d_c^{0.316} \quad (cm/sec) \quad (4.16)$$

Andreini et al demonstrated that Eqn.(4.16) represented their experimental data well for the rising velocity of bubbles in liquid tin, lead and copper under dynamic bubbling conditions. The frequency of bubbles formed at a single submerged orifice was reported to be between 5 to 30 per second. The physical properties of the liquid metals and the bubble sizes they obtained enabled an Eotvos number range between 1.5 and 51 to be covered. The value of the Morton number was about  $1 \cdot 10^{-13}$ . Therefore, Eqn.(4.16) should represent the rise velocity of the bubbles well under the present experimental conditions.

Tables 4.6 and 4.7 give the melt phase mass transfer coefficients for the bubbles,  $k_b$ , calculated according to Eqn.(4.14), for various chlorine concentrations and gas flow rates respectively.

Within the range of the experimental conditions considered, taking a mean mass

**Table 4.6** Experimental melt phase mass transfer coefficients for bubbles for various chlorine concentrations;  $Q=26.22$  cc/sec(730 °C, 1 Atm.)

Cl <sub>2</sub> Concentration (Vol%)	k <sub>b</sub> (m/sec)*10 <sup>6</sup>	
	Al	Al-1wt% Mg
2	1065	330
	837	417
	Av:951	Av:374
10	636	616
	705	741
	Av:671	Av:679
25	794	545
	935	578
	Av:865	Av:562

**Table 4.7** Experimental melt phase mass transfer coefficients for bubbles for various gas flow rates(730 °C, 1 Atm.); Vol% Cl<sub>2</sub>=10

Q (cc/sec) @ 730 °C	k <sub>b</sub> (m/sec)*10 <sup>6</sup>	
	Al	Al-1wt% Mg
26.22	636	616
	705	741
	Av:671	Av:679
56.45	916	393
	687	350
	Av:802	288
		Av:344
91.12	722	567
	751	755
	Av:737	Av:661

transfer coefficient of  $805 \cdot 10^{-6}$  m/sec for bubbles in commercial purity aluminum and  $507 \cdot 10^{-6}$  m/sec for bubbles in the magnesium containing alloy, it is apparent that the amount of calcium that was consumed per unit time on the bubble surfaces was about 60% more in the commercial purity aluminum.

According to Higbie's penetration theory[66], the liquid phase mass transfer coefficients for bubbles with  $Re \gg 1$  is given by the following equation:

$$k = 2 \left( \frac{D}{\pi \tau} \right)^{1/2} \quad (4.17)$$

In the above equation,  $D$  is the diffusion coefficient and  $\tau$  is the sweep time of a fluid element to travel across the bubble surface which is calculated by dividing the diameter of the bubble by its terminal rising velocity.

Denoting the melt phase mass transfer coefficients for bubbles in commercial purity aluminum and in the magnesium containing alloy by  $k_1$  and  $k_2$  respectively, one would have

$$\frac{k_1}{k_2} = \left( \frac{D_1}{D_2} \right)^{0.5} \quad (4.18)$$

In Eqn.(4.18),  $D_1$  and  $D_2$  are the diffusion coefficient of Ca in commercial purity aluminum and in the magnesium containing alloy respectively. Substituting  $805 \cdot 10^{-6}$  and  $507 \cdot 10^{-6}$  m/sec for  $k_1$  and  $k_2$  respectively, one would obtain a diffusion coefficient of Ca 2.5 times higher in commercial purity aluminum than it is in the magnesium containing alloy.

There are several models to predict diffusion coefficients in liquid metals. Some of these models, assuming that the mechanism of diffusion is similar to that for viscous flow, relates the diffusion coefficient to the viscosity of the liquid in the following form:

$$D = F \mu^{-1} \quad (4.19)$$

A brief summary of these models are presented in Appendix C. In all these models the diffusion coefficient changes inversely proportional to the viscosity of the melt.

Several investigators have measured the viscosity of liquid aluminum[67] and aluminum magnesium alloys[46,68,69]. The discrepancy between the measured values of

the viscosities among the several investigators are considerable. There is also disagreement as to whether magnesium decreases or increases the viscosity of aluminum. Nevertheless, their data showed little difference between the absolute values of the viscosities when there is only about 1wt% magnesium in the melt. Gebhardt et al.[46] measured a value of  $1.083 \cdot 10^{-3}$  and  $1.049 \cdot 10^{-3}$  kg/m-sec for the viscosities of aluminum and aluminum-1wt% magnesium alloy respectively at 730 °C. Therefore on the basis of these models one should not expect any appreciable difference between the diffusivity of calcium in liquid aluminum and aluminum-1wt% magnesium alloy. However, these models are of little use other than being useful to predict self-diffusion coefficients in liquid metals as they do not take into consideration interatomic forces between the solute and solvent atoms. For instance, Ma and Swalin[70] tested Sutherland-Einstein(see Appendix C) equation to obtain ionic radii of Al, Zn, Ag, Cu and Ni from experimental diffusion coefficients. Although the radii calculated through the Sutherland-Einstein equation were within an order of magnitude of already known values of these elements, it failed to give the correct numerical order of the diffusion coefficients.

Later, Swalin and Leak[71] showed that interatomic attraction and repulsion between the solute and solvent atoms play an important role in solute diffusivities. These authors measured diffusivity of solutes with increasing valance in liquid silver. They found that the closer the relative valance of the solute to 0 with respect to the solvent the closer the solute diffusivity of the solute to the self-diffusivity of the solvent will be.

Calcium and magnesium are group IIA elements with a valance of +2 whereas aluminum is a group IIIA element with a valance of +3. Therefore, calcium and magnesium have a relative valance of -1 with respect to aluminum. On the basis of the results of Swalin and Leak, the solute diffusivities of Ca and Mg in liquid aluminum should be similar and close to the self diffusivity of aluminum. The diffusion coefficient of magnesium in liquid aluminum at 730 °C was calculated to be  $6.7 \cdot 10^{-9}$  m<sup>2</sup>/sec taking the average of the experimental values of three different investigators(Appendix D). This value is almost identical to the value of the self diffusion coefficient of aluminum that was obtained from the theoretical calculations of Protopapas et al(Appendix D).

Thus, on the basis of the results of Leak and Swalin, one would not expect a 2.5

times difference between the diffusion coefficient of calcium in commercial purity aluminum and aluminum-1wt% magnesium alloy. Consequently, the value of the mass transfer coefficients for bubbles in the magnesium containing alloys and commercial purity aluminum should be similar.

The fact that for both melts, the values of the mass transfer coefficients were close to each other at 10%  $\text{Cl}_2$  concentration at the lowest and the highest gas flow rates supports this hypothesis.

Based on this argument, one should be able to show that the mass transfer coefficients for bubbles in commercial purity aluminum should be close to the ones in the magnesium containing alloys. Looking at the definition of mass transfer coefficient from another angle might be sufficient to achieve this purpose. A mass transfer coefficient can be viewed as a constant of proportionality between a mass flux and a concentration driving force which can be formulated in the following form:

$$\dot{N}'' = k \frac{M}{V} \Delta C \quad (4.20)$$

In the above equation,  $\dot{N}''$  is the mass flux( $\text{kg}/\text{m}^2\text{-sec}$ ),  $M(\text{kg})$  and  $V(\text{m}^3)$  are the mass and volume of the melt and  $\Delta C(\text{wt}\%)$  is the concentration difference, i.e driving force for the mass flux. The mass flux,  $\dot{N}''$  can be defined as:

$$\dot{N}'' = R_b \frac{M}{A} \Delta C \quad (4.21)$$

where  $R_b(\text{sec}^{-1})$  is the calculated rate constant for the bubbles and  $A(\text{m}^2)$  is the total surface area of the bubbles at any instant in the bath. Substituting for  $\dot{N}''$  in Eqn.(4.20) and cancelling the identical terms on the opposite sides of the equation would lead to:

$$R_b = k \frac{A}{V} \quad (4.22)$$

which is in fact identical to Eqn.(4.14). According to Eqn.(4.22), a plot of  $R_b$  versus  $A/V$  should give a straight line with a slope equal to  $k$  which is the mass transfer coefficient for bubbles. This is what was done in Figure 4.17. As seen the slope of the lines obtained for

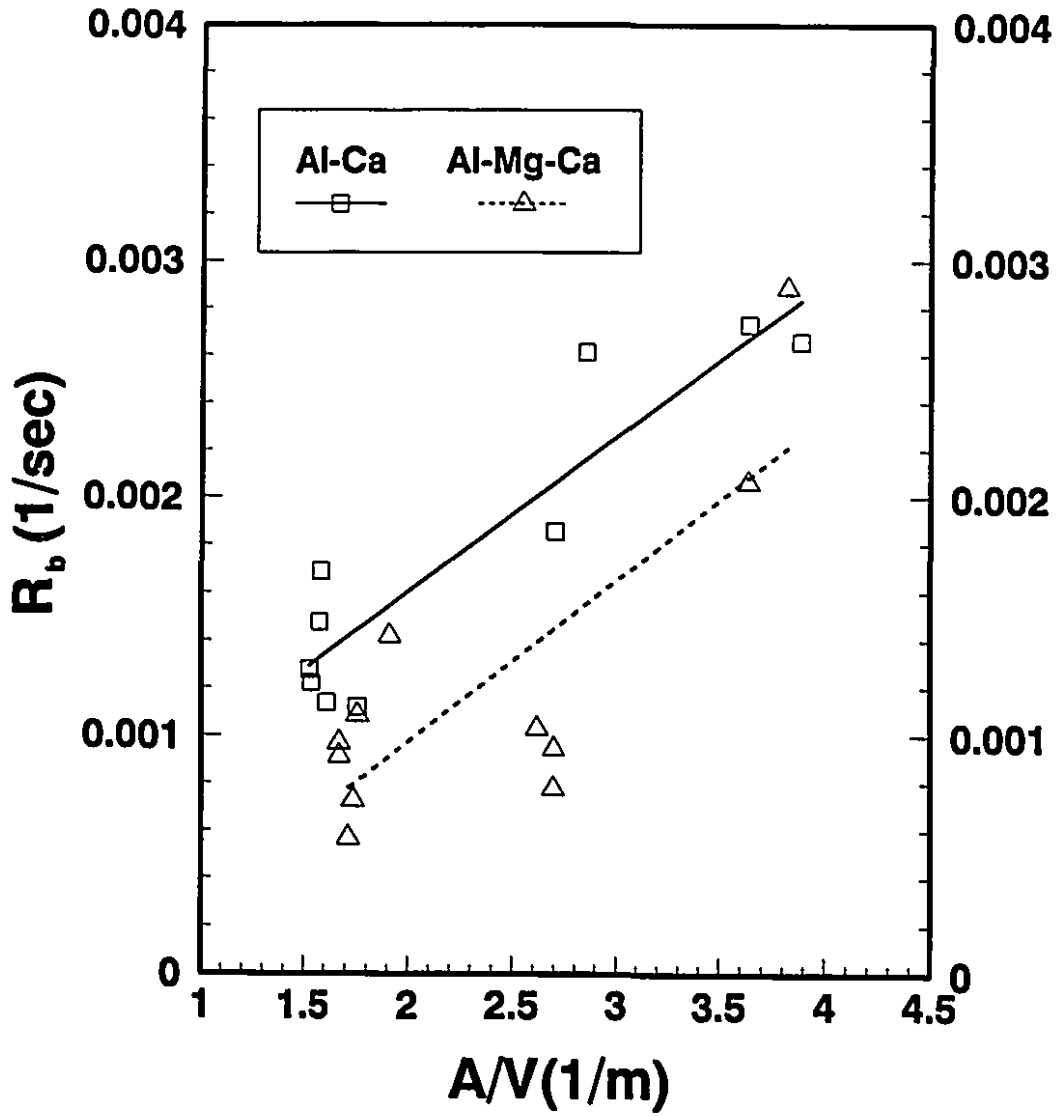


Figure 4.17 Determination of melt phase mass transfer coefficients for bubbles graphically through Eqn.(4.22)

commercial purity aluminum and the magnesium containing alloys are almost identical. In the case of commercial purity aluminum,  $k$  was calculated to be  $653 \cdot 10^{-6}$  m/sec with a correlation coefficient of 0.921 for the linear regression analysis. In the case of the magnesium containing alloys  $k$  was calculated to be  $683 \cdot 10^{-6}$  m/sec with a correlation coefficient of 0.792. In order to see whether the correlation coefficients obtained for the regression analysis really indicate a significance for a strong functional relationship between  $R_b$  and  $A/V$  a significance test[72] for the correlation coefficient was carried out. For a 99% level of significance, the test gave a correlation coefficient of 0.765 and 0.798 for the results obtained for the magnesium containing alloys and for commercial purity aluminum respectively. Since the correlation coefficients obtained by the significance test were lower than those obtained by the regression analysis, there exists a strong functional relationship between  $R_b$  and  $A/V$ .

The importance of the results that the mass transfer coefficients for the bubbles are so close to each other in value in commercial purity aluminum and aluminum-magnesium alloys is that the capacity of the chlorine containing gas bubbles to remove calcium should not be reduced with the presence of magnesium in the bath as claimed by Stevens and Yu[30].

#### IV.F. Summary:

Under the present experimental conditions, the removal of calcium from commercial purity aluminum and aluminum-1wt% magnesium alloys followed first order reaction kinetics with respect to calcium concentration. It was demonstrated that the flux of calcium to the bubble-melt interface was not sufficient to consume chlorine stoichiometrically due to insufficient contact surface area between the bubbles and the melt.

The present data did not allow a firm conclusion to be advanced as to why the removal of calcium was relatively lower at the particular 2%  $Cl_2$  concentration.

Based on the rate constants calculated from the experimental data, the gas bubbles were shown to be the primary reaction site for calcium in commercial purity aluminum. The contribution of the bubbles to the removal of calcium was calculated to be around 70%.

In the case of aluminum-1wt% magnesium alloys, the intermediate reaction products

that are separated from the bubbles contributed to the removal of calcium by as much as 50%. An equal contribution came from the bubbles.

The calculated rate constants suggest that the generation of as large a contact surface area between the bubbles and the melt as possible is more essential for commercial purity aluminum since calcium removal depends primarily on the gas bubbles as the main reaction site. In the case of the magnesium containing alloys, however, more additional reaction sites will be created by the intermediate reaction products that are separated from the gas bubbles.

Mass transfer coefficients calculated for the bubbles showed that the presence of magnesium in the bath should not reduce the capacity of the chlorine containing gas bubbles with respect to elimination of calcium from the bath.

## Chapter 5

### Results and Discussion: Kinetics of Sodium Removal

---

#### V.A. Presentation of the experimental results in graphical and tabular form:

Figures 5.1 through 5.8 show the change in the bulk sodium concentration under various experimental conditions for commercial purity aluminum and aluminum-1wt% magnesium alloys.

The change in the bulk concentration of sodium with time could be represented by an exponentially decaying curve which suggests that transient bulk concentration of sodium can be represented by an equation of the following form:

$$\%Na_t^B = \%Na_i^B e^{-Rt} \quad (5.1)$$

In the above equation,  $\%Na_t^B$  and  $\%Na_i^B$  are the transient and initial sodium concentrations respectively,  $t$  is time and  $R$  is the rate constant.

Rearranging Eqn.(5.1), one obtains:

$$-\ln \frac{\%Na_t^B}{\%Na_i^B} = Rt \quad (5.2)$$

A plot of  $-\ln(\%Na_t^B / \%Na_i^B)$  vs  $t$  will give a straight line, the slope of which is equal to the rate constant  $R$ . The rate constant  $R$  represents the fraction of the impurity that is consumed by reaction per unit time and therefore is a useful measure of the rate of a chemical reaction at a specified temperature.

Tables 5.1 and 5.2 present the rate constants obtained graphically through Eqn.(5.2). In these tables,  $R_o$ ,  $R_{intermittent}$  and  $R_{Ar}$  represent the individual experimental rate constants obtained from continuous chlorination, intermittent and argon injection tests respectively. The numbers in the parenthesis represent the correlation coefficients which is a measure of determination of how closely the data fits a straight line. When the correlation coefficient is  $|1|$  the data falls exactly on a straight line, whereas when it is 0 the data cannot be

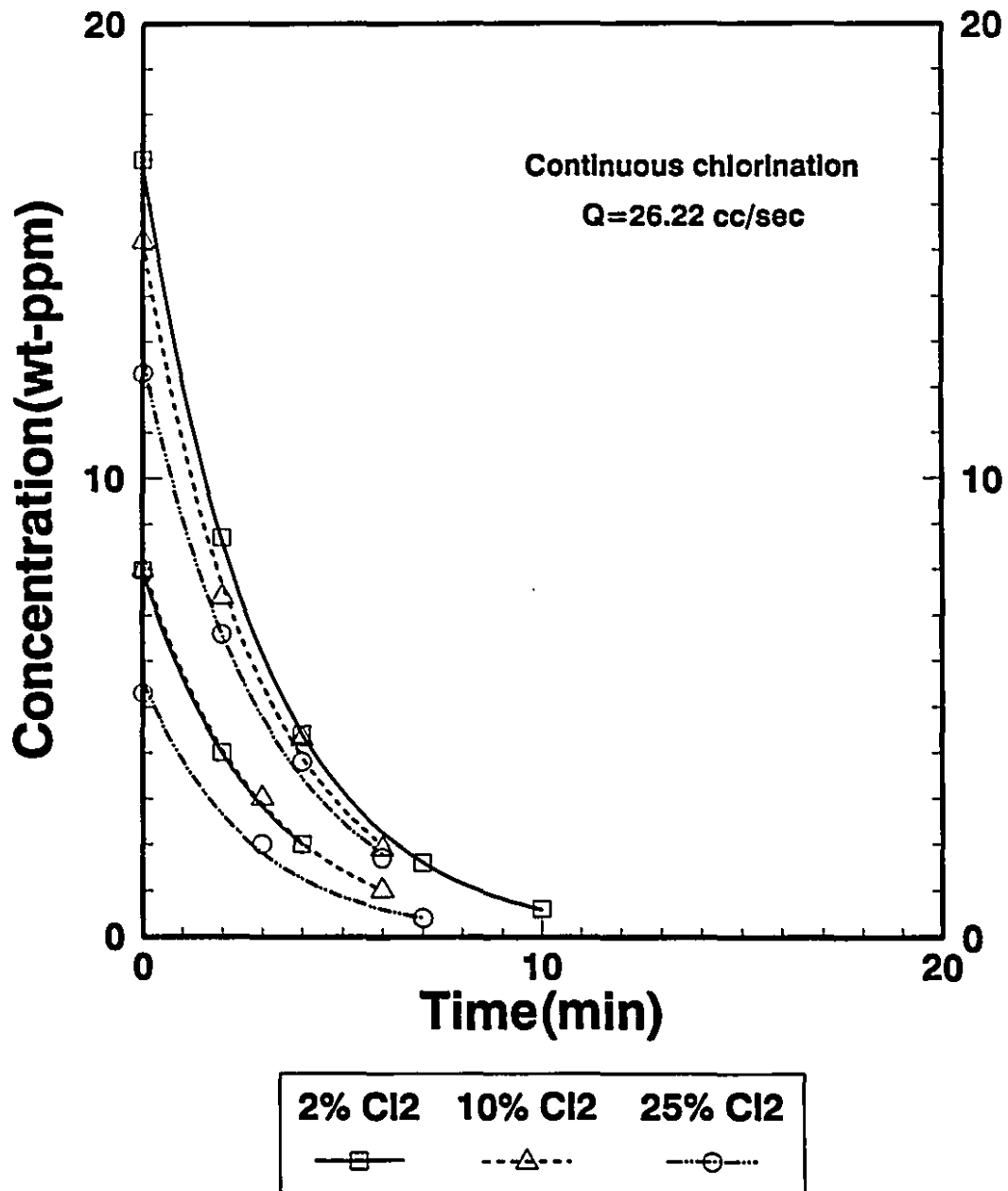


Figure 5.1 Change in sodium concentration in commercial purity aluminum melts versus bubbling time for various chlorine concentrations in Ar-Cl<sub>2</sub> gas mixture injected at a gas flow rate of 26.22 cc/sec (730 °C, 1 Atm.)

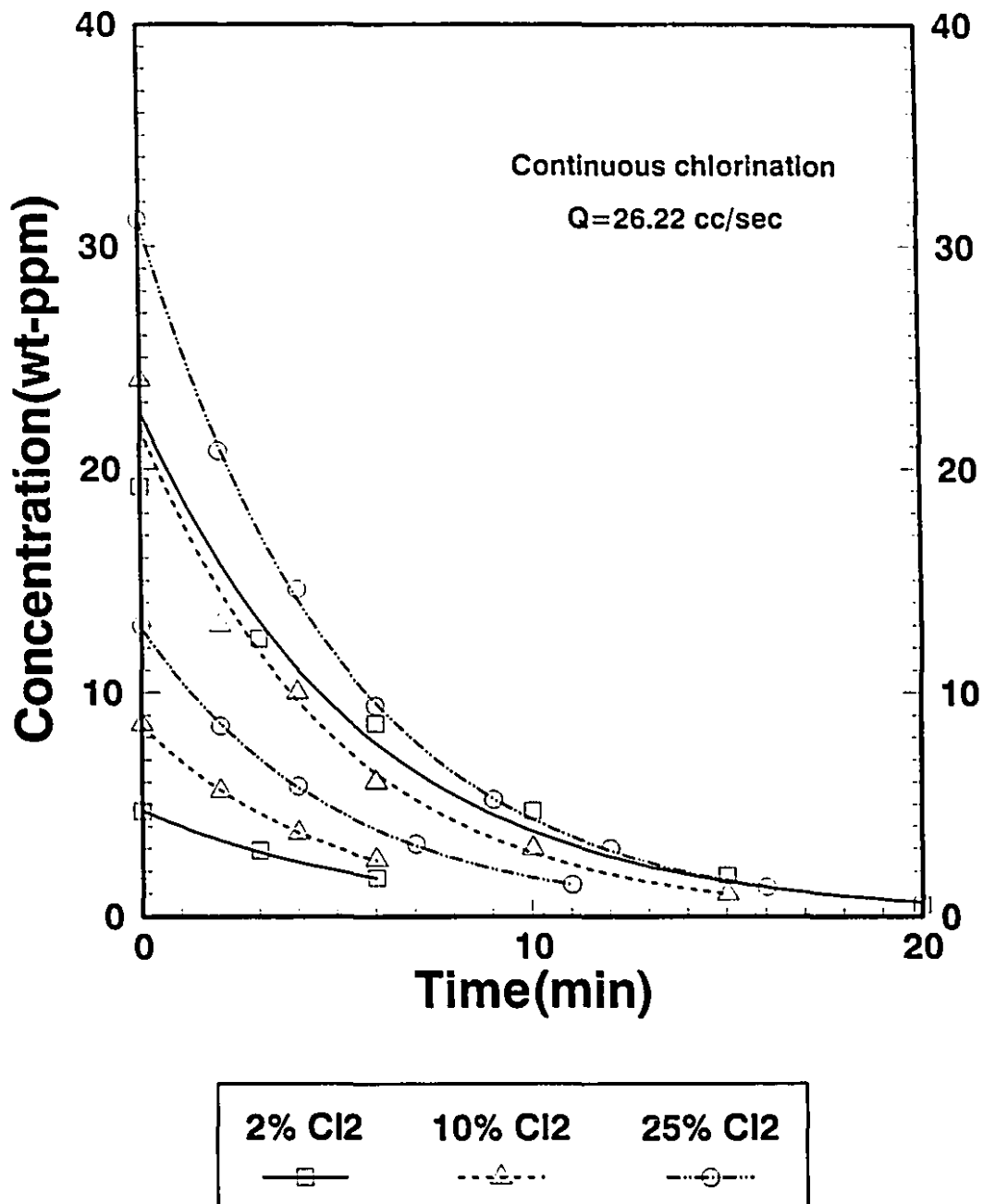


Figure 5.2 Change in sodium concentration in Al-1wt% Mg alloys versus bubbling time for various chlorine concentrations in Ar-Cl<sub>2</sub> gas mixture injected at a gas flow rate of 26.22 cc/sec (730 °C, 1 Atm.)

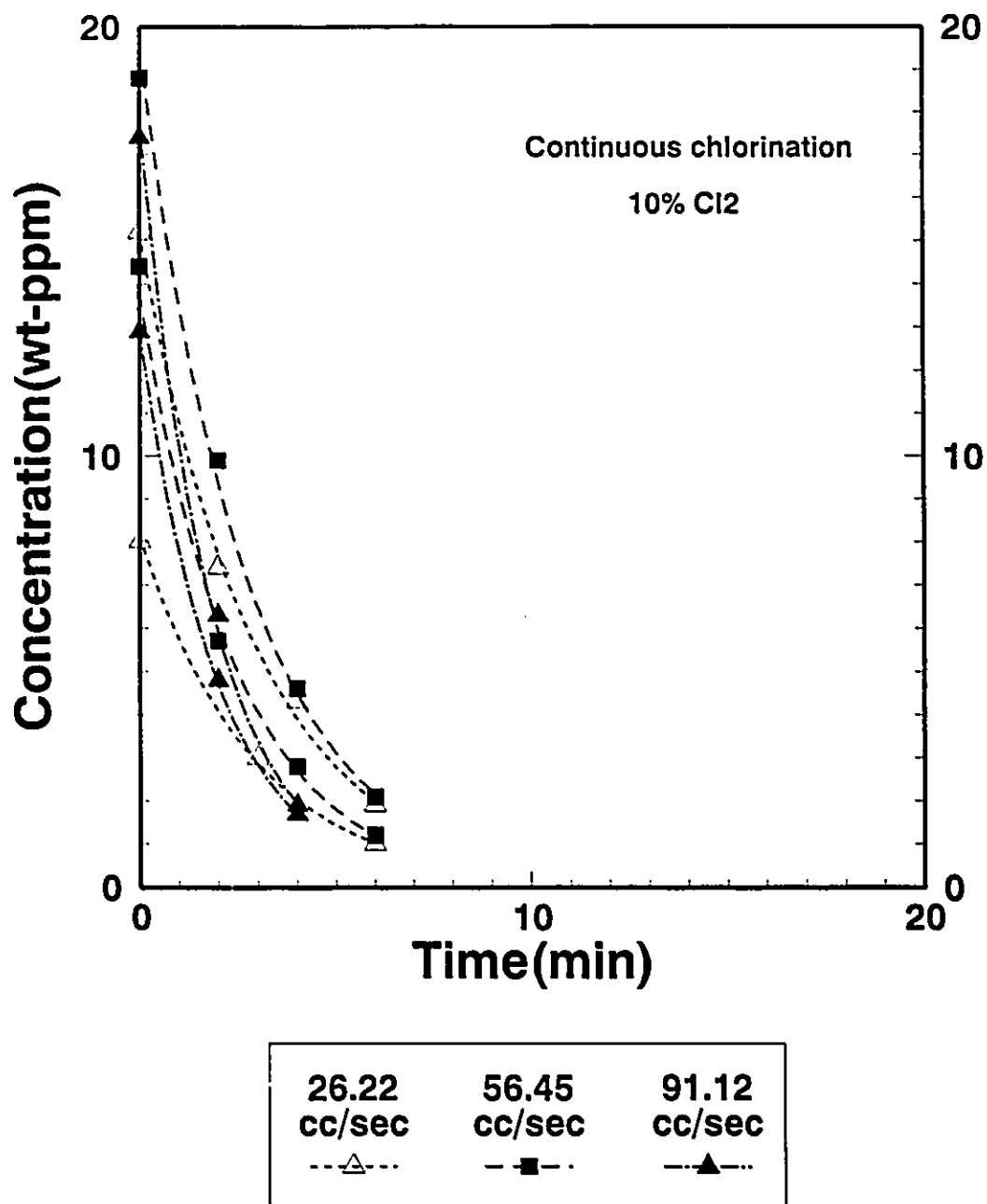


Figure 5.3 Change in sodium concentration in commercial purity aluminum melts versus bubbling time for various gas flow rates (730 °C, 1 Atm.); Vol% Cl<sub>2</sub> = 10

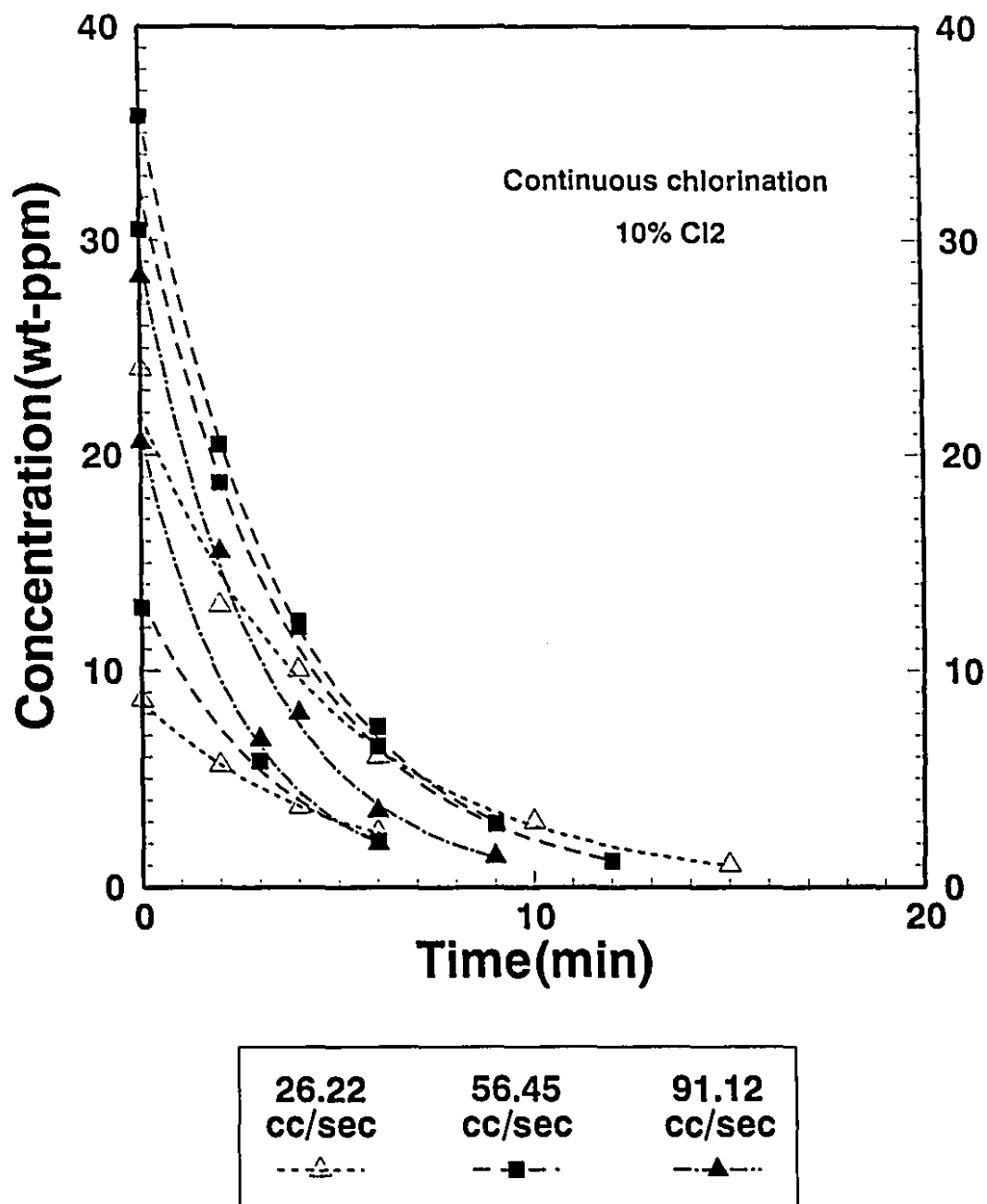


Figure 5.4 Change in sodium concentration in Al-1wt% Mg alloys versus bubbling time for various gas flow rates (730 °C, 1 Atm.); Vol% Cl<sub>2</sub>=10

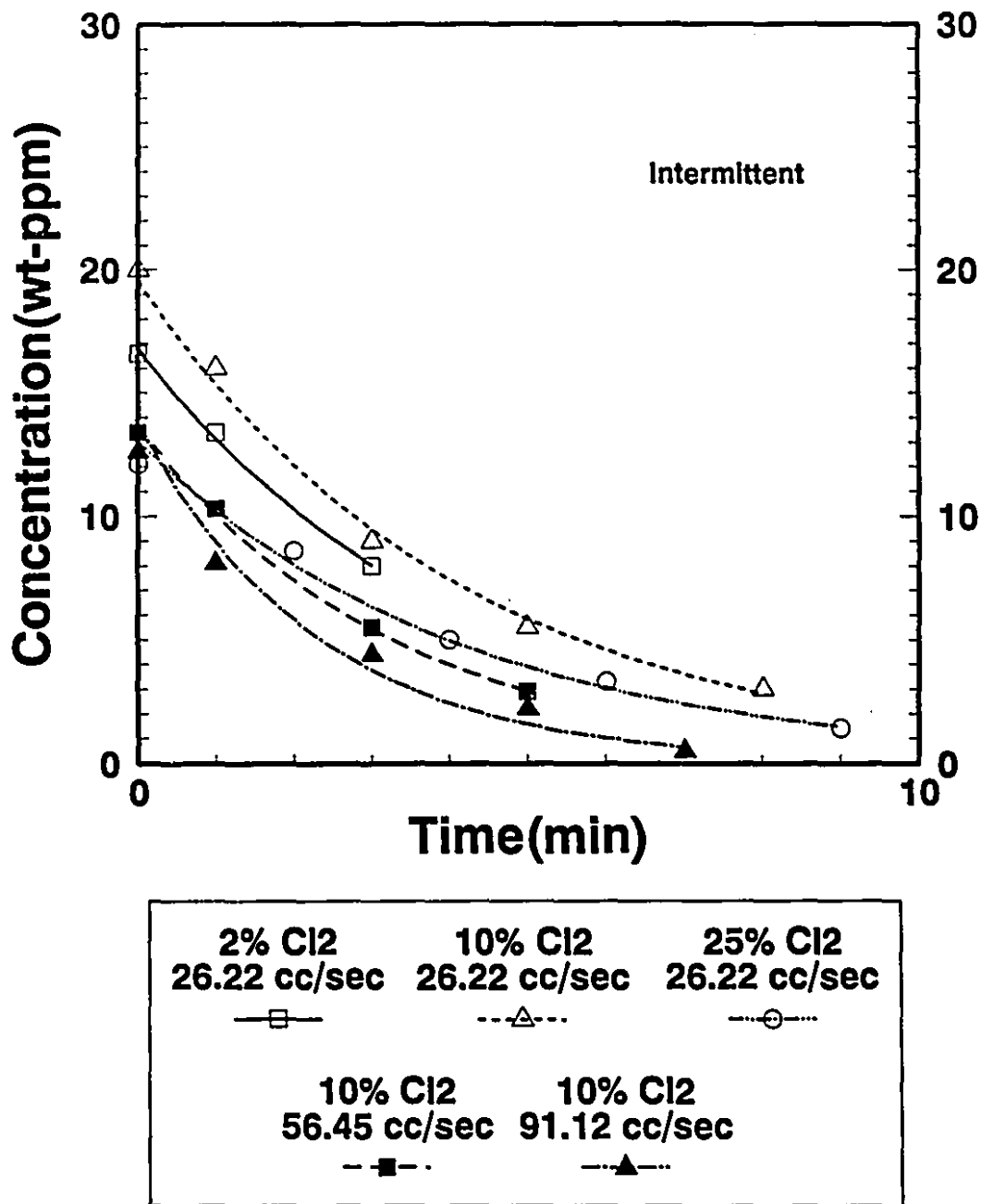


Figure 5.5 Change in sodium concentration in commercial purity aluminum melts versus time for various chlorine concentrations and gas flow rates (730 °C, 1 Atm.) during intermittent tests

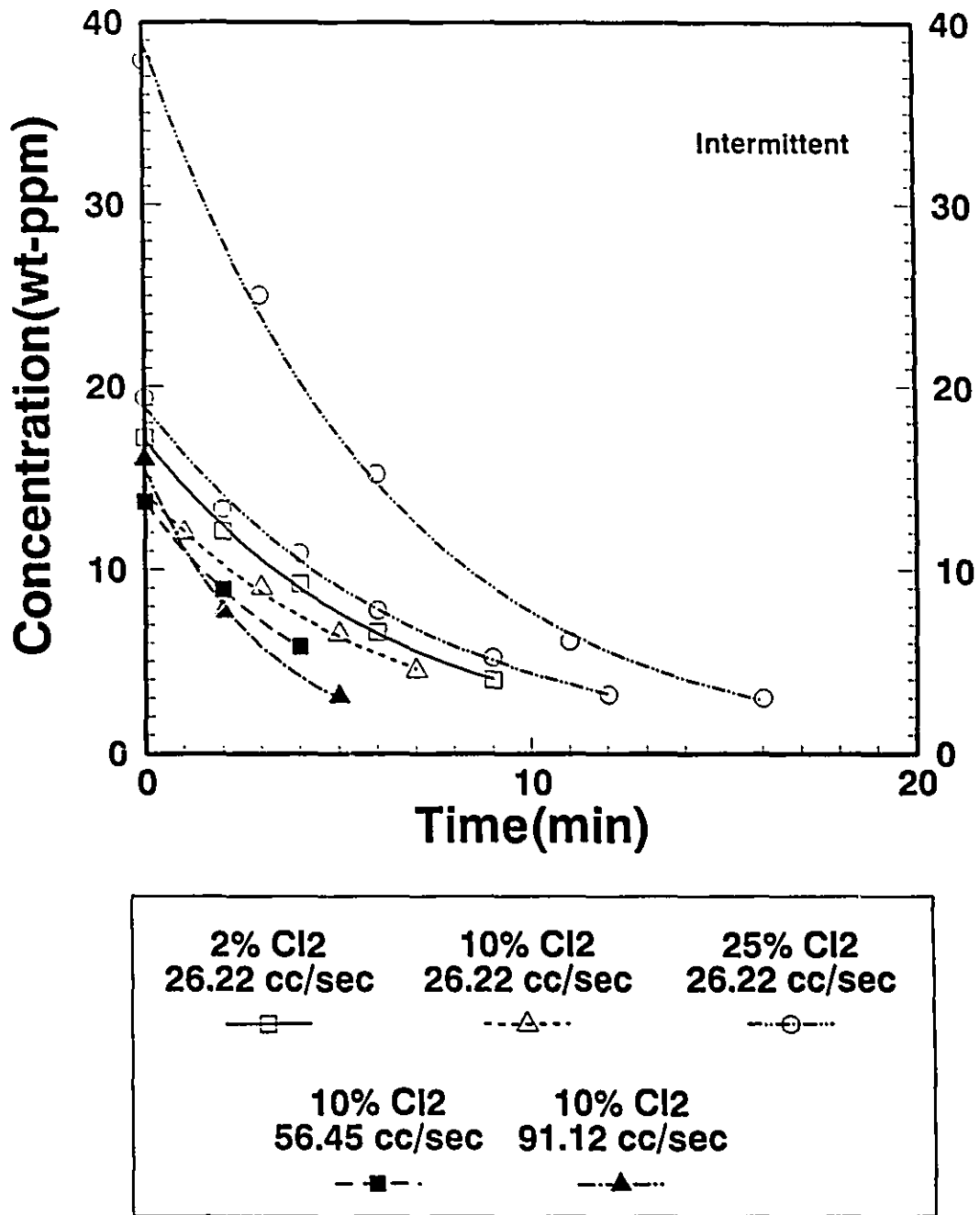


Figure 5.6 Change in sodium concentration in Al-1wt% Mg alloys versus time for various chlorine concentrations and gas flow rates(730 °C, 1 Atm.) during intermittent tests

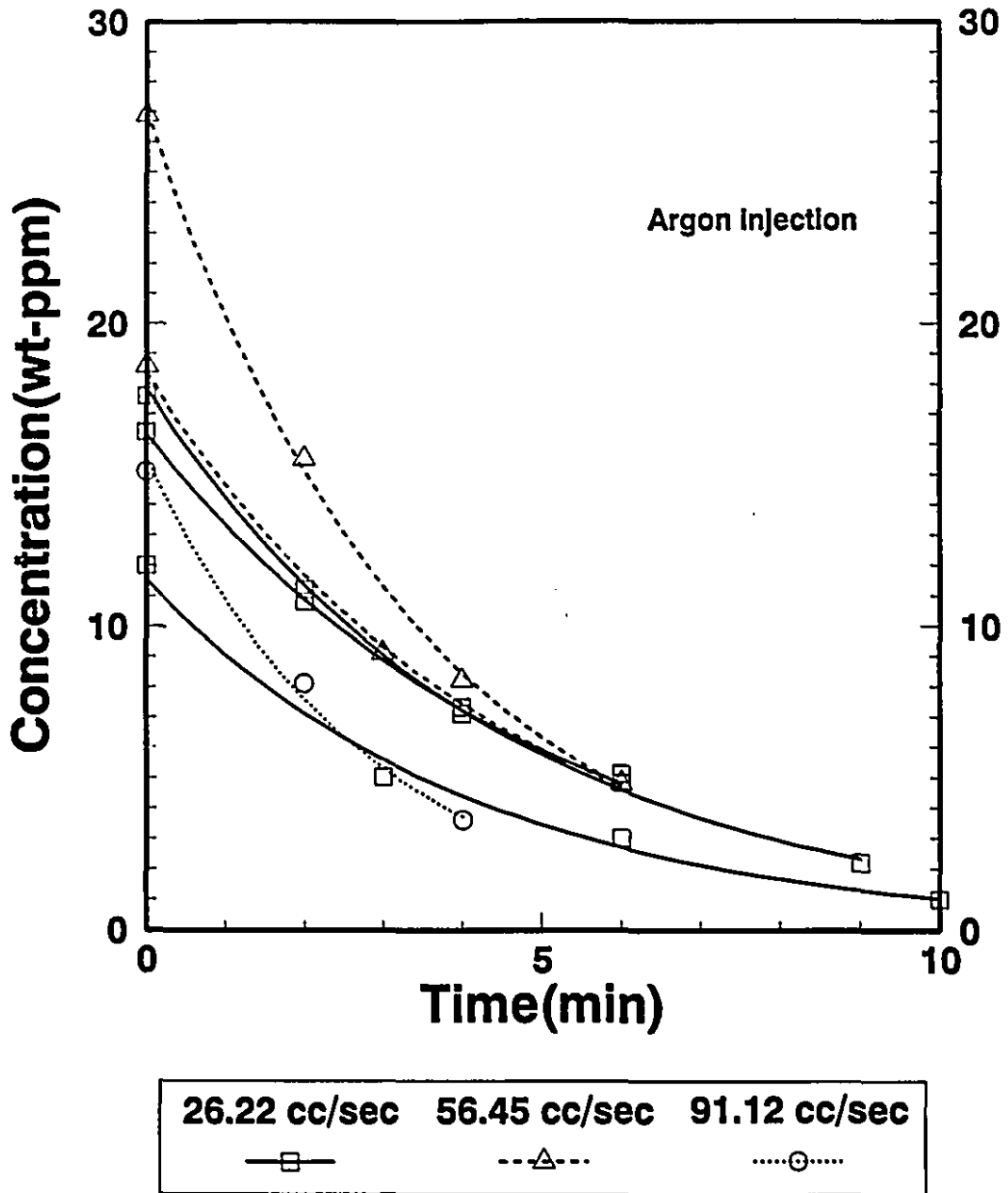
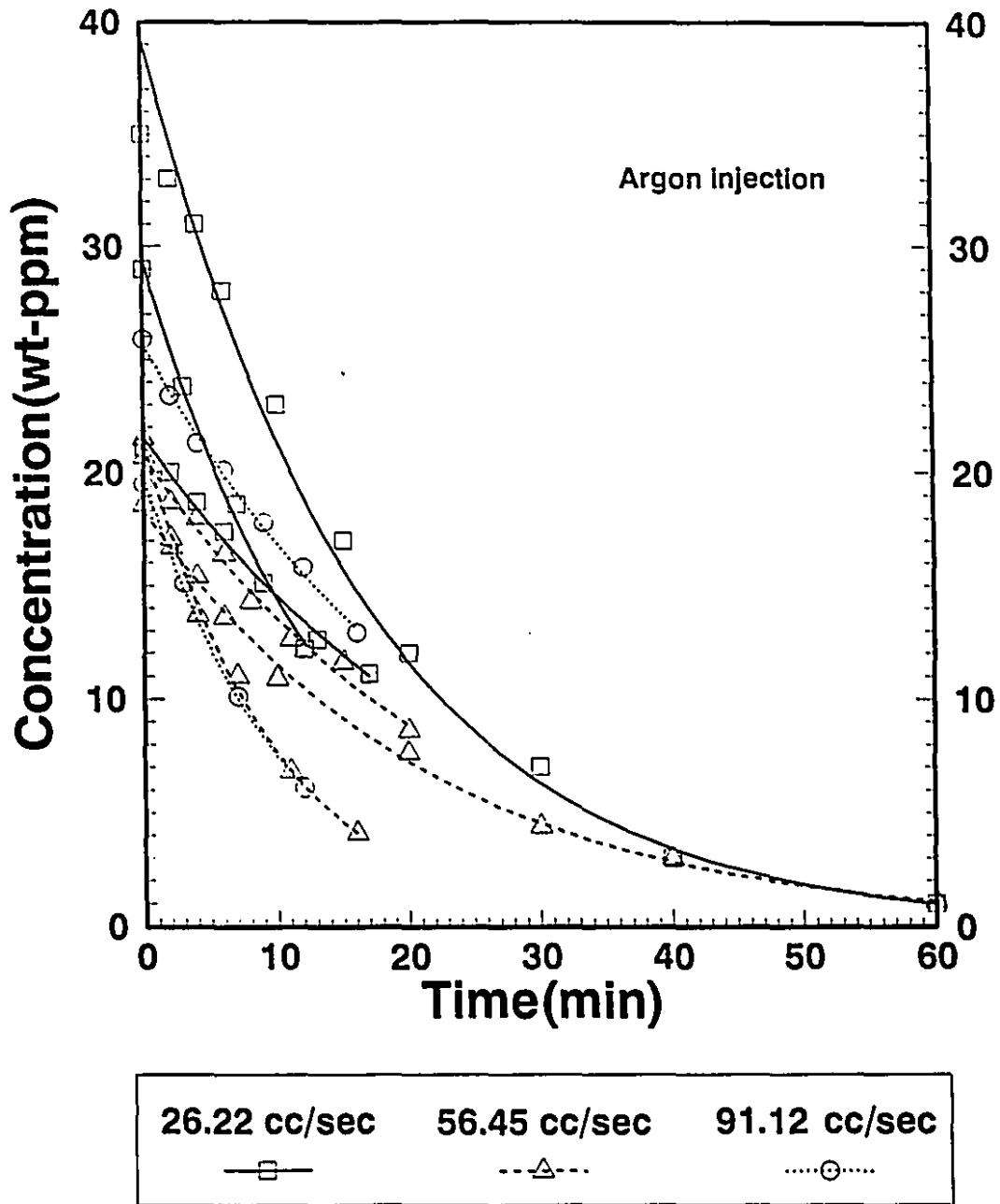


Figure 5.7 Change in sodium concentration in commercial purity aluminum melts versus time for various gas flow rates (730 °C, 1 Atm.) during argon injection tests



**Figure 5.8** Change in sodium concentration in Al-1wt% Mg alloys versus time for various gas flow rates(730 °C, 1 atm.) during argon injection tests

**Table 5.1** Rate constants for various chlorine concentrations in the gas bubbles;  $Q=26.22$  cc/sec(730 °C, 1 Atm.)

Cl <sub>2</sub> Concentration (Vol %)	Rate constant (1/sec)*10 <sup>6</sup>					
	Al			Al-1wt% Mg		
	R <sub>o</sub>	R <sub>intermittent</sub>	R <sub>Ar</sub>	R <sub>o</sub>	R <sub>intermittent</sub>	R <sub>Ar</sub>
2	5765 (1.0) 5600 (0.999) Av:5684	4083 (0.999)	3767 (0.997) 3383 (0.998) 4032 (0.996) Av:3727	2975 (0.990) 2823 (0.999) Av:2899	2667 (0.999)	1193 (0.997) 1017 (0.997) 650 (0.995) Av:953
10	5650 (0.997) 5775 (0.999) Av:5713	4017 (0.998)	3767 (0.997) 3383 (0.998) 4032 (0.996) Av:3727	3416 (0.999) 3416 (0.998) Av:3416	2676 (0.999)	1193 (0.997) 1017 (0.997) 650 (0.995) Av:953
25	5400 (0.996) 6167 (0.998) Av:5784	4017 (0.996)	3767 (0.997) 3383 (0.998) 4032 (0.996) Av:3727	3283 (0.999) 3356 (0.999) Av:3320	2700 (0.999) 2433 (0.998) Av:2567	1193 (0.997) 1017 (0.997) 650 (0.995) Av:953

Table 5.2 Rate constants for various gas flow rates(730 °C, 1 Atm.); Vol% Cl<sub>2</sub>=10

Q (cc/sec) @ 730 °C	Rate constant (1/sec)*10 <sup>6</sup>					
	Al			Al-1wt% Mg		
	R <sub>o</sub>	R <sub>intermittent</sub>	R <sub>Ar</sub>	R <sub>o</sub>	R <sub>intermittent</sub>	R <sub>Ar</sub>
26.22	5650 (0.997) 5775 (0.994) Av:5713	4017 (0.998)	3767 (0.997) 3383 (0.998) 4032 (0.996) Av:3727	3416 (0.999) 3416 (0.998) Av:3416	2676 (0.999)	1193 (0.997) 1017 (0.997) 650 (0.995) Av:953
56.45	6118 (0.998) 6817 (0.994) Av:6468	5133 (0.999)	3767 (0.997) 4833 (0.999) Av:4298	5045 (0.997) 4600 (0.999) 4517 (0.998) Av:4721	3580 (0.996)	1710 (0.998) 712 (0.993) 775 (0.999) Av:1066
91.12	8433 (0.999) 9217 (0.998) Av:8825	7225 (0.982)	5967 (0.997)	6467 (0.999) 5667 (0.998) Av:6067	4995 (0.995)	1626 (0.999) 700 (0.998) Av:1163

represented by a straight line at all. As seen from the tables, the data can be well represented by a straight line. Having presented the raw data in graphical and tabular form, the results can now be tested against the kinetic models described in Chapter 2.

V.B. Stoichiometrically Controlled Removal of Sodium:

Experimental results were first tested for the stoichiometry controlled removal of sodium from aluminum and aluminum-1wt% magnesium alloys.

With appropriate substitution for sodium, Eqn.(2.9) becomes:

$$\frac{E/F + \%Na_i^B}{E/F + \%Na_i^B} = e^{-Ft} \quad (5.3)$$

where E and F are defined by the following equations:

$$E = \frac{2 G_{Cl_2} 100 m_{Na}}{M} \quad (5.4)$$

$$F = \frac{G_{Ar} K f_{Na} 100 m_{Na}}{M P_{atm}} + \frac{k_s A_s \rho}{M} \quad (5.5)$$

In Eqn.(5.3), the reaction of sodium with the crucible wall was assumed to be negligibly small due to higher stability of alumina than that of any oxides of sodium.

In Eqn.(5.3), the term E represents the rate of removal of sodium through stoichiometric reaction with chlorine supplied in the gas bubbles.

The term F is composed of the rate of removal of sodium by evaporation into the bubbles(assuming saturation) and evaporation through the melt surface. In the calculations, the value of F was taken to be the rate constant,  $R_{Ar}$ , which was obtained from the argon injection tests.

Experimental results can now be tested against this model by plotting the left hand side against the right hand side of Eqn.(5.3). Such plots for commercial purity aluminum and aluminum-1wt% magnesium alloys are shown in Figures 5.9. through 5.12. In each graph, the diagonal line represents the theoretical line that the experimental points should

follow if the removal of sodium is stoichiometric.

As seen, experimental points lie below the theoretical line for both commercial purity aluminum and aluminum-1wt% magnesium alloy. As the chlorine concentration and gas flow rate was increased, the downward departure from the theoretical line increased.

These results show that the flux of sodium to the gas bubbles was insufficient to consume all the chlorine in the gas bubbles due to insufficient contact surface area between the bubbles and the melt and/or insufficient residence time of the bubbles in the melt.

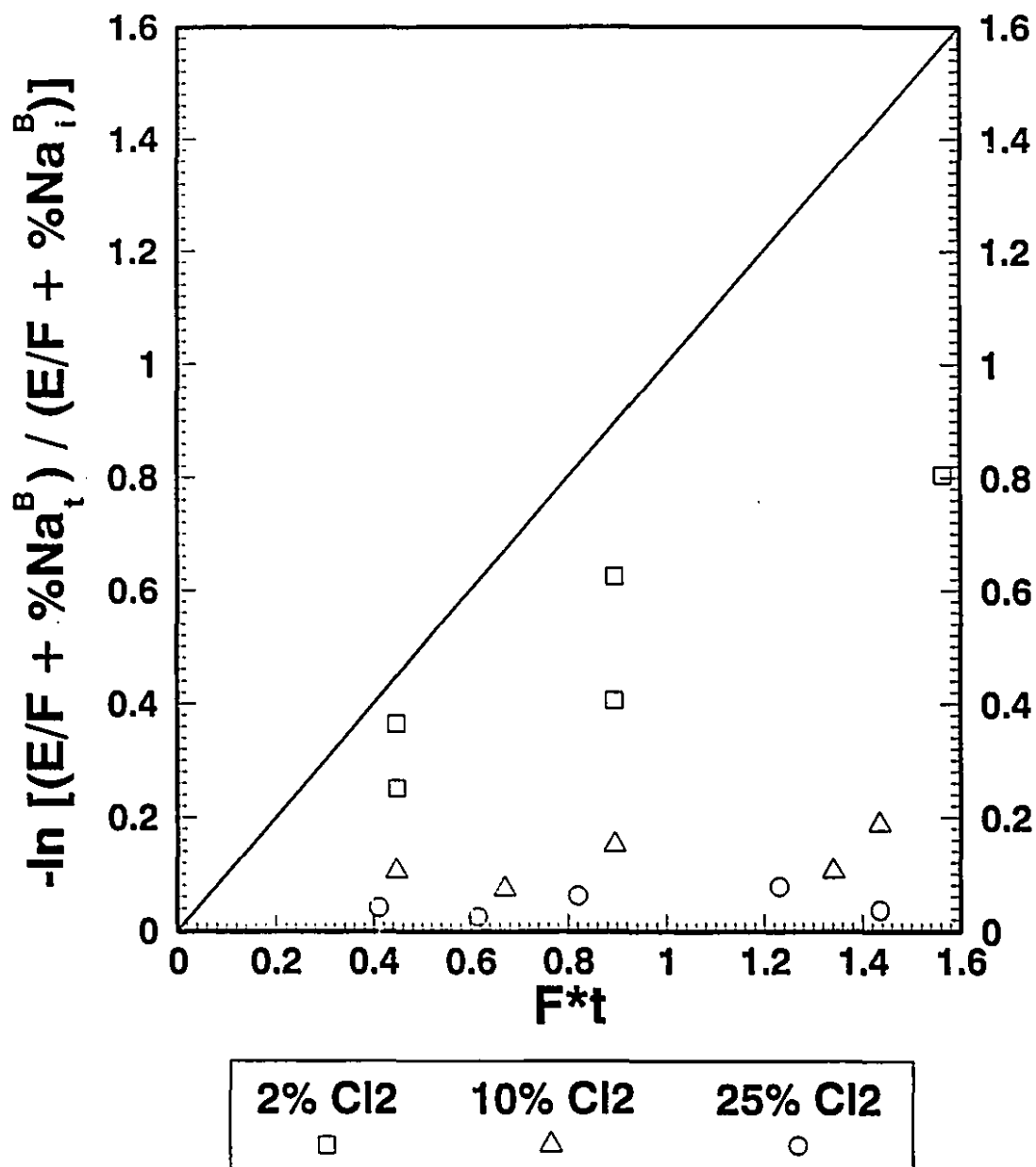


Figure 5.9 Comparison of stoichiometrically controlled removal of sodium versus experimental results for commercial purity aluminum melts;  $Q=26.22$  cc/sec(730 °C, 1 Atm.)

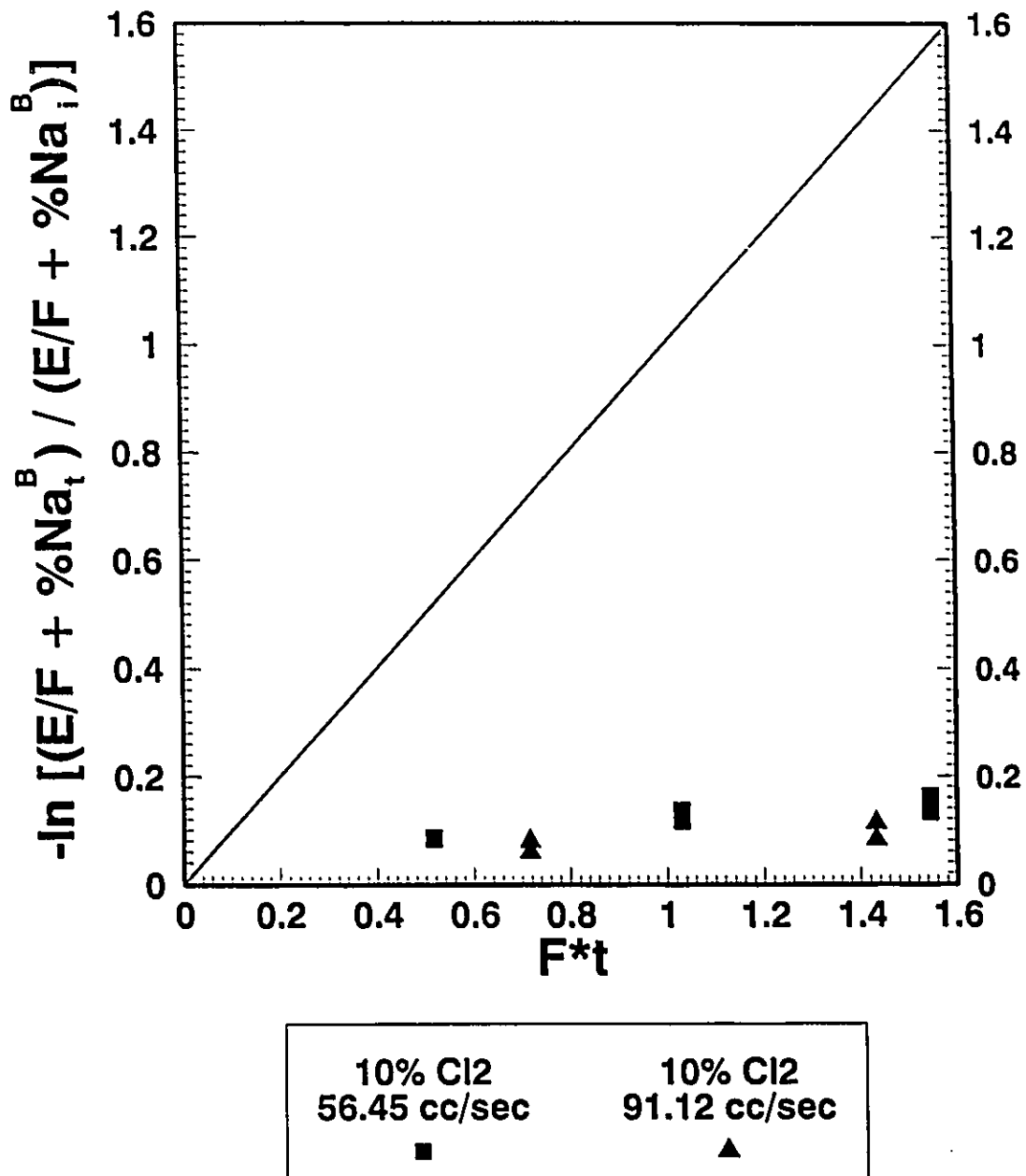


Figure 5.10 Comparison of stoichiometrically controlled removal of sodium versus experimental results for commercial purity aluminum melts at higher gas flow rates (730 °C, 1 Atm.); Vol% Cl<sub>2</sub>=10

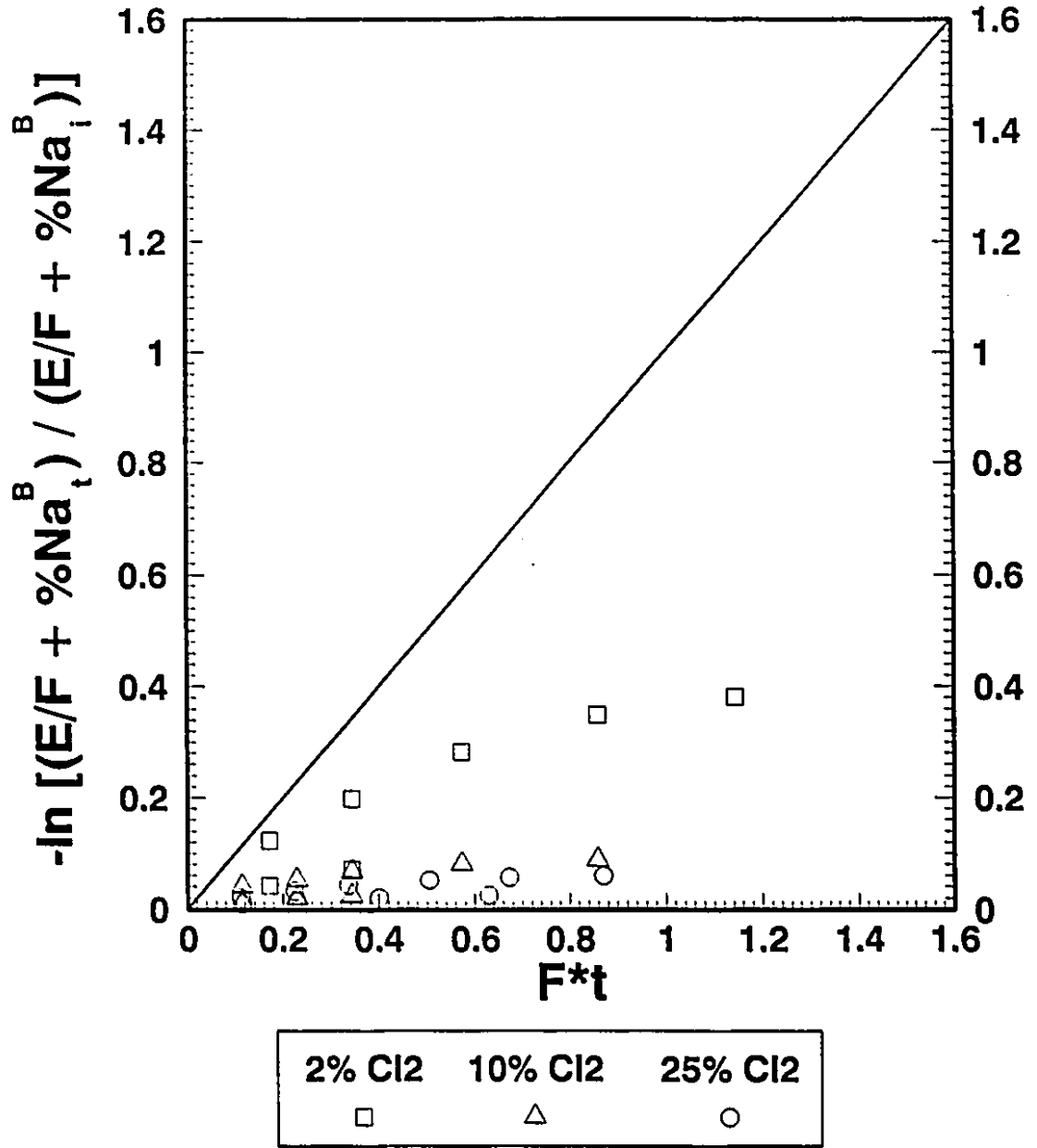


Figure 5.11 Comparison of stoichiometrically controlled removal of sodium versus experimental results for Al-1wt% Mg alloys; Q=26.22 cc/sec(730 °C, 1 Atm.)

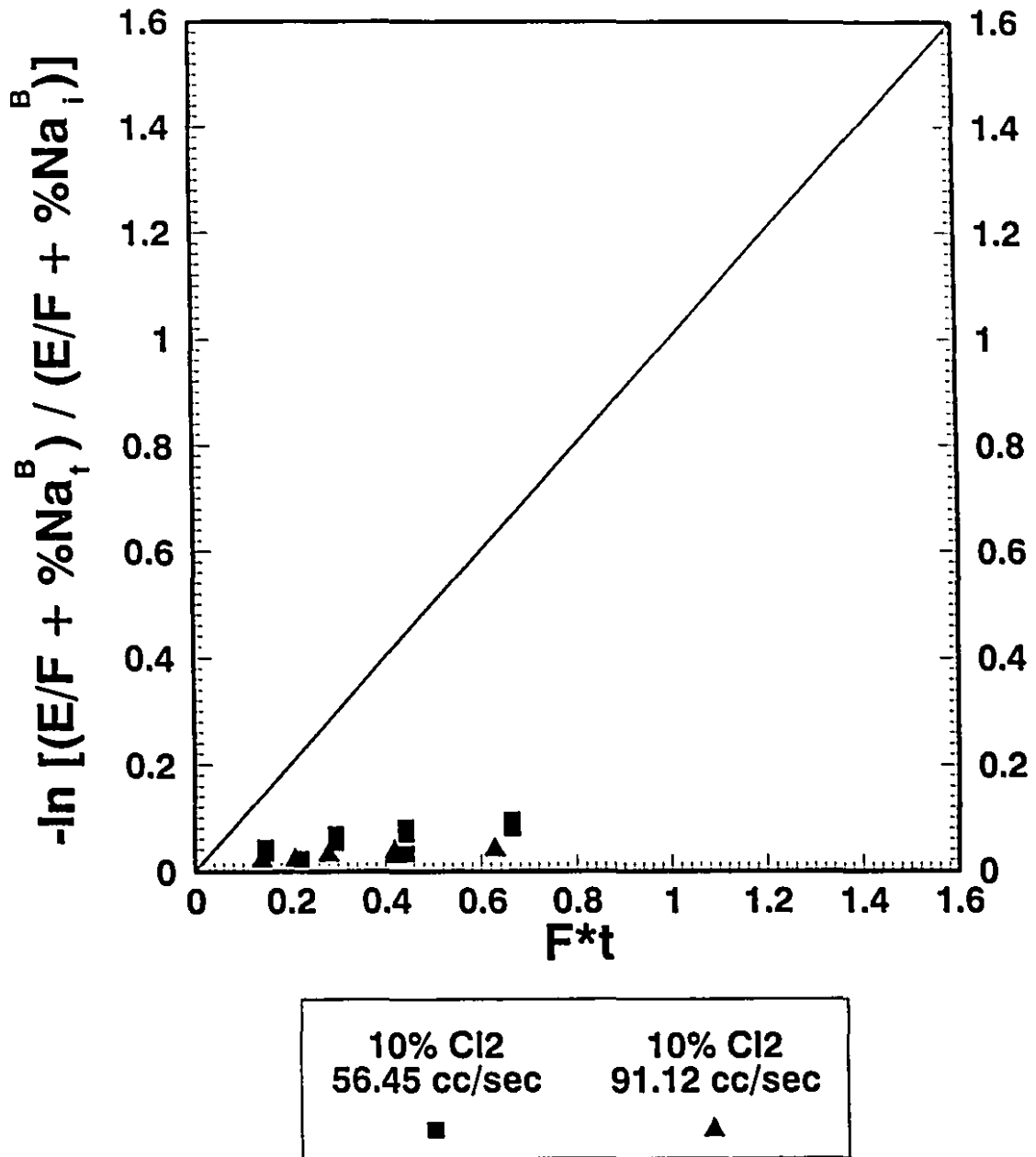


Figure 5.12 Comparison of stoichiometrically controlled removal of sodium versus experimental results for Al-1wt% Mg alloys at higher gas flow rates(730 °C, 1 Atm.); Vol% Cl<sub>2</sub>=10

V.C. Mass Transfer Controlled Removal of Sodium:

For a mass transfer controlled model Eqn.(2.13) applies. With proper substitution for sodium and assuming that the evaporation of sodium is negligibly small, Eqn.(2.13) becomes:

$$-\frac{M d\%Na^B}{100 m_{Na} dt} = \frac{k_b \rho A_b \%Na^B}{100 m_{Na}} + \frac{k_{irp} \rho A_{irp} \%Na^B}{100 m_{Na}} + \frac{k_s \rho A_s \%Na^B}{100 m_{Na}} \quad (5.6)$$

Upon integration of the above equation, one obtains:

$$-\ln \frac{\%Na_t^B}{\%Na_i^B} = \left( \frac{k_b \rho A_b}{M} + \frac{k_{irp} \rho A_{irp}}{M} + \frac{k_s \rho A_s}{M} \right) t \quad (5.7)$$

which can be summarised in the form:

$$-\ln \frac{\%Na_t^B}{\%Na_i^B} = R_o t \quad (5.8)$$

In Figures 5.13 through 5.16 experimental results for commercial purity aluminum and aluminum-1wt% magnesium alloys are presented by plotting the left hand side of Eqn.(5.8) against the right hand side. The line in each figure represents the theoretical line that has a slope of 1. In the figures, the slope of the straight line that would represent the experimental data and the correlation coefficient, C.C, are presented.

As seen for both melts, the agreement between the experimental data and the model is good.

Since the equation that was used to describe a mass transfer controlled removal of sodium was a first order differential equation and there was a good agreement between the experimental data and the model, sodium removal, under the present experimental conditions, was therefore shown to follow first order reaction kinetics.

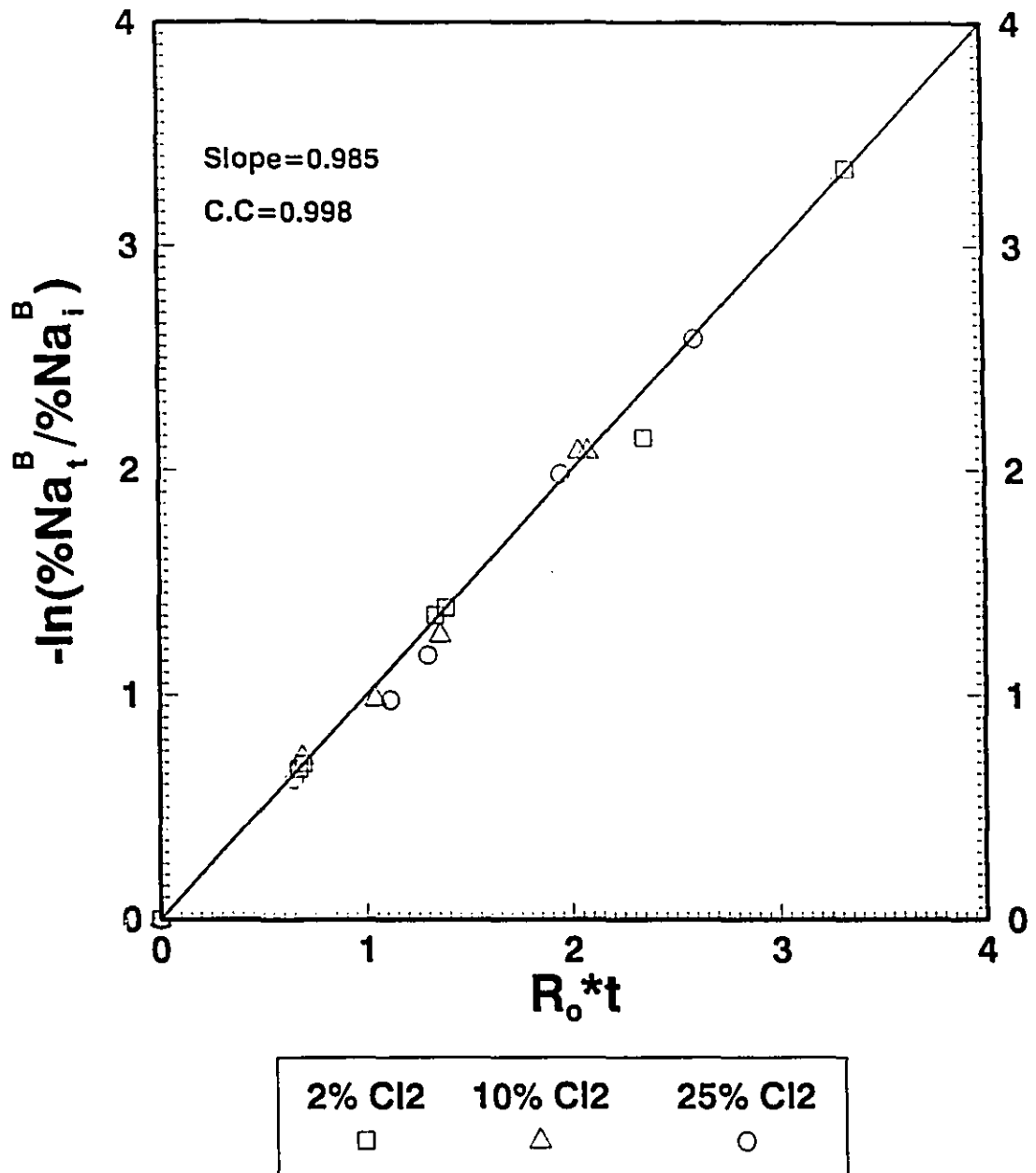
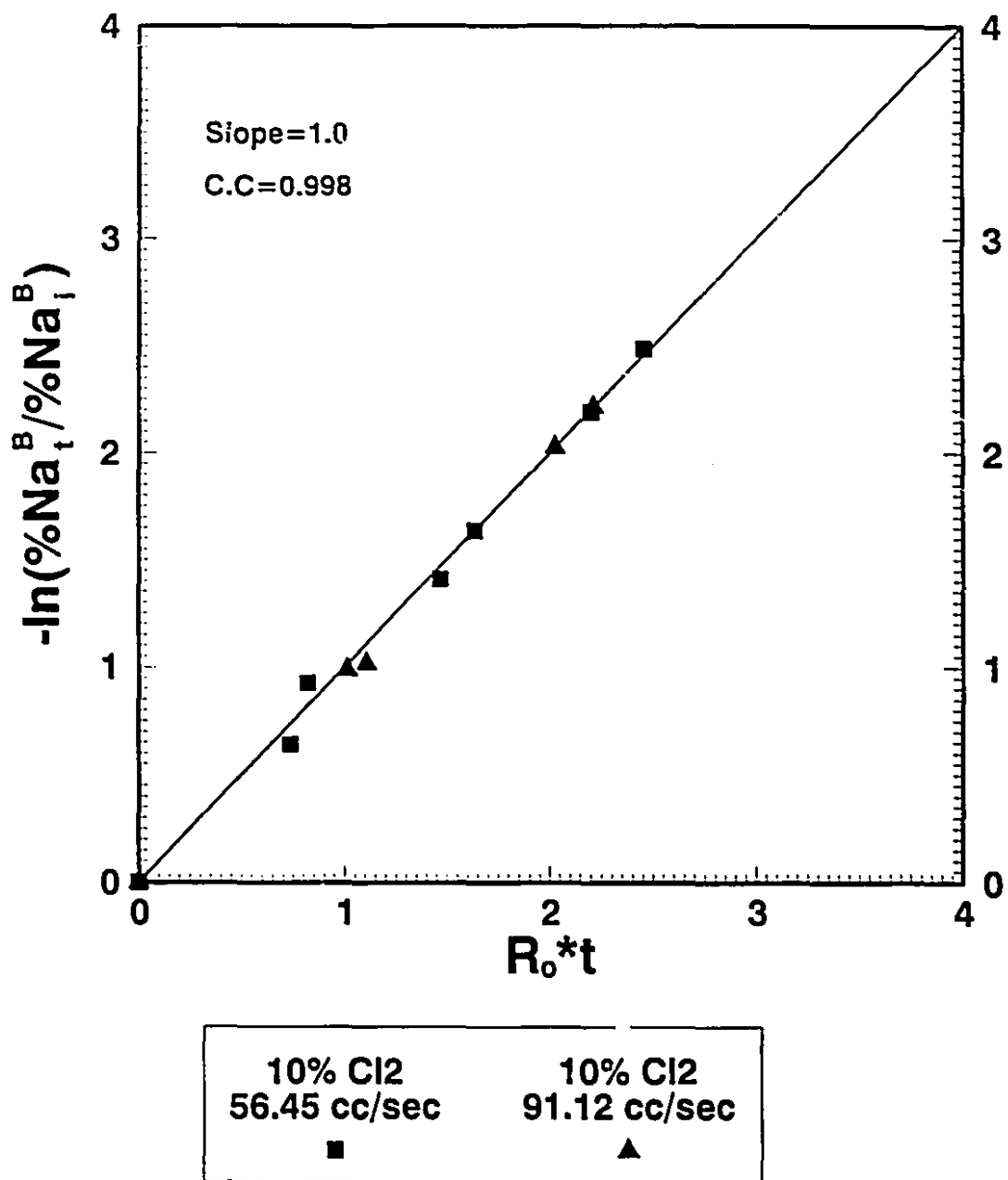


Figure 5.13 Comparison of mass transfer controlled removal of sodium versus experimental results for commercial purity aluminum melts;  $Q=26.22$  cc/sec(730 °C, 1 Atm.)



**Figure 5.14** Comparison of mass transfer controlled removal of sodium versus experimental results for commercial purity aluminum melts at higher gas flow rates (730 °C, 1 Atm.); Vol% Cl<sub>2</sub>=10

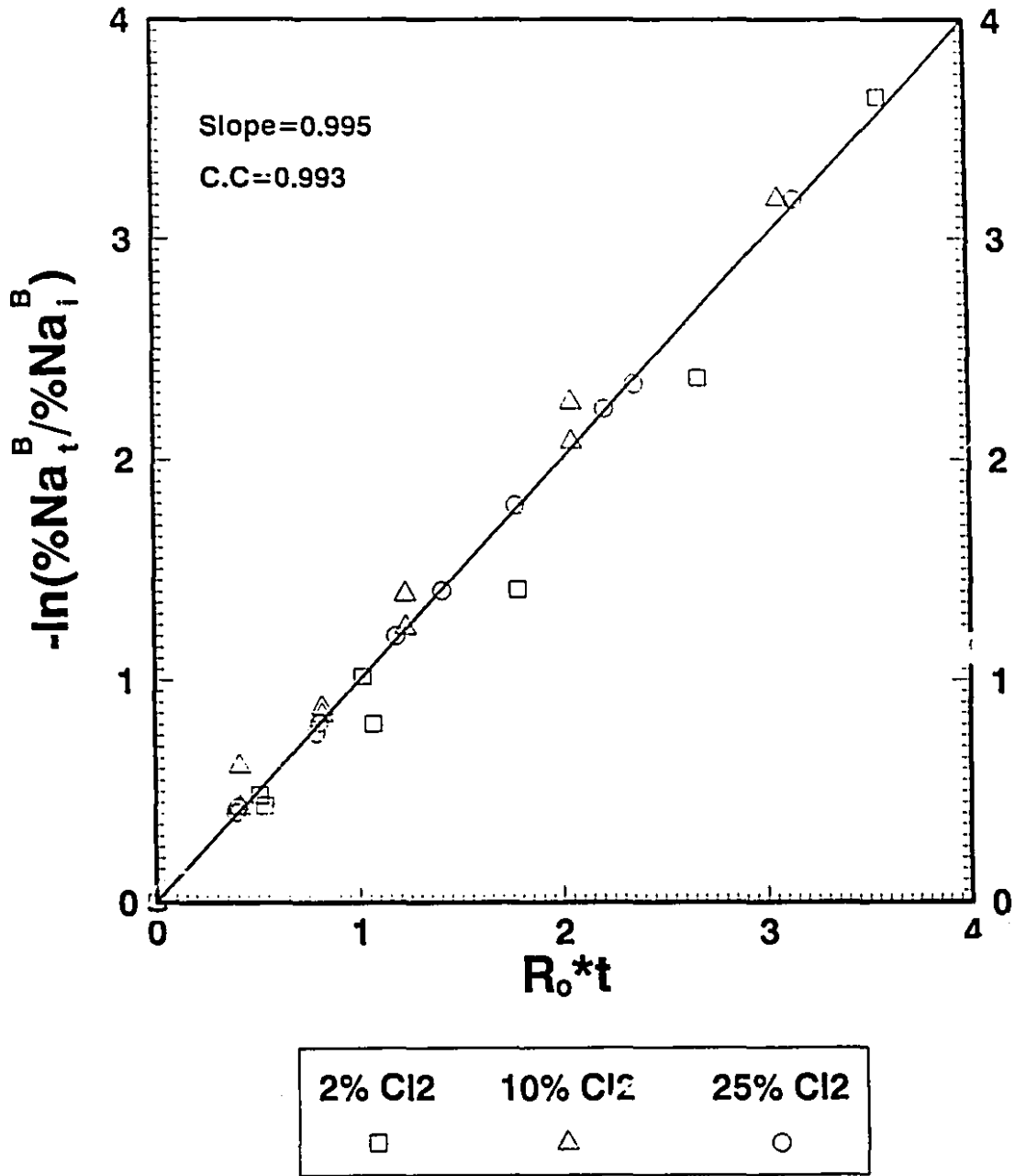


Figure 5.15 Comparison of mass transfer controlled removal of sodium versus experimental results for Al-1wt% Mg alloys; Q=26.22 cc/sec(730 °C, 1 Atm.)

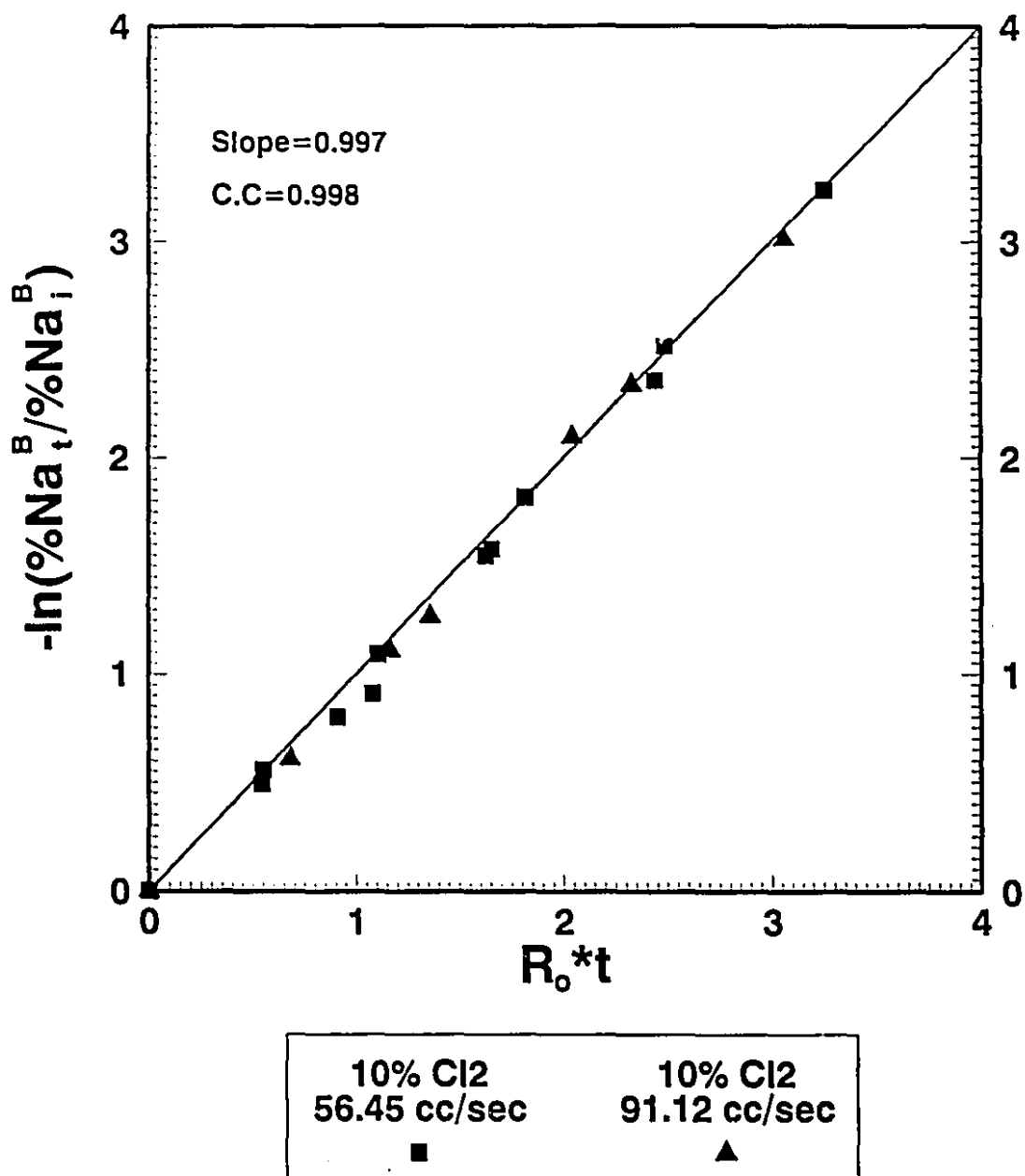


Figure 5.16 Comparison of mass transfer controlled removal of sodium versus experimental results for Al-1wt% Mg alloys at higher gas flow rates (730 °C, 1 Atm.); Vol% Cl<sub>2</sub>=10

V.D. Calculation of Rate Constants for Bubbles, for Evaporation through the Melt Surface and for the Intermediate Reaction Products that are Separated from the Bubbles:

Having demonstrated that the removal of sodium by chlorination from commercial purity aluminum and aluminum-1wt% magnesium alloys followed first order reaction kinetics under the present experimental conditions, the rate constants that made up the overall rate constant in Eqn.(5.7) can now be presented.

In Eqn.(5.7), the overall rate constant,  $R_o$ , contained rate constants for the removal of sodium by reaction on bubble surfaces,  $R_b$ , on *intermediate reaction products that are separated from the bubbles*,  $R_{irp}$ , and by evaporation of the sodium through the melt surface,  $R_s$ .

The overall rate constant can therefore be broken down into the following components:

$$R_o = R_b + R_{irp} + R_s \quad (5.9)$$

The overall rate constants were obtained from the results of the continuous chlorination tests.

$R_{irp}$ , the rate constant for the removal of sodium by reaction on the intermediate reaction products, was calculated from the following equation:

$$R_{irp} = R_{intermittent} - R_{Ar} \quad (5.10)$$

In the above equation,  $R_{Ar}$  was taken to be the average value at the corresponding gas flow rate.  $R_{intermittent}$  is the rate constant that was obtained from the results of intermittent chlorination tests.

$R_b$ , the rate constant for the bubbles, was calculated from:

$$R_b = R_o - R_{irp} - R_s \quad (5.11)$$

In the above equation,  $R_s$ , the rate constant for the evaporation of sodium through the melt surface was taken to be the rate constant  $R_{Ar}$ , which was obtained from the argon injection tests. This is equivalent to saying that the amount of sodium removed from the melt by evaporating into the gas bubbles is negligible. With this assumption Eqn.(5.11) becomes:

$$R_b = R_o - R_{ip} - R_{Ar} \quad (5.12)$$

Rate constants calculated via Eqns.(5.10) and (5.12) together with  $R_o$  and  $R_{Ar}$  are presented in Tables 5.3 and 5.4.

Table 5.3 Summary of the rate constants for various chlorine concentrations in the gas bubbles;  
 $Q=26.22$  cc/sec(730 °C, 1 Atm.)

Cl <sub>2</sub> Concentration (Vol%)	Rate constant (1/sec)*10 <sup>6</sup>							
	Al				Al-1wt% Mg			
	R <sub>o</sub>	R <sub>b</sub>	R <sub>irp</sub>	R <sub>Ar</sub>	R <sub>o</sub>	R <sub>b</sub>	R <sub>irp</sub>	R <sub>Ar</sub>
2	5765	1682		3767	2975	307		1193
	5600	1517	356	3383	2823	184	1714	1017
	Av:5683	Av:1599		4032 Av:3727	Av:2899	Av:246		650 Av:953
10	5650	1633		3767	3416	740		1193
	5775	1758	290	3383	3416	740	1723	1017
	Av:5713	Av:1695		4032 Av:3727	Av:3416	Av:740		650 Av:953
25	5400	1383		3767	3283	717	1747	1193
	6167	2149	290	3383	3356	790	1480	1017
	Av:5784	Av:1766		4032 Av:3727	Av:3320	Av:753	Av:1614	650 Av:953

**Table 5.4** Summary of the rate constants for various gas flow rates(730 °C, 1 Atm.); Vol% Cl<sub>2</sub>=10

Q (cc/sec) @ 730 °C	Rate constant (1/sec)*10 <sup>6</sup>							
	Al				Al-1wt% Mg			
	R <sub>o</sub>	R <sub>b</sub>	R <sub>irp</sub>	R <sub>Ar</sub>	R <sub>o</sub>	R <sub>b</sub>	R <sub>irp</sub>	R <sub>Ar</sub>
26.22	5650	1633		3767	3416	740		1193
	5775	1758	290	3383	3416	740	1723	1017
	Av:5713	Av:1695		4032 Av:3727	Av:3416	Av:740		650 Av:953
56.45	6118	983		3767	5045	1465		1710
	6817	1682	835	4833	4600	1020	2514	712
	Av:6468	Av:1333		Av:4298	4517 Av:4721	937 Av:1141		775 Av:1066
91.12	8433	1208			6467	1472		1626
	9217	1992	1258	5967	5667	672	3832	700
	Av:8825	Av:1600			Av:6067	Av:1072		Av:1163

V.D.1. Effect of Chlorine Concentration:

Table 5.3 gives the rate constants for various chlorine concentrations for commercial purity aluminum and aluminum-1wt% magnesium alloys respectively.

In the case of commercial purity aluminum, within the range of the chlorine concentrations considered, the overall rate constants,  $R_o$ , did not change more than 10% of their mean. The maximum contribution to the removal of sodium was from the evaporation through the melt surface which was calculated to be 65%. The contribution of the bubbles to the removal of sodium was calculated to be 30%, whereas the contribution of the intermediate reaction products that are separated from the bubbles was calculated to be around 5%.

In the case of the aluminum-1wt% magnesium alloys, at the lowest chlorine concentration, the overall rate constant  $R_o$  was about 10% lower than that for higher chlorine concentrations. This result is similar to that obtained for calcium even though the magnitude of the change is smaller for the sodium removal. The maximum contribution to the removal of sodium from the magnesium containing alloy came from the intermediate reaction products that are separated from the bubbles. Taking an average value for  $R_o$  and  $R_{irp}$  over the range of the chlorine concentrations, this contribution was calculated to be 52%. The contribution of the evaporation of sodium through the melt surface to the total removal rate was calculated to be 30%. The contribution of the bubbles, except for the lowest chlorine concentration, was about 22%. At the lowest chlorine concentration this contribution was calculated to be about 8%.

It is important to note that the rate of removal of sodium was always higher from commercial purity aluminum than that from the magnesium containing alloy. This was due to much higher rates of evaporation of sodium through the melt surface. The rate of evaporation of sodium through evaporation from commercial purity aluminum was calculated to be about 4 times higher than that from the magnesium containing alloys.

V.D.2. Effect of Gas Flow Rate:

Table 5.4 gives the rate constants for various gas flow rates for commercial purity aluminum and aluminum-1wt% magnesium alloys respectively. At each gas flow rate, the

percent concentration of the chlorine in the gas bubbles was 10%.

In the case of commercial purity aluminum, the contribution of the evaporation of sodium through the melt surface to the total removal rate stayed around 63% regardless of the gas flow rate. The contribution of the bubbles to the rate of removal of sodium decreased from 30 to 20% with an increase in the gas flow rate from 26.22 to 91.12 cc/sec. The contribution of the intermediate reaction products that are separated from the bubbles increased from 5 to about 13% with increase in the gas flow rate from 26.22 to 56.45 cc/sec and stayed practically the same with further increase in the gas flow rate.

In the case of the magnesium containing alloys, the contribution of the intermediate reaction products to the removal rate of sodium increased from 50 to 63% with increase in the gas flow rate from 26.22 to 91.12 cc/sec. The contribution of the bubbles stayed around 21% whereas the contribution by evaporation through the melt surface decreased from 28 to 20%.

In both cases, the overall rate constants increased with increase in the gas flow rate. This points to the importance of increased melt circulation to bring the impurity containing melt to the reaction zones (i.e bubbles, intermediate reaction products that are separated from the bubbles, melt surface).

On average, the removal rate of sodium by chlorination was 1.5 times higher than it was from the magnesium containing alloys.

V.E. Calculation of the Melt Phase Mass Transfer Coefficients for Bubbles:

Experimental melt phase mass transfer coefficients for the bubbles were first calculated from the rate constant expression for bubbles,  $R_b$ , according to:

$$k_b = \frac{M R_b}{A_b \rho} \tag{5.13}$$

In the above equation, the total surface area of the bubbles,  $A_b$ , at any instant in the bath was calculated from:

$$A_b = \frac{6 Q h}{U d_e} \tag{5.14}$$

where  $Q$  is the gas flow rate,  $h$  is the height of the melt,  $U$  is the terminal rising velocity of the bubbles and  $d_c$  is the diameter of the volume equivalent sphere.

The terminal rising velocity of the bubbles was calculated from the following equation obtained by Andreini et al[65]:

$$U = 29.69 d_c^{0.316} \quad (cm/sec) \quad (5.15)$$

Table 5.5 gives the melt phase mass transfer coefficients for the bubbles,  $k_b$ , calculated according to Eqn.(5.13) for various chlorine concentrations. In the case of commercial purity aluminum, the calculated values of  $k_b$  were higher than those for the magnesium containing alloys(7 times higher at the lowest chlorine concentration and 2.5 times higher at higher chlorine concentrations). In the case of commercial purity aluminum, the values of  $k_b$  were practically the same regardless of chlorine concentration. For magnesium containing alloys, however, the average value of the mass transfer coefficient increased sharply from  $150 \times 10^{-6}$  to  $392 \times 10^{-6}$  m/sec following an increase in  $Cl_2$  concentration from 2 to 10%. This trend was similar to that observed for calcium removal from the magnesium containing alloys.

Table 5.6 gives the melt phase mass transfer coefficients for the bubbles for various gas flow rates. In the case of the magnesium containing alloy, over the range of the gas flow rates investigated, the values of  $k_b$  did not change by more than 25% of their mean. In the case of the commercial purity aluminum however, the mass transfer coefficients dropped sharply by about 60% with an increase in the gas flow rate from 26.22 to 56.45 cc/sec. Except for the lowest gas flow rate, the values of the mass transfer coefficients were similar in both alloys at the same gas flow rates.

Figure 5.17 shows the liquid phase mass transfer coefficients as a function of the bubble diameter  $d_c$ . The mass transfer coefficients encircled in the graph were calculated for commercial purity aluminum at the lowest gas flow rate. To the best of the author's knowledge, the rate of increase of mass transfer coefficients with decrease in bubble diameter, in the case of the commercial purity aluminum, is too high to conform to any mass transfer correlation for bubbles[74].

**Table 5.5** Experimental melt phase mass transfer coefficients for bubbles for various chlorine concentrations;  $Q=26.22$  cc/sec (730 °C, 1 Atm.)

Cl <sub>2</sub> Concentration (Vol%)	$k_b$ (m/sec)*10 <sup>6</sup>	
	Al	Al-1wt% Mg
2	1070	191
	934	108
	Av:1002	Av:150
10	990	386
	1020	397
	Av:1005	Av:392
25	914	410
	1330	465
	Av:1122	Av:438

**Table 5.6** Experimental melt phase mass transfer coefficients for bubbles for various gas flow rates(730 °C, 1 Atm.); Vol% Cl<sub>2</sub>=10

Q (cc/sec) @ 730 °C	k <sub>b</sub> (m/sec)*10 <sup>6</sup>	
	Al	Al-1wt% Mg
26.22	990	386
	1020	397
	Av:1005	Av:392
56.45	285	514
	489	368
	Av:387	346
		Av:409
91.12	332	385
	520	172
	Av:426	Av:279

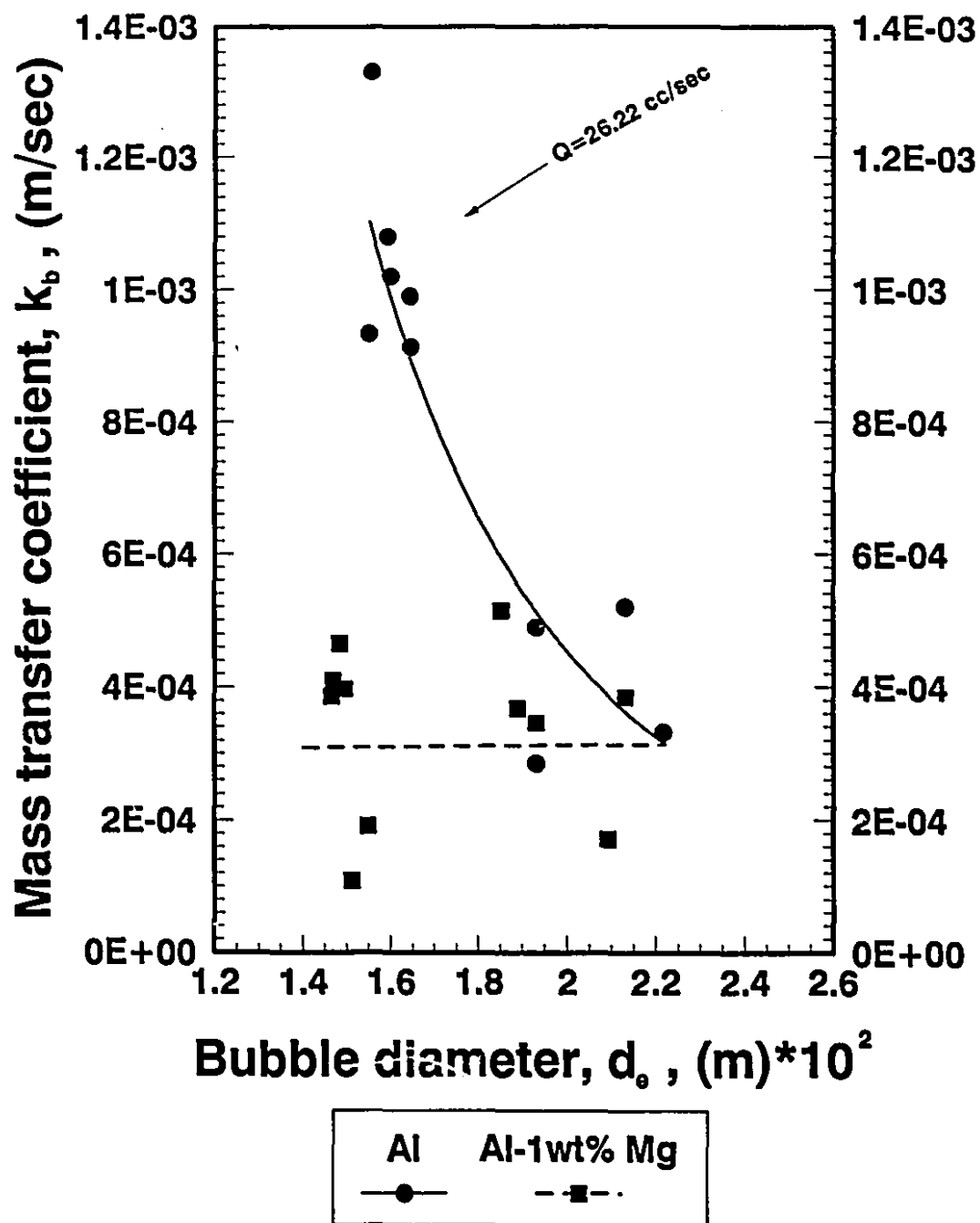


Figure 5.17 Melt phase mass transfer coefficients for bubbles as a function of equivalent bubble diameter

Following the procedure described in Chapter 4., rate constants for bubbles,  $R_b$ , were plotted against bubble surface area to melt volume ratio,  $A/V$ , to calculate mass transfer coefficients from the resulting slopes. The results are shown in Figure 5.13. The linear regression analysis gave a slope of  $-90 \times 10^{-6}$  m/sec with a correlation coefficient of 0.269 for commercial purity aluminum. In the case of the magnesium containing alloy, the linear regression analysis gave a slope of  $300 \times 10^{-6}$  m/sec with a correlation coefficient of 0.772.

The negative value of mass transfer coefficient for bubbles in commercial purity aluminum is meaningless in the light of the mass transfer coefficients already obtained through Eqn.(5.13) and should be discarded. The value of mass transfer coefficient obtained for bubbles in the magnesium containing alloys, however, can be taken to represent well the mass transfer coefficients calculated through Eqn.(5.13). Figure 5.18, unfortunately, does not allow a comparison to be made between the mass transfer coefficients obtained in commercial purity aluminum and that in the magnesium containing alloys.

According to Higbie's penetration theory[66], mass transfer coefficients are proportional to the square root of the diffusion coefficients. According to the results of Leak and Swalin[71], the diffusion coefficient of sodium should be similar in both commercial purity aluminum and aluminum magnesium alloys. Leak and Swalin showed that the closer the relative valance of the solute to 0 with respect to solvent, the closer the solute diffusivity of the solute to the self diffusivity of the solvent will be. Based on their results, the diffusion coefficient of sodium in both commercial purity aluminum and aluminum-1wt% magnesium alloys should be close to the diffusion coefficient of magnesium in liquid aluminum. The relative valance of sodium and magnesium with respect to aluminum is -2 and -1 respectively. The diffusion coefficient of magnesium in liquid aluminum was calculated to be  $6.7 \times 10^{-9}$  m<sup>2</sup>/sec by taking the average of the values of the experimental results of three different investigators(Appendix D). This value is almost identical to the value of self-diffusion coefficient of aluminum that was obtained from the theoretical calculations of Protopapas et al.(Appendix D). Therefore, the diffusion coefficient of sodium in aluminum should be close to that of sodium in the magnesium containing alloys. Any effect of a small difference between the diffusivities on the mass transfer coefficients will be further reduced by the square root dependency of mass transfer coefficient on the

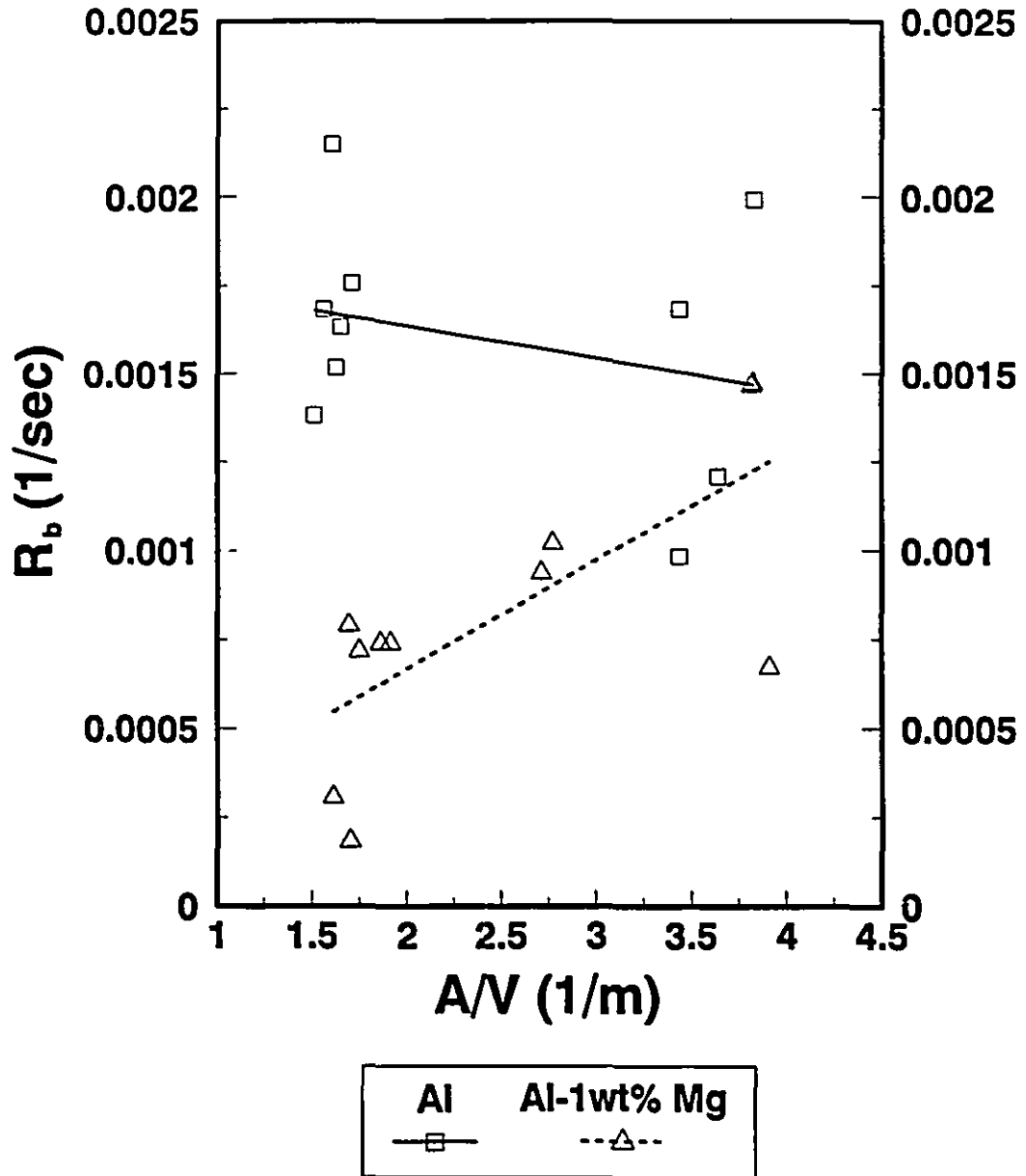


Figure 5.18 Graphical determination of melt phase mass transfer coefficients for bubbles

diffusivities.

Since the removal of sodium is controlled by the mass transfer of sodium in the melt phase, mass transfer coefficients for bubbles in commercial purity aluminum should be close to the ones for the magnesium containing alloys. The fact that the mass transfer coefficients calculated through Eqn.(5.13) for the intermediate and highest gas flow rates are similar in magnitude supports this hypothesis. The mass transfer coefficients calculated for the lowest gas flow rate for commercial purity aluminum, however, does not agree with those for the magnesium containing alloys. This does not allow the author to reach a firm conclusion whether the mass transfer coefficients are the same for the purpose of determining the effect of magnesium in the melt on the capacity of the chlorine containing gas bubbles with respect to sodium removal. Based on the results obtained for calcium removal, it may be reasonable to propose that magnesium should not have any negative effect on the capacity of the chlorine containing gas bubbles in eliminating sodium from the bath.

V.F. Calculation of the Melt Phase Mass Transfer Coefficients for Evaporation through the Melt Surface.

Experimental melt phase mass transfer coefficients,  $k_s$ , were calculated from the following equation:

$$k_s = \frac{R_{Ar} M}{\rho A} \quad (5.16)$$

In the above equation, A is the top surface area of the melt which was  $15.84 \cdot 10^{-3} \text{ m}^2$ , M is the mass of the melt,  $\rho$  is the density which was taken to be 2350 and 2345  $\text{kg/m}^3$  for commercial purity and aluminum-1wt% magnesium alloys respectively.

In calculating melt phase mass transfer coefficients for evaporation of sodium through the melt surface, the amount of sodium removed from the melt by evaporating into the gas bubbles was assumed to be negligibly small. The validity of this assumption can be checked by calculating the rate constants for the removal of sodium by saturating the gas bubbles according to:

$$R_{sat} = \frac{G_{Ar} K f_{Na} 100 m_{Na}}{M P_{atm}} \quad (5.17)$$

where  $G_{Ar}$  is the molar flow rate of the argon gas,  $f_{Na}$  is the activity coefficient of sodium in the melt,  $m_{Na}$  is the molecular weight of sodium,  $M$  is the mass of the melt,  $P_{atm}$  is the atmospheric pressure and  $K$  is the equilibrium constant for the following evaporation equilibrium:

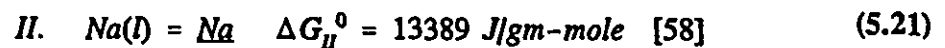


The underline was used to indicate that sodium is dissolved in the melt. Therefore, the equilibrium constant  $K$  is expressed as:

$$K = \frac{P_{Na}}{f_{Na} \%Na} \quad (5.19)$$

For the 1wt% standard state,  $f_{Na}$  will be equal to unity and  $K$  will therefore be equal to the vapour pressure of sodium,  $P_{Na}$ .

For commercial purity aluminum, the equilibrium constant  $K$  at 1000 K was calculated from the following equilibria:



$$\Delta G_{III}^0 = -R T \ln K = -8.314 \cdot 1000 \cdot \ln K \quad (5.23)$$

$$K = 0.986 \text{ atm} = P_{Na} \quad (5.24)$$

In the absence of any thermodynamic data for aluminum-1wt% magnesium alloys, the value of the equilibrium constant for the magnesium containing alloys was assumed to be identical

to that for the pure aluminum.

The values of  $R_{Ar}$  and  $R_{sat}$  are presented in Table 5.7 for various gas flow rates. In the case of commercial purity aluminum,  $R_{sat}$  was only 5% of experimentally determined rate constant  $R_{Ar}$ . In the case of the magnesium containing alloys,  $R_{sat}$  was about 10% of  $R_{Ar}$  at the lowest gas flow rate and reached about as high a 27% of  $R_{Ar}$  at the highest gas flow rate. One should, however, consider that  $R_{sat}$  was calculated for equilibrium conditions and represents the maximum for the fraction of sodium that is removed per unit time by evaporating into the gas bubbles. Consequently, for bubbles whose residence time in the melt was typically at the order of 0.5 seconds, one cannot expect the rate of removal of sodium to be as high by evaporating into the bubbles as that calculated from Eqn.(5.17).

The experimental mass transfer coefficients calculated through Eqn.(5.16) were compared with the mass transfer coefficients that were given by Davenport et al.[75]:

$$k_s = \sqrt{\frac{8}{\pi}} \left( \frac{U_r D}{r} \right)^{0.5} \quad (5.25)$$

This equation was obtained for the mass transfer of the gaseous species into a liquid phase across a gas liquid interface when the gas phase was impinged on the surface of the liquid phase. In Eqn.(5.25),  $U_r$  is the radial velocity at the surface,  $r$  is the radius of the vessel and  $D$  is the diffusion coefficient.

The diffusion coefficient of sodium in both commercial purity aluminum and aluminum-1wt% magnesium alloys was taken to be equal to the self diffusion coefficient of aluminum. The radial velocity at the surface,  $U_r$ , was estimated by carrying out cold model experiments(Appendix E). From the results of these tests, the following equation that related the volumetric gas flow rate to the surface velocity was used to predict  $U_r$  for the molten metal:

$$\frac{U_r r^2}{Q} = 1.074 \left( \frac{Q^2}{r^5 g} \right)^{-0.347} \quad (5.26)$$

The values of the experimental mass transfer coefficients together with the ones calculated according to Eqn.(5.25), are shown in Figures 5.19 and 5.20 as a function of the

surface velocity for commercial purity and aluminum-1wt% magnesium alloys respectively.

In the case of commercial purity aluminum, the mass transfer coefficients calculated from the experimentally obtained rate constants were three to four times higher than those calculated through Eqn.(5.25).

In the case of the magnesium containing alloys, however, in spite of the large scatter in the experimental mass transfer coefficients, the curve representing the experimental mass transfer coefficients lays below the one calculated according to Eqn.(5.25).

Eqn.(5.25) was derived by Davenport et al., by assuming that the mass transfer was controlled in the liquid phase. Under the present experimental conditions, however, there was always a dross layer (mainly  $Al_2O_3$  in the case of the commercial purity aluminum, and  $MgO-Al_2O_3$  in the case of the magnesium containing alloys) that formed on top of the melt surface when argon injection tests were carried out. Therefore, it is reasonable to expect the mass transfer coefficients to be lower than the ones calculated according to Eqn.(5.25) owing to an additional resistance of the dross layer to the mass transfer rate of sodium. This was observed in the case of the magnesium containing alloy but not for commercial purity aluminum.

Table 5.7 Rate constants,  $R_{Ar}$  and  $R_{sat}$ , for various argon gas flow rates(730 °C, 1 Atm.)

Q (cc/sec) @ 730 °C	R (1/sec)*10 <sup>6</sup>			
	Al		Al-1wt% Mg	
	$R_{Ar}$	$R_{sat}$	$R_{Ar}$	$R_{sat}$
26.22	3767	96	1193	98
	3383	96	1017	100
	4032	96	650	97
	Av:3727	Av:96	Av:953	Av:98
56.45	3767	197	1710	203
	4833	199	712	204
	Av:4298	Av:198	775	200
			Av:1066	Av:202
91.12	5967	314	1626	321
			700	320
			Av:1163	Av:320

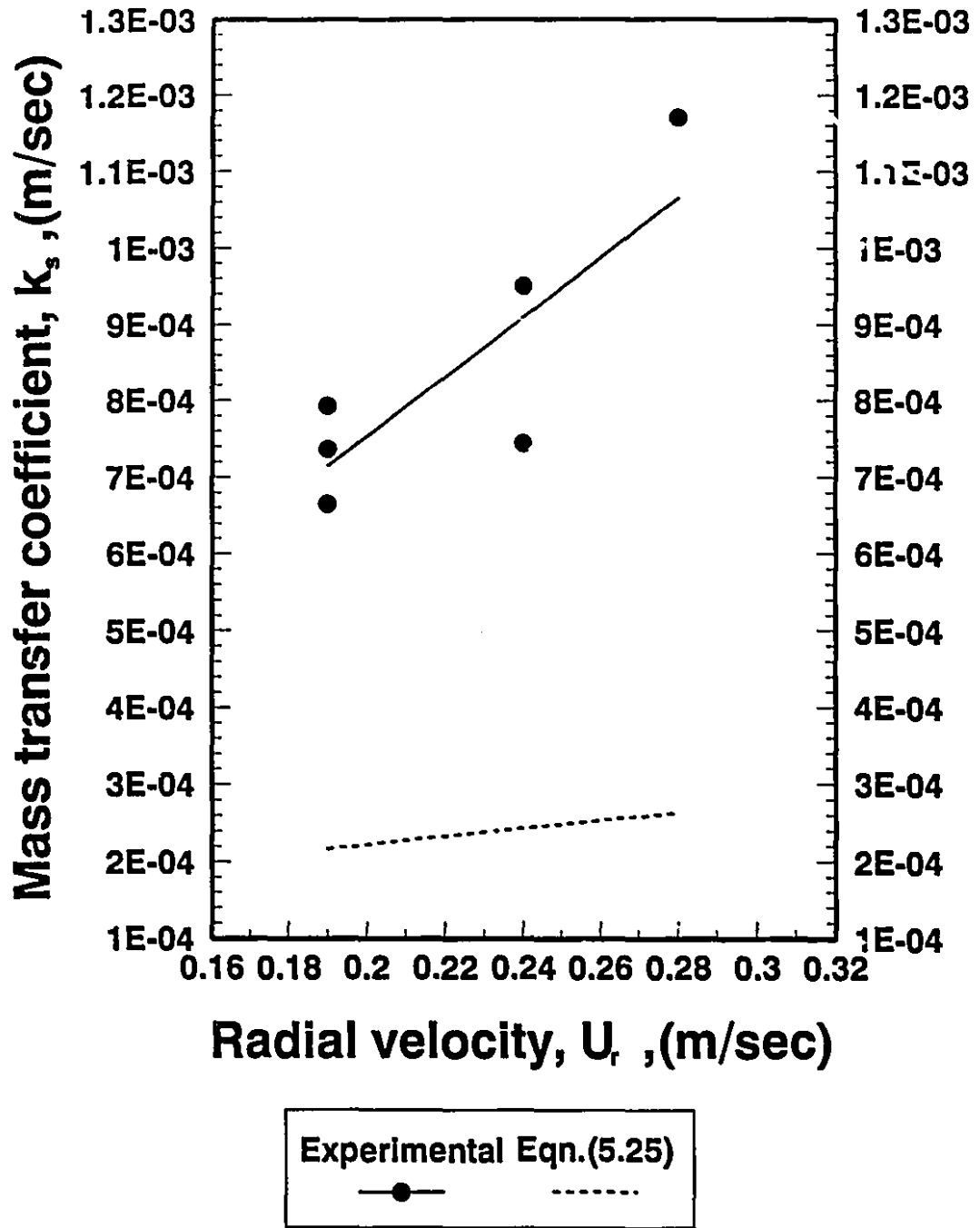


Figure 5.19 Comparison of the experimental melt phase mass transfer coefficients for the evaporation through the melt surface with the theoretical values calculated according to Eqn.(5.25) for commercial purity aluminum.

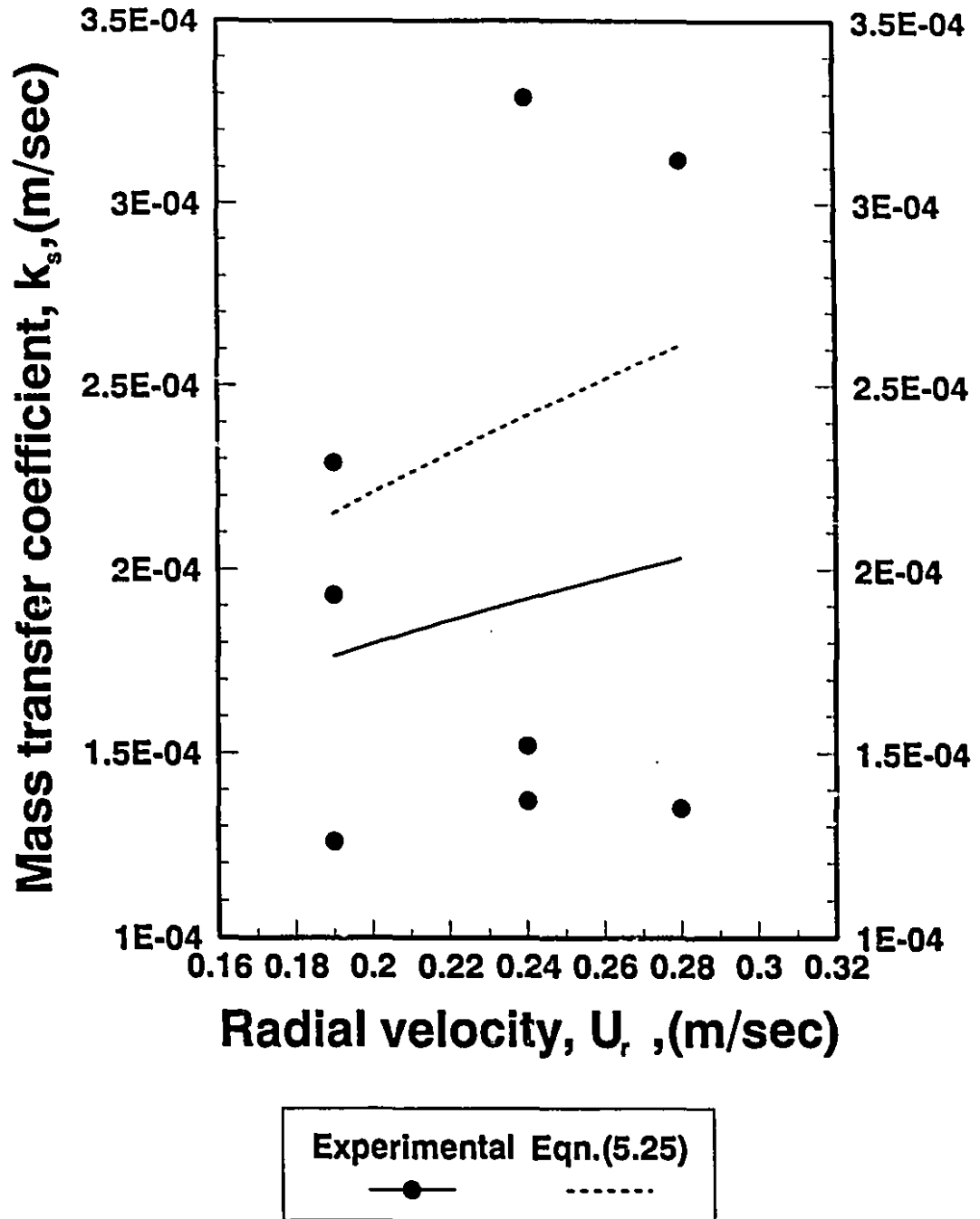


Figure 5.20 Comparison of the experimental melt phase mass transfer coefficients for the evaporation through the melt surface with the theoretical values calculated according to Eqn.(5.25) for Al-1wt% Mg alloys

V.F. Summary:

Under the present experimental conditions, the removal of sodium from commercial purity aluminum and aluminum-1wt% magnesium alloys followed first order reaction kinetics with respect to sodium concentration. It was demonstrated that the flux of sodium to the bubble melt interface was not sufficient to consume the chlorine stoichiometrically due to insufficient contact surface area between the bubbles and the melt.

The rate of removal of sodium from commercial purity aluminum was always higher than it was from the magnesium containing alloys. This was due to higher rate of evaporation of sodium from commercial purity aluminum through the melt surface.

In the case of the commercial purity aluminum, the contribution of evaporation of sodium through the melt surface to the total removal rate of sodium was calculated to be around 65%. This was followed by the bubbles whose contributions were calculated to be between 20 to 30%. The contribution of the intermediate reaction products to the removal rate of sodium was around 5%.

In the case of aluminum-1wt% magnesium alloys, the maximum contribution to the removal of sodium was from the intermediate reaction products that are separated from the bubbles. This contribution was calculated to be between 50 and 60%. The contribution of evaporation of sodium through the melt surface was calculated to be between 20 and 30%. The contribution of the bubbles was between 8 and 20%.

Since the removal of sodium is controlled by the mass transfer of sodium in the melt phase, mass transfer coefficients for bubbles in commercial purity aluminum should be close to the ones for the magnesium containing alloys. The fact that the mass transfer coefficients calculated for the intermediate and highest gas flow rates are similar in magnitude supports this hypothesis. The mass transfer coefficients calculated for the lowest gas flow rate for commercial purity aluminum, however, does not agree with those for the magnesium containing alloys. This does not allow the author to reach a firm conclusion whether the mass transfer coefficients are the same for the purpose of determining the effect of magnesium in the melt on the capacity of the chlorine containing gas bubbles with respect to sodium removal. Based on the results obtained for calcium removal, however, it may be reasonable to propose that magnesium should not have any negative effect on the capacity

of the chlorine containing gas bubbles in eliminating sodium from the bath.

## Chapter 6

### Results and Discussion: Analysis of Contribution of the Intermediate Reaction Products that are Separated from the Bubbles

---

#### VI.1 Introduction:

In Chapters 4 and 5, it was shown that the intermediate reaction products that are separated from the bubbles contributed appreciably to the removal of impurities from the magnesium containing alloys. As explained in the kinetics section in Chapter 2, some of the intermediate reaction products could end up as liquid droplets and/or solid particles in the melt. In order to calculate the contribution of these particles to the removal of the impurities, their number and size distributions were determined by carrying out LiMCA tests. The details of the experimental procedure and the experimental set up for these tests has been presented in Chapter 3.

Figure 6.1 shows the number of particles that were greater than 21 microns as a function of chlorine concentration and gas flow rate before and after chlorination of the melt. As seen after chlorination, the number of particles in the melt increased. The maximum increase in particles was observed at the highest gas flow rate.

The number and size distribution of the particles present in the melt before (the initial condition of the melt) and after the chlorination (final condition of the melt) together with the difference between the two are presented in Tables F1 through F9 in Appendix F.

Figure 6.2 shows a typical LiMCA signal observed before the melt was chlorinated. The signal has a so called asymmetrical bell shape; a name given to it because of a small undershoot of its falling edge below the base line. A typical LiMCA signal observed immediately after chlorination is shown in Figure 6.3. The falling edge of the signal followed a slow exponential decay. It was observed that the overwhelming majority of the signals after the chlorination was of this type. In order to show that these types of signals

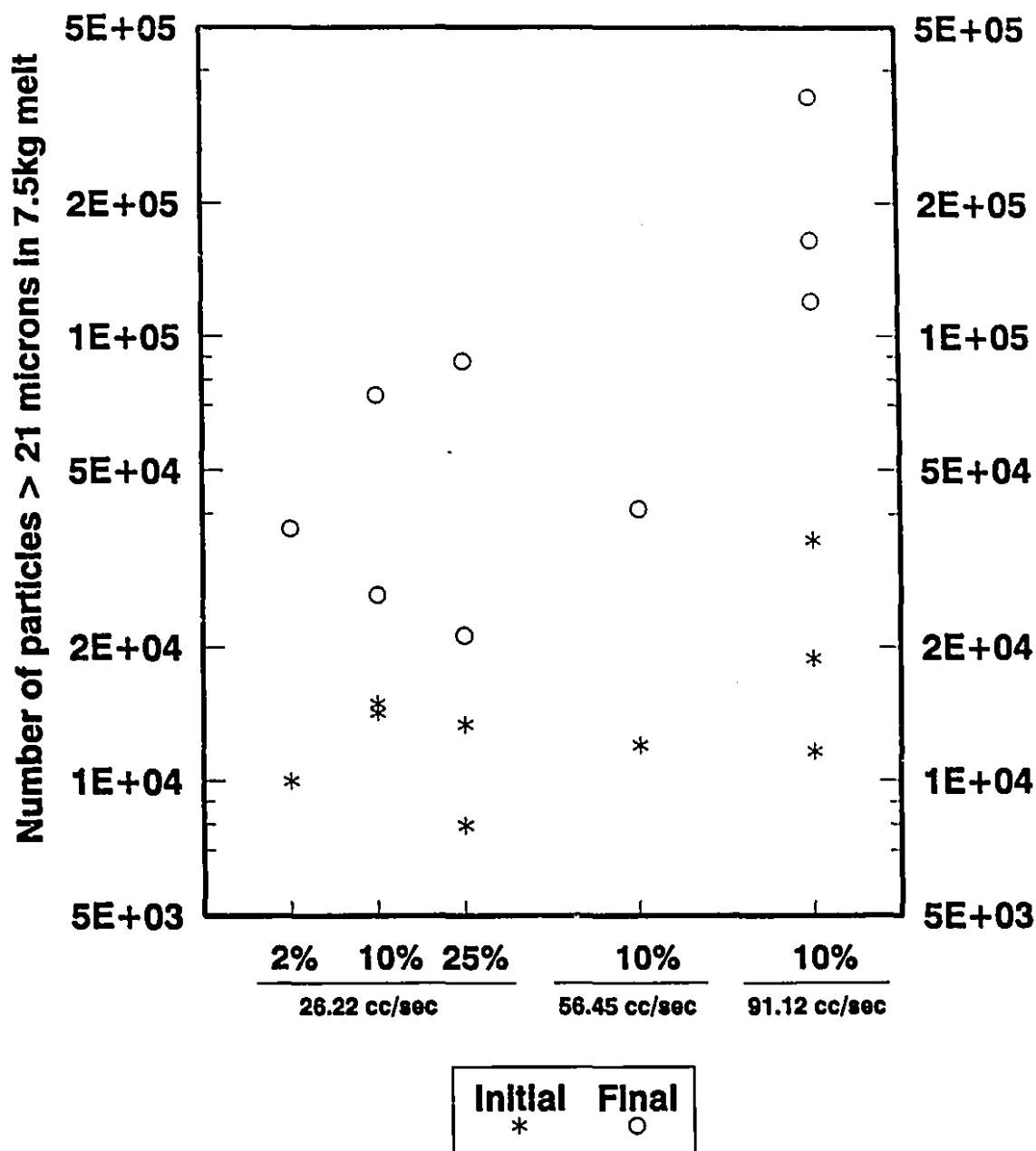
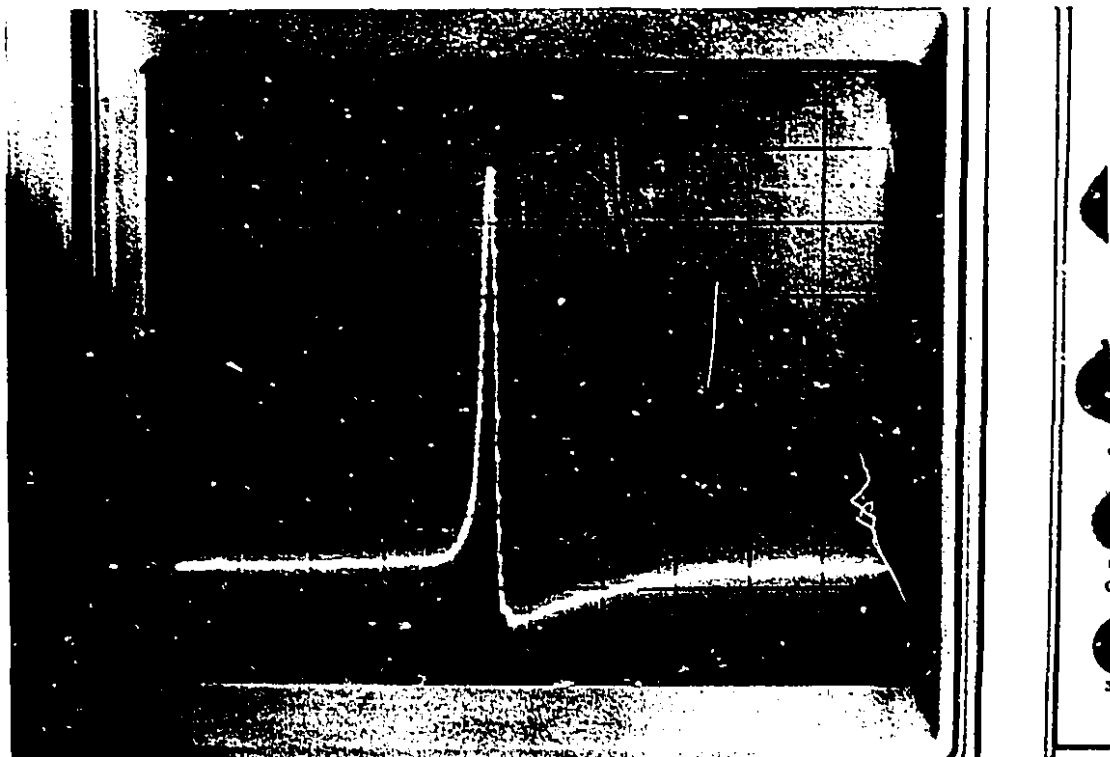
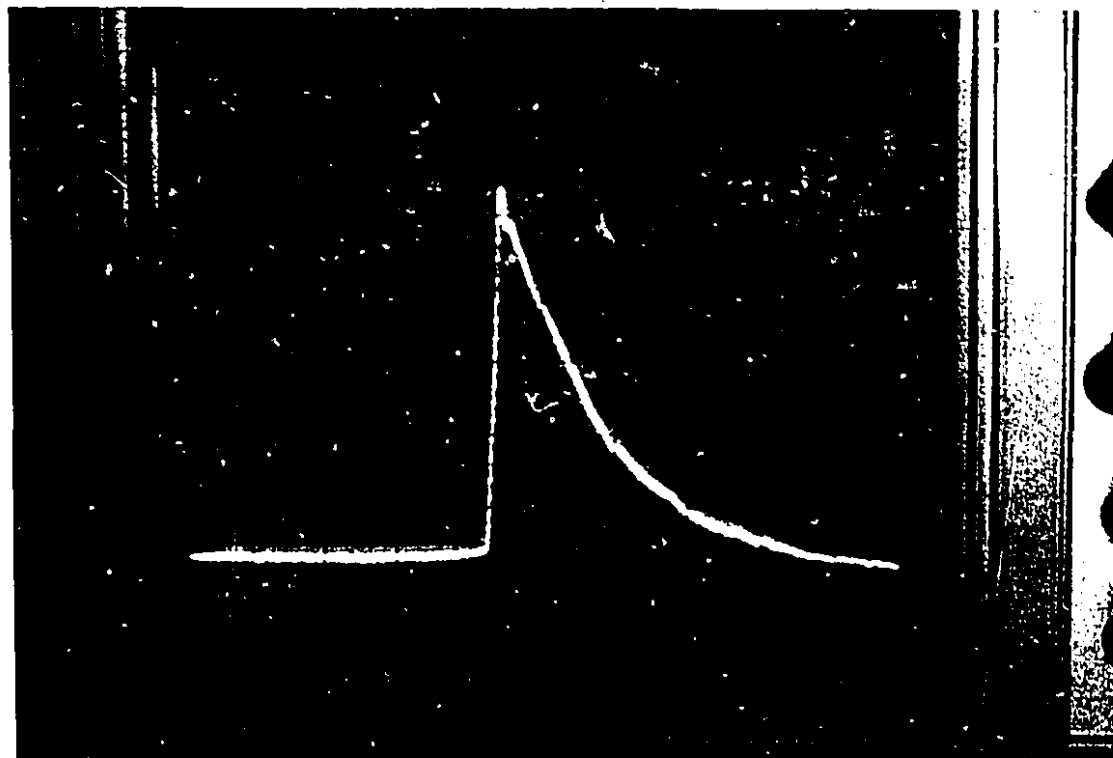


Figure 6.1 Number of particles that are greater than 21 microns in a 7.5 kg melt before and after chlorination as a function of chlorine concentration(Vol%) and gas flow rate(730 °C, 1 Atm.)



**Figure 6.2** A typical LiMCA signal observed before chlorination;  
Horizontal scale=1 ms per division, Vertical scale=0.1 mV  
per division



**Figure 6.3** A typical LiMCA signal observed after chlorination; Horizontal scale=1 ms per division, Vertical scale=0.1 mV per division

were caused by the passage of the  $MgCl_2$  droplets through the orifice, the following test was carried out. First a LiMCA test was carried out in an aluminum-1wt% magnesium alloy that was kept at  $730\text{ }^\circ\text{C}$ . Vacuum was applied in the sampling unit and molten metal aspirated into the sampling tube through the orifice. While the metal was rising inside the tube, signals were monitored on the screen of the oscilloscope. During the rising period of the metal inside the tube, the signals were of an asymmetrical bell shape type. The vacuum was then turned off and pressure was applied to empty the tube. During the emptying period, the signals were again of an asymmetrical bell shape nature. Another LiMCA test was carried using the same melt at the same temperature. However, this time synthetic  $MgCl_2$  crystals were wrapped around the inside electrode using a commercially available aluminum foil. By applying vacuum in the sampling tube, the molten metal was aspirated into the tube. The signals that were observed during the filling period were of asymmetrical bell shape type. The rising metal inside the tube then reached the level of  $MgCl_2$  crystals. Some 10 to 15 seconds were allowed for melting of the crystals to be complete ( $Mp_{MgCl_2}=715\text{ }^\circ\text{C}$  [76]). The pressure was then turned on to empty the tube. The signals during the emptying period were observed to be dominantly of the type that was observed after the chlorination of the melt.

Further, X-Ray diffraction analysis of dross samples collected after the chlorination of the magnesium containing melts showed that the dross indeed contained  $MgCl_2$ . An X-Ray diffraction pattern of a typical dross sample is shown in Figure 6.4. The peaks at angles 14, 30, 35 and 50 were identified to belong to  $MgCl_2$ . The analysis also showed that there were also aluminum and  $MgO.Al_2O_3$  spinel present in the dross.

In order to calculate the contribution of these droplets to the removal of calcium and sodium, rate constants for droplets were calculated through semi-empirically obtained mass transfer coefficients for droplets.

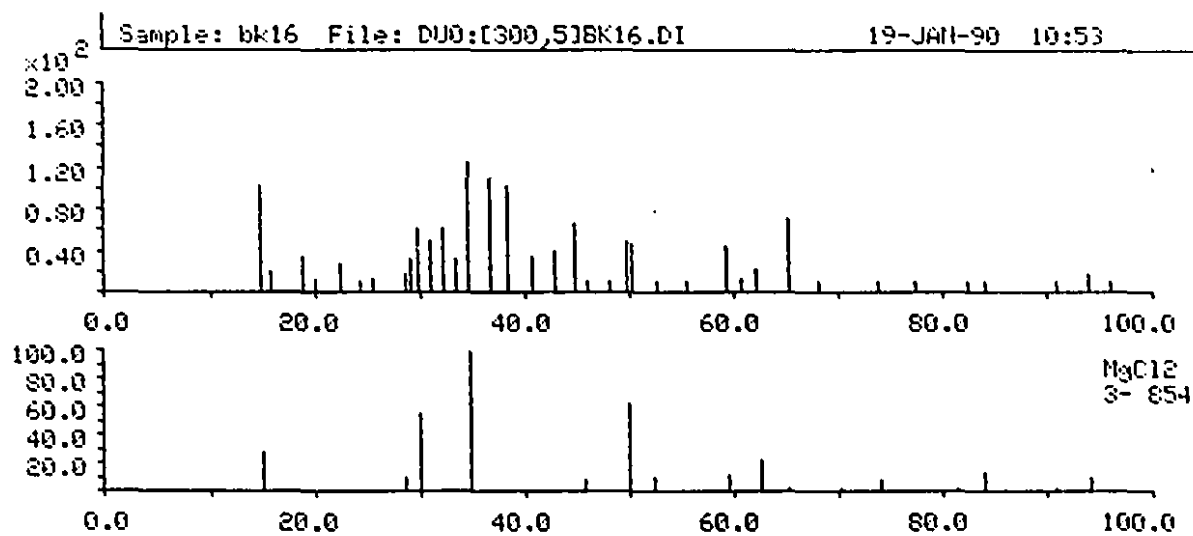


**Figure 6.4** An X-Ray diffraction pattern of a typical dross sample(at the top) together with that of MgCl<sub>2</sub>(at the bottom)

VI.2. Calculation of Rate Constants for Droplets:

Rate constants for the droplets that are separated from the bubbles were calculated from:

$$R_{drp} = \frac{\bar{k} \rho A_{drp}}{M} \quad (6.1)$$

In the above equation  $A_{drp}$  is the total surface area of the droplets at any instant in the bath,  $\rho$  is the density and  $M$  is the mass of the melt respectively.  $\bar{k}$  represents the surface area averaged mass transfer coefficient.

$A_{drp}$  was calculated from:

$$A_{drp} = \sum \pi d_{drp}^2 N_{drp} \quad (6.2)$$

In the above equation,  $d_{drp}$  is the diameter of the droplet,  $N_{drp}$  is the number of droplets in that size respectively.  $N_{drp}$  was taken to be the difference between the final and the initial LiMCA readings. The summation was carried out from  $d_{drp} = 22 \cdot 10^{-6}$  to  $70 \cdot 10^{-6}$  m with an interval of  $3 \cdot 10^{-6}$  m. The surface area averaged mass transfer coefficient,  $\bar{k}$ , was calculated from:

$$\bar{k} = \frac{\sum \pi d_{drp}^2 N_{drp} k_{drp}}{A_{drp}} \quad (6.3)$$

In the above equation the limits of the summation and the step size was the same as Eqn.(6.2). In Eqn.(6.3),  $k_{drp}$  is the theoretical melt phase mass transfer coefficient which was calculated from the following relationship[77]:

$$Sh = 1 + (1 + Pe)^{1/3} \quad (6.4)$$

In the above equation  $Sh$  is the Sherwood number which is defined by:

$$Sh = \frac{k_{dp} d_{dp}}{D} \quad (6.5)$$

Pe, the Peclet number is defined by :

$$Pe = Re * Sc \quad (6.6)$$

where Re, Reynolds number, is defined by:

$$Re = \frac{\rho U d_{dp}}{\mu} \quad (6.7)$$

and finally, Sc, Schmidt number is defined by:

$$Sc = \frac{\mu}{\rho D} \quad (6.8)$$

In Eqns.(6.5) through (6.8), D is the diffusion coefficient of the impurity in the melt,  $\mu$  is the viscosity,  $\rho$  is the density of the melt respectively and U is the terminal velocity of the droplets.

Eqn.(6.4) was recommended by Grace et al[77] for mass transfer correlations for rigid particles for all Peclet numbers in creeping flow. Eqn.(6.4) was stated by Grace et al. to agree within 2% of a numerical solution of the steady convection-diffusion equation and was stated to be valid up to Reynolds number of 1 even though the creeping flow approximation is strictly valid only up to  $Re \leq 0.1$ [78].

According to Bond and Newton[79], internal circulation in a fluid particle could only occur when Eotvos number becomes greater than 4, which is

$$\frac{g \Delta \rho d_{dp}^2}{\sigma} > 4 \quad (6.9)$$

Taking the density of the melt as 2345 kg/m<sup>3</sup> and the density of the MgCl<sub>2</sub> droplets as 1668 kg/m<sup>3</sup>[76],  $\Delta \rho$  becomes 677 kg/m<sup>3</sup>. Taking the surface tension of the melt  $\sigma = 0.8$  N/m[45], one would obtain an Eotvos number of  $4 \cdot 10^{-6}$  and  $4 \cdot 10^{-5}$  for a droplet diameter of 22 and

70 microns respectively. Therefore, the  $\text{MgCl}_2$  droplets can be assumed to be rigid particles for the purpose of mass and momentum transfer calculations.

Since there is a density difference between the  $\text{MgCl}_2$  droplets and the magnesium containing alloys, there will be a relative motion between these droplets and the melt due to the buoyancy. The resulting relative velocity of the droplets can be calculated from Stokes Law which describes the drag force on a submerged rigid sphere in a fluid in creeping flow[78]. According to Stokes Law, the drag force acting on a rigid sphere could be expressed as:

$$F_d = 3 \pi \mu d U \quad (6.10)$$

This force in the present system is balanced by the buoyancy force:

$$F_b = \frac{\pi d^3 \Delta \rho g}{6} \quad (6.11)$$

which will result in a relative velocity  $U$  for a spherical particle:

$$U = \frac{g \Delta \rho d^2}{18 \mu} \quad (6.12)$$

Strictly speaking, Stokes law is valid for up to  $\text{Re}=0.1$ . Figure 6.5 shows Reynolds number as a function of droplet diameter. As seen beyond a particle diameter of about 50 microns the Reynolds number exceeds 0.1. The error that was introduced by extending the creeping flow regime up to  $\text{Re}=0.25$  can be approximately calculated by the calculation of drag coefficients. Drag coefficient, based on the diameter of the sphere, for rigid spheres in the creeping flow regime is given by[80]:

$$C_D = \frac{24}{\text{Re}} \quad (6.13)$$

For  $0.01 < \text{Re} \leq 20$  drag coefficients for rigid spheres can be calculated from the correlation given by Grace et al[81] according to:

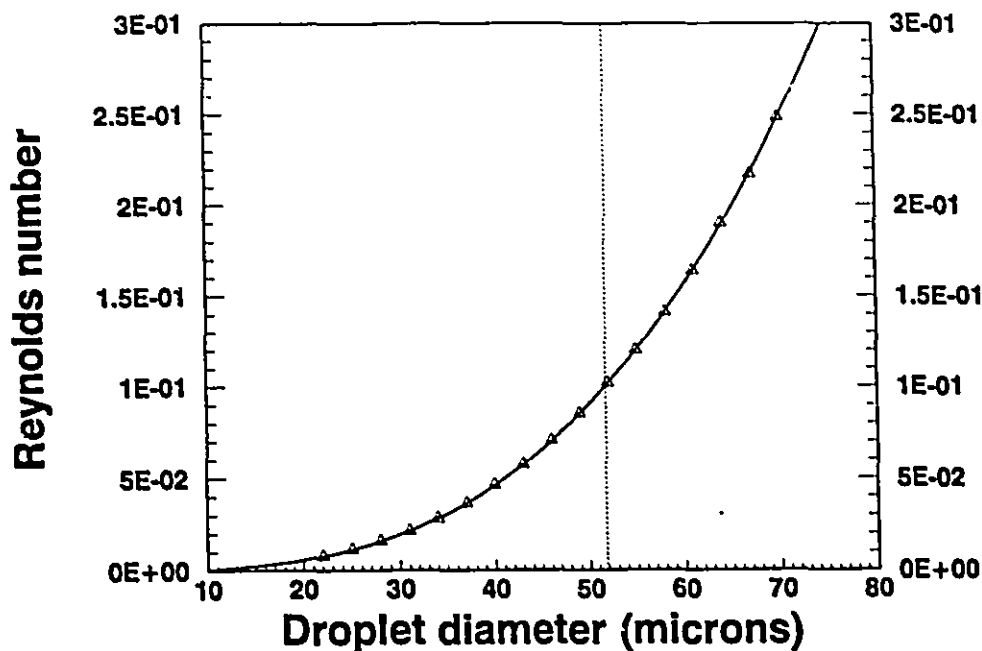


Figure 6.5 Reynolds number as a function of droplet diameter

$$C_D = \frac{24}{Re} [1 + 0.1315 Re^{(0.82 - 0.05 \log Re)}] \quad (6.14)$$

For  $Re=0.25$ , Eqn.(6.13) would give  $\sim 4\%$  lower drag coefficient than Eqn.(6.14). It is also instructive to note that for  $Re=0.1$  Eqn.(6.14) predicts  $C_D$  about 2% higher than that for Eqn.(6.13). Therefore, Eqn.(6.14) would be a good approximation for estimating  $C_D$  up to 0.25. Consequently, extending the Stokes Law up to Reynolds number of 0.25 would not introduce any serious error.

Rate constants for the droplets calculated according to Eqn.(6.1) together with the overall rate constants for calcium and sodium are presented in Table 6.1. As seen the values

Table 6.1 Overall rate constants and rate constants for the droplets for various chlorine concentrations(Vol%) and gas flow rates (730 °C, 1 Atm.)

Q (cc/sec)	Cl <sub>2</sub> Concentration (Vol%)	R <sub>o</sub> <sup>Ca</sup> (1/sec)*10 <sup>6</sup>	R <sub>o</sub> <sup>Na</sup> (1/sec)*10 <sup>6</sup>	R <sub>drp</sub> (1/sec)*10 <sup>6</sup>
26.22	2	1331 1490 Av:1411	2975 2823 Av:2899	11
	10	2217 2550 Av:2384	3416 3416 Av:3416	6 26 Av:16
	25	1828 1883 Av:1856	3283 3356 Av:3320	6 31 Av:19
56.45	10	3067 2983 2817 Av:2956	5045 4600 4517 Av:4721	13
91.12	10	4090 4917 Av:4504	6467 5667 Av:6067	59 49 150 Av:86

of the rate constants for the droplets,  $R_{d,ip}$ , were negligibly small. The maximum contribution of the droplets to the removal of the impurities was at the highest gas flow rate. This contribution was calculated to be 2 and 1.5% for calcium and sodium removal respectively based on the number of droplets detected.

As explained in the kinetics section in Chapter 2, some of the intermediate reaction products could be carried towards the crucible wall and would cover various parts. Their contribution to the removal of the impurities can be determined approximately by calculating the rate constants according to:

$$R'_w = \frac{k'_w \rho A}{M} \quad (6.15)$$

In the above equation,  $k'_w$  represents the melt phase mass transfer coefficient for the intermediate reaction products that cover the crucible wall and was estimated from the mass transfer correlation for flat plates subjected to laminar flow[82] according to:

$$Sh = 0.66 Re^{0.5} Sc^{0.33} \quad (6.16)$$

The velocity of the melt in the Reynolds number was estimated from the correlations given by Sahai and Guthrie[83] for buoyancy driven circulating flows according to:

$$U = \left( \frac{C_D U_b^2 d_c^2 Q \nu}{18 C_\mu C^4 r^2 U_p V_b} \right)^{1/3} \quad (6.17)$$

In the above equation  $U$  is the mean bath recirculation speed,  $r$  is the container radius,  $C_D$  is the drag coefficient for the bubbles,  $U_b$  and  $d_c$  are the velocity and diameter of the bubbles,  $C_\mu$  and  $C$  are constants  $U_p$  is the rise velocity of the bubble plume,  $V_b$  is volume of each bubble and  $\nu$  is the turbulent kinematic viscosity.

Table 6.2 shows the rate constants  $R'_w$  calculated according to Eqn.(6.15) together with the  $R_{i,ip}$  for sodium and calcium removal. As seen from Table 6.2, the intermediate reaction products covering the crucible wall would, at best, contribute to  $R_{i,ip}$  between 18 and 35% for sodium removal and 36 to 67% for calcium removal. Therefore the

discrepancy between the values of the  $R_{irp}$  and  $R_{drp}$  can not be bridged by the intermediate reaction products that would cover the crucible wall.

Table 6.2 Rate constants for various gas flow rates(730 °C, 1 Atm.)

Q (cc/sec)	$R_{irp}^{Na}$ (1/sec)* $10^6$	$R_{irp}^{Ca}$ (1/sec)* $10^6$	$R'_w$ (1/sec)* $10^6$
26.22	1684	890	600
56.45	2514	2020	677
91.12	3882	1991	730

However, one should also consider the effect of the droplets that could not be detected by the LiMCA apparatus. As was evident in Tables F1 through F9 in Appendix F, only particles within the size range of 21 to 70 microns could be detected. It should also be noted that the number of the particles increased towards the smaller particle ranges. If the particle size distribution could be extrapolated beyond 21 micrometer, the contribution of those smaller droplets would be remarkable. The examination of melt samples under SEM showed that indeed the melt contained smaller  $MgCl_2$  particles. Figure 6.5 shows an SEM picture of  $MgCl_2$  particles detected on the surface of an aluminum-1wt% magnesium alloy sample. As seen the size of the particles were about 2 microns. Therefore it is quite possible that the smaller droplets present in large numbers in the melt would help bridge the gap between the calculated contribution of the droplets between the size range of 21 to 70 microns + the contribution of the  $MgCl_2$  that covers the crucible wall and the observed rate constants  $R_{irp}$ .

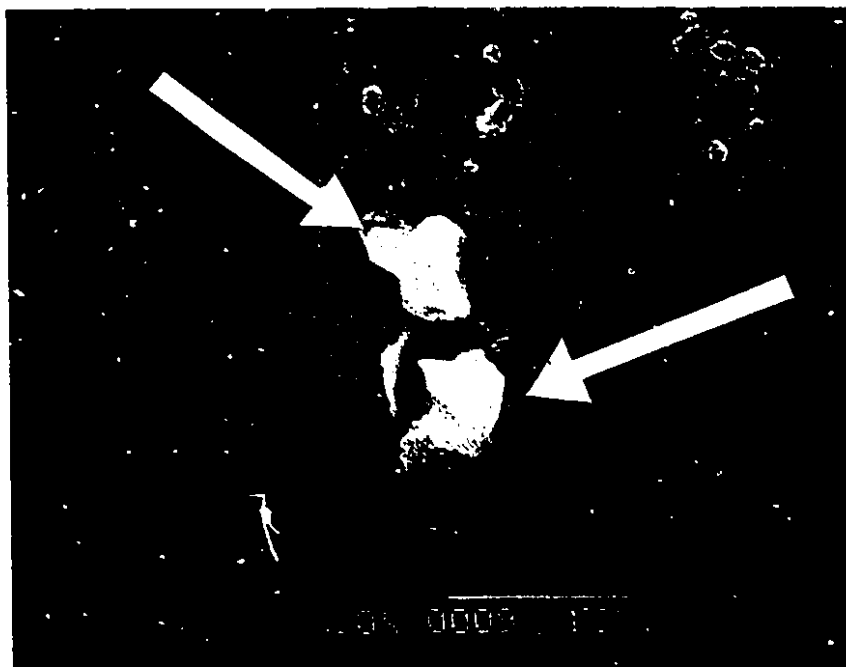


Figure 6.6 An SEM picture of  $MgCl_2$  particles

VI.3. Summary:

The analyses of the LiMCA data showed that the contribution of the  $MgCl_2$  droplets within the size range of 20 to 70 microns was negligibly small. Calculations demonstrated that although the intermediate reaction products that covers the crucible wall could contribute appreciably to the removal of the impurities, the major contribution must come from the  $MgCl_2$  droplets which were smaller than 20 micron in size.

### CONCLUSIONS TO THE THESIS

1. The removal of calcium and sodium from commercial purity aluminum and aluminum-1wt% magnesium alloys by chlorination at 730 °C followed first order reaction kinetics with respect to calcium and sodium concentrations.
2. In the case of the magnesium containing alloys, the  $MgCl_2$  salt phase that was generated by the chlorination action contributed appreciably to the removal of calcium and sodium from aluminum-magnesium alloys. This contribution would reach as high as 60% to the total removal of rate of the impurities.
3. The analysis of the data for the size and number distribution of the  $MgCl_2$  droplets showed that the number of droplets within a size range of 21 to 70 microns had almost negligible contribution to the removal of the impurities from the melt. The rate constants calculated according to the assumption that the crucible wall was entirely covered by an  $MgCl_2$  layer would not account for the discrepancy between the observed rate constants for the  $MgCl_2$  salt phase and the calculated rate constants for the droplets in 21-70 micron size range. The size and number distribution of the droplets led to the conclusion that there must have been smaller droplets in the melt which would provide sufficient mass transfer surface area to account for the observed rate constants for the  $MgCl_2$  salt phase.
4. Experimentally determined melt phase mass transfer coefficients for chlorine containing gas bubbles for the removal of calcium showed that the presence of magnesium does not reduce the capacity of the gas bubbles to eliminate calcium from aluminum melts.
5. The rate of removal of sodium from commercial purity aluminum was always higher than it was from the magnesium containing alloys owing to higher evaporation rate of sodium from the melt surface. While theoretical melt phase mass transfer coefficients for evaporation of sodium from the magnesium containing melts was in fair agreement with the empirical mass transfer coefficients, the empirical mass transfer coefficients for evaporation

through the melt surface of commercial purity aluminum were three to four times higher than the theoretical values.

CLAIMS TO THE ORIGINAL CONTRIBUTIONS TO THE KNOWLEDGE

In the author's opinion, the following are distinct contributions to present knowledge.

- 1) Although chlorination of aluminum melts has been practised in aluminum industry for decades, this is the first time that the effect of chlorine containing gas bubbles on the removal of calcium and sodium was quantitatively demonstrated. It is also the first time that the effect of the  $MgCl_2$  salt phase generated by the chlorination action on the removal of calcium and sodium from the magnesium containing alloys was quantitatively documented.
- 2) This is the first time that mass transfer coefficients for the chlorine containing gas bubbles for the removal of calcium and sodium were determined.
- 3) Contrary to earlier belief, it was demonstrated that the presence of magnesium does not reduce the ability of chlorine containing gas bubbles to eliminate calcium from the magnesium containing melts.
- 4) This is the first time that size and number distributions of  $MgCl_2$  salt droplets, within a 21-70 microns in diameter, together with their contribution to the removal of calcium and sodium has been documented.

### SUGGESTIONS FOR FUTURE WORK:

During the course of this study two unresolved phenomena were observed to occur. The first of these was the relatively slower rate of removal of sodium and calcium from the magnesium containing alloys at the lowest chlorine concentration and the second was unaccountably high values of evaporation of sodium from commercial purity aluminum.

For the first phenomenon, although the experimental results indicated that there was comparable contribution from the  $MgCl_2$  salt phase to the removal of sodium and calcium at that particularly low chlorine concentration, surface tension measurements between a chlorine containing gas phase and a magnesium containing aluminum melt by a maximum bubble pressure method would shed some light on the interfacial phenomenon taking place between the gas and the melt phase. It is well known by now that even minute amount of oxygen present in an inert gas would cause an oxide film to form between the gas phase and the aluminum melt which would inhibit mass transfer between the phases. Hicter\* presented very interesting results of surface tension measurements done by maximum bubble pressure technique. He showed that in the presence of chlorine gas the oxide film would break up which would manifest itself in a reduced value of interfacial tension between liquid aluminum and the gas. Similar experiments could be carried out to find the limit of chlorine concentration to break the oxide film and help understand the phenomena taking place at the gas-melt interface. Comparative studies between the magnesium containing alloys and liquid  $MgCl_2$  would also be used to verify the formation of an  $MgCl_2$  layer on the surface of the bubbles.

For the second phenomenon regarding higher evaporation rates of sodium from commercial purity aluminum, it would be worthwhile to investigate the permeability of  $Al_2O_3$  versus  $Al_2O_3 \cdot MgO$  oxide layer to the evaporation of sodium from the melts. It would also be worthwhile to investigate the effect of thickness of the dross layer which is partly made of oxides on the evaporation rate of sodium from the melts.

\* *J.M. Hicter, "Foundry practices used to obtain high grade aluminum alloys", Revue de L'Aluminium, 1982, pp.471-479*

---

REFERENCES:

1. J.E. Gruzleski, "The art and science of modification-twenty years of progress", a paper presented in the AFS Conference May 2-7, 1992, Milwaukee, Wisconsin, USA
2. C.E. Ransley, D.E. Talbot, "The embrittlement of Aluminum-Magnesium alloys by Sodium", *Journal of the Institute of Metals*, v.88, 1959, pp.150-158
3. M. Yoshida, K. Oka, Y. Iijima, "Calcium contamination by filter and its effect on edge cracking of Al-Mg alloy plates", *Sumitomo Keikinzoku Giho*, v.26, n.4, Oct. 1985, pp. 195-202
4. D.N. Fager, M.V. Hyatt, H.T. Diep, "A preliminary report on cleavage fracture in AL-Li alloys", *Scripta Metallurgica*, v.20, 1986, pp 1159-1164
5. W.S. Miller, M.P. Thomas, J. White, "Sodium induced cleavage fracture in high strength aluminum alloys", *Scripta Metallurgica*, v.21, 1987, pp. 663-668
6. D. Webster, "The effect of low melting point impurities on the properties of aluminum-lithium alloys", *Metallurgical Transactions A*, v.18A, 1987, pp.2181-2193
7. T. Kobayoshi, M. Niinami, K. Degawa, "Temperature dependence of impact toughness in Al-Li-Cu-Mg-Zr alloys", *Materials Science and Technology*, v.5, 1989, pp.1013-1019
8. S.P. Lynch, "Fracture of 8090 Al-Li alloy plate; II. Sustained-load crack growth in dry air at 50-200 °C", *Materials Science and Engineering*, v.A136, 1991, pp.45-57
9. P.A. Foster, "Melting point of cryolite", *Journal of the American Ceramic Society*, v.51, 1968, pp.107-109
10. N.W. Philips, R.H. Singleton, E.A. Hollingshead, "Liquidus curves for aluminum cell electrolyte; II. Ternary systems of Cryolite-Alumina with sodium fluoride, sodium chloride, and aluminum fluoride", *Journal of the Electrochemical Society*, v.102, n.12, 1955, pp.690-692

11. A. Feterny and E.A. Hollingshead, "Liquidus curves for aluminum cell electrolyte; III. Systems Cryolite and Cryolite-alumina with aluminum-fluoride and calcium-fluoride", *Journal of the Electrochemical Society*, v.107, n.12, 1960, pp.993-997
12. K. Grjotheim, C. Krohn, M. Malinovsky, K. Matiasovsky, J. Thonstad, "Aluminium Electrolysis, Fundamentals of the Hall-Heroult Process", 2nd ed., Aluminium-Verlag GMBH, Dusseldorf, 1982
13. K. Grjotheim, K. Matiasovsky, "Impurities in the aluminum electrolyte", *Aluminium*, v.59, n.9, 1983, pp.E298-E304
14. E.W. Dewing, "The chemistry of the alumina reduction cell", *Canadian Metallurgical Quarterly*, v.30, n.3, 1991, pp.153-161
15. P. Fellner, K. Grjotheim, K. Matiasovsky, J. Thonstad, "Current efficiency measurements in laboratory aluminum cells", *Canadian Metallurgical Quarterly*, v.8, n.2, 1969, pp.245-248
16. J. Thonstad, A. Slattavik, J. Abrahamsen, "The behaviour of calcium in aluminium electrolysis", *Aluminium*, v.49, n.10, 1973, pp.647-677
17. M. Ishihara, K. Mukai, "Impurity levels in aluminum as influenced by raw materials and processing methods", *Transactions of the Metallurgical Society of AIME*, v.236, 1966, pp.192-196
18. E.F. Emley, V. Subramanian, "In-line treatment of liquid aluminum by the F.I.L.D and other processes", *Light Metals 1974*, 103rd AIME annual meeting, Dallas, Texas, pp.649-670
19. A. Aarflot, F. Patak, "Dynamic vacuum treatment of molten aluminum and its alloys", *Light Metals 1976*, v.2, 105th AIME annual meeting, Las Vegas, Nevada, pp.389-401
20. J. Clumpner, J. Dore, W.L. Hoffmann, "MINT, A new aluminum melt in-line treatment system", *Light Metals 1981*, 110th AIME annual meeting, Chicago, Illinois, pp.751-757
21. P. Achim, G. Dube, "Removal of lithium in commercial metal", *Light Metals 1982*, 111th AIME annual meeting, Dallas, Texas, pp.903-918

22. G. Dube, V.N. Newbery, "TAC, A novel process for the removal of lithium and other alkalis in primary aluminum", Light Metals 1983, 112.th AIME meeting, Atlanta, Georgia, pp.991-1003
23. J.M Hicter, "ALPUR refining process", Light Metals 1983, 112.th AIME meeting, Atlanta, Georgia, pp.1005-1022
24. S. Kastner, J. Kruger, F. Patak, "Refining of virgin aluminum by scavenging gas treatment", Raffinationsverfahren Metall., Int. Symp, 1983, pp.36-53
25. O. Hjelle, T.A. Engh, B. Rosch, "Removal of sodium from aluminum-magnesium alloys by purging with argon and  $Cl_2$ ", International seminar on refining and alloying of aluminum and ferro alloys, August 26-28 1985, Torondheim, Norway, pp.345-360
26. T. Pedersen, E.M. Myrbostad, "Refining and alloying of aluminum by injection", Light Metals 1986, 115.th TMS annual meeting, New Orleans, Lousiana, pp.759-765
27. J.G. Stevens, H. Yu, "A computer model of a stirred tank reactor in trace alkaline elements removal from aluminum melt-The Alcoa 622 process", Light Metals 1986, 115.th TMS annual meeting, New Orleans, Lousiana, pp.837-845
28. E. Myrbostad, T. Pedersen, K. Venas, S.T. Johansen, "The ASV in-line system for refining of aluminum", Light Metals 1986, 115.th TMS annual meeting, New Orleans, Lousiana, pp.861-866
29. J. Kruger, C. Seebauer, "Natrium-und Lithiumentfernung aus Huttenaluminium durch Salzbehandlung in der Ruhrpfanne", Erzmetall, v.40, n.7/8, 1987, pp.376-382
30. J.G. Stevens, H. Yu, "Mechanisms of sodium, calcium and hydrogen removal from an aluminum melt in a stirred tank reactor-the Alcoa 622 process", Light Metals 1988, 117.th TMS annual meeting, Phoenix, Arizona, pp.437-443
31. C. Celik, D. Dautre, "Theoretical and experimental investigation of furnace chlorine fluxing", Light Metals 1989, 118.th TMS annual meeting, Las Vegas, Nevada, pp.793-800

32. G.P. Walker, T.A. Zeliznak, S.R. Sibley, "Practical Degassing with the R.D.U", Light Metals 1989, 118.th TMS annual meeting, Las Vegas, Nevada, pp.777-782
33. R.R. Corns, T.P. Rack, "AGA MIX 14, Practical implementation of aluminum degassing," Light Metals 1989, 118.th TMS annual meeting, Las Vegas, Nevada, pp.783-792
34. M. Nilmani, P.K. Thay, C.J. Siemensen, D.W. Irwin, "Gas fluxing operation in aluminum melt refining, laboratory and plant investigations", Light Metals 1990, 119.th TMS annual meeting, Anaheim, California, pp.747-754
35. F. Achard, C. Leroy, "Pre-treatment in potlines crucibles: The MIXAL process", Light Metals 1990, 119.th TMS annual meeting, Anaheim, California, pp.765-768
36. P. Waite, D. Bernard, "Recent experience with the use of sulphur hexafluoride for aluminum fluxing", Light Metals 1990, 119.th TMS annual meeting, Anaheim, California, pp.775-784
37. Private communication
38. W.T. Thompson, G. Erickson, C.W Bale, A.D. Pelton, "F\*A\*C\*T: Guide to the operations", 1988
39. G.K. Sigworth, T.A Engh, "Refining of liquid aluminum-A review of important chemical factors", Scandinavian Journal of Metallurgy, v.11, 1982, pp.143-149
40. D.R. Gaskell, "Introduction to Metallurgical Thermodynamics", McGraw-Hill Kogakusha Ltd., 1973
41. J.C. Mitchell and C.S. Samis, "Activity of sodium in the Na-Al system and NaF and AlF<sub>3</sub> activities in NaF-AlF<sub>3</sub> melts", Transactions of the Metallurgical Society of AIME, v.245, June 1969, pp.1227-1234
42. R. Hultgren, R.L. Orr, P.D. Andersen, K.K. Kelly, "Selected values of the thermodynamic properties of Metals and Alloys", John-Wiley & Sons, 1963
43. H.H. Kellog, "Thermodynamic relationships in chlorine metallurgy", Journal of Metals, v.188, 1950, pp.862-872

44. R. Clift, J.R. Grace, M.E. Weber, "Bubbles, Drops, and Particles", Academic Press, 1978, pp.23-28
45. G. Lang, "GieBeigenschaften und Oberflächenspannung von Aluminium und binaren Aluminiumlegierungen; Teil III: Oberflächenspannung", Aluminium, 1973, v.49, n.3, pp.231-238
46. E. Gebhardt, M. Becker, S. Dorner, "Dichte und Viskosität von Schmelzen aus Aluminium und Aluminiumlegierungen", Aluminium, v.31, n.7/8, pp.315-321
47. M. Sano, K. Mori, "Bubble formation from single nozzles in liquid metals", Transactions of the JIM, v.17, 1976, pp.344-352
48. J. Botor, "Mass transfer surface in the process of liquid metal bubbling", Metallurgia I Odlewnictwo, v.7, n.4, 1981, pp.393-405
49. G.A. Irons, R.I.L. Guthrie, "Bubble formation at nozzles in pig iron", Metallurgical Transactions B, v.9B, 1978, pp.101-110
50. W. Siemes, "Gasblasen in Flüssigkeiten, Teil I: Entstehung von Gasblasen an nach oben gerichteten kreisförmigen Düsen", Chemie-Ing-Techn, v.26, n.8/9, 1954, pp.479-496
51. R.R. Hughes, A.E. Handlos, H.D. Evans, R.L. Mayrock, "The formation of bubbles at simple orifices", Chemical Engineering Progress, v.51, n.12, 1955, pp.557-563
52. L. Davidson, E.H. Amick, "Formation of gas bubbles at horizontal orifices", American Institute of Chemical Engineers Journal, v.2, n.3, 1956, pp.337-342
53. W.B. Hayes, B.W. Hardy, C.D. Holland, "Formation of gas bubbles at submerged orifices", American Institute of Chemical Engineers Journal, v.5, n.3, 1959, pp.319-324
54. J.F. Davidson, B.O.G. Schuler, "Bubble formation at an orifice in an inviscid liquid", Institution of Chemical Engineers Transactions, v.38, 1960, pp.335-342
55. A. Kupferberg, G.J. Jameson, "Bubble formation at a submerged orifice above a gas chamber of finite volume", Institution of Chemical Engineers

- 
- Transactions, v.47, 1969, pp.T241-T250
56. T. Tadaki, S. Maeda, "The size of bubbles from single orifices", *Kogaku Kogaku*(Abridged addition), v.1, n.1, 1963, pp.55-60
  57. D.J. McCann, R.G.H. Prince, "Bubble formation and weeping at a submerged orifice", *Chemical Engineering Science*, v.24, 1969, pp.801-814
  58. W.H. Coulter, "High speed automatic blood cell counter and cell size analyzer", *Proceedings of the National Electronic Conference*, 1956, pp.1034-1042
  59. R.W. DeBlois, C.P. Bean, "Counting and sizing of submicron particles by the resistive pulse technique", *The Review of Scientific Instruments*, v.41, n.7, 1970, pp.909-916
  60. J.C. Maxwell, "A Treatise on Electricity and Magnetism", Clarendon Press, 3rd ed., v.1, 1904, p.429
  61. D. Doutre, "The development and application of a rapid method of evaluating molten metal cleanliness", Ph.D Thesis, 1984, McGill University, Montreal, Canada
  62. V. Lee, F.Dallaire, "LIMCA Programme to interface with TN 7200 MCA", McGill University, Montreal, Canada
  63. F.Dallaire, in Preliminary Technical Report on LIMCA Signal Analysis Equipment, 1990, McGill University, Montreal, Canada
  64. W.Geller, "Theory of the degassing of metal baths by rinsing gas", Translated from *Zeitschrift Metallkunde*, v.35, n.11, pp.213-217, 1943, Henry Brucher Translations, n.1656
  65. R.J. Andreini, J.S. Foster, R.W. Callen, "Characterization of gas bubbles injected into molten metals under laminar flow conditions", *Metallurgical Transactions B*, v.8B, 1977, pp.625-631
  66. R. Higbie, "The rate of absorption of a pure gas into a still liquid during short periods of exposure", *Transactions of the American Institute of Chemical Engineers*, v.31, 1934-1935, pp.365-389
  67. T. Iida, R.I.L. Guthrie, "The Physical Properties of Liquid Metals",

- 
- Clarendon Press, Oxford, 1988, p.188
68. F. Lihl, E. Nachtigall, A.Schwiger,"Viscosimetric measurements on liquid aluminum and aluminum alloys", Funfte Internat. Leichtmetalltagung, Leoben, 1968-1969, pp.33-38
  69. W.R.D. Jones, W.L. Bartlett,"The viscosity of aluminum and binary aluminum alloys", Journal of the Institute of the Metals, v.81, 1952-53, pp.145-152
  70. C.H. Ma, R.A. Swalin,"A study of solute diffusion in liquid tin", Acta Metallurgica, v.8, June 1960, pp.288-395
  71. R.A. Swalin, V.G. Leak,"Diffusion of heterovalent solutes in liquid silver", Acta Metallurgica, v.13, May 1965, pp.471-478
  72. J.E. Freud,"Statistics; A first course", 3.rd ed.,Prentice-Hall, 1970
  73. R. Hultgren, P.D. Desal, D.T. Hawkins, M. Gleiser, K.K. Kelly, D.D. Wagman,"Selected values of the Thermodynamic Properties of the Elements", ASM, 1973, p.332
  74. R. Clift, J.R. Grace, M.E. Weber,"Bubbles, Drops, and Particles", Academic Press, 1978
  75. W.G. Davenport, D.H. Wakelin, A.V. Bradshaw,"Interaction of both bubbles and gas jets with liquids", in Heat and Mass Transfer in Process Metallurgy, ed. by A.W.D. Hills, pp.207-241
  76. C.J. Smithells, E.A. Brandes,"Metals Reference Book", 5.th ed., Butterworths, London, 1976
  77. R. Clift, J.R. Grace, M.E. Weber,"Bubbles, Drops, and Particles", Academic Press, 1978, p.49
  78. R.B. Bird, W.E. Steward, E.N. Lightfoot,"Transport Phenomena", John Wiley & Sons, 1960, p.59
  79. W.N. Bond, D.A. Newton, Philosophical Magazine and Journal of Science, v.5, 1928, pp.794-800
  80. R.B. Bird, W.E. Steward, E.N. Lightfoot,"Transport Phenomena", John Wiley & Sons, 1960, p.193

- 
81. R. Clift, J.R. Grace, M.E. Weber, "Bubbles, Drops, and Particles", Academic Press, 1978, p.112
  82. R.I.L. Guthrie, "Engineering in Process Metallurgy", Clarendon Press, Oxford, 1989, p.295
  83. Y. Sahai, R.I.L Guthrie, "Hydrodynamics of gas stirred melts: Part I. Gas/Liquid coupling", Metallurgical Transactions B, v. 13B, 1982, pp.193-202

APPENDICES

APPENDIX	Page
A Estimation of the exit temperature of the fluxing gas into the melt	178
B Experimental data for gas fluxing experiments	183
C Theoretical relationships for the determination of diffusivities in liquid metals	195
D Estimation of self-diffusion coefficient of aluminum and diffusion coefficient of magnesium in aluminum at 730 °C	198
E Prediction of the surface velocity	201
F Size and number distribution of the particles	206
G Sources of error	215

APPENDIX A

Estimation of the exit temperature of the fluxing gas into the melt

In order to estimate the exit temperature of the fluxing gas into the melt a heat balance calculation was carried out. In the calculations it was assumed that the resistance to heat transfer through the wall of the lance(1 mm in thickness) was negligible and the wall temperature was constant and equal to the temperature of the melt(730 °C). Control volume chosen for the calculations is shown in Figure A1.

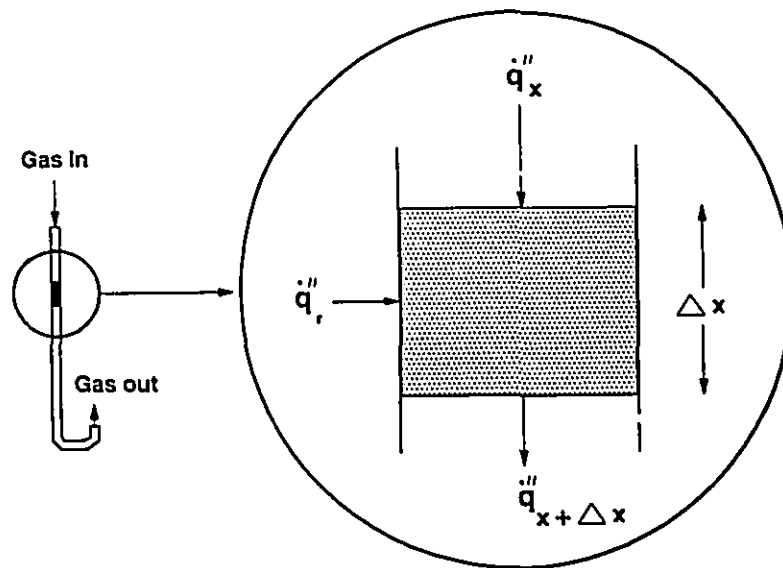


Figure A1. The control volume chosen for the calculations

$\dot{q}''_x$  and  $\dot{q}''_{x+\Delta x}$  are heat fluxes carried in and out of the control volume respectively by the flowing gas.  $\dot{q}''_r$  is the heat flux into the control volume by convection from the wall of the lance. The amount of heat transferred into the control volume per unit time is given by:

$$\text{Heat in} = \dot{q}_x'' \frac{\pi D^2}{4} + \dot{q}_R'' \pi D \Delta x \quad (\text{A.1})$$

The amount of heat transferred out of the control volume per unit time is given by:

$$\text{Heat out} = \dot{q}_{x+\Delta x}'' \frac{\pi D^2}{4} \quad (\text{A.2})$$

Under steady state conditions Heat in=Heat out and one obtains:

$$\frac{d\dot{q}_x''}{dx} = \frac{4}{D} \dot{q}_r'' \quad (\text{A.3})$$

where:

$$\dot{q}_x'' = \rho C_p U T_B \quad (\text{A.4})$$

$$\dot{q}_r'' = h (T_w - T_B) \quad (\text{A.5})$$

In the above equation,  $\rho$  is the density,  $C_p$  is the heat capacity,  $U$  is the velocity and  $T_B$  is the bulk temperature of the melt respectively,  $h$  is the heat transfer coefficient and  $T_w$  is the wall temperature. Integrating Eqn.(A.3) between  $x=0$  and  $X=L$  with corresponding initial bulk temperature of the gas  $T_B^i$  and exit temperature  $T_B^e$ , one would obtain:

$$T_B^e = T_w - (T_w - T_B^i) e^{-\left(\frac{4 h L}{D \rho C_p U}\right)} \quad (\text{A.6})$$

In the calculations, exit temperature  $T_B^e$  was calculated for  $L=1$  mm and the calculations were repeated until the actual length of the lance below the melt surface(22 cm) was reached. After each calculation, the physical properties and the velocity of the gas were recalculated.

The heat transfer coefficient,  $h$ , was calculated from the following relationships[A1].

$$\frac{h D}{k} = 1.356 (x^*)^{-1/3} - 0.7 \quad \text{for } x^* \leq 0.02 \quad (\text{A.7})$$

$$\frac{h D}{k} = 3.657 + 9.641 (x^+ 10^3)^{-0.488} e^{-28.6 x^+} \quad \text{for } x^+ > 0.02 \quad (\text{A.8})$$

where  $x^+$  is defined as:

$$x^+ = \frac{2 x}{D} \frac{1}{Pr Re} \quad (\text{A.9})$$

In the above equation  $Pr$ , is a Prandtl, and  $Re$ , is a Reynolds number which are defined as:

$$Pr = \frac{\mu C_p}{k} \quad ; \quad Re = \frac{\rho U D}{\mu} \quad (\text{A.10})$$

In the above equations  $\mu$  is the viscosity, and  $k$  is the thermal conductivity of the gas respectively.

The argon gas with the following properties[A2] was chosen for the calculations:

$$\mu = 222 \cdot 10^{-6} \text{ gm/cm-sec (@20 } ^\circ\text{C, 1 Atm.)}$$

$$k = 42.57 \cdot 10^{-6} \text{ cal/cm-sec-K (@25 } ^\circ\text{C, 1 Atm.)}$$

$$\rho = 1.947 \cdot 10^{-3} \text{ gm/cm}^3 \text{ (@25 } ^\circ\text{C, 1 Atm.)}$$

$$C_p = 0.124 \text{ cal/g-K (@20 } ^\circ\text{C, 1 Atm.)}$$

The result of the calculations are shown in Figure A2 for three different gas flow rates. The horizontal dotted line represents the temperature of the bath(730 °C). According to the calculations the temperature of the argon gas at the exit point reached the melt temperature for the lowest and intermediate gas flow rates and was about 17 °C lower at the highest gas flow rate. In Figure A3, listing of the FORTRAN program that was used for the calculations is presented.

References:

- A1. W.M. Rohsenow, J.P. Hartnett, E.N. Ganic, "Handbook of Heat Transfer Applications", 2nd ed., 1985, McGraw-Hill
- A2. Weast, R.C., Astle, M.J., Beyer, W.H., CRC Handbook of Chemistry and Physics, 68 th edition

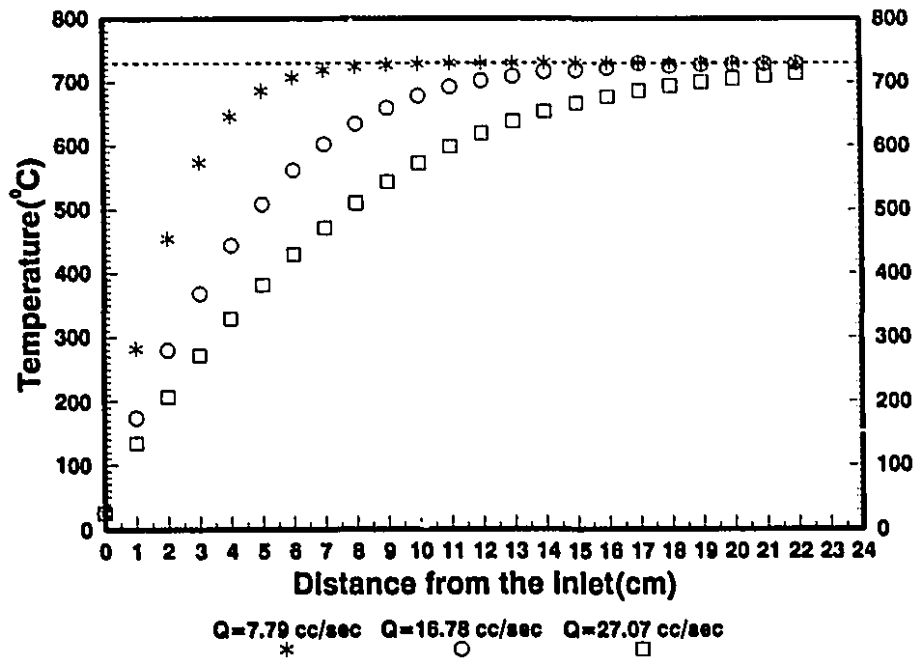


Figure A2. Temperature of the gas as a function of distance from the entry point into the lance

```

DOUBLE PRECISION CP,VIS,RHO,TK,TC,VIN,TIN,TOUT
DOUBLE PRECISION TW,XPLUS,RE
OPEN(11,FILE='C:\BAHA\DATA3',FORM='FORMATTED')
CP=0.124
VIS=222E-6
RHO=1.947E-3
TK=42.57E-6
C.....
VIN=215.0
TIN=298.0
C.....
TW=1003.0
C.....
D=0.4
DELX=0.1
PR=VIS*CP/TK
RE=RHO*VIN*D/VIS
BOY=22.0
M=BOY/DELX
C.....
DO 1 I=1,M
X=DELX*I
XPLUS=2*X/(RE*PR*D)
IF (XPLUS.LE. 0.02) GOTO 2
TC=TK/D*(3.657+9.641/(1E3*XPLUS)**0.488*DEXP(-28.6*XPLUS))
GOTO 4
2 TC=TK/D*(1.356/XPLUS**0.3333-0.7)
4 TOUT=TW-(TW-TIN)*DEXP(-4*DELX*TC/(D*RHO*CP*VIN))
US=TC*D/TK
WRITE(11,102) X,XPLUS
WRITE(11,103) TC,TK
WRITE(11,104) RE,US
WRITE(11,105) TOUT
RE=RE*VIS
RHO=TIN/TOUT*RHO
VIN=TOUT/TIN*VIN
VIS=(TOUT/TIN)**0.8*VIS
TK=(TOUT/TIN)**0.8*TK
TIN=TOUT
RE=RE/VIS
CP=PR*TK/VIS
WRITE(11,99) CP
1 CONTINUE
WRITE(*,100) X
WRITE(*,101) TOUT
99 FORMAT('CP=',5X,F5.2)
100 FORMAT(5X,F5.2)
101 FORMAT(5X,F7.2)
102 FORMAT('X=',F15.11,' ',XPLUS=',F15.11)
103 FORMAT('TC=',F15.11,' ',TK=',F15.11)
104 FORMAT('RE=',F15.11,' ',NUS=',F15.11)
105 FORMAT('TOUT=',F7.2)
STOP
END

```

Figure A3. Listing of the computer programme used in the calculations of results presented in Figure A2.

## APPENDIX B

Experimental data for gas fluxing experimentsExperimental data for Calcium removal from commercial purity aluminum:Continuous chlorination:

<b>#1.</b> %Cl <sub>2</sub> =2 Q=26.22 cc/sec f=11.5 bub/sec d <sub>c</sub> =1.613 cm		<b>#2.</b> %Cl <sub>2</sub> =2 Q=26.22 cc/sec f=12.5 bub/sec d <sub>c</sub> =1.569 cm		<b>#3.</b> %Cl <sub>2</sub> =10 Q=26.22 cc/sec f=14 bub/sec d <sub>c</sub> =1.56 cm	
Time(min)	wt-ppm Ca	Time(min)	wt-ppm Ca	Time(min)	wt-ppm Ca
0	45.4	0	36	0	52
2	37.4	3	22	3	38
4	31	6	16	7	25
6	24.3	10	9	12	15
9	18	15	5	22	4
13	11.6	25	1	37	1
17	6.6				
22	3.5				
<b>#4.</b> %Cl <sub>2</sub> =10 Q=26.22 cc/sec f=11.5 bub/sec d <sub>c</sub> =1.666 cm		<b>#5.</b> %Cl <sub>2</sub> =25 Q=26.22 cc/sec f=11.5 bub/sec d <sub>c</sub> =1.619 cm		<b>#6.</b> %Cl <sub>2</sub> =25 Q=26.22 cc/sec f=12 bub/sec d <sub>c</sub> =1.569 cm	
Time(min)	wt-ppm Ca	Time(min)	wt-ppm Ca	Time(min)	wt-ppm Ca
0	45.2	0	43.4	0	40.9
2	34.7	2	32.8	3	26
4	27.9	4	28.4	6	20
6	23.1	6	22.1	10	11.9
9	17	9	16.2	15	6
12	11.6	12	11.6		
16	7.6	16	6.6		
		20	4.8		

<p>#7. %Cl<sub>2</sub>=10 Q=56.45 cc/sec f=17 bub/sec d<sub>c</sub>=1.851 cm</p>		<p>#8. %Cl<sub>2</sub>=10 Q=56.45 cc/sec f=15 bub/sec d<sub>c</sub>=1.93 cm</p>		<p>#9. %Cl<sub>2</sub>=10 Q=91.12 cc/sec f=16 bub/sec d<sub>c</sub>=2.216 cm</p>	
Time(min)	wt-ppm Ca	Time(min)	wt-ppm Ca	Time(min)	wt-ppm Ca
0	45	0	40.6	0	43
3	25.8	3	25	3	21.6
6	15.8	6	17	6	12
9	8.5	10	9.4	9	5.8
12	4.3	15	4.3		
<p>#10. %Cl<sub>2</sub>=10 Q=91.12 cc/sec f=16.5 bub/sec d<sub>c</sub>=2.193 cm</p>					
Time(min)	wt-ppm Ca				
0	44				
3	23.9				
6	13.9				
12	3.3				

Intermittent tests:

<p>11. %Cl<sub>2</sub>=2 Q=26.22 cc/sec</p>		<p>#12. %Cl<sub>2</sub>=10 Q=26.22 cc/sec</p>		<p>#13. %Cl<sub>2</sub>=25 Q=26.22 cc/sec</p>	
Time(min)	wt-ppm Ca	Time(min)	wt-ppm Ca	Time(min)	wt-ppm Ca
0	36	0	37.5	0	38.9
3	33	2	35.3	3	33.1
6	29	4	30.6	6	29.8
9	25	7	28.4	9	26.6
13	22			13	24
<p>#14. %Cl<sub>2</sub>=10 Q=56.45 cc/sec</p>		<p>#15. %Cl<sub>2</sub>=10 Q=91.12 cc/sec</p>			
Time(min)	wt-ppm Ca	Time(min)	wt-ppm Ca		
0	32.3	0	36.3		
3	27.8	2	32		
6	25.9	5	27.1		
		8	21		
		12	18.3		
		16	14.9		

Argon injection tests:

#16. Q=26.22 cc/sec		#17. Q=56.45 cc/sec		#18. Q=91.12 cc/sec	
Time(min)	wt-ppm Ca	Time(min)	wt-ppm Ca	Time(min)	wt-ppm Ca
0	44.1	0	40	0	38.7
3	43.3	3	39.5	3	36.7
6	43.4	6	39	6	37.2
10	42.8	10	38	10	35.5
25	39.4	25	35	15	34.5
40	36.4	35	34	20	33.3
60	31.9			25	32.7
				35	31.2
				45	29.7

Experimental data for Calcium removal from magnesium containing alloys:Continuous chlorination:

<p>#1. %Cl<sub>2</sub>=2 Q=26.22 cc/sec f=15 bub/sec d<sub>c</sub>=1.476 cm</p>			<p>#2. %Cl<sub>2</sub>=2 Q=26.22 cc/sec f=15.5 bub/sec d<sub>c</sub>=1.46 cm</p>		
Time(min)	wt-ppm Ca	wt% Mg	Time(min)	wt-ppm Ca	Wt% Mg
0	49.6	1.031	0	47.2	1.05
3	41.1	1.0319	2	38.6	1.036
6	30.4	1.0267	4	35.4	1.06
10	21.4	1.0296	6	28.8	1.066
15	12.1	1.0334	9	21.4	1.056
25	7.4	1.021	12	17.4	1.067
			16	10.9	1.063
<p>#3. %Cl<sub>2</sub>=10 Q=26.22 cc/sec f=17 bub/sec d<sub>c</sub>=1.462 cm</p>			<p>#4. %Cl<sub>2</sub>=10 Q=26.22 cc/sec f=14 bub/sec d<sub>c</sub>=1.56 cm</p>		
Time(min)	wt-ppm Ca	wt% Mg	Time(min)	wt-ppm Ca	wt% Mg
0	40	1.09	0	47	1.016
3	26	1.07	3	29.5	1.0115
6	16	1.07	6	22	1.0066
10	9	1.07	10	12	1.0098
15	4	1.04			
25	1	1.06			
<p>#5. %Cl<sub>2</sub>=25 Q=26.22 cc/sec f=14 bub/sec d<sub>c</sub>=1.525 cm</p>			<p>#6. %Cl<sub>2</sub>=25 Q=26.22 cc/sec f=14 bub/sec d<sub>c</sub>=1.516 cm</p>		
Time(min)	wt-ppm Ca	wt% Mg	Time(min)	wt-ppm Ca	wt% Mg
0	47	1.063	0	46.7	1.06
6	23	1.0541	2	34.8	1.039
15	9	1.0357	4	27.1	1.043
			6	21.8	1.068
			9	17.1	1.0308
			12	11.3	1.053
			16	7.6	1.036

<p>#7. %Cl<sub>2</sub>=10 Q=56.45 cc/sec f=14 bub/sec d<sub>c</sub>=1.975 cm</p>			<p>#8. %Cl<sub>2</sub>=10 Q=56.45 cc/sec f=15 bub/sec d<sub>c</sub>=1.93 cm</p>		
Time(min)	wt-ppm Ca	wt% Mg	Time(min)	wt-ppm Ca	wt% Mg
0	50	0.9936	0	41	1.0
3	32	0.9981	3	21	1.0
6	18	0.9825	6	14	1.0
10	8	0.9811			
<p>#9. %Cl<sub>2</sub>=10 Q=56.45 cc/sec f=15 bub/sec d<sub>c</sub>=1.93 cm</p>			<p>#10. %Cl<sub>2</sub>=10 Q=91.12 cc/sec f=16 bub/sec d<sub>c</sub>=2.216 cm</p>		
Time(min)	wt-ppm Ca	wt% Mg	Time(min)	wt-ppm Ca	wt% Mg
0	39	0.96	0	47	1.0187
3	21	0.955	3	20	0.9984
6	12	0.95	6	8	0.988
12	5	0.94			

Intermittent tests:

<p>#11. %Cl<sub>2</sub>=2 Q=26.22 cc/sec</p>			<p>#12. %Cl<sub>2</sub>=10 Q=26.22 cc/sec</p>		
Time(min)	wt-ppm Ca	wt% Mg	Time(min)	wt-ppm Ca	wt% Mg
0	29.7	1.072	0	36.9	1.056
3	26.6	1.07	3	28.8	1.015
6	23	1.056	6	23.3	1.0366
9	21	1.06	11	18	1.047
13	16.4	1.06	16	12	1.036
17	13.8	1.07			
<p>#13. %Cl<sub>2</sub>=25 Q=26.22 cc/sec</p>			<p>#14. %Cl<sub>2</sub>=10 Q=56.45 cc/sec</p>		
Time(min)	wt-ppm Ca	wt% Mg	Time(min)	wt-ppm Ca	wt% Mg
0	30	1.14	0	24	1.054
3	25.6	1.14	3	15	1.0498
6	21.9	1.15	6	12.1	1.0497
9	17.5	1.145	9	7.6	1.048
14	14	1.16			

#15. %Cl <sub>2</sub> =10 Q=91.12 cc/sec		
Time(min)	wt-ppm Ca	wt% Mg
0	23.7	1.085
3	16.5	1.088
6	14	1.084
9	7.4	1.087

Argon injection tests:

#16. Q=26.22 cc/sec			#17. Q=56.45 cc/sec		
Time(min)	wt-ppm Ca	wt% Mg	Time(min)	wt-ppm Ca	wt% Mg
0	45	1.03	0	49.9	1.023
3	44.5	1.03	3	48.5	1.023
6	44.5	1.02	6	50.6	1.025
10	44	1.03	10	47.9	1.024
15	43	1.03	15	47.7	1.014
25	42	1.0	25	46.3	1.02
40	40	1.0	40	45.7	1.023
		1.1	60	45.9	1.011

#18. Q=91.12 cc/sec		
Time(min)	wt-ppm Ca	wt% Mg
0	50	0.973
3	49	1.0
6	47.5	0.9817
10	46.9	0.974
15	46.7	0.979
25	46	0.985
40	45	0.9795

Data for Sodium removal from commercial purity aluminumContinuous chlorination:

<p>#1. %Cl<sub>2</sub>=2 Q=26.22 cc/sec f=12 bub/sec d<sub>c</sub>=1.59 cm</p> <table border="1"> <thead> <tr> <th>Time(min)</th> <th>wt-ppm Na</th> </tr> </thead> <tbody> <tr><td>0</td><td>8</td></tr> <tr><td>2</td><td>4</td></tr> <tr><td>4</td><td>2</td></tr> </tbody> </table>	Time(min)	wt-ppm Na	0	8	2	4	4	2	<p>#2. %Cl<sub>2</sub>=2 Q=26.22 cc/sec f=13 bub/sec d<sub>c</sub>=1.548 cm</p> <table border="1"> <thead> <tr> <th>Time(min)</th> <th>wt-ppm Na</th> </tr> </thead> <tbody> <tr><td>0</td><td>17</td></tr> <tr><td>2</td><td>8.7</td></tr> <tr><td>4</td><td>4.4</td></tr> <tr><td>7</td><td>1.6</td></tr> <tr><td>10</td><td>0.6</td></tr> </tbody> </table>	Time(min)	wt-ppm Na	0	17	2	8.7	4	4.4	7	1.6	10	0.6	<p>#3. %Cl<sub>2</sub>=10 Q=26.22 cc/sec f=12 bub/sec d<sub>c</sub>=1.642 cm</p> <table border="1"> <thead> <tr> <th>Time(min)</th> <th>wt-ppm Na</th> </tr> </thead> <tbody> <tr><td>0</td><td>15.2</td></tr> <tr><td>2</td><td>7.4</td></tr> <tr><td>4</td><td>4.3</td></tr> <tr><td>6</td><td>1.9</td></tr> </tbody> </table>	Time(min)	wt-ppm Na	0	15.2	2	7.4	4	4.3	6	1.9
Time(min)	wt-ppm Na																															
0	8																															
2	4																															
4	2																															
Time(min)	wt-ppm Na																															
0	17																															
2	8.7																															
4	4.4																															
7	1.6																															
10	0.6																															
Time(min)	wt-ppm Na																															
0	15.2																															
2	7.4																															
4	4.3																															
6	1.9																															
<p>#4. %Cl<sub>2</sub>=10 Q=26.22 cc/sec f=12 bub/sec d<sub>c</sub>=1.642 cm</p> <table border="1"> <thead> <tr> <th>Time(min)</th> <th>wt-ppm Na</th> </tr> </thead> <tbody> <tr><td>0</td><td>8</td></tr> <tr><td>3</td><td>3</td></tr> <tr><td>6</td><td>1</td></tr> </tbody> </table>	Time(min)	wt-ppm Na	0	8	3	3	6	1	<p>#5. %Cl<sub>2</sub>=25 Q=26.22 cc/sec f=11 bub/sec d<sub>c</sub>=1.64 cm</p> <table border="1"> <thead> <tr> <th>Time(min)</th> <th>wt-ppm Na</th> </tr> </thead> <tbody> <tr><td>0</td><td>12.3</td></tr> <tr><td>2</td><td>6.6</td></tr> <tr><td>4</td><td>3.8</td></tr> <tr><td>6</td><td>1.7</td></tr> </tbody> </table>	Time(min)	wt-ppm Na	0	12.3	2	6.6	4	3.8	6	1.7	<p>#6. %Cl<sub>2</sub>=25 Q=26.22 cc/sec f=13 bub/sec d<sub>c</sub>=1.55 cm</p> <table border="1"> <thead> <tr> <th>Time(min)</th> <th>wt-ppm Na</th> </tr> </thead> <tbody> <tr><td>0</td><td>5.3</td></tr> <tr><td>3</td><td>2</td></tr> <tr><td>7</td><td>0.4</td></tr> </tbody> </table>	Time(min)	wt-ppm Na	0	5.3	3	2	7	0.4				
Time(min)	wt-ppm Na																															
0	8																															
3	3																															
6	1																															
Time(min)	wt-ppm Na																															
0	12.3																															
2	6.6																															
4	3.8																															
6	1.7																															
Time(min)	wt-ppm Na																															
0	5.3																															
3	2																															
7	0.4																															
<p>#7. %Cl<sub>2</sub>=10 Q=56.45 cc/sec f=15 bub/sec d<sub>c</sub>=1.929 cm</p> <table border="1"> <thead> <tr> <th>Time(min)</th> <th>wt-ppm Na</th> </tr> </thead> <tbody> <tr><td>0</td><td>18.8</td></tr> <tr><td>2</td><td>9.9</td></tr> <tr><td>4</td><td>4.6</td></tr> <tr><td>6</td><td>2.1</td></tr> </tbody> </table>	Time(min)	wt-ppm Na	0	18.8	2	9.9	4	4.6	6	2.1	<p>#8. %Cl<sub>2</sub>=10 Q=56.45 cc/sec f=15 bub/sec d<sub>c</sub>=1.929 cm</p> <table border="1"> <thead> <tr> <th>Time(min)</th> <th>wt-ppm Na</th> </tr> </thead> <tbody> <tr><td>0</td><td>14.4</td></tr> <tr><td>2</td><td>5.7</td></tr> <tr><td>4</td><td>2.8</td></tr> <tr><td>6</td><td>1.2</td></tr> </tbody> </table>	Time(min)	wt-ppm Na	0	14.4	2	5.7	4	2.8	6	1.2	<p>#9. %Cl<sub>2</sub>=10 Q=91.12 cc/sec f=16 bub/sec d<sub>c</sub>=2.215 cm</p> <table border="1"> <thead> <tr> <th>Time(min)</th> <th>wt-ppm Na</th> </tr> </thead> <tbody> <tr><td>0</td><td>12.9</td></tr> <tr><td>2</td><td>4.8</td></tr> <tr><td>4</td><td>1.7</td></tr> </tbody> </table>	Time(min)	wt-ppm Na	0	12.9	2	4.8	4	1.7		
Time(min)	wt-ppm Na																															
0	18.8																															
2	9.9																															
4	4.6																															
6	2.1																															
Time(min)	wt-ppm Na																															
0	14.4																															
2	5.7																															
4	2.8																															
6	1.2																															
Time(min)	wt-ppm Na																															
0	12.9																															
2	4.8																															
4	1.7																															
<p>#10. %Cl<sub>2</sub>=10 Q=91.12 cc/sec f=18 bub/sec d<sub>c</sub>=2.13 cm</p> <table border="1"> <thead> <tr> <th>Time(min)</th> <th>Wt-ppm Na</th> </tr> </thead> <tbody> <tr><td>0</td><td>17.4</td></tr> <tr><td>2</td><td>6.3</td></tr> <tr><td>4</td><td>1.9</td></tr> </tbody> </table>	Time(min)	Wt-ppm Na	0	17.4	2	6.3	4	1.9																								
Time(min)	Wt-ppm Na																															
0	17.4																															
2	6.3																															
4	1.9																															

Intermittent tests:

<p>#11. %Cl<sub>2</sub>=2 Q=26.12 cc/sec</p>		<p>#12. %Cl<sub>2</sub>=10 Q=26.12 cc/sec</p>		<p>#13. %Cl<sub>2</sub>=25 Q=26.12 cc/sec</p>	
Time(min)	wt-ppm Na	Time(min)	wt-ppm Na	Time(min)	wt-ppm Na
0	16.6	0	20	0	12.1
1	13.4	1	16	2	8.6
3	8	3	9	4	5
		5	5.5	6	3.3
		8	3	9	1.4
<p>#14. %Cl<sub>2</sub>=10 Q=56.45 cc/sec</p>		<p>#15. %Cl<sub>2</sub>=10 Q=91.12 cc/sec</p>			
Time(min)	wt-ppm Na	Time(min)	wt-ppm Na		
0	13.4	0	12.6		
1	10.3	1	8.1		
3	5.5	3	4.4		
5	2.9	5	2.2		
		7	0.5		

Argon injection tests:

<p>#16. Q=26.22 cc/sec</p>		<p>#17. Q=26.22 cc/sec</p>		<p>#18. Q=26.22 cc/sec</p>	
Time(min)	wt-ppm Na	Time(min)	wt-ppm Na	Time(min)	wt-ppm Na
0	17.6	0	16.4	0	12
2	11.2	2	10.8	3	5
4	7.1	4	7.3	6	3
6	5.1	6	4.8	10	1
9	2.2				
<p>#19. Q=56.22 cc/sec</p>		<p>#20. Q=56.22 cc/sec</p>		<p>#21. Q=91.12 cc/sec</p>	
Time(min)	wt-ppm Na	Time(min)	wt-ppm Na	Time(min)	wt-ppm Na
0	18.6	0	26.9	0	15.1
3	9.1	2	15.5	2	8.1
6	4.8	4	8.2	4	3.6
		6	4.8		

Data for the removal of Sodium from the magnesium containing alloy:Continuous chlorination:

<p>#1. %Cl<sub>2</sub>=2 Q=26.22 cc/sec f=13 bub/sec d<sub>c</sub>=1.548 cm</p>			<p>#2. %Cl<sub>2</sub>=2 Q=26.22 cc/sec f=14 bub/sec d<sub>c</sub>=1.51 cm</p>		
Time(min)	wt-ppm Na	wt% Mg	Time(min)	wt-ppm Na	wt% Mg
0	19.2	0.8327	0	4.7	0.99
3	12.4	0.83	3	2.9	0.982
6	8.6	0.827	6	1.7	0.99
10	4.7	0.822			
15	1.8	0.831			
20	0.5	0.8149			
<p>#3. %Cl<sub>2</sub>=10 Q=26.22 cc/sec f=17 bub/sec d<sub>c</sub>=1.548 cm</p>			<p>#4. %Cl<sub>2</sub>=10 Q=26.22 cc/sec f=16 bub/sec d<sub>c</sub>=1.492 cm</p>		
Time(min)	wt-ppm Na	wt% Mg	Time(min)	wt-ppm Na	wt% Mg
0	8.6	1.0369	0	24	1.1
2	5.6	1.0272	2	13	1.09
4	3.7	1.0232	4	10	1.07
6	2.5	1.0251	6	6	1.07
			10	3	1.06
			15	1	1.05
<p>#5. %Cl<sub>2</sub>=25 Q=26.22 cc/sec f=15.5 bub/sec d<sub>c</sub>=1.466 cm</p>			<p>#6. %Cl<sub>2</sub>=25 Q=26.22 cc/sec f=15 bub/sec d<sub>c</sub>=1.482 cm</p>		
Time(min)	wt-ppm Na	wt% Mg	Time(min)	wt-ppm Na	wt% Mg
0	31.2	0.923	0	13	1.07
2	20.8	0.902	2	8.5	1.06
4	14.6	0.906	4	5.8	1.05
6	9.4	0.889	7	3.2	1.05
9	5.2	0.882	11	1.4	1.03
12	3	0.8895			
16	1.3	0.8759			

<p>#7. %Cl<sub>2</sub>=10 Q=56.45 cc/sec f=17 bub/sec d<sub>c</sub>=1.851 cm</p>			<p>#8. %Cl<sub>2</sub>=10 Q=56.45 cc/sec f=16 bub/sec d<sub>c</sub>=1.889 cm</p>		
Time(min)	wt-ppm Na	wt% Mg	Time(min)	wt-ppm Na	wt% Mg
0	12.9	0.8284	0	35.8	1.02
3	5.8	0.8292	2	20.5	0.98
6	2.1	0.8099	4	12	0.988
			6	7.4	1.01
			9	2.9	0.99
<p>#9. %Cl<sub>2</sub>=10 Q=91.12 cc/sec f=18 bub/sec d<sub>c</sub>=2.13 cm</p>			<p>#10. %Cl<sub>2</sub>=10 Q=91.12 cc/sec f=19 bub/sec d<sub>c</sub>=2.09 cm</p>		
Time(min)	wt-ppm Na	wt% Mg	Time(min)	wt-ppm Na	wt% Mg
0	20.6	0.7448	0	28.4	1.066
3	6.8	0.7278	2	15.5	1.047
6	2	0.7171	4	8	1.031
			6	3.5	1.03
			9	1.4	1.0

Intermittent tests:

<p>#11. %Cl<sub>2</sub>=2 Q=26.22 cc/sec</p>			<p>#12. %Cl<sub>2</sub>=10 Q=26.22 cc/sec</p>		
Time(min)	wt-ppm Na	wt% Mg	Time(min)	wt-ppm Na	wt% Mg
0	17.2	0.963	0	14	1.01
2	12.1	0.95	1	12	1.0
4	9.2	0.975	3	9	0.995
6	6.6	0.979	5	6.5	0.98
9	4	0.965	7	4.5	0.97
<p>#13. %Cl<sub>2</sub>=25 Q=26.22 cc/sec</p>			<p>#14. %Cl<sub>2</sub>=25 Q=26.22 cc/sec</p>		
Time(min)	wt-ppm Na	wt% Mg	Time(min)	wt-ppm Na	wt% Mg
0	37.9	1.207	0	19.4	1.02
3	25	1.21	2	13.3	0.99
6	15.2	1.189	4	10.9	0.99
11	6.1	1.19	6	7.8	1.017
16	3	1.2	9	5.2	1.0
			12	3.2	1.0

#15. %Cl <sub>2</sub> =10 Q=56.45 cc/sec			#16. %Cl <sub>2</sub> =10 Q=91.12 cc/sec		
Time(min)	wt-ppm Na	wt% Mg	Time(min)	wt-ppm Na	wt% Mg
0	13.7	1.046	0	16	1.018
2	8.9	1.0495	2	7.7	0.998
4	5.8	1.05	5	3.1	1.015

Argon injection tests:

#16. Q=26.22 cc/sec			#17. Q=26.22 cc/sec		
Time(min)	wt-ppm Na	wt% Mg	Time(min)	wt-ppm Na	wt% Mg
0	29	1.06	0	35	1.18
3	23.8	1.06	2	33	1.19
7	18.6	1.04	4	31	1.19
12	12.2	1.04	6	28	1.18
			10	23	1.18
			15	17	1.18
			20	12	1.18
			30	7	1.17
			40	3	1.16
			60	1	1.17

#18. Q=26.22 cc/sec			#19. Q=56.45 cc/sec		
Time(min)	wt-ppm Na	wt% Mg	Time(min)	wt-ppm Na	wt% Mg
0	21.1	1.075	0	21.5	1.04
2	20	1.0783	2	17.1	1.04
4	18.7	1.1232	4	13.7	1.046
6	17.4	1.0955	7	11	1.038
9	15.1	1.0926	11	6.8	1.045
13	12.6	1.068	16	4.1	1.045
17	11.1	1.0575			

#20. Q=56.45 cc/sec			#21. Q=56.45 cc/sec		
Time(min)	wt-ppm Na	wt% Mg	Time(min)	wt-ppm Na	wt% Mg
0	20.7	1.06	0	18.6	1.097
2	18.7	1.06	2	16.7	1.11
4	18	1.09	4	15.4	1.098
6	16.4	1.1	6	13.6	1.097
8	14.3	1.08	10	10.9	1.098
11	12.6	1.088	20	7.6	1.108
15	11.6	1.1	30	4.4	1.086
20	8.6	1.0569	40	3	1.07
			60	1.1	1.06

#22. Q=91.12 cc/sec			#23. Q=91.12 cc/sec		
Time(min)	wt-ppm Na	wt% Mg	Time(min)	wt-ppm Na	wt% Mg
0	19.5	1.01	0	25.9	1.11
3	15.1	1.01	2	23.4	1.11
7	10.1	1.0	4	21.3	1.129
12	6.1	1.01	6	20.1	1.16
			9	17.8	1.19
			12	15.8	1.39
			16	12.9	1.17

## APPENDIX C

### Theoretical relationships for the determination of diffusivities in liquid metals:

In the following, theoretical relationships that were derived assuming that the mechanism of diffusion is similar to that for viscous flow, for the determination of diffusivities are presented. These theories have been presented in a critical review paper by Edwards et.al.[C1] They are presented here to serve as a quick reference.

In all the relationships, the diffusivities conforms to the following form:

$$D = F \mu^{-1} \quad (C.1)$$

#### C.1. Stokes-Einstein Equation:

Einstein derived an equation for diffusion in colloidal solutions based on considerations of Brownian movements. He obtained a relationship of the form:

$$D = \frac{k T}{6 \pi r \mu} \quad (C.2)$$

Where k is the Boltzmann constant. In the derivation of the above equation, the following assumptions were made:

- a) The solution is ideal
- b) The diffusing particles are hard spheres and move with uniform velocity
- c) The solvent is a continuous medium
- d) The spheres that make up both the medium and the solute are regarded as non-interacting.

#### C.2. Sutherland-Einstein Equation:

Sutherland presented a correction factor to Stokes-Einstein equation which takes into account friction between the diffusing particle and the medium. With this correction, the

original Stokes-Einstein equation takes the form:

$$D = \frac{k T}{6 \pi r \mu} \left[ \frac{1 + \frac{2 \mu}{\beta r}}{1 + \frac{3 \mu}{\beta r}} \right] \quad (\text{C.3})$$

In the above equation  $\beta$  is the coefficient of sliding friction between the diffusing particle and medium. When the diffusing particle is large compared to the particles of the medium  $\beta$  equals infinity and the above equation becomes the Stokes-Einstein equation. When the radius of the diffusing particle is approximately equal to that of the medium  $\beta$  becomes 0. In this case the above equation becomes:

$$D = \frac{k T}{4 \pi r \mu} \quad (\text{C.4})$$

The above equation is known as the Sutherland or Sutherland-Einstein equation.

### C.3. Walls and Upthegrove's Equation:

Walls and Upthegrove developed a three parameter equation for predicting diffusion coefficients. They obtained a relationship in the following form:

$$D = \frac{k T}{2 \pi r (2b + 1) \mu} \quad (\text{C.5})$$

in the above equation  $b$  is defined as the ratio of atomic radius of a diffusing particle to its interatomic spacing. When  $b=1/2$ , the above equation reduces to the Sutherland equation.

### C.4. Eyring's Equation:

Eyring et.al presented a model for diffusion based on their theory of absolute reaction rates and using the concept that the liquid structure contains a number of holes and void spaces.

The equation resulting from this model which describes diffusion as an activated process is given by:

$$D = \frac{\lambda_1 k T}{\lambda_2 \lambda_3 \mu} \quad (\text{C.6})$$

In the above equation  $\lambda_1$  and  $\lambda_2$  are interatomic distances perpendicular to the direction of motion and  $\lambda_3$  is the distance in the direction of motion.

Reference:

- C1. J.B. Edwards, E.E. Huckle, J.J. Martin, "Diffusion in binary liquid-metal systems", Part 2, Metallurgical Reviews, 120, 1968, pp 13-28

APPENDIX D

Estimation of self-diffusion coefficient of aluminum and diffusion coefficient of magnesium in aluminum at 730 °C

D.1. Estimation of self-diffusion coefficient of aluminum:

The self diffusion coefficient of aluminum at 730 °C was estimated graphically from the data of Protopapas et al.[D1] Their data together with the estimated value of the self diffusion coefficient of aluminum at 730 °C are shown in Figure D1.

Reference:

- D1. P. Protopapas, H.C. Andersen, N.H. Parlee, "Theory of transport in liquid metals. I. Calculation of self diffusion coefficients", *The Journal of Chemical Physics*, v.59, n.1, 1973, pp.15-25

D.2. Estimation of diffusion coefficient of magnesium in aluminum:

The diffusion coefficient of magnesium in aluminum at 730 °C was estimated graphically from the data presented in the following references:

References

- D2. J.B. Edwards, E.E. Huccke, J.J. Martin, "Diffusion in binary liquid-metal systems", Part I, *Metallurgical Reviews*, 120, 1968, pp 1-12
- D3. F.C. Dimayuga, "Vacuum Refining of Molten Aluminum", Ph.D Thesis, 1986, McGill University, Montreal, Canada

In Figure D2, Ref.1 and Ref.2 refer to the original references cited in Reference D2, and Ref.3 refers to the original reference cited in Reference D3. These original references are cited below:

*Ref.1. K. Emura, Tetsu to Hagene, 1939,25,24*

*Ref.2. H.A. Belosevsky, Legki Metallurgy, 1973,6,(10),18*

*Ref.3. K. Kovacora, M. Sipocz, "DIMETAZ, Proc. Intn'l. Conf. Diffusion Metals and Alloys", ed.by F.J.Kedves and D.L.Beke, Trans. Tech. SA, Switzerland, 1982, pp 533*

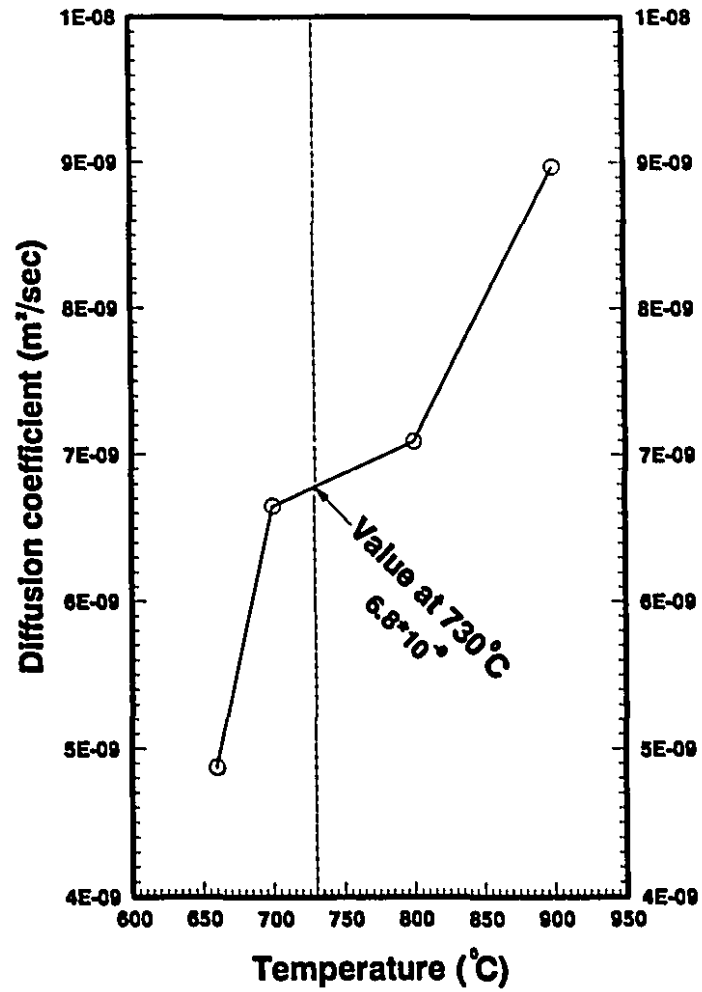


Figure D1. Self-diffusion coefficient of aluminum as a function of temperature[D1]

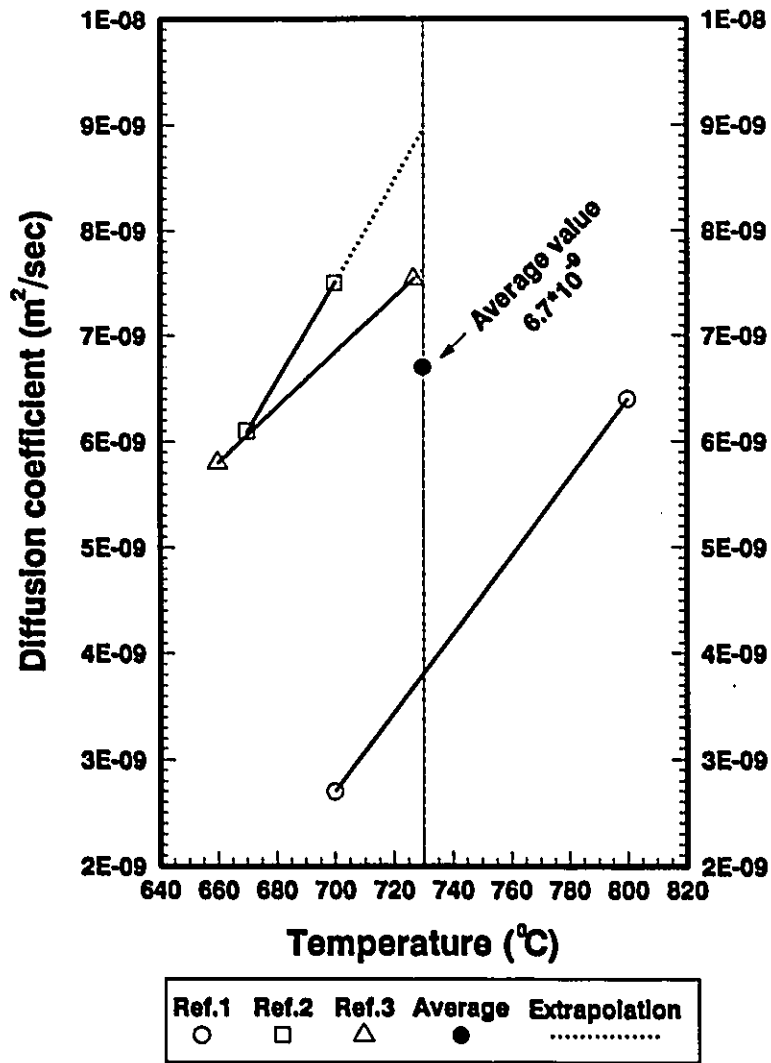


Figure D2. Diffusion coefficient of magnesium in liquid aluminum[D2,D3]

APPENDIX E

Prediction of the surface velocity

In order to predict surface velocities, a set of cold model experiments were carried out.

E.1. Theory:

The important variables that will control the fluid velocity,  $U$ , at the surface of the melt were decided to be volumetric gas flow rate  $Q$ , density of the liquid  $\rho_l$ , density of the gas  $\rho_g$ , viscosity of the liquid  $\mu$ , radius of the container  $r$ , height of the melt  $h$ , gravitational acceleration  $g$ , and speed of the rotation of the impeller  $\omega$ .

In a compact form, the velocity of the liquid at the melt surface can be represented by the following equation:

$$U = f(Q, \rho_l, \rho_g, \mu, r, h, g, \omega) \tag{E.1}$$

A dimensional analysis can be carried out by following the Buckingham's pi theorem[E1] to reduce the number of variables into dimensionless groups. Buckingham's pi theorem states that the number of dimensionless groups will be equal to the number of variables minus the number of dimensions that the variables contain.

Presenting the number of variables and their dimensions in the MLT system in the following form

$U$	$Q$	$\rho_l$	$\rho_g$	$\mu$	$r$	$h$	$g$	$\omega$
$LT^{-1}$	$L^3T^{-1}$	$ML^{-3}$	$ML^{-3}$	$ML^{-1}T^{-1}$	$L$	$L$	$LT^{-2}$	$T^{-1}$

one would see that the number of dimensionless pi groups will be equal to  $9-3=6$ .

Following the procedure described by Isaacson and Isaacson[E1], one would arrive at the following equation:

$$\frac{U r^2}{Q} = f \left( \underbrace{\frac{\rho_l}{\rho_g}}_{\Pi_1}, \underbrace{\frac{r}{h}}_{\Pi_2}, \underbrace{\frac{Q^2}{r^5 g}}_{\Pi_3}, \underbrace{\frac{r^3 \omega}{Q}}_{\Pi_4}, \underbrace{\frac{Q \rho_l}{\mu r}}_{\Pi_5} \right) \quad (\text{E.2})$$

Complete similarity between a model and a prototype requires that all the relevant dimensionless  $\Pi$  groups have the same corresponding values for the model and for the prototype. This means that the dimensionless group  $\Pi_1$  that contains the surface velocity will be the same for the model and prototype provided that the other  $\Pi$  groups are the same for the model and the prototype.

As far as  $\Pi_3$ ,  $\Pi_4$  and  $\Pi_5$  are concerned, the similarity will be achieved by keeping the height of the bath, radius of the container, volumetric gas flow rate and speed of impeller rotation the same for the model and the prototype. Of course one would also have to have the same geometrical configuration as well as the same dimensions for the impeller and the gas injection lance.

The difficulty, however, will arise in matching the  $\Pi$  groups that contain the physical properties of the fluids.

In the case of the density ratios, taking the density of liquid aluminum as 2350 and argon density as 0.487 kg/m<sup>3</sup> (@730 °C) one would obtain  $\Pi_2$  for the prototype as:

$$\Pi_2 = \frac{2350}{0.487} = 4825 \quad (\text{E.3})$$

Ordinary tap water is a common fluid for its abundance and readily availability for modelling purposes. If one is to use tap water the value of the  $\Pi_2$  will be the same for the model only with a gas of density of 0.2072 kg/m<sup>3</sup>.

Helium with a density of 0.166 kg/m<sup>3</sup> @21 °C[E2] is 20% less dense than the required gas density. However, for the purpose of obtaining an estimate value for the surface velocities in the absence of another gas with a closer match to a density of 0.2072 kg/m<sup>3</sup>, the 20% difference will be welcome.

In the case of  $\Pi_6$ , taking the viscosity of liquid aluminum as 1.083\*10<sup>-3</sup> kg/m-sec

@730 °C, one would obtain  $\Pi_6$  for the prototype as:

$$\Pi_6 = \frac{2350}{1.083 \cdot 10^{-3}} \frac{Q}{r} = 2.17 \cdot 10^6 \frac{Q}{r} \quad (\text{E.4})$$

For the model, substituting 1000 kg/m<sup>3</sup> for the density and 0.001 kg/m-sec for the viscosity of water @20 °C one would obtain

$$\Pi_6 = \frac{1000}{1 \cdot 10^{-3}} \frac{Q}{r} = 1 \cdot 10^6 \frac{Q}{r} \quad (\text{E.5})$$

Therefore in order to match  $(\Pi_6)_m = (\Pi_6)_p$  one would have to either increase the gas flow rate twice or reduce the size of the container by half. If one proceeds to do that he will run into problems in matching  $(\Pi_4)_m = (\Pi_4)_p$ ,  $(\Pi_5)_m = (\Pi_5)_p$  and  $(\Pi_1)_m = (\Pi_1)_p$  owing to varying powers of exponents of r and Q in these dimensionless groups.

Therefore at this point one has to make simplifying assumptions. The dimensionless group  $\Pi_6$  is a modified form of the Reynolds number which is the ratio of inertial forces over viscous forces. For a typical gas flow rate of  $56.45 \cdot 10^{-6}$  m<sup>3</sup>/sec and a container radius of 0.07 m, the Reynolds number for the prototype and the model can be calculated to be 1750 and 806 respectively. This means that the viscous forces will be about 3 orders of magnitude smaller than the inertial forces.

The dimensionless group  $\Pi_4$  is a modified form of the Froude number which is the ratio of the inertial forces over gravitational forces. Again taking same numerical values for Q and r one would obtain the value of  $\Pi_4$  to be  $193.3 \cdot 10^{-6}$  which means that the gravitational forces (buoyancy forces in this case) will be 3 orders of magnitude higher than the inertial forces.

The implication of these calculations is that the viscous forces are negligibly small and therefore the dimensionless group  $\Pi_6$  can be discarded from consideration.

With these simplifying assumptions and approximations, the surface velocity of the fluid determined by helium injection into water should give a fair estimate of the surface velocities generated by argon injection into liquid aluminum and aluminum-1 wt% magnesium alloys.

E.2 Experimental:

In the experiments, the height of the water column, radius of the container and the speed of rotation of the impeller were the same as those in the molten metal experiments. The geometrical configuration as well as the dimensions of the impeller and the gas injection lance were kept the same as those in the prototype.

The gas flow rate covered the range used in the prototype. 0.5 cm diameter paper chips were dropped on the centre of the water surface and their motions were recorded by a film recorder. The velocity of the paper chips was determined by tracing the paper chips frame by frame in slow motion (30 frames/sec) on a TV screen.

E.3 Results:

Figure E1 shows the surface velocities as a function of gas flow rate. Up to 60 cc/sec gas flow rate, the surface velocity increased with increase in the gas flow rate. After this, the surface velocities reached a plateau. With increase in the gas flow rate beyond 100 cc/sec, the surface velocity dropped. This was possibly the result of increased degree of wave generation at the surface which would oppose the outward radial velocity component of the fluid.

Figure E2 shows the dimensionless surface velocity  $\Pi_1$  as a function of the modified Froude number  $\Pi_4$ . The last point in the previous figure was not included in this figure. A regression analysis gave an equation of the following form:

$$\frac{U r^2}{Q} = 1.074 \left( \frac{Q^2}{r^5 g} \right)^{-0.347} \quad (\text{E.6})$$

References:

- E1. E.de St Q. Isaacson, M.de St Q. Isaacson, "Dimensional Methods in Engineering and Physics", Edward Arnold, 1975
- E2. G.A. Cook, "Argon, Helium and Rare Gases", Volume 1. History, Occurrence, and Properties, Interscience Publishers, 1961

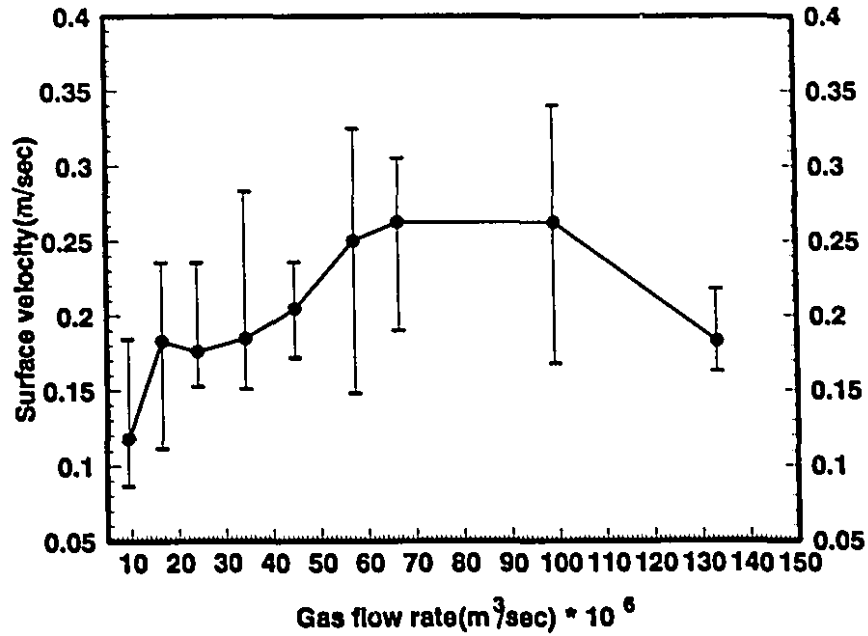


Figure E1. Radial surface velocity as a function of gas flow rate(at NTP)

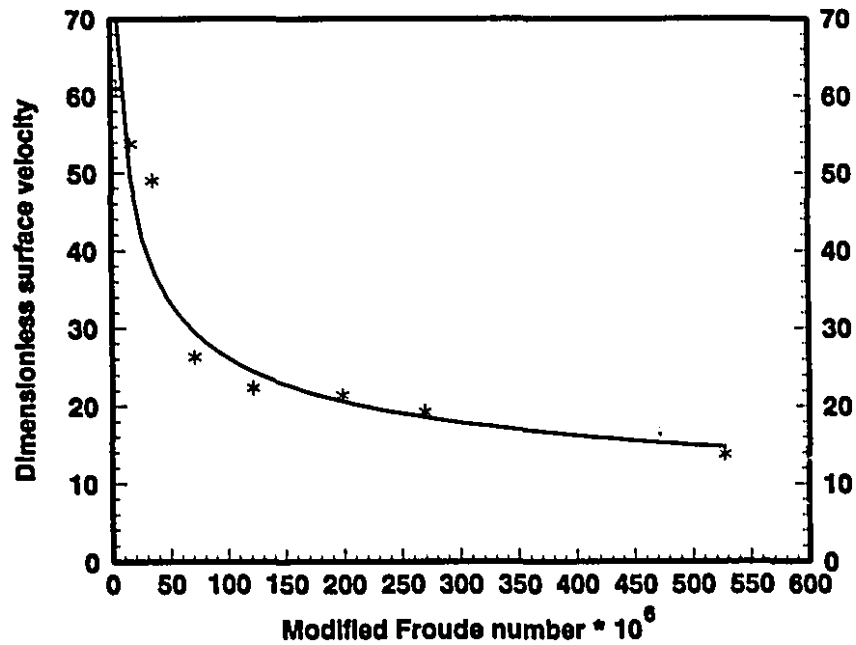


Figure E2. Dimensionless radial surface velocity as a function of Modified Froude number

APPENDIX F:Size and number distribution of the particles

**Table F1.** Size and number distribution of the particles in the melt (7.5 kg) before and after chlorination;  
 $Q=26.22$  cc/sec(730 °C, 1 Atm), Vol% Cl<sub>2</sub>=2

Particle size range ( $\mu\text{m} \times 10^6$ )	Number of particles		
	Initial	Final	Difference
21-23	3789	16298	12509
24-26	1010	8610	7600
27-29	1136	4613	3477
30-32	1010	2460	1450
33-35	1263	1845	582
36-38	379	1538	1159
39-41	0	308	308
42-44	253	308	55
45-47	379	0	-379
48-50	0	0	0
51-53	379	923	544
54-56	253	0	-253
57-59	0	0	0
60-62	0	0	0
63-65	0	0	0
66-68	0	0	0
69-71	126	0	-126
<b>Total</b>	<b>9978</b>	<b>36900</b>	<b>26922</b>

**Table F2.** Size and number distribution of the particles in the melt (7.5 kg) before and after the chlorination;  
 $Q=26.22$  cc/sec(730 °C, 1 Atm), Vol%  $Cl_2=10$

Particle size range ( $m \cdot 10^6$ )	Number of particles		
	Initial	Final	Difference
21-23	3000	10548	7548
24-26	4000	5626	1626
27-29	400	3868	3468
30-32	1400	1875	475
33-35	200	1172	972
36-38	1600	820	-780
39-41	800	586	-214
42-44	400	234	-166
45-47	0	352	352
48-50	800	234	-566
51-53	600	117	-483
54-56	400	234	-166
57-59	400	234	-166
60-62	0	117	117
63-65	0	0	0
66-68	200	0	-200
69-71	0	117	117
<b>Total</b>	<b>14200</b>	<b>26136</b>	<b>11936</b>

Table F3. Size and number distribution of the particles in the melt (7.5 kg) before and after chlorination;  $Q=26.22$  cc/sec(730 °C, 1 Atm), Vol%  $Cl_2=10$

Particle size range ( $m \cdot 10^6$ )	Number of particles		
	Initial	Final	Difference
21-23	5746	25075	19329
24-26	2704	17988	15284
27-29	1183	9812	8629
30-32	1183	5451	4268
33-35	676	5451	4775
36-38	338	1090	752
39-41	507	4361	3854
42-44	169	545	376
45-47	338	0	-338
48-50	169	1090	921
51-53	338	1635	1297
54-56	507	545	38
57-59	0	0	0
60-62	338	0	-338
63-65	169	0	-169
66-68	0	545	545
69-71	507	0	-507
Total	14872	73589	58716

**Table F4.** Size and number distribution of the particles in the melt (7.5 kg) before and after chlorination;  
 $Q=26.22$  cc/sec( $730^{\circ}\text{C}$ , 1 Atm), Vol%  $\text{Cl}_2=25$

Particle size range ( $\text{m} \cdot 10^6$ )	Number of particles		
	Initial	Final	Difference
21-23	4246	6200	1954
24-26	738	6200	5462
27-29	738	3200	2462
30-32	923	2200	1277
33-35	0	1600	1600
36-38	0	600	600
39-41	554	400	-154
42-44	369	0	-369
45-47	0	600	600
48-50	0	0	0
51-53	185	0	-185
54-56	0	0	0
57-59	185	0	-185
60-62	0	0	0
63-65	0	0	0
66-68	0	0	0
69-71	0	200	200
<b>Total</b>	<b>7938</b>	<b>21200</b>	<b>13262</b>

Table F5. Size and number distribution of the particles in the melt before and after chlorination;  $Q=26.22$  cc/sec(730 °C, 1 Atm), Vol%Cl<sub>2</sub>=25

Particle size range (m*10 <sup>6</sup> )	Number of particles		
	Initial	Final	Difference
21-23	3100	38745	35645
24-26	2696	18450	15754
27-29	1752	11993	10241
30-32	1618	3690	2072
33-35	1213	3690	2477
36-38	270	0	-270
39-41	270	1845	1575
42-44	404	2768	2364
45-47	539	2768	2229
48-50	135	0	-135
51-53	270	923	653
54-56	135	923	788
57-59	135	0	-135
60-62	0	923	923
63-65	135	0	-135
66-68	135	0	-135
69-71	539	923	384
Total	13345	87638	74293

**Table F6.** Size and number distribution of the particles in the melt (7.5 kg) before and after chlorination;  
 $Q=56.45$  cc/sec(730 °C, 1 Atm), Vol%  $Cl_2=10$

Particle size range ( $m \cdot 10^6$ )	Number of particles		
	Initial	Final	Difference
21-23	3750	14019	10269
24-26	3500	9301	5801
27-29	1250	5392	4142
30-32	250	3640	3390
33-35	750	2426	1676
36-38	1250	1213	-37
39-41	750	944	194
42-44	250	944	694
45-47	0	1078	1078
48-50	250	270	20
51-53	0	674	674
54-56	0	270	270
57-59	0	135	135
60-62	0	404	404
63-65	0	0	0
66-68	0	0	0
69-71	0	135	135
<b>Total</b>	<b>12000</b>	<b>40844</b>	<b>28844</b>

Table F7. Size and number distribution of the particles in the melt (7.5 kg) before and after chlorination; Q=91.12 cc/sec(730 °C, 1 Atm), Vol% Cl<sub>2</sub>=10

Particle size range (m*10 <sup>6</sup> )	Number of particles		
	Initial	Final	Difference
21-23	11422	134378	122956
24-26	1713	67189	65476
27-29	2856	44564	41708
30-32	0	27767	27767
33-35	571	18511	17940
36-38	571	10626	10056
39-41	0	10284	10284
42-44	0	10284	10284
45-47	0	5485	5485
48-50	0	5828	5828
51-53	571	2057	1486
54-56	571	2057	1486
57-59	0	1714	1714
60-62	571	2057	1486
63-65	0	2742	2742
66-68	0	343	343
69-71	0	2743	2743
Total	18846	348630	329784

**Table F8.** Size and number distribution of the particles in the melt (7.5 kg) before and after chlorination;  
 $Q=91.12$  cc/sec( $730^{\circ}\text{C}$ ), Vol%  $\text{Cl}_2=10$

Particle size range ( $\text{m} \cdot 10^6$ )	Number of particles		
	Initial	Final	Difference
21-23	5996	46800	40804
24-26	2398	22950	20552
27-29	1542	14400	12858
30-32	685	9000	8315
33-35	343	7350	7007
36-38	514	4800	4286
39-41	0	3600	3600
42-44	0	3600	3600
45-47	0	1950	1950
48-50	0	1950	1950
51-53	0	900	900
54-56	0	750	750
57-59	171	0	-171
60-62	0	300	300
63-65	0	150	150
66-68	0	300	300
69-71	0	1050	1050
<b>Total</b>	<b>11648</b>	<b>119850</b>	<b>108202</b>

**Table F9.** Size and number distribution of the particles in the melt (7.5 kg) before and after chlorination;  
 $Q=91.12$  cc/sec(730 °C, 1 Atm), Vol%  $Cl_2=10$

Particle size range ( $m \cdot 10^6$ )	Number of particles		
	Initial	Final	Difference
21-23	11995	57800	45805
24-26	3058	25000	21942
27-29	6586	31600	25014
30-32	3058	14200	11142
33-35	2822	9400	6578
36-38	1646	6200	4554
39-41	1176	5200	4024
42-44	706	4400	3694
45-47	470	2000	1530
48-50	470	1800	1330
51-53	470	2400	1930
54-56	235	1000	765
57-59	470	800	330
60-62	470	800	330
63-65	0	0	0
66-68	706	400	-306
69-71	470	2000	1530
Total	34808	165000	130192

APPENDIX G:Sources of error

There are two sources of error in the gas fluxing experiments. These are 1) Measurement of the gas flow rate, 2) Chemical analysis of the melt samples

The flowmeters used for measuring argon and chlorine gas flow rates were Gilmont compact flowmeters. These flowmeters were periodically calibrated by using a standard soap-meter for chlorine gas and by using a wet-test meter for argon gas flow rate. Corrections to the gas flow rate for various line pressures were done by using the correction charts supplied with the flowmeters. As presented in Figure 3.5 in Chapter 3, the calibration chart for the chlorine gas gave different slopes within the gas flow rate range of 0-3 cc/sec at NTP. For the lowest chlorine gas flow rate under the experimental conditions the position of the float was at 15 which is very close to the point of sharp deflection. Any small change of line pressure would have pronounced effect on the flow rate at that point. At the particular gas flow rate where volume% Cl<sub>2</sub> was stated to be 2% it is expected that the error in the chlorine gas flow rate was in the range of  $\pm 75\%$ . At higher chlorine concentrations the error should be much less than the above stated value. In the case of the calibration for the argon gas flow rate the functional relationship between float position and gas flow rate at NTP was linear and the author does not expect any appreciable error for the flow rate of the argon.

The chemical analysis of the melt samples was carried out by using an optical emission spectrometer in the Alcan Research and Development Centre at Kingston. The detection limit for the calcium and sodium was stated to be to be 0.5 wt-ppm. Accuracy of the measurements was stated to be of the same order as the detection limit. Therefore at a level of 1 wt-ppm concentration level the error was at the order of  $\pm 50\%$  which decreases as the concentration of the above mentioned elements increases.